CHEMICAL REVIEWS

pubs.acs.org/CR

Review

Graphene-Based Metal–Organic Framework Hybrids for Applications in Catalysis, Environmental, and Energy Technologies

Kolleboyina Jayaramulu,*[,‖] Soumya Mukherjee,[‖] Dulce M. Morales, Deepak P. Dubal, Ashok Kumar Nanjundan, Andreas Schneemann, Justus Masa, Stepan Kment, Wolfgang Schuhmann, Michal Otyepka, Radek Zbořil,* and Roland A. Fischer*

Cite This: *Chem. Rev.* 2022, 122, 17241–17338

Read Online

ACCESS | Metrics & More | Article Recommendations

ABSTRACT: Current energy and environmental challenges demand the development and design of multifunctional porous materials with tunable properties for catalysis, water purification, and energy conversion and storage. Because of their amenability to de novo reticular chemistry, metal–organic frameworks (MOFs) have become key materials in this area. However, their usefulness is often limited by low chemical stability, conductivity and inappropriate pore sizes. Conductive two-dimensional (2D) materials with robust structural skeletons and/or functionalized surfaces can form stabilizing interactions with MOF components, enabling the fabrication of MOF nanocomposites with tunable pore characteristics. Graphene and its functional derivatives are the largest class of 2D materials and possess remarkable compositional versatility, structural diversity, and controllable surface chemistry. Here, we critically review current knowledge concerning the growth, structure, and properties of graphene derivatives, MOFs, and their graphene@MOF composites as well as the associated structure–property–performance relationships. Synthetic strategies for preparing graphene@MOF composites and tuning their properties are also comprehensively reviewed together with their applications in gas storage/separation, water purification, catalysis (organo-, electro-, and photocatalysis), and electrochemical energy storage and conversion. Current challenges in the development of graphene@MOF hybrids and their practical applications are addressed, revealing areas for future investigation. We hope that this review will inspire further exploration of new graphene@MOF hybrids for energy, electronic, biomedical, and photocatalysis applications as well as studies on previously unreported properties of known hybrids to reveal potential "diamonds in the rough".

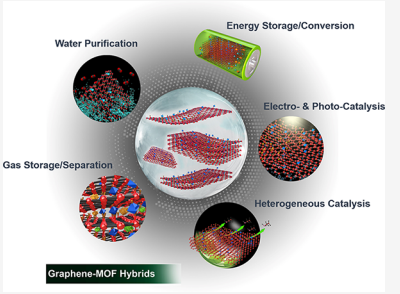

CONTENTS

Received: April 25, 2022
Published: November 1, 2022

https://doi.org/10.1021/acs.chemrev.2c00270
Chem. Rev. 2022, 122, 17241–17338

1. INTRODUCTION

Motivated by the need to reduce carbon footprints and develop clean energy conversion and storage technologies, considerable research effort has been invested into the design and engineering of porous materials. Metal−organic frameworks (MOFs) are a relatively new class of crystalline materials formed by the coordination of metal ions/clusters and organic bridging ligands.[1−9] Because of their high specific surface areas, substantial pore volumes, high concentrations of active metal sites, adjustable structures, and tunable pore diameters, MOFs have diverse applications in fields including gas storage/separation,[10,11] catalysis,[12−15] water harvesting,[16−19] sensing,[20−25] water purification,[26] supercapacitors,[27−31] and batteries.[32−37] Although MOFs are either insulators or poor conductors and thus have inherently limited conductivity,[38,39] they can perform extremely well in catalytic applications and energy storage systems such as supercapacitors and batteries.

Efforts have been made to improve the conductivity of MOFs by developing hybrid materials in which MOFs are integrated with various conductive guests including conductive polymers,[40−43] quantum dots,[44] or carbonaceous materials.[45−47] A wealth of two-dimensional (2D) materials have come to the fore in the past few decades, including but not limited to 2D transition-metal carbides, nitrides, and carbonitrides (MXenes),[48] molybdenum disulfide (MoS_2),[49] boron nitride (BN),[50] and carbon allotropes (fullerenes,[51] carbon nanotubes,[52] graphene, etc.). An allotrope of carbon, graphene refers to a monolayer of hexagonally arranged carbon atoms, a layer that is typically only one C atom (diameter ≈ 0.33 nm) thick. Since its first discovery in 2004,[53] graphene-based materials have witnessed a meteoric rise (ca. 10 000 scientific articles published every year, plus the 2013 launch of *Graphene Flagship* as a €1 billion European Union scientific research initiative) which is a testament to the unique combination of graphene's extraordinary properties. Thanks to its high thermal as well as electrical conductivity and theoretical surface area of 2630 m^2/g,[54−57] such a rich confluence of record-high physical and chemical properties endorses the proverbial expression "wonder material" for graphene.[58] Notably, the ultrathin thickness (ideally a single molecular layer) and the large lateral extension endow graphene-based materials with properties suitable for membranes used in environmental applications, specifically those with high flux and low transparent resistance.[59−62] In addition, the smart integration of MOFs with graphene and its derivatives was shown to significantly enhance the efficiency of energy conversion and storage devices while reducing their fabrication costs, thereby creating new opportunities for real-world applications. Graphene-based MOF hybrids share the advantages of both of their constituents and have therefore recently attracted considerable scientific interest.

Global industrialization has created a number of serious environmental problems including hazardous levels of water and air pollution in some places. Consequently, several ongoing research efforts seek to develop improved adsorbents for air and water purification. MOFs are among the most promising adsorbents for this purpose because of their high porosity, structural diversity, and remarkable ion exchange behavior.[63−66] However, their large void spaces and poor stability limit their applications in this context.[67−70] To address these problems, researchers have developed hybrid materials by combining graphene-based materials with MOFs. The resulting composites alleviate a key weakness of MOFs, namely, their ultralow atom density, and therefore have superior adsorptive properties. The incorporation of graphene-based materials into MOFs can also form more active structures for reactive adsorption.[71,72]

Electrode materials for energy conversion and storage devices need high electrical conductivity, a high surface area with an adequate pore volume, good crystallinity to ensure a high energy output, and high structural stability that must be reinforced via appropriate material/electrode design to ensure long cycling performance.[73,74] The development of improved electrode materials will require a deep understanding of interfacial electrode−electrolyte chemistry, including the roles of cations and anions in the electrochemical double-layer region, their dynamic behavior during electrochemical conversion, and their correlations. The synergistic properties of MOFs and graphene have been exploited to create composite frameworks incorporating few-layer graphene sheets with large interlayer spacings. This approach is seen as an attractive way to prepare conductive materials with hierarchical pore structures and high surface areas. In these composites, functionalized graphene derivatives form stabilizing covalent and noncovalent interactions with MOF nanoparticles that promote their growth while also controlling their structure, size, and shape.[75−79]

Previous reviews have provided excellent coverage of the literature on certain specific types of MOF composites including composites with 2D materials,[80−82] carbon-based materials,[45−47] and nanoparticles.[83−86] In addition, a few reviews have focused on the structure−property−performance relationships of graphene@MOF hybrids for energy and environmental applications.[87−91] However, despite the vast potential of MOF/graphene-based materials, there has been no effort to

https://doi.org/10.1021/acs.chemrev.2c00270
Chem. Rev. 2022, 122, 17241−17338

comprehensively review what is known about their fabrication, general structure−property−performance relationships, and rational design. This review therefore aims to describe, summarize, and analyze the literature on graphene@MOF hybrids and their applications in catalysis, environmental remediation, and energy storage/conversion. The review is divided into five main sections. Section 2 provides a general introduction to the research field and the motivation for using graphene@MOF hybrids in various applications. Section 3 focuses on the material properties necessary for applications in catalysis, environmental remediation, and energy conversion/storage. Key properties of graphene@MOF hybrid materials including their conductivity, stability, and textural, morphological, and surface properties are discussed and compared to those of their constituent materials (i.e., MOFs and graphene derivatives) to derive guidelines for designing and preparing hybrids suitable for specific applications. Section 4 summarizes published synthetic approaches to graphene@MOF hybrids and explains how different approaches can be related to the design guidelines established in the preceding section. Section 5 focuses on the potential applications of graphene@MOF hybrids in catalysis, energy, and environmental technologies, referring back to the previously established guidelines to explain how the properties of the hybrids' constituent materials and their synergies enable high performance in targeted applications. Section 6 offers some general conclusions concerning the state of the art and highlights some promising future developments of graphene@MOF hybrids as well as elucidating current challenges and drawbacks. Overall, this review aims to provide a comprehensive overview of all major aspects of graphene@MOF hybrids, in contrast to previous reviews that focused on specific subareas within this field.

1.1. Scope of this Review

Since graphene's discovery in 2004, it has found diverse applications in high-speed electronics, data storage systems, supercapacitors, solar cells, electrochemical sensing, textile engineering, printing technology, and biomedical engineering.[92−95] Hybrid materials incorporating graphene have also been prepared and used in various fields. Of the known types of graphene-based hybrid materials, graphene@MOF hybrids are particularly interesting. These materials were first described in 2009 by the research group of Teresa J. Bandosz[96] and have subsequently attracted considerable academic interest, leading to the publication of many research articles. Graphene@MOF hybrid materials have since been used in areas including catalysis, energy storage and conversion, gas storage/separation, biomedicine, water treatment, and sensing.[97]

Despite having attracted such interest, the potential of graphene@MOF hybrids has yet to be fully explored, largely because of our limited understanding of their structure−property relationships and the difficulty of fully characterizing these materials. This review therefore provides a critical overview of current knowledge concerning the structure−property relationships of graphene@MOF hybrids by comparing the properties of known hybrids to those of their constituent materials including MOFs, graphene, and their functionalized derivatives. We also discuss several hybridization strategies for preparing graphene@MOF hybrids with specific desired properties and highlight the challenges of characterizing graphene@MOF hybrids. We anticipate that wider recognition of these challenges and the precautions that are needed to overcome them will encourage researchers to use appropriate characterization protocols and thereby improve the quality of the literature in this area. The next section of the review focuses on synthetic methods that enable rational fabrication of graphene@MOF hybrids with properties tailored to specific applications followed by an overview of the reported applications of graphene@MOF hybrids in catalysis, environmental remediation, and energy technology. This systematic study of recent advances in this field of graphene@MOF hybrids provides a broad overview of the field's rapidly evolving state of the art and is expected to spur further research on these remarkable materials. We conclude by highlighting future directions and research opportunities in the field of graphene@MOF hybrids.

2. OVERVIEW OF THE STRUCTURE AND PROPERTIES—DESIGN CRITERIA TOWARD APPLICATIONS

2.1. Properties of Pristine Materials

The pristine constituent materials of graphene@MOF hybrids, namely, graphene derivatives and MOFs, have a number of interesting and useful properties in their own right. However, their usefulness in certain applications is limited by some intrinsically unfavorable characteristics. This section briefly introduces the properties of these materials and the challenges they present and shows how the hybridization of MOFs with graphene derivatives can overcome some of these challenges.

2.1.1. Graphene. Graphene is a two-dimensional (2D) carbon allotrope[98] that was first isolated by mechanical peeling (exfoliation) of individual atomic layers of graphite in 2004.[53] While the exfoliation method produces high-quality graphene, it is impractical for large-scale production. Larger graphene sheets with sizes on the order of meters can be grown via chemical vapor deposition (CVD).[99,100] Alternatively, graphene can be obtained by (electro)chemical exfoliation of graphite or chemical or thermal reduction of graphene oxide.[101−103]

A graphene sheet is essentially a single graphite layer consisting of sp^2-hybridized carbon atoms arranged in a flat honeycomb-like lattice. This structure gives graphene unique physical and chemical properties. For example, graphene only absorbs 2.3% of white light and is therefore highly optically transparent.[104] In addition, it has no band gap because its valence and conductive bands touch at the Dirac point, making it a semimetal.[105] Its electrical (2×10^5 cm^2/(Vs))[106] and thermal (5×10^3 W/mK)[107] conductivities exceed those of copper, but its electrical conductivity is highly sensitive to impurities, dopants, chemical functionalization, adsorbates, and the number of stacked graphene layers in the sample. The adsorption of a single molecule can be enough to appreciably affect graphene's electronic properties, which can be exploited when designing sensors[108] and also means that the electronic properties of graphene can change substantially when it is incorporated into composite materials. Another notable property of graphene is its very high surface area of 2630 m^2/g. Its chemical composition makes graphene flexible but also strong and rather chemically inert. Atoms and molecules cannot pass through graphene sheets. Finally, graphene is a hydrophobic material whose colloidal suspensions in water and various polar solvents are unstable and prone to restacking and precipitation.

Some sensing, electronic, and biological applications of graphene benefit from significant modulation of its properties, which may include band gap opening or the introduction of specific hydrophilic functional groups on its surface. This can be

https://doi.org/10.1021/acs.chemrev.2c00270
Chem. Rev. 2022, 122, 17241−17338

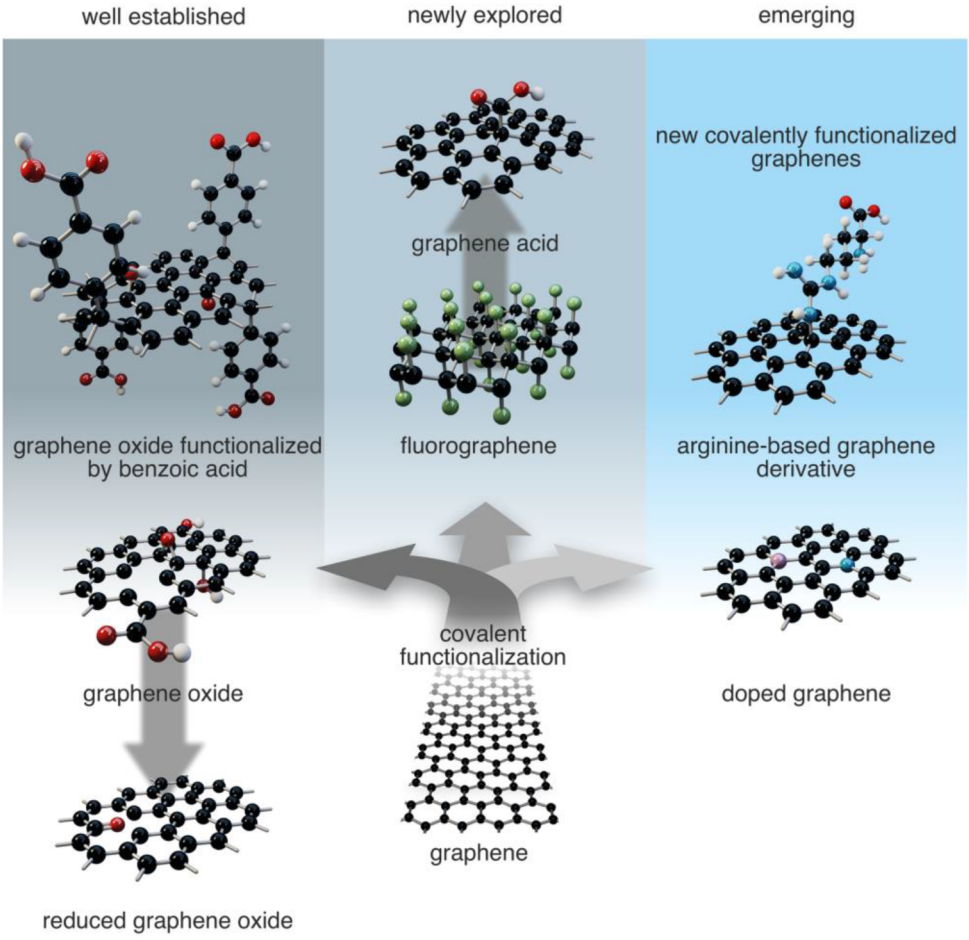

Figure 1. Schematic depiction of various graphene derivatives that have been hybridized with MOFs. Graphene itself lacks suitable functional groups for covalent hybridization with MOF. However, graphene oxide, reduced graphene oxide, and benzoic acid-functionalized graphene oxide have all been successfully combined with MOFs. Chemistry of fluorographene derivatives such as graphene acid also allows formation of stable nanocomposites with MOFs. Novel graphene derivatives and variously doped graphenes offer new possibilities for hybridization with MOFs. Carbon, oxygen, fluorine, and nitrogen centers are represented in black, red, green, and blue, respectively.

achieved through graphene functionalization.[109] Both covalent and noncovalent methods for graphene functionalization have been established. Noncovalent functionalization involves the formation of graphene composites that are stabilized solely by noncovalent interactions, primarily London dispersion interactions.[110] Such composites are readily prepared by simply mixing their components and cause only gentle modulation of graphene's properties.[111] Covalent graphene functionalization leads to the formation of graphene derivatives or doped graphene sheets whose properties may differ substantially from those of pristine graphene.

2.1.2. Graphene Derivatives. Pristine graphene (a nanoallotrope of pure carbon) contains no chemical functional groups amenable to covalent functionalization and cross-linking with other molecules or materials. To overcome this disadvantage, many research groups have attempted to imprint chemical functionality at the edges of graphene sheets and/or on the graphene surface (i.e., the basal plane). Covalent functionalization of graphene leads to significant modulation of its properties because sp^2 carbons are replaced by sp^3 carbons in the lattice, leading to the introduction of scattering centers and lattice imbalance. This causes band gap opening and reduces conductivity and can give rise to magnetism. Because pure graphene is rather chemically inert, its direct covalent functionalization requires treatment with highly reactive species such as cold atomic plasma,[112] ozone,[113] or free radicals.[114] Many different graphene derivatives have been prepared (see Figure 1), and these materials have been reviewed extensively.[109,115] We therefore focus here only on particularly prominent or promising graphene derivatives that have already been used in composites with MOFs or could beneficially be incorporated into such composites.

The most important graphene derivatives at present are undoubtedly graphene oxide (GO),[102] halogenated graphenes,[116] and graphane.[112] GO is usually prepared by extensive oxidation of graphene or by oxidizing graphite to graphite oxide and then exfoliating it to obtain GO. Oxidation introduces various oxygen-containing chemical groups on the graphene surface and gives rise to several types of structural defects. GOs are chemically complex materials featuring oxygen-containing functional groups attached to both edges (e.g., carboxyl groups) and the surface (e.g., epoxy and hydroxyl groups) of the graphene lattice.[102,117] GO therefore has a negative surface charge and is dispersible in water. It should be noted that the chemical composition of GO depends on the method used in its synthesis. The oxygen-containing functional groups of GO enable cross-linking and facilitate its immobilization in nanocomposites that are stabilized by electrostatic interactions and

https://doi.org/10.1021/acs.chemrev.2c00270
Chem. Rev. 2022, 122, 17241−17338

hydrogen bonding. Unfortunately, GO is nonconductive, which limits its potential applications. Its conductivity can be restored by chemical or thermal reduction; both chemically reduced GO (rGO) and thermally reduced GO (trGO) have a lower density of oxygen-containing functional groups than GO. While this reduces their capacity for cross-linking and immobilization, it has the benefit that rGO and trGO are conductive and can retain their conductivity in nanocomposites.[118,119] The presence of oxygen-containing functional groups on the graphene surface has been used to prepare nanocomposites with MOFs, as discussed later in this review. Nucleation centers for the growth of MOF on top of graphene can also be introduced by functionalization of GO and rGO. For instance, Loh et al. functionalized rGO with benzoic acid and used the resulting material to prepare composites with MOF-5.[77]

Fluorographene (FG) is a stoichiometrically fluorinated stable graphene derivative in which graphene's flat sp^2 carbon lattice is converted into a hexagonal lattice of tetrahedral (sp^3) carbons each bearing one fluorine atom. FG is therefore nonconductive and hydrophobic.[120] It is also readily available because it can be prepared by exfoliating graphite fluorite, which is a commercially available industrial lubricant.[121] A great advantage of FG is that it undergoes a range of chemical reactions, enabling the preparation of diverse homogeneously surface-functionalized graphene derivatives[122] such as cyanographene and graphene acid (GA) (Figure 1). These materials stand out among the known graphene derivatives due to their well-defined chemical composition and extensive functionalization (their degree of functionalization is typically above 10%), which means that they have many interaction/reaction sites that can be exploited in the fabrication of nanocomposites. For instance, GA can be cross-linked with amines,[123] enzymes,[124] and nanoparticles[125] because its content of −COOH functional groups suitable for cross-linking with other materials is around 15%.[123] GA was also recently hybridized with the amine-functionalized MOF UiO-66.[75] The highly reproducible synthesis of GA together with its stability and conductivity make it well suited for electrochemical applications[126,127] and for fabricating cross-linked conductive composites. It is worth noting that highly fluorinated graphite powder can also be oxidized using a modification of Hummer's method to obtain highly fluorinated GO, which was efficiently hybridized with the zeolitic imidazolate framework ZIF-8 ($Zn(mim)_2$, where Hmim = 2-methylimidazole) to obtain a material that was very effective in oil−water separation.[128] Particular attention should be paid to newly emerging graphene derivatives because they offer unique properties and chemical functionality that can be exploited to prepare novel hybrid materials.

The graphene lattice can also be modified within the plane by doping, i.e., by substituting carbon atoms with other either lightweight (e.g., B and N) or heavy elements (e.g., transition metals).[129] The properties of such doped graphenes depend on the doping element and its concentration. The doping element modulates the graphene band gap, may introduce magnetism, and can function as a reactive center, which may be useful in catalysis.[130] Doped graphenes can be prepared by CVD, bottom-up synthesis, photochemical methods, and wet chemical methods[129] or by treatment of graphene derivatives.[131] Such doped graphenes can be utilized as nanocomposite building blocks that introduce new features.

2.1.3. Metal−Organic Frameworks (MOFs). Metal organic frameworks are an interesting class of organic−inorganic hybrid materials with porous architectures consisting of metal ions/clusters and multifunctional organic linkers.[132,133] The interesting physicochemical properties of these materials include exceptionally high surface areas (peak value ≈ 10 000 $m^2\ g^{-1}$),[134−138] low densities, hierarchical pore structures, and widely tunable properties, giving them many advantages over conventional porous materials such as zeolites and porous carbons.[139−141] Because of their remarkable physicochemical properties, MOFs have been used in diverse applications including gas storage/separation,[135,142] sensing/molecular recognition,[143,144] energy storage/conversion,[145,146] catalysis,[147,148] and drug delivery.[149−151] Interest in the study and synthesis of these materials has increased dramatically over the last two decades; the progress of this research field was illustrated by a review published by Furukawa et al. in 2013, according to which >20 000 MOFs have been synthesized.[152] More recent articles estimate that over 100 000 individual MOFs have been prepared and reported.[153,154] The most prominent feature of MOFs is their tunability, which enables the creation of a vast range of structures with different porosity, stability, and morphology.[155,156] The structure and properties of MOFs can be adjusted by altering their metal ions/clusters and ligands or by following different synthetic procedures. However, their practical usefulness is often limited by their structural stability: many of these materials are unstable under harsh thermal and chemical environment.[68,157] Moreover, many MOFs are moisture sensitive, which further limits their potential applications.[158] A range of methods have been proposed to overcome this problem and enable the full potential of MOFs to be exploited.[67] One particularly attractive approach is to hybridize MOFs with other materials such as functionalized graphene or other 2D layered materials.[159] The beneficial effects of fabricating graphene@MOF hybrids are discussed briefly in the next section.

2.1.4. MOF-Graphene/Graphene-Derivative Nanocomposites. As described above, MOFs have many advantageous properties that make them attractive materials for diverse applications. However, their practical utility is limited by some of their physicochemical features, namely, low conductivity, poor stability in various environments, and low mechanical processability. Their usability can be increased by hybridization with other materials because some of the resulting nanocomposites are not subject to these limitations. Graphene and its derivatives seem to be particularly attractive materials for hybridization with MOFs due to their high conductivity and chemical stability. It should be noted that all graphene derivatives are potential MOF structuring agents due to their flat but flexible sheet structure. This feature together with the wealth of MOF structures and morphologies and the availability of graphene-type lattices bearing diverse functionality (graphene derivatives) could enable the fabrication of a vast portfolio of graphene/MOF composites with useful properties.

Most nanocomposites of MOFs and graphene-based materials that have been reported to date were formed by hybridizing MOFs with GO or rGO/trGO. In the pioneering studies of the Bandosz group, GO was used as a structuring agent for MOFs; the first GO-MOF-5 hybrid (MOF-5 = $Zn_4O(bdc)_3$ with bdc^{2-} = 1,4-benzenedicarboxylate) adopted a layered sandwich structure with alternating layers of GO and MOF.[96] The structure of the MOF-5/GO nanocomposite was stabilized by interactions between the epoxy groups of GO and the ZnO_4 clusters of MOF-5; the MOF's metal SBUs (secondary building units) formed coordinative bonds with the oxygen-containing functional groups of GO and in turn functioned as nucleation

https://doi.org/10.1021/acs.chemrev.2c00270
Chem. Rev. 2022, 122, 17241−17338

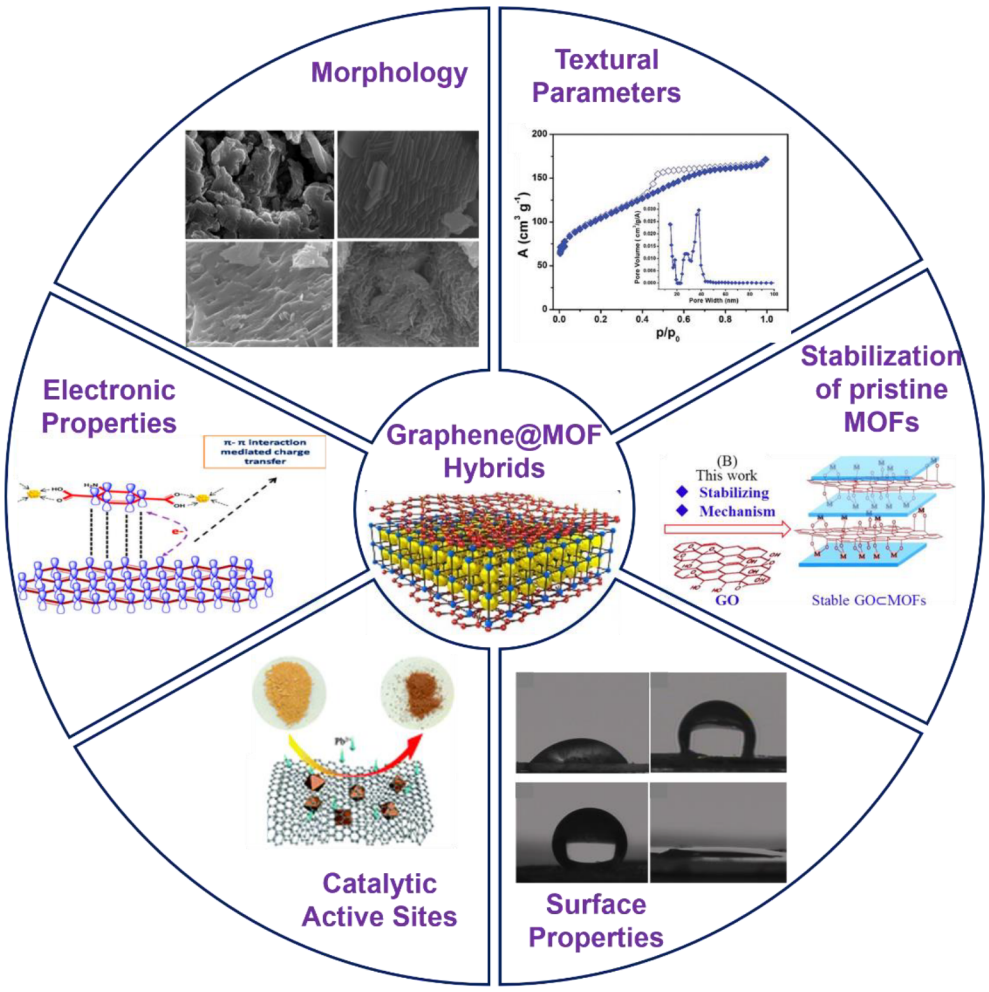

Figure 2. Schematic illustration of the properties enhanced by the hybridization of graphene/derivatives and MOFs, which include textural properties (Reproduced with permission from ref 76. Copyright 2021 John Wiley & Sons, Inc.), morphological properties (Reproduced with permission from ref 96. Copyright 2009 John Wiley & Sons, Inc.), electronic properties (Reproduced with permission from ref 169. Copyright 2018 American Chemical Society.), active sites (Reproduced with permission from ref 170. Copyright 2019 Royal Society of Chemistry.), surface property (Reproduced with permission from ref 128. Copyright 2016 John Wiley & Sons, Inc.), and stability of pristine MOFs (Reproduced with permission from ref 171. Copyright 2018 American Chemical Society.).

centers for the growth of MOF crystals. The growth of MOFs on the GO surface generates a microporous nanocomposite whose porosity can be controlled by varying the content of GO and the choice of MOF.[96,160,161] The microporosity of a MOF/GO nanocomposite also depends on the compatibility of the MOF's structural features with those of GO. Mounting of the cubic MOFs MOF-5 or HKUST-1 (Hong Kong University of Science and Technology; Cu_3BTC_2 with BTC^{3-} = 1,3,5-benzenetricarboxylate) onto GO surfaces leads to well-structured nanocomposites, whereas very disordered nanocomposites are obtained when using the spherical MIL-100(Fe) (Matériaux de l'Institut Lavoisier; $Fe_3O(H_2O)_2(X)(BTC)_2$ with $X = F^-$ or OH^-).[161] The approach of using GO as a structuring agent for MOF growth pioneered by Petit and Bandosz was further elaborated by Loh et al., who used benzoic acid-functionalized rGO (BFG) as a nucleation template for growing MOF/BFG nanowires. In addition to its structural role, the functionalized rGO introduced conductivity into the MOF/rGO nanocomposites,[77] which were subsequently utilized in electrocatalysis.[162−164] The ability to tailor the porosity of MOF/GO nanocomposites is also beneficial for gas adsorption,[161,165] as discussed in section 2.2.1, and in the previously discussed separation of oil and water using composites of ZIF-8 with highly fluorinated GO. In this case, the highly fluorinated GO prepared from highly fluorinated graphite using the modified Hummers method endowed the nanocomposite with mesoporosity that complemented the intrinsic microporosity of the ZIF-8 nanocrystals.[128] More recently, a covalently connected nanocomposite of the amine-functionalized MOF UiO-66 ($Zr_6O_4(OH)_4(NH_2\text{-bdc})_6$, where NH_2-bdc denotes the 2-amino-1,4-benzenedicarboxylate dianion) was prepared using graphene acid as a templating agent. The resulting material exhibited hierarchical porosity and conductivity while also containing imide and amine groups that can serve as interaction sites for CO_2. These features were exploited for electrochemical sensing of CO_2; the material displayed a very fast response and had a quick recovery time of ∼18 s when exposed to 100% CO_2 at 200 °C.[75] The simple fabrication and useful properties of nanocomposites of MOFs with graphene acid indicate that this recently discovered graphene derivative is a valuable MOF templating agent whose potential warrants further exploration.

Nanocomposites of MOFs with graphene derivatives have traditionally been prepared using one-pot methods in which MOF precursors are mixed with the graphene derivative.

https://doi.org/10.1021/acs.chemrev.2c00270
Chem. Rev. 2022, 122, 17241−17338

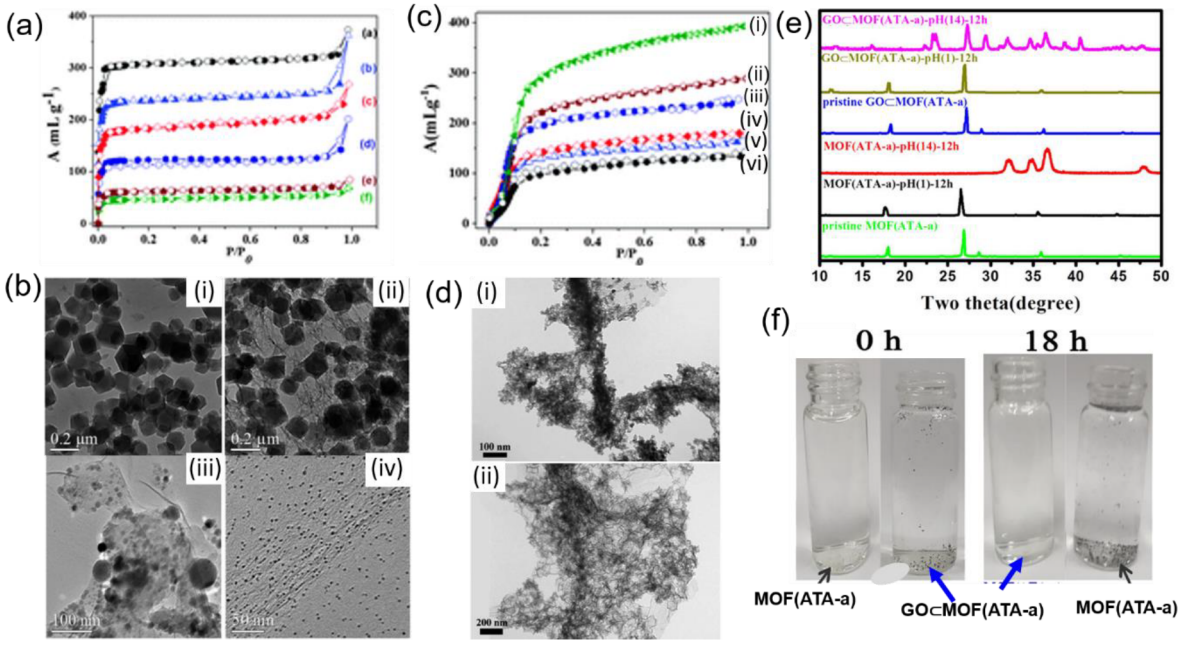

Figure 3. (a) Nitrogen sorption isotherm of GO@ZIF-8. (b) TEM images illustrating the morphologies of (i) ZG-0, (ii) ZG-1, (iii) ZG-10, and (iv) ZG-20. (c) CO_2 adsorption−desorption isotherms of (i) ZG-20, (ii) ZG-10, (iii) ZG-4, (iv) ZG-2, (v) ZG-1, and (vi) ZG-0 at 195 K. Reproduced with permission from ref 172. Copyright 2013 Royal Society of Chemistry. (d) TEM images of C-rGO-ZIF catalysts prepared using (i) 2.5 and (ii) 10 mL of a 2 mg mL^{-1} GO solution. Reproduced with permission from ref 173. Copyright 2019 Royal Society of Chemistry. (e) PXRD patterns of pristine [MOF(ATA-a)], pristine [GO⊂MOF(ATA-a)], [MOF(ATA-a)], and [GO⊂MOF(ATA-a)] after soaking for 12 h in solutions of pH 1 and 14. (f) Optical images of [MOF(ATA-a)] and [GO⊂MOF(ATA-a)] (left) before and (right) after dispersion in a pH 1 solution for 18 h. Reproduced with permission from ref 171. Copyright 2018 American Chemical Society.

However, other methods also exist. For example, GO can be reacted with metal ions (e.g., Zn^{2+}) that then guide MOF nucleation by reacting with MOF building blocks such as trimesic acid (H_3BTC) and $ZnCl_2$ in the presence of a structuring agent such as triethanolamine. This approach was used to prepare functionalized MOF@GO nanocomposites.[166] Layer-by-layer (LBL) deposition can also be used to synthesize MOF@GO nanocomposites: LBL deposition of a GO suspension on a semicontinuous ZIF-8 layer yielded a ZIF-8/GO nanocomposite film with promising performance in hydrogen separation and purification.[167] A membrane for hydrogen separation was also prepared by the related dip-coating−rubbing method (DCRM). DCRM is a two-step process that was used to prepare low-defective MOF membranes grown on a MOF/graphene composite supported on a porous carbonaceous film. In the first step, a thin layer of the ZIF-8@graphite nanocomposite was deposited on the carbon surface and then rubbed to form a stable seed layer, on which additional MOF layers could be grown, for example, by solvothermal growth.[168]

2.2. Exploiting Hybridization To Combine and Enhance the Properties of MOFs and Graphene Derivatives

The preceding discussion clearly shows that hybridizing MOFs with graphene to form graphene@MOF hybrids makes it possible to circumvent the limitations of the individual materials and exploit their synergistic properties. This section provides a detailed overview of current knowledge concerning the influence of graphene and MOF hybridization on the textural, morphological, and electronic properties of graphene@MOF hybrids as well as their stability, wettability, and active sites (Figure 2). In addition, this section describes ways in which the different properties of graphene@MOF hybrids can be tuned to improve their practical usefulness.

2.2.1. Textural Properties—Surface Area and Pore Size Distribution. The textural properties of graphene@MOF hybrids (surface area, pore volume, pore diameter, etc.) are among their most important features and strongly influence their performance in various applications. Because graphene@MOF hybrids consist of MOFs and graphene, their textural properties can be tuned by manipulating these components. This is exemplified by the hierarchically porous HFGO@ZIF-8 graphene@MOF hybrid prepared by our research group.[128] In the synthesis of this hybrid, ZIF-8 nanocrystals act as pillars that support HFGO nanosheets, giving rise to the hierarchical porous structure; the ZIF-8 nanocrystals confer microporosity, while mesoporosity results from the emergence of a structure in which HFGO nanosheets are supported by ZIF-8 nanopillars. The nitrogen adsorption−desorption isotherm of this hybrid (Figure 3a) shows both type-I and type-IV character, confirming the presence of micro- and mesopores, respectively. Furthermore, a pore size analysis using nonlocal density functional theory indicated the presence of pores with sizes of 1 and 3 nm, which were assigned to micro- and mesopores, respectively. The presence of both pore types gave the hybrid a high adsorption capacity, leading to high performance in oil−water separation. A similar hierarchically porous hybrid was prepared by combining the MOF UiO-66-NH_2 with graphene acid (GA).[76] The microporosity of the resulting GA@UiO-66-NH_2 hybrid originated from the UiO-66-NH_2 nanocrystals, while its mesoporosity originated from the covalent bonding between GA and UiO-66-NH_2, which controlled the spacing between the GA layers. The hybrid had a type-IV nitrogen sorption isotherm, confirming the presence of mesopores. In addition, the GA@

https://doi.org/10.1021/acs.chemrev.2c00270
Chem. Rev. 2022, 122, 17241−17338

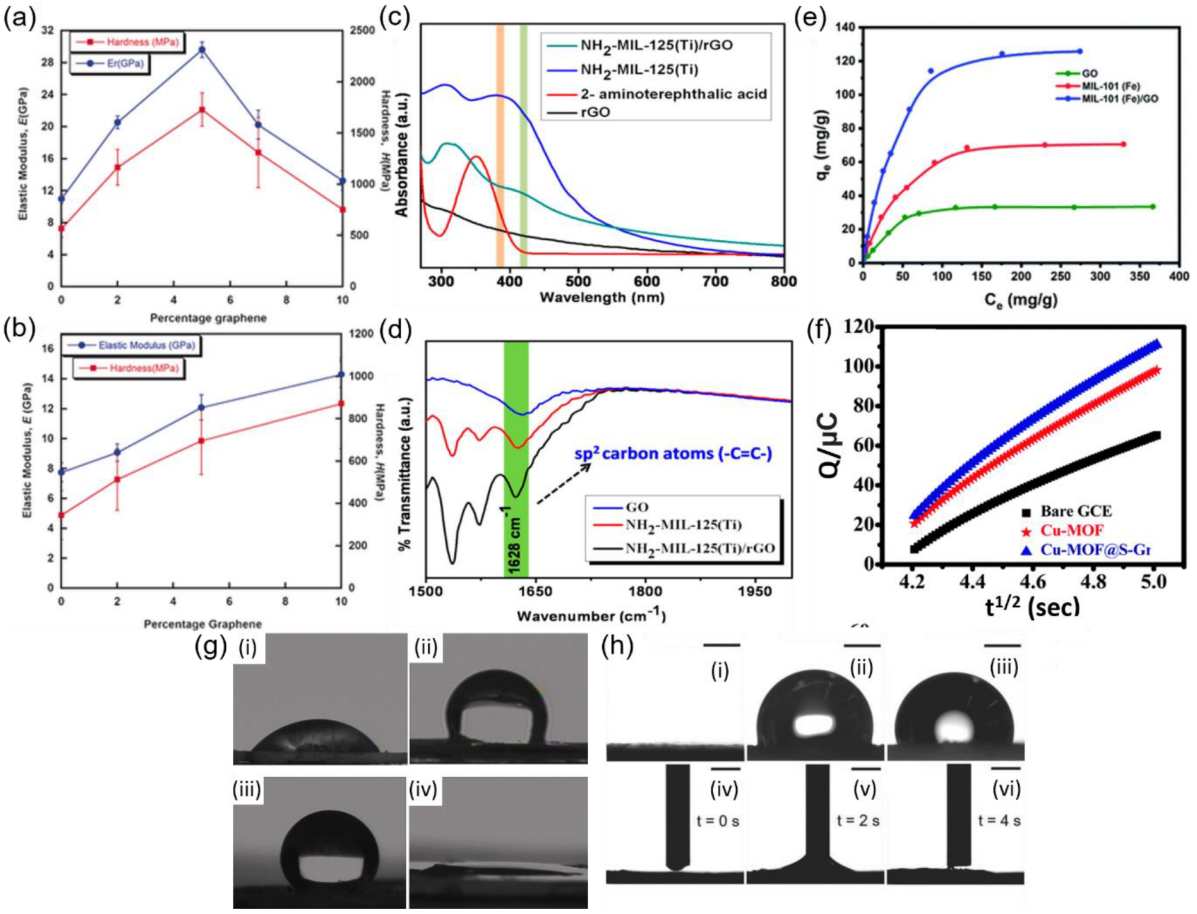

Figure 4. Hardness and elastic modulus of (a) MgBFG-*X* and (b) NiBFG-*X*, where *X* denotes the wt % of graphene in composites with M_2DOBDC; M = Mg^{2+} and Ni^{2+}. Reproduced with permission from ref 175. Copyright 2016 John Wiley & Sons, Inc. (c) UV−vis spectra of NH_2-MIL-125(Ti)/rGO, NH_2-MIL-125(Ti), 2-aminoterephthalic acid, and rGO. (d) Expanded FTIR spectra of NH_2-MIL-125(Ti)/rGO, NH_2-MIL-125(Ti), and GO. Reproduced with permission from ref 169. Copyright 2018 American Chemical Society. (e) Pb^{2+} adsorption capacity of MIL-101(Fe)/GO, MIL-101(Fe), and GO measured at room temperature. Reproduced with permission from ref 170. Copyright 2019 Royal Society of Chemistry. (f) Cottrell plots generated to determine the electrochemically active surface area (ECSA) of a bare GCE and GCEs modified with Cu-MOF@S-Gr and Cu-MOF. Reproduced with permission from ref 177. Copyright 2022 Royal Society of Chemistry. (g) Water droplets on the surfaces of (i) ZIF-8, (ii) HFGO, and (iii) HFGO@ZIF-8 hybrid for which the water contact angles are 56°, 125°, and 162°, respectively, and (iv) oil droplet on the surface of the superoleophilic HFGO@ZIF-8 showing its oil contact angle of 0°. Reproduced with permission from ref 128. Copyright 2016 John Wiley & Sons, Inc. (h) Optical images of water droplets on the surfaces of (i) Al-BTC MOG, (ii) fluorinated graphene oxide (FGO), and (iii) FGO@MOG hybrid. Images iv−vi show the hexadecane contact angles observed at different time intervals on the surface of the FGO@MOG hybrid. Reproduced with permission from ref 178. Copyright 2017 John Wiley & Sons, Inc.

UiO-66-NH_2 hybrid had a BET surface area of 600 m^2 g^{-1} and a pore volume of 1.09 cm^3 g^{-1}.

2.2.2. Morphological Properties—Particle Size and Shape. The structures of graphene@MOF hybrids depend strongly on the morphology (size and shape) of their constituent particles. Control over particle morphology can thus be used to rationally tune the structural features of graphene@MOF hybrids to improve their practical usefulness. In 2013, Kumar et al. showed that the morphology of the ZIF-8 MOF was modified when grown on a GO surface and studied the gas adsorption properties of various GO@ZIF-8 hybrids.[172] In addition, we showed that the morphology of the ZIF-8 crystals in these hybrids could be controlled by altering the GO content of the hybrids. A series of GO@ZIF-8 hybrids designated ZG-*x* (where *x* represents the wt % of GO) was synthesized, and their morphology was studied by transmission electron microscopy, revealing that increasing the content of GO changed the shape and size of the ZIF-8 particles: the particle size was reduced from ∼100−150 nm in pristine ZIF-8 to ∼4 nm in ZG-20. This reduction was accompanied by a change in particle shape, from hexagonal to spherical (see Figure 3b). Raman spectroscopy demonstrated the formation of bonds between the GO sheets and the Zn(II) ions of ZIF-8, explaining the size-controlling and structure-directing activity of the GO sheets. This bonding was attributed to the presence of surface −OH and −COOH groups on the GO sheets that coordinated the Zn(II) ions and thereby influenced the growth of the ZIF-8 crystals. The morphological variation of the ZG-*x* hybrids also changed their structure and therefore influenced their capacity for CO_2 uptake: as the GO wt % increased from 0 to 20, the CO_2 uptake capacity increased from 27.2 to 72 wt % at 1 atm and 195 K, as shown in Figure 3c. A similar recent study examined the influence of the graphene content of the rGO-ZIF-derived C-rGO-ZIF catalyst on its catalytic activity.[173] C-rGO-ZIF catalysts with different GO contents were prepared by simple one-pot reactions between GO solutions of different concentrations, PVP, Zn^{2+} ions, Fe^{3+} ions, and 2-methylimidazole followed by pyrolysis of the prepared catalyst. Hybrids with different GO contents had

https://doi.org/10.1021/acs.chemrev.2c00270
Chem. Rev. 2022, 122, 17241−17338

different morphologies: at low concentration, the GO appeared curled in the hybrid, but the GO sheets became more planar and less curled as the GO concentration increased. Figure 3d shows TEM images of C-rGO-ZIF catalysts with low and high GO contents, which clearly show that the curliness of the GO sheets was eliminated when the GO content was high. The curliness was due to the variation in the surface potential of GO induced by the attachment of Zn^{2+} ions to its surface;[174] reducing the hybrid's content of GO increased the relative concentration of Zn^{2+} ions, causing the graphene sheets to curl. Since curled graphene cannot effectively support Zn^{2} ions, C-rGO-ZIF catalysts with high GO contents were needed to achieve good performance in oxygen reduction reactions (ORRs).

2.2.3. Mechanical−Chemical−Thermal Stability. The thermal stability of graphene@MOF hybrids is vitally important for their practical use under industrially relevant conditions; they must be stable enough to withstand harsh chemical and thermal conditions without loss of structural integrity even under mechanical stress. Although pristine MOFs are unstable under such conditions, previous studies have shown that graphene@MOF hybrids exhibit greater mechanical, chemical, and thermal stability. For example, Su et al. showed that the thermal and chemical stability of a metastable MOF polymorph could be increased by encapsulation in GO.[171] Specifically, a MOF based on the organic ligand ATA (5-amino-1*H*-tetrazole) was found to have two polymorphs that were designated [MOF(ATA-a)] and [MOF(ATA-b)]. The [MOF(ATA-a)] polymorph dominates in freshly prepared material but is chemically and thermally unstable and thus undergoes a polymorphic transition to the more stable polymorph [MOF-(ATA-b)] after being kept under a nitrogen environment for 3 months or upon heating to 120 °C for 7.5 h. Adding GO to a solution of [MOF(ATA-a)] yielded a composite designated [GO⊂MOF(ATA-a)] in which the MOF was encapsulated between GO sheets, increasing its thermal and chemical (acidic and basic) stability. Its high chemical stability was demonstrated by performing a PXRD analysis, which showed that its PXRD pattern was not significantly affected by being dispersed in acidic (pH 1) or basic (pH 14) media (Figure 3e). In addition, when dispersions of [MOF(ATA-a)] and [GO⊂MOF(ATA-a)] were kept in a pH 1 solution, the nonencapsulated MOF dissolved after 18 h but the encapsulated composite [GO⊂MOF(ATA-a)] remained stable, as shown in Figure 3f. Analysis of the encapsulated composite's thermal stability revealed that its decomposition temperature (T_d) was 377.4 °C, which is higher than that of the common heat-resistant explosive 1,3,5-triamino-2,4,6-trinitrobenzene (T_d = 321 °C). The improved stability of [MOF(ATA-a)] (T_d = 374.5 °C) upon GO encapsulation was attributed to the coordination of GO to the polymorphic MOF. Because of its remarkable thermal and chemical stability, the [GO⊂MOF(ATA-a)] composite was identified as a promising heat-resistant explosive. Other studies have shown that hybridization with graphene derivatives can improve the mechanical stability of MOFs as well as their thermal and chemical stability. For example, Rao et al. found that covalent bonding to benzoic acid-functionalized graphene (BFG) derived from GO improved the mechanical properties of M_2DOBDC (MOF-74; M = Co^{2+}, Mg^{2+}, or Ni^{2+}; $DOBDC^{4-}$ = 2,5-dioxido-1,4-benzenedicarboxylate).[175] In the resulting hybrids, the carboxylate groups of both BFG and DOBDC coordinate to the metal centers of the MOF. To determine how the properties of these systems varied with their graphene content, hybrids with different BFG contents by weight were prepared. These hybrids were designated MBFG-*x* (M = metal; *x* = wt % of BFG). The mechanical properties of NiBFG-*x* and MgBFG-*x* were studied by nanoindentation and evaluated by plotting their hardness (H) and elastic modulus (E) against their graphene content, giving the results shown in Figure 4a and 4b. Figure 4a shows that upon raising the BFG content from 0 to 5 wt %, the H and E of NiBFG-*x* both increased linearly. In addition, for BFG concentrations up to 5 wt %, MgBFG-*x* had higher values of H and E than NiBFG-*x*, which was attributed to the ionic character of the Mg−O bonds. However, the H and E values of MgBFG-*x* declined when the BFG content of the composite exceeded 5 wt %; this was attributed to BFG agglomeration at higher concentrations. These results demonstrate that the mechanical properties of pristine MOFs can be increased by hybridization with graphene derivatives and tuned by varying the content of graphene within the composite.

2.2.4. Electronic Properties—Conductivity and Magnetism. MOFs usually have poor electrical conductivity, whereas graphene and many of its derivatives are good conductors. Consequently, graphene@MOF hybrids often exhibit greater conductivity than the parent MOFs. For example, Karthik et al. recently showed that hybridization with rGO could be used to manipulate the electronic properties of the MOF NH_2-MIL-125(Ti) ($Ti_8O_8(OH)_4(NH_2\text{-bdc})_6$).[169] The increased electrical conductivity of the resulting hybrids was exploited in photocatalytic H_2 production. UV−vis spectroscopy revealed the formation of noncovalent interactions between rGO and NH_2-MIL-125(Ti); adding rGO to NH_2-MIL-125(Ti) shifted the MOF's characteristic peak from 380 to 415 nm, indicating a transfer of electron density between the hybrid's two components (Figure 4c). The formation of covalent interactions between rGO and NH_2-MIL-125(Ti) would be expected to cause C═C bond cleavage and the replacement of sp^2 carbon centers with sp^3 centers, which would reduce the intensity of the C═C bonds at 1628 cm^{-1}. However, FTIR spectroscopy (Figure 4d) provided no evidence for the presence of sp^3 carbons after adding rGO to NH_2-MIL-125(Ti) because the intensity of the C═C peak at 1628 cm^{-1} was unchanged, indicating that no covalent bonding occurred between the two components. The IR signal of the organic ligand's amine group was also unaffected, further confirming that the interaction between rGO and NH_2-MIL-125(Ti) is purely noncovalent. The only possible electronic transition between rGO and the MOF involves excitation of electrons from the π orbital of the benzene ring of the MOF's organic ligand to the π orbitals of rGO, so the transition was assumed to occur via $\pi-\pi$ interactions. These interactions suppress electron−hole recombination by facilitating fast electron transport, which was suggested to explain why the composite's photocatalytic activity exceeded that of pristine NH_2-MIL-125(Ti). Another recent report described the fabrication of a composite of rGO and the 2D layered MOF Co-TCPP (comprising Co^{2+} ions and H_4TCPP = *meso*-tetrakis(4-carboxyphenyl)porphyrin) for use as an anode material for Li-ion batteries.[176] In this case, rGO served as an antistacking agent to prevent stacking of the MOF layers. In addition, because rGO is electrically conductive, it increased the hybrid's electrical conductivity and thus facilitated electron-transfer processes. As a result, the hybrid's performance as an anode material exceeded that of the parent MOF. These results show that the high electrical conductivity of graphene and its derivatives can be exploited to create MOF-containing hybrid materials with improved conductivity and electronic

https://doi.org/10.1021/acs.chemrev.2c00270
Chem. Rev. 2022, 122, 17241−17338

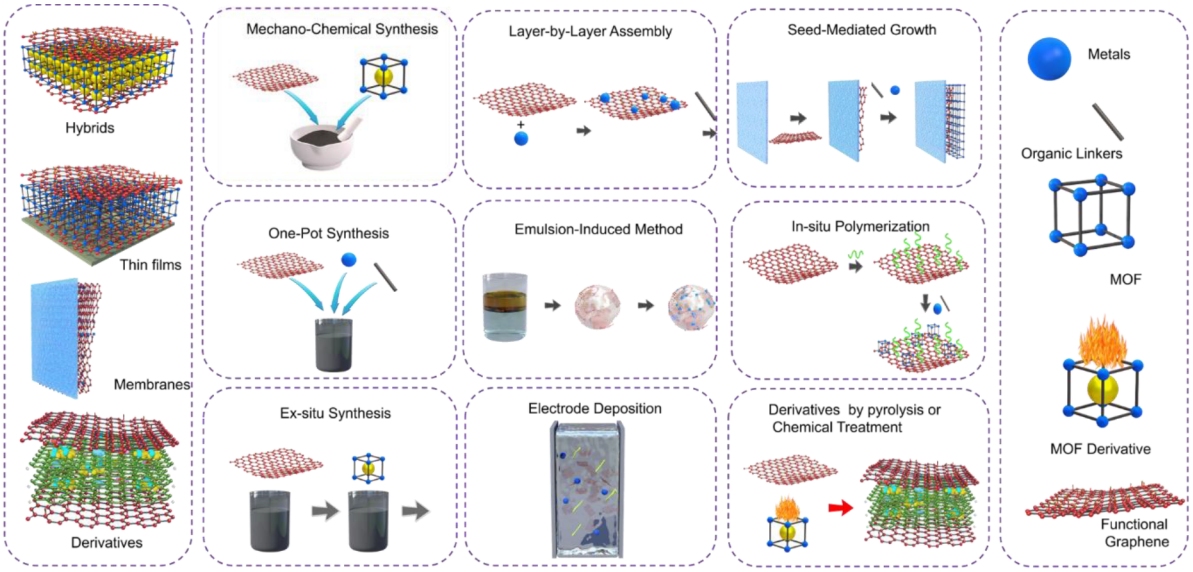

Figure 5. Synthetic approaches used to prepare graphene@MOF hybrids.

properties that can be tuned to improve their performance in applications involving electron conduction.

2.2.5. Active Sites: Functional Groups and Metal Sites. Hybridization with graphene derivatives can alter the structures of MOFs, leading to increased exposure of their active sites. As a result, graphene@MOF hybrids can exhibit superior catalytic, adsorptive, and sensing performance when compared to the parent MOFs. For example, a hybrid of GO with MIL-101(Fe) ($Fe_3O(X)(H_2O)_2(bdc)_3$ with X = OH^- or F^-) was prepared by a simple hydrothermal process to improve the Pb(II) ion removal activity of MIL-101(Fe).[170] The resulting MIL-101(Fe)/GO hybrid was capable of removing Pb(II) ions from solution by adsorption onto active sites within the MOF component. Importantly, the incorporation of GO in the hybrid increased the proportion of free oxygen and hydroxide groups on the MOF component, leading to increased removal of Pb(II) ions. Figure 4e shows the Pb(II) ion removal capacity of MIL-101(Fe), GO, and MIL-101(Fe)/GO.

The Pb(II) ion removal capacity was highest for MIL-101(Fe)/GO, confirming that the hybrid had the greatest number of adsorption sites (i.e., free oxygen and hydroxide groups) and that hybridization with graphene derivatives can alter the number of exposed active sites within a MOF. A similar increase in the number of active sites was also observed when sulfur-doped graphene (S-Gr) was used as a support for MOF-2(Cu), which is based on the organic ligand 1,4-benzenedicarboxylate and Cu^{2+} ions (Cu_2bdc_2).[177] The S-Gr sheets directed the growth of MOF-2(Cu) over their surfaces and simultaneously increased the number of electroactive sites in the resulting hybrid. The increased number of electroactive sites in the Cu-MOF@S-Gr composite was determined by calculating its electrochemically active surface area (ECSA). Figure 4f shows Cottrell plots generated to determine the ECSA of a glassy carbon electrode (GCE), a Cu-MOF-modified GCE, and a Cu-MOF@S-Gr-modified GCE. The ECSA of the electrodes increased in the order GCE < Cu-MOF (MOF-2(Cu)) < Cu-MOF@S-Gr, indicating that the electrode modified with the Cu-MOF@S-Gr hybrid had a higher density of electroactive sites than the other tested surfaces, leading to higher rates of mass transfer and electron transfer. As a result, the Cu-MOF@S-Gr-modified GCE exhibited high conductivity and electroanalytic utility and activity, enabling its use as an effective sensor for the detection of dopamine, acetaminophen, and H_2O_2.

2.2.6. Surface Properties—Wettability. The wettability of a material is related to its surface properties. For example, the most commonly examined form of wettability (hydrophilicity) depends on the presence of polar hydrophilic groups on the material's surface. In contrast, hydrophobicity is associated with rough material surfaces and the presence of terminating groups with low surface energy such as alkyl chains or fluorinated moieties. The surface properties of MOFs, and hence their wettability, can be tuned by hybridization with graphene derivatives. Most MOFs are highly moisture sensitive because they have an abundance of polar functional groups at their surfaces and are therefore hydrophilic, which allows water molecules to readily disrupt coordinative bonds between the organic linker and the metal ions. However, many graphene derivatives are quite hydrophobic and can therefore be used to adjust the surface properties and moisture sensitivity of MOFs. In 2016, Jayaramulu et al. reported the preparation of hydrophobic graphene@MOF composites containing various graphene derivatives including a highly fluorinated graphene oxide (HFGO). Because the HFGO was extensively fluorinated, its surface free energy was substantially lower than that of GO, making it hydrophobic, as evidenced by its water contact angle (WCA) of 125°. A composite of HFGO and the MOF ZIF-8 was prepared using a simple one-pot synthetic process[128] and was found to be superhydrophobic with a WCA of 162°, which is remarkable given that pristine ZIF-8 is hydrophilic and has a WCA of just 56°. Hybridization with HFGO thus profoundly altered the surface properties of ZIF-8, making it both superhydrophobic and superoleophilic; the oil contact angle (OCA) of HFGO@ZIF-8 was 0°. Consequently, the HFGO@ZIF-8 hybrid exhibited good performance in oil−water separation (Figure 4g). Our research group has also reported the hybridization of the metal organic gel (MOG) Al-BTC, which is based on MIL-101(Al), with fluorinated graphene oxide (FGO) to obtain a FGO@MOG hybrid.[178] This hybrid material is hydrophobic due to the presence of pendant C−F groups with low surface energy. Like HFGO@ZIF-8, the FGO@MOF hybrid was water repellent and oil absorbing with a WCA of 120° and an OCA of 0° (Figure 4h). Because of its hydrophobic

https://doi.org/10.1021/acs.chemrev.2c00270
Chem. Rev. 2022, 122, 17241−17338

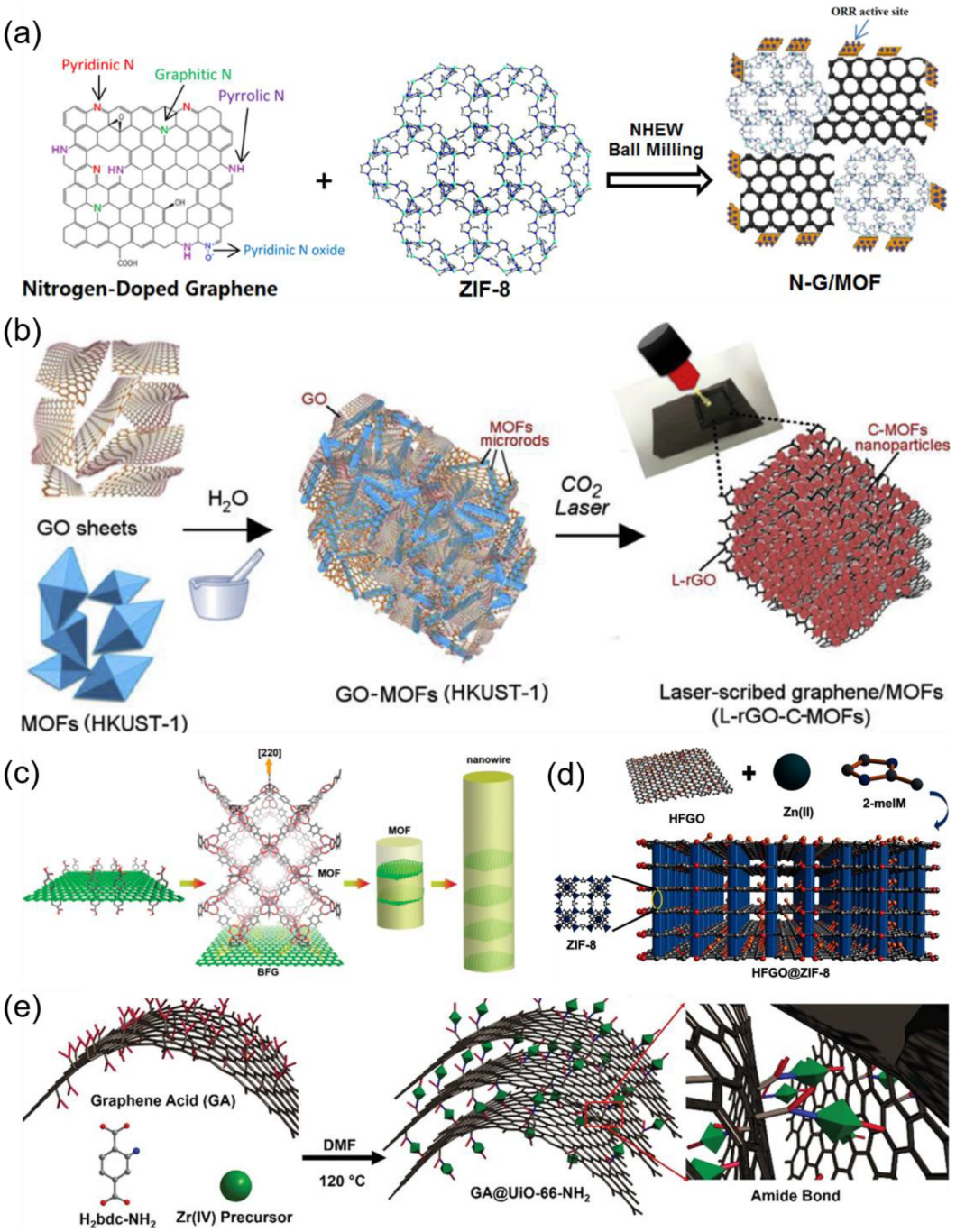

Figure 6. (a) Synthesis of an N-G/MOF hybrid. Reproduced with permission from ref 182. Copyright 2018 Elsevier. (b) Synthesis of a GO-MOF hybrid by physical mixing and its conversion into a 3D composite nanostructure by laser treatment. Reproduced with permission from ref 184. Copyright 2020 Elsevier. (c) Schematic depiction of a BFG-MOF composite and a nanowire formed from this material. Reproduced with permission from ref 77. Copyright 2010 American Chemical Society. (d) Illustrative representation of HFGO@ZIF-8 composite and the components required for its synthesis. Reproduced with permission from ref 128. Copyright 2016 John Wiley & Sons, Inc. (e) Synthesis of a GA@UiO-66-NH_2 composite with amide linkages between UiO-66-NH_2 and GA. Reproduced with permission from ref 76. Copyright 2021 John Wiley & Sons, Inc.

and oleophilic nature, the FGO@MOF hybrid was tested in oil–water separation. The ability to convert strongly hydrophilic MOFs and MOGs into strongly hydrophobic composites through hybridization with graphene derivatives clearly demonstrates the scope for tuning the surface properties and wettability of MOFs using graphene derivatives.

3. SYNTHETIC STRATEGIES FOR GRAPHENE@MOF HYBRIDS AND THEIR DERIVATIVES

Over the past decade, many graphene@MOF hybrids have been prepared through various synthetic routes, as shown in Figure 5. Some of these routes rely on unique methodologies, while others are based on more conventional single-step and multistep syntheses. The one-pot method is the most popular method for graphene@MOF hybrid synthesis because of its simplicity. However, some more complex methods have been developed to

https://doi.org/10.1021/acs.chemrev.2c00270
Chem. Rev. 2022, 122, 17241−17338

prepare hybrids with properties tailored to specific applications. The following sections outline the known methods for synthesizing graphene@MOF hybrids.

3.1. Mechanochemical Synthesis

Physical mixing is a simple and easily processable method for preparing graphene@MOF hybrids by mechanical treatment of both of their components. This treatment may be as simple as grinding the samples together in a mortar, but more complex approaches using different types of mechanical mills such as ball mills are also common. Despite their simplicity, these methods are often disregarded because they can yield hybrids whose performance is worse than that of materials prepared in other ways. For instance, the specific capacitance of the covalent graphene@MOF hybrid GA@UiO-66-NH_2 (GA = graphene acid) prepared using a solvothermal method was found to be superior to that of a physical mixture obtained by mechanically grinding the MOF UiO-66-NH_2 with GA,[76] probably because the parallel formation of the UiO-66-NH_2 crystals and the covalent bonds between the MOF and the GA during the solvothermal process yielded a more homogeneous product. Put another way, the structure-directing capabilities of GA cannot be exploited if the hybrid is formed by physical grinding. Another report examined a 1:2 hybrid of mesoporous graphene (MG, i.e., graphene with a high mesopore content and volume) with MOF-520 ($Al_8(OH)_8(BTB)_4(HCOO)_4$, where BTB^{3-} is 4,4′,4″-benzene-1,3,5-tryil-tribenzoate). The adsorption capacity of samples prepared by physical grinding was compared to that of samples prepared by in-situ synthesis of the MOF in a graphene-containing solution.[179] This revealed that the in-situ process generated additional pores at the interface of the graphene sheets and MOF crystals, resulting in superior adsorption performance. A number of other reports have similarly shown that graphene@MOF hybrids synthesized by physical mixing underperform on several counts than those prepared by other methods.[180,181]

Despite their limitations, physical mixing methods can still produce graphene@MOF hybrids with interesting and useful properties. For example, Zhuang et al. used a wet ball-milling technique to prepare a hybrid of a MOF with N-doped graphene whose electrochemical catalytic performance rivaled that of Pt/C, making it an interesting alternative to noble-metal catalysts.[182] The precursors for this synthesis were ZIF-8 and N-doped graphene (N-G) with the N-doped graphene having been synthesized by nanoscale high-energy wet ball milling (NHEW) of melamine with graphene oxide. The hybrid catalyst was prepared by mixing equal masses of ZIF-8 and N-G dispersed in deionized water, transferring the resulting dispersion to a grinding jar containing ZrO_2 balls and grinding it at various speeds using NHEW for 16 h, as shown in Figure 6a. The insoluble components of the suspension were then removed by centrifugation in a 0.1 M solution of NaOH in deionized water, after which the solid catalyst was filtered out and dried. The physicochemical properties of the N-G/MOF hybrid depended on the grinding speed; the most favorable outcome was obtained by grinding at 350 rpm. A simpler method of preparing graphene@MOF hybrids by mixing their components with a mortar and pestle has also been successfully implemented. Tung et al. used this method to prepare graphene@MOF hybrids to detect volatile organic compounds (VOCs).[183] Three different MOFs, namely, HKUST-1, UiO-66, and ZIF-8, were combined with pristine graphene (pG) in ratios of 1:1 and 1:2 and then ground. The pG was synthesized by exfoliating expanded graphite in an aqueous suspension of GO. In the resulting hybrids, the pristine graphene acts as a highly conductive chemiresistive matrix with finite sensing selectivity. After 20 min of grinding pG with the MOF, the mixture was subjected to mild sonication for 30 min followed by tip sonication for another 30 min. Three-dimensional graphene@MOF hybrids for high-performance supercapacitors have similarly been prepared by simple mechanical grinding.[184] The synthesis of one such 3D carbon composite is depicted schematically in Figure 6b: HKUST-1 and a 2 mg/mL GO solution were mixed such that the weight ratio of the MOF to GO was 1:1, ground in a mortar, and then stirred for 10 min after transferring the ground mixture into a beaker. The resulting homogeneous GO-HKUST-1 paste was used to prepare thin films by the drop-casting method. Finally, supercapacitor electrodes coated with the L-rGO-C-MOF composite were prepared by laser treatment of the GO-HKUST-1 composite film.

3.2. Wet Chemical Methods

3.2.1. One-Pot/In-Situ Synthesis. One-pot synthesis is the most widely used method for preparing graphene@MOF hybrids because of its convenience and simple reaction conditions. In general, one-pot syntheses involve adding graphene or one of its derivatives to a solution of MOF precursors and then heating this reaction mixture at an appropriate temperature for a defined time. Reaction parameters including the concentration of the reactants, temperature, time, and solvent can strongly influence the product's structural and physicochemical properties.

The first report on graphene@MOF hybrids was presented by Bandosz and Petit in 2009. This publication also introduced the one-pot synthetic strategy, which was used to prepare hybrids of MOF-5 and GO.[96] Briefly, the synthesis involved dissolving GO in a round-bottomed flask containing a solution of 1,4-benzenedicarboxylic acid (H_2bdc) and $Zn(NO_3)\cdot 6H_2O$ in *N*,*N*-dimethylformamide (DMF) under solvothermal conditions. Upon cooling, the obtained product was washed with DMF, dispersed in chloroform for 2 days, and then vacuum dried for 6 h at ∼135 °C to obtain MOF-5-GO. This methodology was used to prepare MOF-5-GO hybrids with GO contents of 5, 10, and 20 wt %. According to the authors, the tetrahedral ZnO_4 secondary building unit (SBU) of the MOF can form hydrogen bonds with the hydroxyl groups on the GO surface, where they function as seeds for the growth of MOF-5 crystals attached to the GO sheets. A second layer of GO can then bind to the MOF-5 crystals grown on the surface of the first GO sheet, leading to the formation of a GO-MOF-5-GO sandwich. Repetition of this process ultimately yields the MOF-5-GO hybrid. A similar hybrid material was prepared using MOF-5 with benzoic acid-functionalized graphene (BFG) instead of GO.[77] The synthetic procedure in this case was similar to that described above; the only differences were that the reaction mixture was not stirred during refluxing and the reaction time was only 6 h, after which the product was solvent exchanged and then vacuum dried for 3 h at 90 °C. The hybridization of BFG with MOF-5 yielded a hybrid nanowire (Figure 6c) with photoelectric transport properties not seen in pristine MOF-5.

Our research group has made extensive use of the one-pot approach to synthesize graphene@MOF hybrids.[75,76,128,178,185,186] In one case, highly fluorinated graphene oxide was used to prepare a hydrophobic HFGO@ZIF-8

https://doi.org/10.1021/acs.chemrev.2c00270
Chem. Rev. 2022, 122, 17241−17338

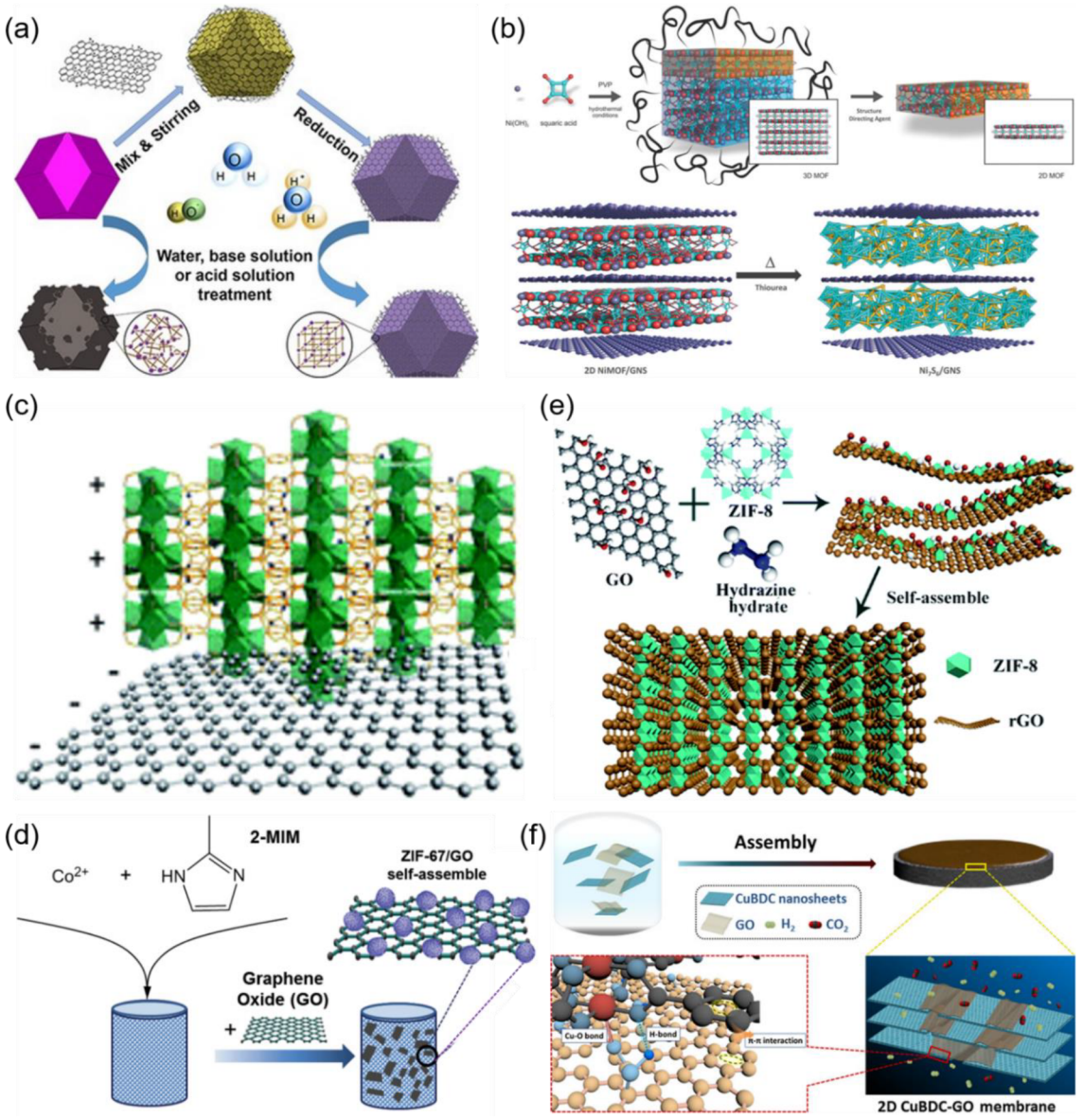

Figure 7. (a) Direct mixing approach for coating rGO on a MOF to increase MOF stability. Reproduced with permission from ref 190. Copyright 2017 John Wiley & Sons, Inc. (b) Generic diagram illustrating (top) the conversion of a 3D MOF into a 2D MOF under the structure-directing action of PVP and (bottom) the formation of a heterobilayer hybrid of nickel sulfide with 2D graphene under solvothermal conditions in the presence of thiourea. Reproduced with permission from ref 191. Copyright 2019 John Wiley & Sons, Inc. (c) Electrostatic interactions between negatively charged GO and positively charged UiO-66-NH_2 MOF. Reproduced with permission from ref 187. Copyright 2014 Royal Society of Chemistry. (d) Schematic representation of the self-assembled synthesis of ZIF-67/GO composites. Reproduced with permission from ref 188. Copyright 2015 Royal Society of Chemistry. (e) Preparation of ZIF-8@GO hybrid hydro/aerogels by self-assembly of GO and ZIF-8 in the presence of hydrazine hydrate. Reproduced with permission from ref 193. Copyright 2017 Royal Society of Chemistry. (f) Diagrammatic illustration of the synthesis of MOF-2(Cu)-GO composite membranes over Al_2O_3, showing the diverse interactions responsible for the self-assembly of the GO and MOF nanosheets. Reproduced with permission from ref 189. Copyright 2019 American Chemical Society.

hybrid[128] by simply sonicating HFGO in chloroform to induce exfoliation before adding 2-methyl imidazole and $Zn(NO_3)_2 \cdot 6H_2O$ to the resulting solution and stirring to obtain a precipitate that was dried to provide HFGO@ZIF-8 as a gray powder. As with the MOF-5-GO hybrids discussed above, ZIF-8 nucleation at the surface oxygen groups of HFGO generated pillar-like ZIF-8 units that in turn supported sandwiching HFGO layers. A related class of graphene@MOF hybrids was recently reported in which the graphene sheets are bound to the MOF via covalent rather than noncovalent bonds.[75,76] An illustrative member of this class is GA@UiO-66-NH_2, which has potential applications in asymmetric supercapacitors[76] and chemiresistive CO_2 sensing.[75] The GA@UiO-66-NH_2 hybrid was prepared from a suspension of graphene acid (carboxylate-functionalized graphene), which was exfoliated in DMF by sonication. Subsequently, NH_2-bdc, $ZrCl_4$, HCl, and 4-amino-benzoic acid as a modulator were added to the graphene acid solution, and the reaction mixture was sonicated to dissolve all of the components. The hybrid GA@UiO-66-NH_2 was finally obtained by heating this reaction mixture at 120 °C in an oven for 48 h. The full synthetic process is illustrated in Figure 6d, which highlights the formation of covalent amide bonds between UiO-66-NH_2 and GA. This novel strategy yielded a hybrid material with high thermal and chemical stability, a

https://doi.org/10.1021/acs.chemrev.2c00270
Chem. Rev. 2022, 122, 17241−17338

hierarchical pore structure, a high specific surface area, and good conductivity.

3.2.2. Ex-Situ Synthesis. In ex-situ synthesis, a presynthesized MOF is mixed with graphene or its derivatives to obtain graphene@MOF hybrids. This approach differs from in-situ synthesis, which involves synthesizing the MOF in the presence of graphene in the same reaction vessel. Although in-situ synthesis is very promising for single-step preparation of graphene@MOF hybrids, the graphene in the reaction mixture interferes with the MOF synthesis process and affects its structural properties, so ex-situ synthetic pathways are often preferred.[46]

This method is based on the direct mixing of a prepared MOF into a solution of a graphene derivative. In some ways it is similar to the previous discussed physical mixing method, where the two components are directly mixed by mechanical force. However, unlike in physical mixing, hybrid formation in this method occurs via a wet chemical pathway. Furthermore, this method involves the synthesis of graphene@MOF hybrids by the self-assembly of a MOF and graphene. The self-assembly process is mainly driven by electrostatic interactions.[187,188] However, $\pi-\pi$ interactions, hydrogen bonding, or coordinative bonds may also be important.[189] Although this strategy is formally an ex-situ approach, the self-assembly of a graphene derivative and a MOF can also be induced in a single pot as in an in-situ pathway.[188]

Zhang and co-workers successfully prepared a MOF@rGO composite by a three-step process involving MOF growth, hybridization of MOF with GO, and reduction of the MOF@GO composite.[190] Three different MOFs were used in this work, namely, ZIF-67, ZIF-8, and UiO-66. The UiO-66 samples were synthesized by thermal treatment of a solution of $ZrCl_4$ and H_2bdc in DMF containing acetic acid as a modulator at 120 °C for 1 day. To prepare ZIF-67 and ZIF-8, methanolic solutions of $Co(NO_3)_2{\cdot}6H_2O$ with Hmim and $Zn(NO_3)_2{\cdot}6H_2O$ with Hmim, respectively, were left at room temperature for 1 day without stirring. In the next step, a methanolic dispersion of ZIF-67 or an aqueous dispersion of one of the other two MOFs was prepared and added to a GO solution to form the MOF@GO hybrids. Finally, the in-situ-generated hybrid was reduced to MOF@rGO by adding ascorbic acid and heating the reaction mixture for 2 h at 60 °C. The MOFs in MOF@rGO composites were more resistant to moisture and acidic or basic conditions than pristine MOFs due to the presence of a protective rGO layer around the MOF, as shown in Figure 7a.

Our research group used a similar direct mixing strategy to prepare 2D $Ni(C_4O_4)(H_2O)_2$/graphene nanosheets that were then treated with thiourea via a solvothermal route to obtain nickel sulfide/graphene nanosheets.[191] To obtain 2D $Ni(C_4O_4)(H_2O)_2$/graphene nanosheets, 2D $Ni(C_4O_4)(H_2O)_2$ was prepared by dissolving polyvinylpyrrolidone (PVP, which served as a structure-directing agent) in an aqueous solution of $Ni(OH)_2$ to which an aqueous solution of squaric acid ($H_2C_4O_4$) was added. The resulting reaction mixture was then subjected to a solvothermal reaction in a PTFE-lined reactor vessel at 180 °C for 1 day to enable the growth of 2D $Ni(C_4O_4)(H_2O)_2$. The structure-directing agent played an important role in guiding the synthesis of the 2D MOF; in its absence, a 3D MOF was obtained, as shown in Figure 7b. In the second step, exfoliated graphene was added to an ethanolic solution of the 2D MOF under sonication for 30 min. The resulting solution was then heated overnight in a PTFE-lined reactor at 100 °C to obtain 2D $Ni(C_4O_4)(H_2O)_2$/graphene nanosheets. Finally, the 2D $Ni(C_4O_4)(H_2O)_2$/graphene nanosheets were subjected to solvothermal treatment with an ethanolic solution of thiourea to obtain nickel sulfide/graphene nanosheets (Figure 8b).

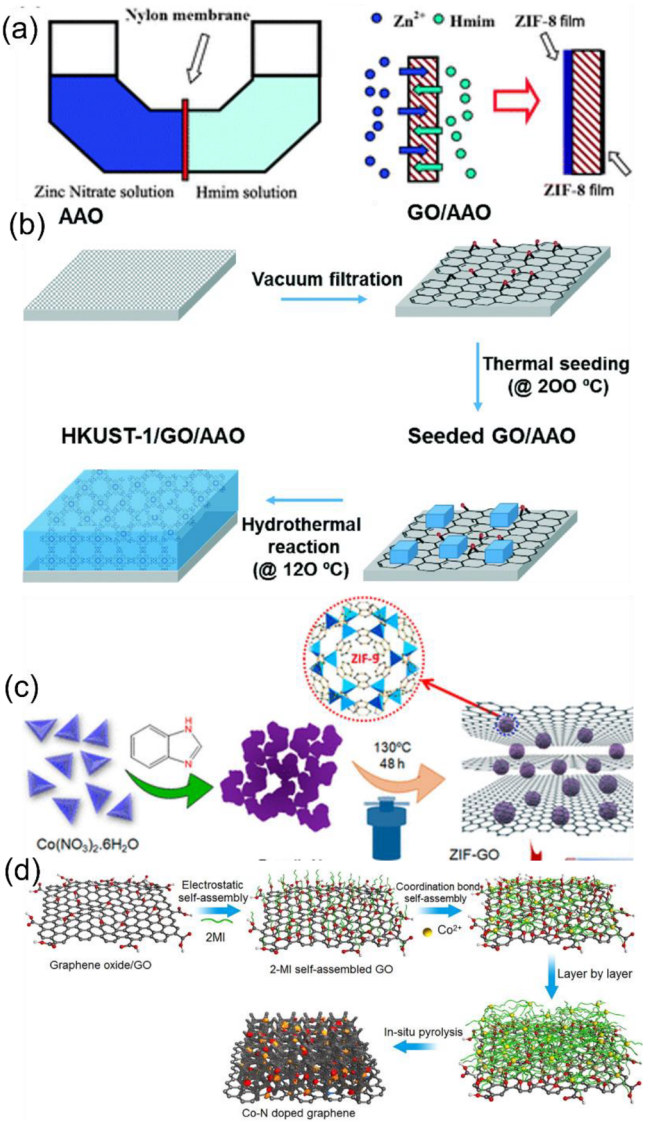

Figure 8. (a) Representation of (left) a diffusion cell and (right) formation of ZIF-8 films by contradiffusion of metal ions and linker molecules through a nylon membrane. Reproduced with permission from ref 201. Copyright 2011 Royal Society of Chemistry. (b) Descriptive schematic for the synthesis of a HKUST-1/GO hybrid on AAO substrate by seeded growth of HKUST-1 on GO film. Reproduced with permission from ref 202. Copyright 2016 Royal Society of Chemistry. (c) Synthetic process for the solvothermal synthesis of a ZIF-9/GO hybrid. Reproduced with permission from ref 203. Copyright 2018 American Chemical Society. (d) Layer-by-layer self-assembly of Co-MOF on GO followed by pyrolysis of the resultant hybrid to Co−N-doped graphene. Reproduced with permission from ref 204. Copyright 2019 Elsevier.

In a very recent report, Zhang et al. presented the direct synthesis of a poly(styrenesulfonate) substituted graphene (PSS-Gr) and Cu-TCPP (Cu_2TCPP) MOF-based composites for highly sensitive and simultaneous detection of dihydroxybenzene isomers.[192] The poly(styrenesulfonate)-substituted graphene was prepared by a chemical reduction pathway involving the formation of a stable dispersion of PSS and GO

https://doi.org/10.1021/acs.chemrev.2c00270
Chem. Rev. 2022, 122, 17241−17338

in water by ultrasonication. The dispersion was then heated in an oil bath at 95 °C for 10 min, after which N_2H_4 was added to the reaction mixture and the solution was aged for 3 h. The reaction mixture was then centrifuged to obtain PSS-Gr, which was washed with water and dried overnight at 65 °C. To synthesize Cu-TCPP nanosheets, an ethanol/DMF solution (3:1, v/v) of trifluoroacetic acid, $Cu(NO_3)_2{\cdot}3H_2O$, and PVP was prepared by ultrasonication. The solution of TCPP in DMF was then added dropwise to the above solution, which was then stirred, sonicated, and heated for 3 h at 80 °C to obtain red nanosheets of Cu-TCPP. Finally, solutions of Cu-TCPP and PSS-Gr nanosheets were mixed by ultrasonication for 2 h to form the PSS-Gr@Cu-TCPP composite.

In 2014, Shen et al. reported the use of this strategy to assemble a rGO-UiO-66-NH_2 composite from UiO-66-NH_2 and GO.[187] As shown in Figure 7c, the self-assembly of the two components was driven by electrostatic interactions between the UiO-66-NH_2 MOF (which is positively charged due to its $-NH_2$ groups) and the GO (which is negatively charged due to its surface carboxylate groups). For the synthesis of the hybrid, GO and UiO-66-NH_2 were dispersed in water separately and these dispersions were mixed with UiO-66-NH_2 NPs to GO ratios of 1:0.01, 1:0.02, 1:0.03, 1:0.05, and 1:0.1. The obtained suspensions were then subjected to solvothermal treatment under the conditions used for UiO-66-NH_2 synthesis. During this process, the GO was reduced to rGO, resulting in the formation of the final rGO-UiO-66-NH_2 composite. Another report showed that the self-assembly of graphene and a MOF can be performed in a single pot by a stepwise process. Lin et al. used this approach to prepare self-assembled hybrids of ZIF-67 and GO[188] by slowly adding a GO dispersion to a ZIF-67 synthesis solution and then stirring the resulting reaction mixture for 1 day. The synthetic process is illustrated in Figure 7d, which shows that ZIF-67 NPs were formed by the reaction of Co^{2+} and Hmim, and the resulting NPs were then assembled on GO nanosheets to form ZIF-67/GO hybrids. The self-assembly strategy has also been used to synthesize graphene@MOF hybrid gels. In one case, the electrostatic self-assembly of ZIF-8 NPs with GO nanosheets in the presence of the reducing agent hydrazine was used to prepare MOF@rGO hybrid hydro/aerogels.[193] Figure 7e illustrates the synthesis of a ZIF-8@rGO hydrogel. In this process, ZIF-8 NPs were attached to GO nanosheets due to the coordination of their Zn^{2+} ions to hydroxyl, carboxyl, and epoxy groups. Hydrazine acted as a reducing agent that removed polar functional groups from the GO surface and thereby increased the likelihood of forming $\pi-\pi$ interactions; this facilitated the self-assembly of rGO nanosheets and thus led to the formation of ZIF-8/rGO hydrogels. The gels were macro/microporous and had a BET surface area of 168 m^2/g.

Graphene@MOF composite membranes can also be prepared using self-assembly processes; Cheng et al. electrostatically assembled a 2D MOF with GO to obtain a hybrid membrane for removing Cs^+ ions.[194] In this study, the 2D Co-MOF Co_2(TCPP)(bpy) was synthesized by slowly adding a solution of TCPP in DMF/ethanol to a DMF/ethanol solution of $Co(NO_3)_2{\cdot}6H_2O$, polyvinylpyrrolidone (PVP), and 4,4-bipyridine (bpy). The resulting reaction mixture was then sonicated and heated to 80 °C to obtain the cobalt porphyrin MOF, which was collected by centrifugation after 24 h and then kept in DMF. In the subsequent step, a suspension of GO in DMF was added to the Co-MOF dispersion and the reaction mixture was stirred magnetically. The hybrid membrane was finally obtained by vacuum filtration of this solution over an organic membrane and peeling the sample off the organic membrane. Like electrostatic interactions, hydrogen-bonding interactions can play important roles in directing the self-assembly of graphene and MOFs into hybrid materials. Yang et al. synthesized graphene@MOF hybrid-based 2D membranes by hydrogen-bonding-assisted self-assembly of MOF-2(Cu) with GO.[189] In this case, the MOF-2(Cu) was synthesized by a diffusion-mediated pathway in which solutions of bdc and $Cu(NO_3)_2$ were layered above each other in a test tube. After obtaining MOF-2(Cu) nanosheets, a mixed dispersion was prepared by sonicating a mixture of MOF-2(Cu) and GO dispersions. The obtained mixed dispersion was then transformed into a MOF-2(Cu)-GO membrane by vacuum filtration on an Al_2O_3 support (Figure 7f). The hybridization of MOF-2(Cu) with GO nanosheets was driven by hydrogen bonding, $\pi-\pi$ interactions, and Cu-O coordination and caused the empty spaces between MOF-2(Cu) nanosheets to be filled with GO nanosheets, as shown in Figure 7f. The prepared MOF-2(Cu)-GO membrane was used to separate H_2/CO_2 mixtures.

3.2.3. Growth of MOFs on Graphene Surfaces. There are several strategies that have been introduced to grow MOFs on top of graphene surfaces, and they are discussed below, most prominently the layer-by-layer assembly of MOFs and the emulsion-induced approach.

3.2.3.1. Layer-by-Layer Assembly. The layer-by-layer synthesis of graphene@MOF hybrids is a promising strategy for preparing well-ordered layered hybrid structures that enables maximal use of their active sites.[195] This synthetic approach involves growing the graphene@MOF hybrid by forming MOFs on a graphene/derivative via layer-by-layer assembly of its precursors. In general, GO is used as a substrate for anchoring layers of MOF precursors, which are loaded in a stepwise manner. The graphene derivative can be loaded stepwise by using a metal source in the first step and a linker in the second step or in the opposite order by loading the linker in the first step and the metal source in the second. The growth steps may all be performed in the same pot, or alternatively, the procedure may call for extraction of an intermediate that is then processed further. The first step usually involves a reaction between a graphene derivative dispersion and a linker with a metal salt being added in a second step.[196] Alternatively, the graphene derivative may first be impregnated with a metal salt in a suitable solvent with the linker being added to the resulting solution in the second step.[197−200]

However, in some cases, the building blocks are not assembled on the GO surface; instead, direct MOF growth occurs at the surface and the self-assembly of the components gives rise to a graphene@MOF hybrid structure.[205] In 2017, Yu et al. presented a general pathway for the layer-by-layer synthesis of graphene@MOF hybrid structures using ZIF-67 (Co-$(mim)_2$), HKUST-1, and ZIF-8 as representative MOFs.[195] This technique enabled the layer-by-layer assembly of a Zn-TCPP MOF with zinc acetate over a GO-anchored substrate. More recently, Cai et al. used a layer-by-layer strategy to prepare carbon-based bifunctional electrocatalysts.[204] Figure 8d presents a schematic overview of this process, which was used to prepare ZIF-67/GO hybrids that were subsequently subjected to pyrolysis. The ZIF-67/GO hybrid was obtained by preparing a dispersion of GO in distilled water and then adding an aqueous solution of Hmim. After stirring for 1 h, powdered Hmim/GO was collected by centrifugation. This treatment formed a linker layer on the GO surface. This Hmim/

https://doi.org/10.1021/acs.chemrev.2c00270
Chem. Rev. 2022, 122, 17241−17338

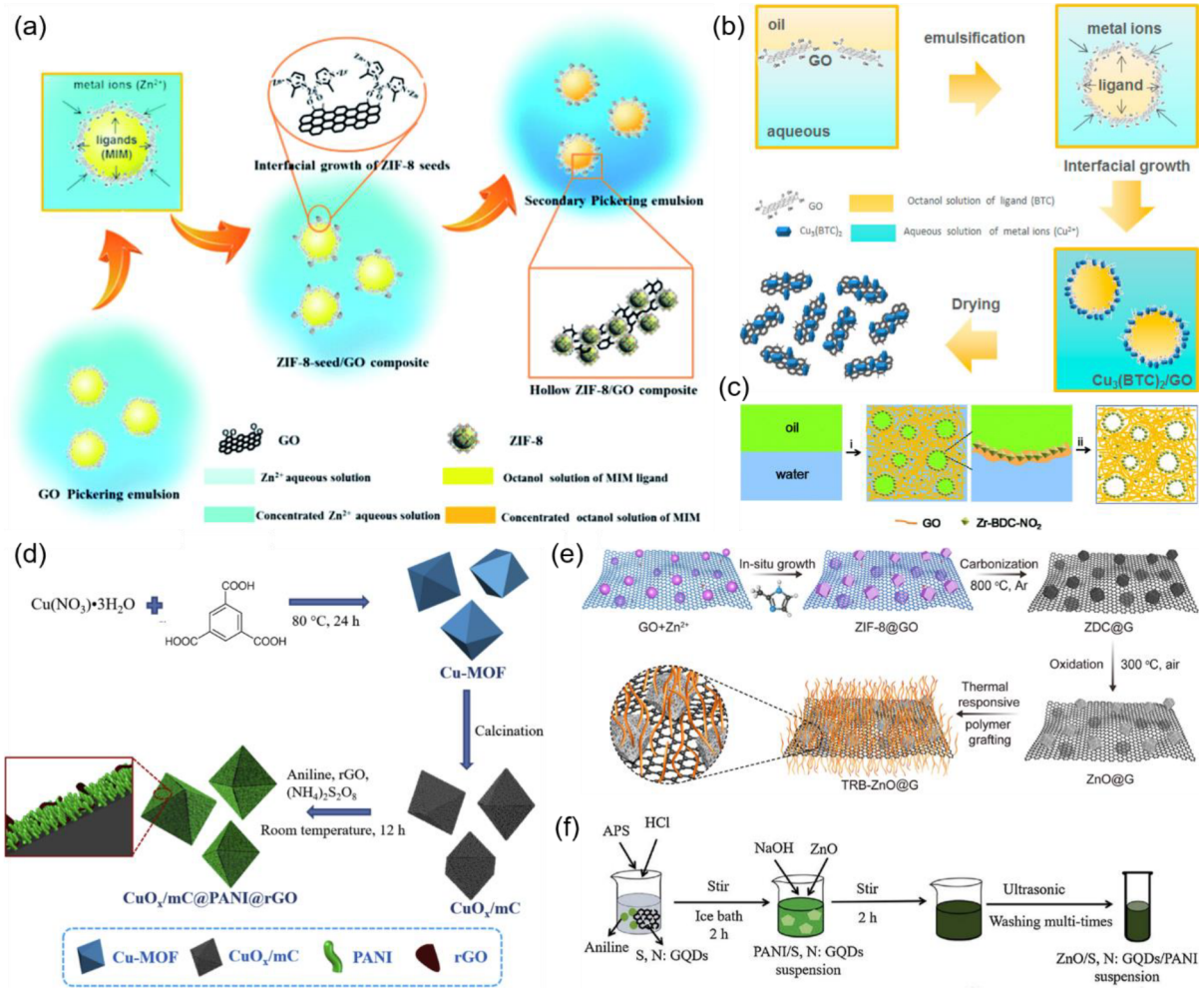

Figure 9. (a) Synthesis of a ZIF-8/GO composite using the Pickering emulsion-based strategy. Reproduced with permission from ref 207. Copyright 2015 Royal Society of Chemistry. (b) Synthetic route for the interfacial growth of a HKUST-1/GO composite in a GO-stabilized Pickering emulsion. Reproduced with permission from ref 208. Copyright 2015 American Chemical Society. (c) Mechanism of Pickering emulsion stabilization by GO and Zr-BDC-NO_2 (i), and synthesis of a Zr-BDC-NO_2/GO composite from the stabilized emulsion. Reproduced with permission from ref 209. Copyright 2017 Royal Society of Chemistry. (d) Schematic depiction of the synthesis of a CuO_x/mC@PANI@rGO composite by in-situ polymerization. Reproduced with permission from ref 211. Copyright 2018 Elsevier. (e) Diagrammatic representation of 2D TRB-ZnO@G nanosheet synthesis. Reproduced with permission from ref 212. Copyright 2019 American Chemical Society. (f) Representation of the systematic synthesis of a ZnO/S, N: GQDs/PANI nanocomposite by in-situ polymerization of aniline in the presence of GQDs. Reproduced with permission from ref 213. Copyright 2019 Elsevier.

GO solution was then added to an aqueous solution of cobalt acetate, and the resulting solution was stirred and centrifuged. Finally, the product was collected by vacuum drying the as-obtained ZIF-67/GO hybrid at 85 °C. These two steps were then repeated up to 10 times to further build up the MOF structure. The ZIF-67/GO hybrid was subsequently pyrolyzed at various temperatures under N_2 gas to obtain Co−N-doped porous graphene.

3.2.3.2. Emulsion-Induced Approach. Another approach to the synthesis of graphene@MOF hybrids makes use of Pickering emulsions, which differ from conventional surfactant-stabilized emulsions in that they are stabilized by colloidal particles (usually micro/nanoparticles). Pickering emulsions are frequently studied in materials science.[206] In this synthetic approach, the graphene@MOF hybrid is prepared at the emulsion's oil−water interface.

The Pickering emulsion-induced approach was used by Bian et al. for the in-situ synthesis of hollow ZIF-8/GO hybrids.[207] In this synthetic process, which is depicted in Figure 9a, a Pickering emulsion was prepared by mixing *n*-octanol (containing Hmim) and water (containing Zn^{2+} ions) in the presence of emulsion-stabilizing GO nanosheets. In the emulsion, coordinative and electrostatic interactions caused Zn^{2+} ions to adsorb onto the GO surface, where they functioned as seeds. Interfacial nucleation at the interface of the Pickering emulsion droplets then led to the synthesis of ZIF-8 particles and the formation of a hollow ZIF-8/GO composite whose growth was accelerated by the formation of secondary Pickering emulsions. The same research group synthesized a HKUST-1/GO composite for CO_2 adsorption using the Pickering emulsion strategy.[208] As in their first study, a Pickering emulsion stabilized by GO nanosheets was generated from an *n*-octanol/water mixture. The ligand H_3BTC was dissolved in *n*-octanol, while $Cu(NO_3)_2$ and GO were dissolved in water, and the two solutions were mixed at 2000 rpm in the presence of the nonionic emulsifier B25. To induce the formation of HKUST-1 at the droplet interface of the emulsion, it was heated to 60 °C for 1 h. Composites were prepared using different volumes (2, 5, and 10 mL) of the GO

https://doi.org/10.1021/acs.chemrev.2c00270
Chem. Rev. 2022, 122, 17241−17338

suspension (2 mg/mL). Figure 9b depicts the synthesis of a HKUST-1/GO composite via this approach.

In another report, GO nanosheets and the Zr-based MOF UiO-66-NO_2 ($Zr_6O_4(OH)_4(NO_2\text{-bdc})_6$, where $NO_2\text{-bdc}^{2-}$ = 2-nitro-1,4-benzenedicarboxylate) were used to stabilize a Pickering emulsion (see Figure 9c).[209] The UiO-66-NO_2 MOF was synthesized in a Teflon reactor by a simple solvothermal process in which 2-nitro-1,4-benzenedicarboxylic acid and $ZrCl_4$ were heated to 60 °C in a mixture of DMF and deionized water. To synthesize the Pickering emulsion, GO and UiO-66-NO_2 were thoroughly dispersed in water by ultrasonication and an equal volume of cyclohexane was added. The concentration of the GO solution was kept constant at 1 mg/mL, while the concentration of UiO-66-NO_2 was 0.2, 0.25, or 0.5 mg/mL. The prepared cyclohexane/water/UiO-66-NO_2/GO system was then thoroughly sonicated using 5 s ultrasound bursts applied at 20 s intervals. Finally, the UiO-66-NO_2/GO composite was obtained by freeze drying under liquid nitrogen to remove liquids from the emulsion. The emulsion of UiO-66-NO_2 MOF and GO was an oil-in-water emulsion in which the MOF and the GO were both located in the aqueous phase due to their hydrophilicity. There was dynamic exchange of both the MOF and the GO between the emulsion interface and the aqueous phase, and hydrogen-bond formation between the GO nanosheets and the MOF led to their cross-linking and the formation of the UiO-66-NO_2/GO composite, which was collected by freeze drying. More recently, Nugmanova et al. used the Pickering emulsion strategy to prepare SURMOF/GO hybrids (SURMOF = surface-anchored MOF).[210] Pickering emulsions were prepared by mixing an oil phase [Zn(II) *meso*-tetra(4-pyridyl)porphyrin (ZnTPyP MOF in chloroform)] with a water phase (GO and $Zn(OAc)_2{\cdot}2H_2O$ in aqueous ethanol) in a sealed vial that was then ultrasonicated. After sonication, 0.5 mL of ethanol was added to the mixture, the sonication was repeated, and the vial was heated in an oven at 70 °C for 48 h. The above process with minor changes was also used to synthesize a SURMOF/GO hybrid based on the MOF ZnDPyDCPP [Zn(II) *meso*-di(4-pyridyl)-di(4-carboxyphenyl)-porphyrin].

3.3. Deposition of Graphene@MOF Hybrids on Functional Substrates

This section will discuss the preparation of graphene@MOF hybrids on top of functional substrates to either prepare thin films or deposit the hybrids on top of porous supports or electrodes.

3.3.1. Seeded Growth. The seeded growth method, also known as the secondary growth method, is used to prepare thin films of MOFs on various substrates.[202] Broadly speaking, this method involves synthesizing a seed solution and then inducing secondary growth to obtain the desired product. There are many seeding strategies including step-by-step seeding,[214] microwave-assisted seeding,[215] rubbing,[216] reactive seeding,[217] and thermal seeding.[218] The applicability of this strategy is mainly limited by the difficulty of preparing defect-free MOF films and the substrate dependence of the seeding process.

Hu et al. overcame the challenge of preparing defect-free MOF thin films by using 2D ZIF-8/GO hybrid-based seeds to prepare ultrathin MOF membranes.[219] The fabrication of ZIF-8/GO membranes began with the synthesis of 2D ZIF-8/GO hybrid seeds by adding a GO solution (1:4 v/v in water and methanol) to a mixture of 2-methylimidazole (Hmim) and $Zn(NO_3)_2{\cdot}6H_2O$ in methanol. After stirring the obtained solution for a set reaction time (5 h, 3 h, or 20 min), the precipitated seeds were collected and washed three times with methanol. A porous anodic aluminum oxide (AAO) substrate was then coated twice with the ZIF-8/GO seed suspension. Finally, ZIF-8/GO membranes were synthesized by growing the seed layer on the AAO surface using the contradiffusion method (Figure 8a).[201] As shown in Figure 8a, the seed layer-coated AAO substrate was used to separate solutions of Hmim and Zn^{2+} ions (Zn^{2+}:Hmim molar ratio = 1:8) with the seed layer of the AAO substrate facing the Zn^{2+} ion solution. After crystallization for 1 or 3 h, the MOF membrane was removed, washed with methanol, and dried overnight.

The thermal seeding approach was utilized by Kim et al. to achieve seeded growth of HKUST-1-based thin films on a GO/AAO substrate.[202] As in the work described above, a seed solution was first prepared by mixing an ethanolic solution of an organic ligand (trimesic acid) and an aqueous solution of a metal salt ($Cu(NO_3)_2{\cdot}3H_2O$). The resulting solution was stirred for 15 min at 298 K and then for 6 h at 120 °C to obtain a seed solution that was then used to coat a heated GO/AAO substrate. Physisorbed MOF seeds were removed from the seeded substrate by sonication in ethanol for 1 min. For secondary seed growth, the as-prepared seeded GO/AAO substrate, an aqueous solution of $Cu(NO_3)_2{\cdot}3H_2O$, and an ethanolic solution of trimesic acid were heated together in a reactor for 6 h at 120 °C. The resulting membrane was then washed with ethanol and left overnight in an oven at 80 °C. The complete synthetic process is summarized in Figure 7b.

In all of the above cases, the oxygen-containing surface functional groups of GO were considered essential for the successful loading of MOF seeds onto the supporting surface and thereby enabling the synthesis of defect-free thin films. In another recent report, the seed growth approach was used to prepare a ZIF-9-GO composite that served as a self-sacrificial template for the synthesis of Co_3O_4 nanocrystals incorporating N-doped graphitic carbon (Co_3O_4@N-GC).[203] In this case, benzimidazole and $Co(NO_3)_2{\cdot}6H_2O$ were dissolved in DMF, GO was added, and the resulting mixture was sonicated for 2 h to ensure homogeneous dispersion of the GO. The reaction mixture was then stirred for 2 h to form a seeding solution that was transferred to a reactor and heated for 2 days at 130 °C to induce solvothermal growth. This resulted in the formation of ZIF-9-GO composites (Figure 7c) that were ground into fine powders and carbonized at different temperatures to obtain Co_3O_4@N-GC.

3.3.2. Deposition on Porous Supports. Graphene@MOF composite-based thin films or hybrid membranes have been synthesized for various applications. In most cases, a thin film of the graphene@MOF hybrid is synthesized over a substrate. This can be achieved either by loading an already synthesized graphene@MOF composite onto a substrate or by depositing the graphene and MOF separately.[222] In addition to thin-film synthesis on a substrate, hybrid membranes have been prepared by filtration[223] and electrochemical deposition.[224]

In 2016, Kung et al. reported the synthesis of thin films based on MOF-525 ($Zr_6O_4(OH)_4(TCPP)_3$) and graphene nanoribbons (GNRs).[225] The films were synthesized on conducting ITO glass (indium tin oxide) by a simple casting process. The MOF-525/GNRs hybrid was obtained by heating a solution of $ZrOCl_2{\cdot}8H_2O$ and benzoic acid in DMF for 2 h at 180 °C. After cooling, GNRs and H_4TCPP were added and the composite MOF-525/GNRs was obtained after heating the resulting mixture at 80 °C for 1 day. To prepare thin films of this

https://doi.org/10.1021/acs.chemrev.2c00270
Chem. Rev. 2022, 122, 17241−17338

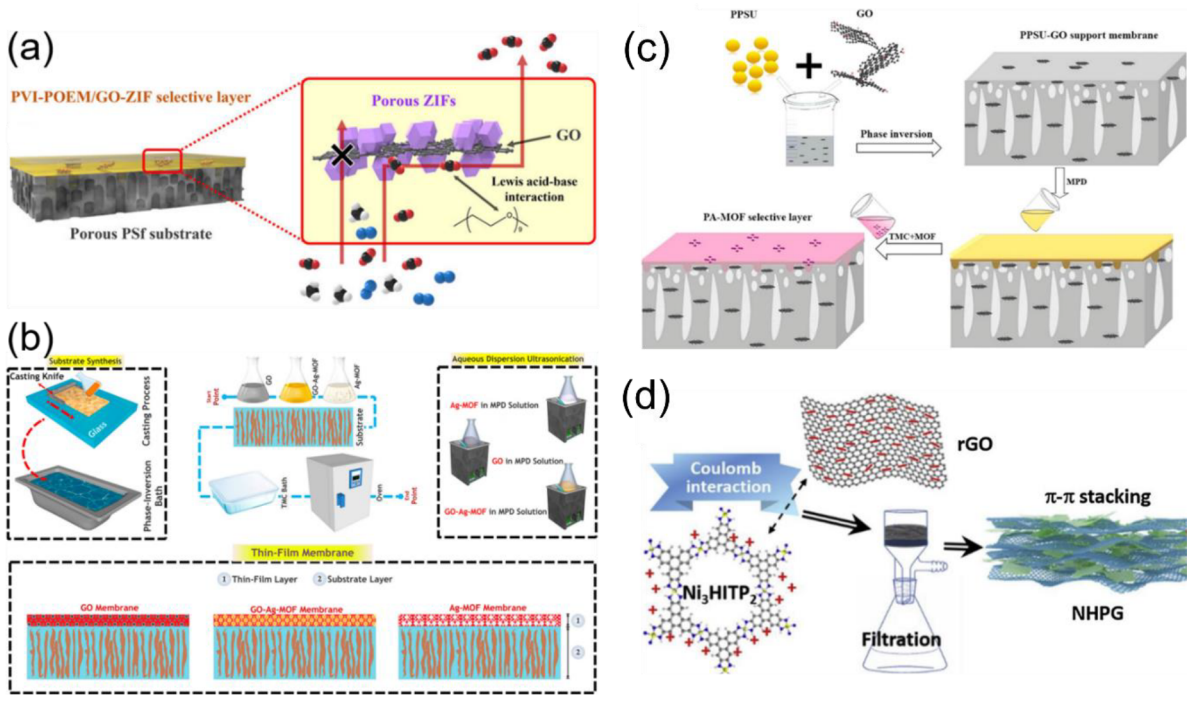

Figure 10. (a) Mixed-matrix composite GO-ZIF thin-film membrane on a PSf substrate and gas permeation pathway through this membrane. Reproduced with permission from ref 220. Copyright 2021 American Chemical Society. (b) Schematic depiction of the synthesis of a GO-Ag-MOF composite-based thin-film membrane and different thin-film membranes prepared on the substrate layer. Reproduced with permission from ref 221. Copyright 2018 American Chemical Society. (c) Preparation of a thin-film nanocomposite membrane by formation of a PA-MOF-selective layer on a PPSU-GO support membrane. Reproduced with permission from ref 222. Copyright 2018 Elsevier. (d) Filtration-assisted fabrication of a composite thin film based on Ni_3HITP_2 and rGO (NHPG). Reproduced with permission from ref 223. Copyright 2020 Elsevier.

composite, it was thoroughly dispersed in DMF and the resulting suspension was cast on ITO glass. The MOF-525/GNRs hybrid thin film was finally collected after air drying. A simple casting method was also used by Lee et al. to prepare mixed-matrix GO-ZIF-8/ZIF-67 composite membranes on a polysulfone (PSf) substrate.[220] The composite was prepared by mixing a methanolic solution of Hmim with a GO suspension in methanol/deionized water, sonicating the resulting reaction mixture for 30 min, and then stirring it for 2 h before adding a methanolic solution of $Zn(NO_3)_2{\cdot}6H_2O$ and $Co(NO_3)_2{\cdot}6H_2O$ and stirring overnight. For membrane fabrication, GO-ZIF-8/ZIF-67 was thoroughly dispersed in aqueous ethanol. A casting solution was then prepared by dissolving a PVI-POEM copolymer (PVI-POEM is poly(vinyl imidazole)-*co*-poly(oxyethylene methacrylate)) in the GO-ZIF-8/ZIF-67 suspension. The PSf substrate was coated with a layer of poly(trimethylsilyl)propyne in hexane using the bar-coating method. The modified PSf substrate was then homogeneously coated with the GO-ZIF-8/ZIF-67 casting solution and dried. The synthesized composite membrane on the PSf substrate and its use in gas separation are shown in Figure 10a.

Another report on the preparation of thin-film nanocomposite (TFN) membranes was presented by Firouzjaei et al., who made use of interfacial polymerization.[221] The PES (poly(ether sulfone)) substrate was synthesized by the phase separation technique shown in Figure 10b. Briefly, a cast solution of polyvinylpyrrolidone (PVP) and PES in DMF was prepared and then overlaid on a coagulation bath consisting of a solution of water, sodium dodecyl sulfate, and DMF. To prepare the GO-Ag-MOF thin-film membrane, the PES substrate was immersed in a solution of 1,3-phenylenediamine containing a dispersion of the GO-Ag-MOF nanocomposite. Finally, the as-obtained PES substrate was dipped in a solution of trimesoyl chloride in *n*-hexane and dried at 80 °C. The step-by-step synthesis of the thin-film membrane and the preparation of the nanomaterial dispersion in 1,3-phenylenediamine are shown in Figure 10b. In all of the studies discussed above, the synthesis of thin films on a substrate was performed using already synthesized graphene@MOF hybrids. An alternative approach was developed by Golpour et al., who fabricated thin films by synthesizing graphene@MOF hybrids over a substrate.[222] A schematic depiction of their synthesis of a PA-UiO-66-NH_2/PPSU-GO membrane is shown in Figure 10c. To begin with, a support membrane consisting of GO and polyphenylsulfone (PPSU) was formed by dissolving GO and PPSU in *N*-methylpyrrolidone to prepare a polymer solution that was degassed at room temperature for 1 day, cast on nonwoven polyester, and finally coagulated in deionized water. A selective polyamide layer was then deposited on this substrate by immersing it in an aqueous solution of piperazine before successively layering 1,3-phenylenediamine and a solution of trimesoyl chloride (TMC) and the MOF UiO-66-NH_2 in hexane on the support membrane before curing the membrane at 70 °C to induce interfacial polymerization with concomitant formation of the graphene@MOF hybrid. Another recent report by Mu et al. demonstrated the formation of a thin film based on GO and the MOF Ni_3HITP_2 (HITP = 2,3,6,7,10,11-hexaaminotriphenylene hexahydrochloride) using a filtration-based process as shown in Figure 10d.[223] To prepare the MOF, $NiCl_2{\cdot}6H_2O$ and HITP·6HCl were dissolved in distilled water under stirring. $NH_3{\cdot}H_2O$ was added to the resulting solution, and the mixed solution was stirred for 3 h at 65 °C. Ni_3HITP_2 MOF was obtained from the reaction mixture by centrifugation followed by washing and drying. The MOF powder was then dispersed in distilled water and rGO to

https://doi.org/10.1021/acs.chemrev.2c00270
Chem. Rev. 2022, 122, 17241−17338

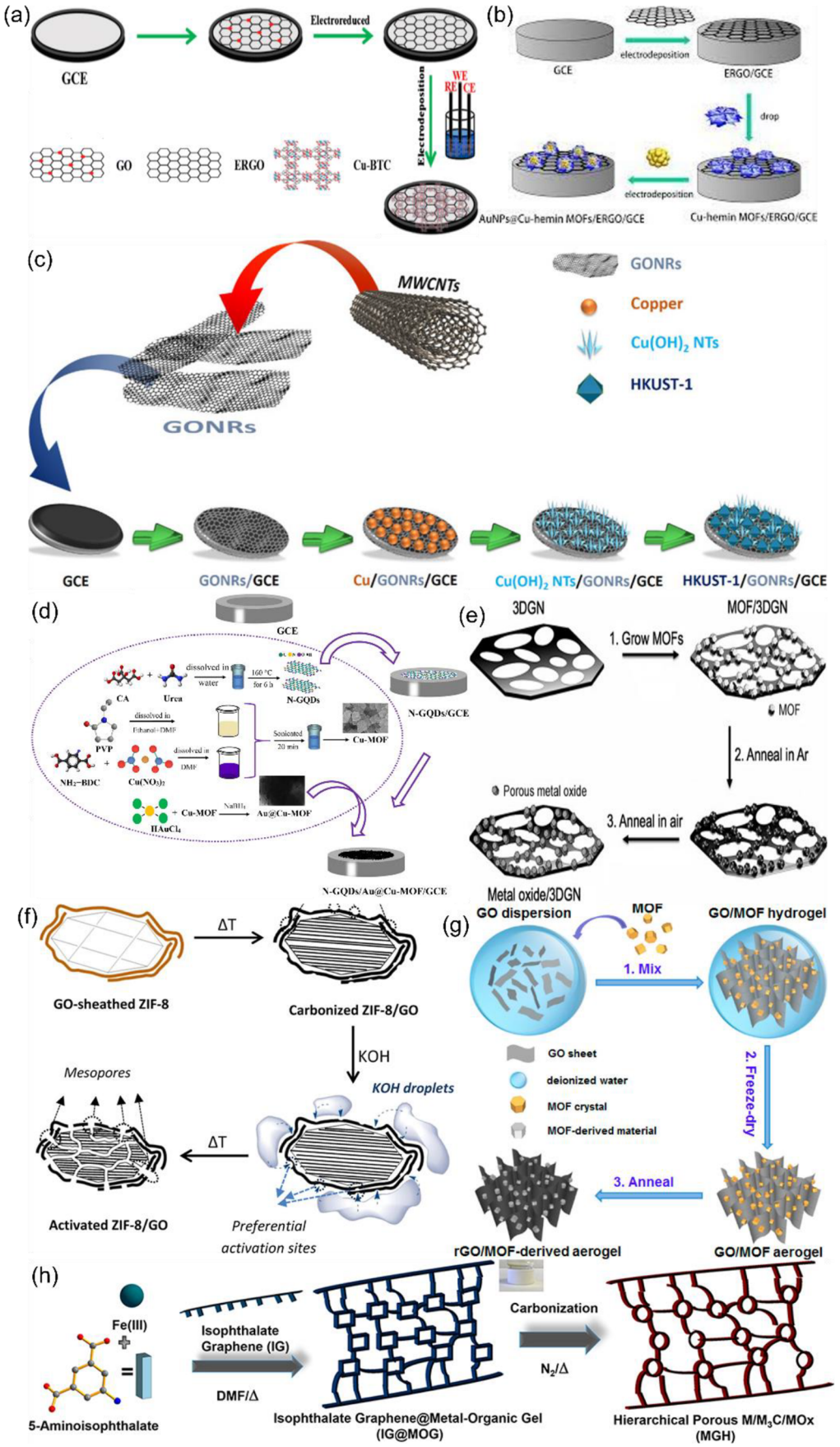

Figure 11. (a) Schematic representation of the synthesis of an ERGO and HKUST-1-based composite by electrode deposition. Reproduced with permission from ref 226. Copyright 2018 Springer. (b) Preparation of a HKUST-1/GONRs/GCE composite via synthesis of HKUST-1 on the surface of a GONR-modified GCE. Reproduced with permission from ref 227. Copyright 2020 American Chemical Society. (c) Process for the synthesis of an

https://doi.org/10.1021/acs.chemrev.2c00270
Chem. Rev. 2022, 122, 17241−17338

Figure 11. continued

Au nanoparticle-loaded Cu-hemin MOF/ERGO composite on the surface of a GCE. Reproduced with permission from ref 228. Copyright 2020 World Scientific Publishing Ltd. (d) Synthesis of N-GQDs, Cu-MOF, and an N-GQDs/Au@Cu-MOF/GCE composite on the GCE surface. Reproduced with permission from ref 229. Copyright 2020 Elsevier. (e) Preparation of a MOF/3DGN hybrid-derived metal oxide/3DGN composite. Reproduced with permission from ref 230. Copyright 2014 John Wiley & Sons, Inc. (f) Formation of a mesoporous-activated ZIF-8/GO composite by carbonization and subsequent activation of a GO-sheathed ZIF-8 composite. Reproduced with permission from ref 231. Copyright 2017 American Chemical Society. (g) Formation of an rGO/MOF aerogel from a GO/MOF hydrogel. Reproduced with permission from ref 232. Copyright 2017 American Chemical Society. (h) Synthesis of an IG-based MOG@IG composite gel and its carbonization to form a hierarchically porous $M/M_3C/MO_x$ composite. Reproduced with permission from ref 79. Copyright 2020 Frontiers Media S.A.

obtain a dispersion of Ni_3HITP_2-rGO that was filtered under vacuum through a filtration membrane. The prepared membrane was then freeze dried and removed from the filtration membrane.

In order to test graphene@MOF hybrids in electrochemical applications, for instance, electrochemically sensing the deposition or formation of graphene and MOF on the electrode surface (i.e., glassy carbon electrodes (GCE)) is necessary. In the following, different studies on the preparation of MOF@graphene hybrid-decorated electrodes will be discussed. Wang et al. synthesized an electrochemical sensor for 2,4,6-trinitrophenol detection by depositing electrochemically reduced GO (ERGO) and HKUST-1 on GCE.[226] The HKUST-1/ERGO/GCE system was fabricated using a stepwise process in which the presynthesized MOF was directly cast on an ERGO-coated GCE as shown in Figure 11a. A dispersion of GO was first cast on a clean GCE surface, after which the surface was washed with water and dried under N_2. Electroreduction of the GO on the GCE surface was then performed by cyclic scanning in phosphate buffer until a steady curve was obtained. To fabricate the final hybrid, the resulting ERGO-coated GCE was dipped in a suspension of the HKUST-1 MOF in DMF containing $NaNO_3$, and cyclic scanning was performed to induce electrodeposition of the MOF on the ERGO/GCE system. As an alternative to direct MOF casting on GCE, a recent report by Jalal et al. showed that graphene@MOF hybrids can be prepared by growing the MOF on a GCE surface.[227] As shown in Figure 11b, multiwalled carbon nanotubes (MWCNTs) were used to prepare GO nanoribbons (GONRs) that were then loaded onto the GCE by applying a GONR suspension to the electrode and drying it at ambient temperature. HKUST-1 was deposited on the resulting GONR/GCE in a stepwise fashion, as shown in Figure 11b. Briefly, the process involved electrodeposition of Cu clusters on the modified electrode surface. This was done using a solution containing ammonium sulfate and copper sulfate with a fixed deposition potential of −250 mV for 5 min. The elemental copper in the as-synthesized Cu/GONRs/GCE electrode was then oxidized to copper nanotubes by dipping the electrode in a mixed solution of deionized water, NaOH, and ammonium persulfate to obtain the intermediate copper nanotube composite-coated electrode $Cu(OH)_2$ NTs/GONRs/GCE.

Finally, the HKUST-1/GONRs/GCE system was obtained by immersing $Cu(OH)_2$ NTs/GONRs/GCE in a H_3BTC solution for 4 min. This hybrid electrode was successfully used as an electrochemical sensor to detect the drug Imatinib. Similarly, Shahrokhian et al. designed a graphene@MOF hybrid on GCE by the stepwise synthesis of the cobalt analogue of HKUST-1 (Co_3BTC_2) on a GCE.[233] Briefly, a GO suspension was dispersed on the surface of the GCE, after which the electrode was dried in an oven. For the synthesis of the MOF on a GCE, nanoflakes of $Co(OH)_2$ were electrodeposited on GO/GCE by immersing the electrode in a $Co(NO_3)_2$ solution containing potassium nitrate as a supporting electrolyte. Electrodeposition was induced by applying an electrode potential of −1.1 V (vs Ag/AgCl) to the solution for 5 min, which caused the reduction of the GO and formation of the $Co(OH)_2$/rGO/GCE electrode. Finally, the loaded $Co(OH)_2$ was used to form a MOF composite by immersing $Co(OH)_2$/rGO/GCE in a solution of H_3BTC for 2.5 min. This caused the initially blue electrode deposited material to become pink, clearly demonstrating the formation of the $Co_3(BTC)_2$ MOF on the modified GCE.

The electrode deposition strategy was also recently used to prepare a hybrid of GO with metal NP-loaded MOFs: as shown in Figure 11c, Wang et al. successfully loaded gold nanoparticles onto a hybrid of ERGO and a Cu-hemin MOF that was prepared on a GCE.[228] After cleaning the GCE, a GO suspension was dropped onto its surface. The electrode was then dried, and the GO was reduced in a phosphate buffer solution at a fixed potential of −1.4 V. The Cu-hemin MOF was synthesized by mixing a hemin solution in phosphate buffer with an aqueous solution of $Cu(NO_3)_2{\cdot}3H_2O$ at room temperature. After 2 h, the Cu-hemin MOF was collected as a brownish-black powder. An aqueous dispersion of this MOF was dispersed on the ERGO/GCE to obtain the Cu-hemin MOFs/ERGO/GCE after drying the modified electrode in air. Finally, the AuNPs@Cu-hemin MOFs/ERGO/GCE electrode was prepared by immersing the Cu-hemin MOFs/ERGO/GCE in a solution of $HAuCl_4$ and applying a fixed potential of −0.2 V for 3 min. In the same year, Hatamluyi et al. synthesized a gold NP-loaded graphene@MOF composite using the electrodeposition method.[229] In this case, nitrogen-doped graphene quantum dots (N-GQDs) served as the graphene derivative of the graphene@MOF hybrid, while the MOF component was NO_2-MOF-2(Cu), which is a copper-based MOF prepared from NH_2-BDC and $Cu(NO_3)_2$; its stoichiometric formula is $Cu_2(NO_2\text{-bdc})_2(DMF)_2$. Details of the synthesis of N-GQDs and Cu-MOF are shown in Figure 11d. In contrast to the approach of Wang et al., in this case the gold NPs were loaded onto the Cu-MOF before loading the resulting MOF onto a GCE modified with N-GQDs. The loading of Au NPs on the Cu-MOF was done by adding $NaBH_4$ and $HAuCl_4$ to a solution of Cu-MOF in double-distilled water and stirring for 1 h. For the synthesis of the graphene@MOF hybrid on the GCE, separate dispersions of N-GQDs and Au@Cu-MOF in DMF were successively cast on the GCE as shown in Figure 11d. It should be noted that the modified GCE obtained after casting the dispersion of N-GQDs was dried before loading the Au@Cu-MOF dispersion.

3.4. Graphene@MOF Hybrids with Polymers

Polymeric graphene@MOF hybrids can be obtained by the polymerization of monomer molecules in the presence of the graphene and MOF precursors. The polymerized product can be obtained either by adding the MOF and graphene derivative separately or by adding a preformed graphene@MOF hybrid to a monomer solution that is subsequently polymerized.

https://doi.org/10.1021/acs.chemrev.2c00270
Chem. Rev. 2022, 122, 17241−17338

This synthetic approach was recently used by He et al. to prepare a composite material containing HKUST-1-derived metal oxide@mesoporous carbon (mC), rGO, and polyaniline (PANI).[211] The Cu-MOF was prepared by a simple hydrothermal reaction of H_3BTC and $Cu(NO_3)_2{\cdot}3H_2O$ in a Teflon reactor for 24 h at 140 °C. The resulting HKUST-1 was then calcined at 300, 500, 700, or 900 °C to obtain MOF-derived $CuO_x@mC_y$ (y = heating temperature), as shown in Figure 9d. An aniline solution was then prepared by dissolving aniline in aqueous HCl at room temperature and mixed with preformed 3D rGO. Finally, the MOF-derived $CuO_x@mC_y$ was added to the solution together with an oxidant—$(NH_4)_2S_2O_8$ in HCl—and in-situ polymerization was allowed to proceed for 12 h, after which the composite CuO_x@mC@PANI was isolated by centrifuging the reaction mixture and drying the collected solid material. The full synthetic process is depicted schematically in Figure 9d. An alternative approach in which the MOF and graphene derivatives are not added separately was demonstrated by Fan et al., who performed polymerization on ZnO@graphene nanosheets and thereby showed that polymerized graphene@MOF hybrids can be prepared from nonpolymerized hybrids.[212] Briefly, a methanolic solution of GO and $Zn(NO_3)_2$ was quickly poured into a methanolic solution of Hmim, which was then stirred to induce the formation of ZIF-8 on the GO surface. The synthesized hybrid was then carbonized at 800 °C, after which the derived material was oxidized in air at 300 °C to obtain ZnO-doped graphene nanosheets (ZnO@G; see Figure 9e). Polymeric thermally responsive brushes (TRB) were then anchored on the ZnO@G nanosheets by in-situ polymerization of *N*-isopropylacrylamide (NIPAM), as shown in Figure 9e. Polymerization was typically induced by heating a mixture of NIPAM and well-dispersed ZnO@G nanosheets under Ar at 70 °C, adding a solution of the radical initiator azobis(isobutyronitrile) (AIBN) in DMF, and allowing the reaction to proceed for 6 h. The synthesized TRB-ZnO@G nanosheets were collected by centrifugation and purified by washing with DMF/ethanol/water and ethanol.

A similar strategy involving fabricating polymerized graphene@MOF hybrids using a graphene@MOF composite was employed by Barakzehi et al. to prepare polyester fabric modified with MIL-53(Al) (AlOH(bdc)) and coated with rGO/PPy (PPy-polypyrrole).[234] To begin with, the MIL-53(Al)-coated fabric was prepared by in-situ synthesis of the MOF in the presence of polyethylene terephthalate (PET). This was achieved by dipping PET fabric in $Al(NO_3)_3{\cdot}9H_2O$ for 30 min and then removing the fabric and washing it with deionized water. The dried fabric was then immersed in a solution of Na_2bdc, washed, and dried again. The process of dipping in the metal salt and immersion in Na_2bdc was repeated different numbers of times to obtain PET/MOF-*n*, where *n* denotes the number of repeated cycles. GO was then loaded onto PET/MOF-*n* by soaking the modified fabric in a GO solution, after which the loaded GO was reduced to rGO by dipping the fabric in an ascorbic acid solution for 15 min at 95 °C, forming PET/MOF-*n*/rGO hybrids. Finally, the polymerized composite was synthesized by in-situ polymerization of pyrrole on PET/MOF-*n*/rGO, which was achieved by dipping PET/MOF-*n*/rGO in a pyrrole solution in an ice bath for 30 min. A ferric chloride solution was then added to the reaction mixture, and polymerization was allowed to proceed for 2.5 h.

In another recent report, in-situ polymerization was used to prepare a ternary composite containing S- and N-codoped quantum dots of graphene (S, N: GQDs), ZIF-8-derived ZnO polyhedral, and polyaniline.[213] The S, N: GQDs were prepared by heating an aqueous solution of thiourea and citric acid in an autoclave for 4 h at 160 °C and then centrifuging the reaction mixture for 30 min at 5000 rpm. ZnO polyhedra were synthesized by calcinating ZIF-8 under nitrogen at 350 °C. Finally, the ternary composite was obtained by in-situ polymerization as shown in Figure 9f. Briefly, polymerization was induced by preparing a solution of aniline and S, N: GQDs in aqueous HCl, to which a solution of ammonium peroxydisulfate (APS) in deionized water was slowly added under stirring while cooling the reaction mixture in an ice bath. ZnO and NaOH were added once the solution changed color from green to colorless. The greenish-black ZnO/S, N: GQDs/PANI composite precipitated after stirring for 4 h (see Figure 9f).

3.5. Derivatives of Graphene@MOF Hybrids

Pristine MOFs are interesting self-sacrificial templates for preparing various derived materials, including carbon systems, metal oxides, and metal oxide-decorated carbon systems, with interesting performance in different applications, especially in the electrochemical field.[235−237] Sacrificial templating has also been used to prepare high-performance materials from graphene@MOF hybrids. This synthetic method generally involves high-temperature treatment of the hybrid in a tube furnace under an inert nitrogen or argon atmosphere. The heating temperature strongly affects the structure and properties of the derived material and is therefore generally carefully optimized.

An example of self-sacrificial templating using graphene@MOF hybrids was reported by Cao et al., who prepared MOF-derived metal oxide-coated hybrids with graphene.[230] Two MOFs, ZIF-8 and MIL-88B(Fe) ($Fe_3O(OH)(bdc)_3$), were hybridized with three-dimensional graphene (3DGN) in a one-pot reaction. Both of the resulting MOF/3DGN hybrids were then annealed at 450 °C for 1 h under argon before being heated in air at 380 °C for 1 h to obtain Fe_2O_3/3DGN and ZnO/3DGN. This process is illustrated in Figure 11e, which shows that during the reaction the MOFs were converted into the corresponding metal oxides while the 3D structure of GR remained stable but its surface was covered with the metal oxide. In the case of the ZnO/3DGN hybrid, the concentration of ZIF-8 precursors and the heating temperature were the main factors used to tune the size of ZIF-8 nanocrystals on 3DGN and to thereby control the size of the ZnO structures in the derived ZnO/3DGN hybrid. Martin-Jimeno et al. reported another ZIF-8 based ZIF-8/GO hybrid that was prepared using the three-step method shown in Figure 11f.[231] Briefly, GO-covered ZIF-8 was obtained by sonicating an aqueous dispersion of GO in a solution of a Zn salt and poly(vinylpyrrolidone) for 1 h. This dispersion was then mixed with a preheated (40 °C) methanolic solution of Hmim, and the resulting reaction mixture was stirred for 2 h to obtain the GO-sheathed ZIF-8 hybrid, which was then carbonized under nitrogen at 700 °C. Finally, the carbonized hybrid was chemically activated by mixing it with KOH and heating the mixture under nitrogen at 600−1000 °C. After washing the activated GO/ZIF-8 hybrid with water using a Soxhlet extractor, it was vacuum dried. The prepared hybrid had a high specific surface area (1300−1400 m^2/g) and mesopores (3−4 nm). The synthetic strategy used in its fabrication was therefore named nanopore lithography because it transferred mesoporous patterns onto the ZIF-8-derived carbon. The high surface area and mesoporous nature of GO/ZIF-8 hybrid

https://doi.org/10.1021/acs.chemrev.2c00270
Chem. Rev. 2022, 122, 17241−17338

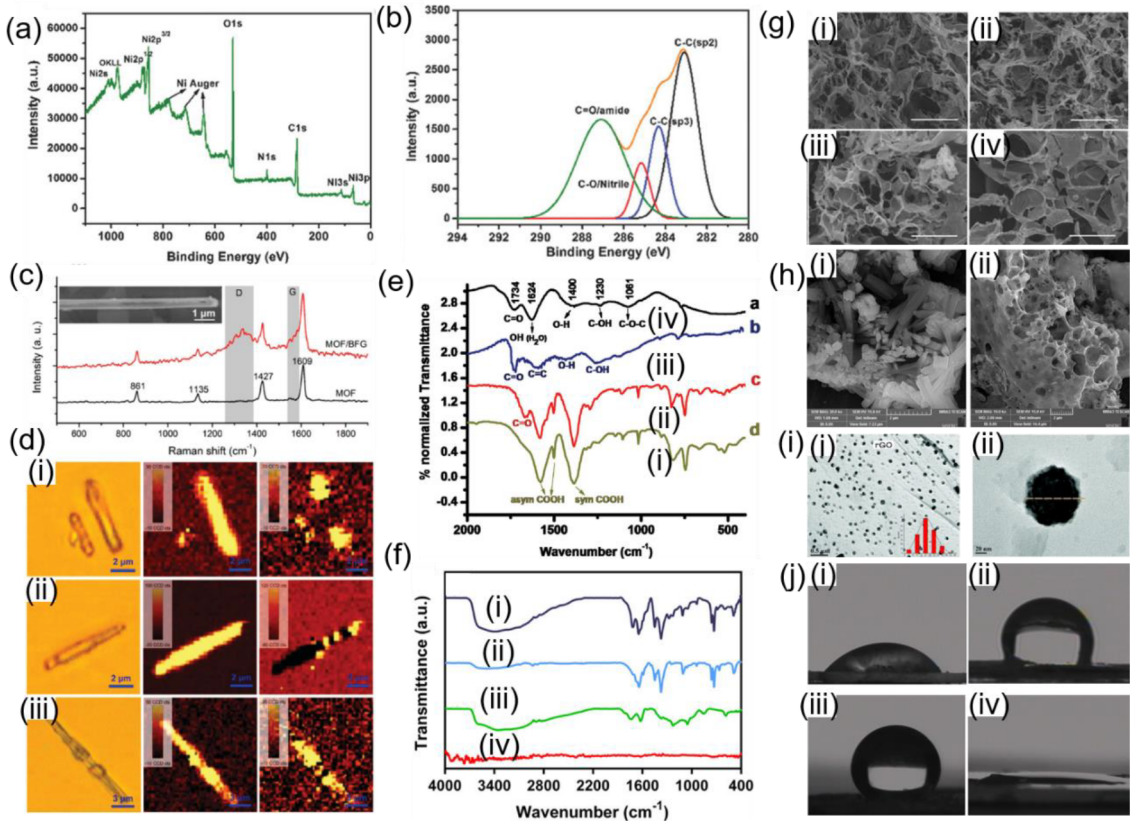

Figure 12. (a) XPS spectrum of an NGO/MOF-74(Ni) hybrid showing the different elements (Ni, N, C, and O) it contains. (b) Deconvoluted C 1s XPS spectrum of an NGO/MOF-74(Ni) hybrid. Reproduced with permission from ref 238. Copyright 2017 John Wiley & Sons, Inc. (c) Raman spectra of MOF-5/BFG and MOF-5. (Inset) SEM image of a single MOF/BFG nanowire. (d) Raman mapping spectra of composite MOF/BFG nanowires. (Left to right) Raman maps of the G and D bands in nanowire samples superimposed on the corresponding optical images. (e) Normalized FTIR spectrum of (i) MOF-5, (ii) the MOF-5/BFG hybrid, (iii) BFG, and (iv) GO. Reproduced with permission from ref 77. Copyright 2010 American Chemical Society. (f) FTIR spectra of (i) HKUST-1/GONRs, (ii) HKUST-1, (iii) GONRs, and (iv) MWCNTs. Reproduced with permission from ref 227. Copyright 2020 American Chemical Society. (g) Morphology of UiO-66-NO_2/GO composites. SEM images of UiO-66-NO_2/GO composites with UiO-66-NO_2:GO ratios of (i) 1:5, (ii) 1:4, (iii) 1:3, and (iv) 1:2. Reproduced with permission from ref 209. Copyright 2017 Royal Society of Chemistry. (h) SEM images used to characterize the morphology of (i) pristine MOF-2(Cu) and (ii) the MOF-2(Cu)-graphene hybrid. Reproduced with permission from ref 239. Copyright 2018 Springer Nature. (i) TEM images of (i) the Cu/Cu_2O@C-rGO composite and (ii) a single Cu/Cu_2O@C nanoparticle. (Inset of i) Size distribution range of Cu/Cu_2O@C nanoparticles in the Cu/Cu_2O@C-rGO composite. Reproduced with permission from ref 240. Copyright 2018 Royal Society of Chemistry. (j) Photographs showing the water contact angles of (i) ZIF-8 (56°), (ii) HFGO (125°), and (iii) HFGO@ZIF-8 (162°) and the oil contact angle of (iv) HFGO@ZIF-8 (0°). Reproduced with permission from ref 128. Copyright 2016 John Wiley & Sons, Inc.

improved its electrochemical performance; the hybrid had a higher charging/discharging rate and capacitance than alternative materials.

In addition to graphene/MOF hybrids, graphene/MOF hybrid gels have been reported as suitable precursors for preparing derived materials. In this context, Xu and co-workers described the synthesis of a GO/MOF aerogel-derived hybrid material.[232] Crystals of MIL-101(Fe) were prepared by a one-pot synthesis and then transferred into a dispersion of GO in water as shown in Figure 10g. The obtained solution was then converted into a GO/MOF hybrid gel by vigorous shaking. This hydrogel was freeze dried to obtain the corresponding GO/MOF hybrid aerogel by removing water. The same procedure was used to prepare hybrid aerogels of GO with several other MOFs including ZIF-8, Sn-MOF($K_2Sn(bdc)_3$), Ni-MOF ($Ni_3(OH)_2(C_8H_4O_4)_2(H_2O)_4$), MOF-5, and Ni-MOF/Fe-MOF. The derived hybrid gel (denoted rGO/Fe_2O_2) was then annealed at 450 °C under nitrogen and at 380 °C under air to obtain a material that was used as a supercapacitor electrode with a good specific capacitance of 869 F/g at a current density of 1 A/g. Our research group recently prepared some metal-containing graphene hybrids (MGH) by pyrolyzing isophthalate-functionalized fluorographene (IG) with an iron metal−organic gel consisting of Fe^{3+} ions and 5-aminoisophthalic acid at different temperatures.[79] A schematic representation of the synthesis of the gel and MGH is shown in Figure 11h. Briefly, the solvothermal treatment of the metal−organic gel precursors and IG in DMF yielded a hybrid black gel (MOG@IG) that was dispersed and stirred, centrifuged, washed, and dried. This treatment yielded a MOG@IG powder that was pyrolyzed at various temperatures (400, 600, and 800 °C) in a tube furnace under nitrogen to obtain MGH-*x* (where *x* denotes the pyrolysis temperature). Remarkably, MGH-600 exhibited magnetic properties and was also successfully used in an electrochemical dopamine sensor.

4. CHARACTERIZATION OF GRAPHENE@MOF HYBRIDS AND ITS CHALLENGES

Graphene@MOF hybrids have been characterized using several techniques including spectroscopic techniques such as X-ray

https://doi.org/10.1021/acs.chemrev.2c00270
Chem. Rev. 2022, 122, 17241−17338

photoelectron (XPS), Raman, and infrared (IR) spectroscopies, microscopy techniques such as scanning electron microscopy (SEM) and transmission electron microscopy (TEM), elemental mapping techniques such as energy-dispersive X-ray (EDX) mapping, powder X-ray diffraction (PXRD), physisorption, contact angle (CA) measurement, and thermogravimetric analysis (TGA). The application of these techniques to graphene@MOF hybrids and the interpretation of their output are discussed below.

Knowledge of the interactions between the components of graphene@MOF hybrids is essential for understanding their properties and stability. XPS is an excellent tool for probing these interactions. For example, the nature of the recently reported covalent amide bonding between GA and UiO-66-NH_2 in the GA@UiO-66-NH_2 composite was determined by XPS.[75] In addition to revealing the different types of atoms present in a graphene@MOF hybrid, XPS spectra provide information on their chemical nature and state. Thus, the XPS characterization of an NGO/MOF-74 composite (NGO = nitrogen-doped GO)[238] demonstrated the presence of C, O, N, and Ni(II) atoms (as shown in Figure 12a), and deconvolution of the C 1s XPS spectra further revealed four peaks corresponding to C−O, C═O, C−C (sp^2), and C−C (sp^3) bonds (Figure 12b). Similarly, the deconvoluted N 1s spectrum showed three different types of nitrogen atoms corresponding to graphitic, pyridine, and pyrrole nitrogens. The presence of Ni^{2+} ions was confirmed by the position of the Ni $2p_{3/2}$ (872 eV) and Ni $2p_{1/2}$ (854.1 eV) peaks, which agreed well with previous reports.

Carbon materials are often characterized by Raman spectroscopy. The Raman spectrum of graphene features two bands known as the G and D bands that are assigned to in- and out-of-plane vibrations of the sp^2 carbon atoms, respectively. The ratio of the intensities of the D band (I_D) and the G band (I_G) is used as a measure of the defect content of carbon materials; a high I_D/I_G ratio indicates the presence of defects. This analytical use of the I_D/I_G ratio is illustrated by a recent study in which rGO@LDH, a composite of rGO with layered double hydroxide (LDH), was synthesized by reductively anchoring ZIF-67 nanoparticles on a GO surface. Raman spectroscopy revealed that the I_D/I_G ratio of the composite was 0.95, whereas that of its GO precursor was only 0.85, indicating that the reductive anchoring process increased the defect content of the graphene structure.[199] The higher concentration of defects in rGO@ZIF-67 hybrids in turn improved the nucleation of LDH on the rGO nanosheets. Raman spectra and Raman mapping can also be used in combination to determine the location of graphene sheets in graphene@MOF hybrids, as exemplified by the analysis of MOF-5/BFG hybrid nanowires using micro-Raman spectroscopy with Raman mapping.[77] The Raman spectrum of MOF-5 has four distinct bands whose positions do not shift upon formation of the MOF-5/BFG composite, and the only additional bands seen in the Raman spectrum of the composite are the D and G bands at 1609 and 1590 cm^{-1}, respectively (Figure 12c). Neither of these bands overlap with any bands in the Raman spectrum of the MOF, so the D band was used to determine the location of graphene within the hybrid nanowires. Inspection of the Raman mapping images presented in Figure 12d revealed three different positions of graphene in the MOF/BFG nanowire; the top, middle, and bottom images show samples in which graphene is present at the tip (mostly), along the axis, and along the complete nanowire. Since the graphene was mostly present at the tips of the nanowires, it was suggested that the nanowires formed via a tip-growth mechanism. These results were consistent with SEM images (see the inset of Figure 12c) showing that the nanowires had smooth surfaces, which implies that the graphene was intercalated within the nanowires rather than being adsorbed on their surfaces.

Fourier transform infrared (FTIR) spectroscopy can be used to identify the functional groups present in a sample and to determine their density within the analyzed material. For example, a previous report showed that benzene-functionalized graphene (BFG) has a stronger C═O band than pristine GO, indicating that the density of carbonyl groups in BFG exceeds that in GO.[77] The successful integration of BFG with MOF-5 to form a MOF/BFG hybrid was also confirmed by FTIR spectroscopy, as shown in Figure 12e: the FTIR spectrum of BFG (spectrum i) has a C═O stretch at 1730 cm^{-1} assigned to the carboxylate groups present at its surface, whereas the C═O stretch of the MOF/BFG composite (spectrum ii) is red shifted to 1675 cm^{-1}. This was attributed to the bidentate coordination of Zn clusters in MOF-5 by the carboxylate groups of BFG, demonstrating the successful formation of the composite. Another study used comparative analysis of the FTIR spectra of graphene@MOF composites and their components to obtain the information about the composite's synthesis. Figure 12f shows the FTIR spectra of the HKUST-1/GONRs composite and its building blocks: HKUST-1, GONRs, and MWCNT.[227] The FTIR spectrum of the MWCNT (spectrum i) has no peaks assigned to functional groups, whereas peaks assigned to −CO (alkoxy) (1055 cm^{-1}), C═C (1623 cm^{-1}), −OH (3360 cm^{-1}), C═O (1734 cm^{-1}), and −CO (epoxy) (1227 cm^{-1}) groups are present in the FTIR spectrum of GONRs (spectrum ii). The FTIR spectrum of the HKUST-1/GONRs composite (spectrum iv) features the characteristic peaks of both GONRs and HKUST-1 (spectrum iii), demonstrating the successful hybridization of these components.

Scanning electron microscopy (SEM) is a powerful tool for analyzing the morphology of material samples. Field emission SEM analysis of the BFG@Cd-PBM hybrid (Cd-PBM = $Cd_4(azpy)_2(pyrdc)_4(H_2O)_2$, azpy = 4,4′-azopyridine, and pyrdc = pyridine-2,3-dicarboxylate) revealed that the composite had a plate-like morphology.[185] Because of its usefulness in morphological characterization, SEM is frequently used to determine how the morphology of graphene@MOF hybrids is affected by varying the ratio of graphene to MOF.[209] Figure 12g shows SEM images of UiO-66-NO_2/GO composites with UiO-66-NO_2 to GO ratios of 1:5, 1:4, 1:3, and 1:2. Confocal laser scanning microscopy studies had previously established that reducing the GO content of the composites increased the sizes of their macropores, and the SEM images revealed that it also affected the interactions between the GO and the MOF. The same approach was used to investigate the binding between MOF-2Cu crystals (consisting of Cu^{2+} ions and 1,4-benzodicarboxylate) and graphene in a MOF-2(Cu)-graphene composite.[239] Figure 12h shows an SEM image of MOF-2(Cu) in which its cubic crystals can be seen. This MOF features Cu_2 paddlewheels in which each Cu center is coordinated to four oxygen centers from four bdc linkers, forming a $Cu_2(bdc)_2$ unit; the two axial positions of the paddlewheel are capped by a coordinated DMF molecule. This resulted in a sheet-like morphology in which weak interactions caused the sheets to stack on top of one another. SEM micrographs of the MOF-2(Cu)-graphene hybrid (see Figure 12h) showed that graphene was intercalated between MOF-2(Cu) sheets, forming a sandwich-like structure.

https://doi.org/10.1021/acs.chemrev.2c00270
Chem. Rev. 2022, 122, 17241−17338

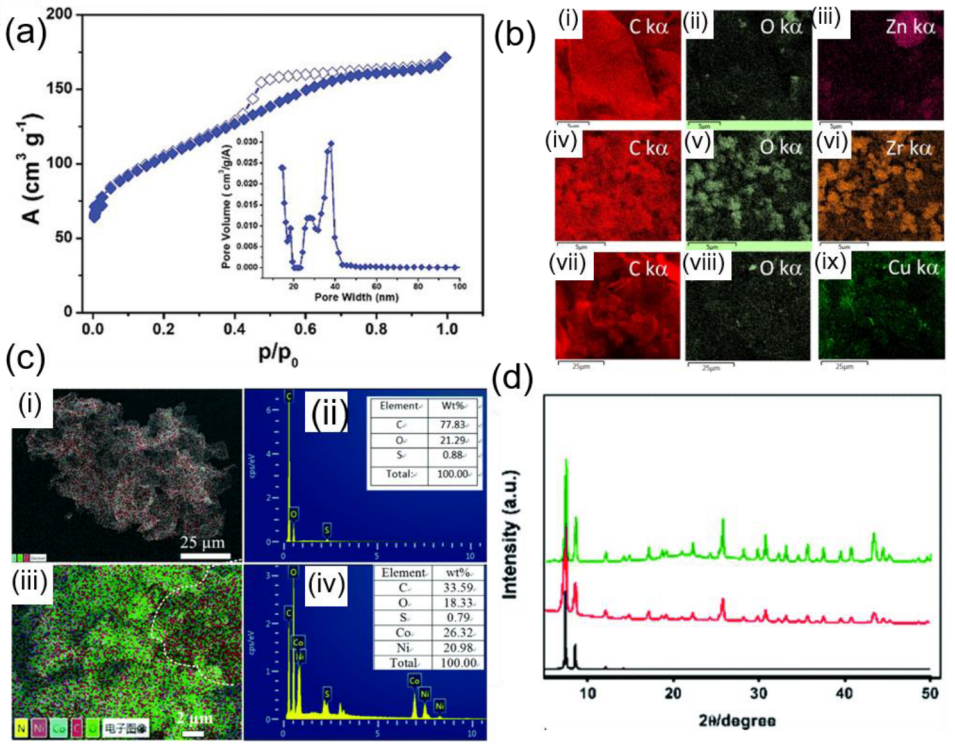

Figure 13. (a) Nitrogen adsorption−desorption isotherm of GA@UiO-66-NH$_2$ and its pore size distribution (inset). Filled and empty squares show adsorption and desorption data, respectively. Reproduced with permission from ref 76. Copyright 2020 John Wiley & Sons, Inc. (b) Elemental mapping images of (i−iii) Gr-ZIF-8, (iv−vi) Gr-UiO-66, and (vii−xi) Gr-HKUST-1 composites. Reproduced with permission from ref 183. Copyright 2020 Elsevier. (c) EDX measurements used to determine the elemental wt % of C, S, O, and Ce. Reproduced with permission from ref 244. Copyright 2021 Elsevier. (d) PXRD patterns of UiO-66-NH$_2$ (black line), synthesized UiO-66-NH$_2$ (red line) and the GA@UiO-66-NH$_2$ composites (green line). Reproduced with permission from ref 75. Copyright 2021 Royal Society of Chemistry.

TEM is also frequently used to study the morphology of material samples. It provides a closer view of the material than SEM because its resolution is usually higher. Consequently, it has been widely used to study the morphology of graphene, MOFs, and their hybrids. For instance, TEM analysis of ZIF-8, HFGO, and HFGO@ZIF-8 confirmed that the HFGO in the composite had a sheet-like structure in which some of the sheets were twisted and that the ZIF-8 nanocrystals were hexagonal and uniformly distributed on the surfaces of HFGO sheets between the layers.[128] Due to the high resolution of TEM, small species such as metal nanoparticles can be reliably imaged. For instance, TEM images of a Cu/Cu$_2$O@C-rGO composite prepared by carbonizing a Cu-BTC/GO hybrid[240] showed that the Cu/Cu$_2$O@C nanoparticles were homogeneously distributed in Cu/Cu$_2$O@C-rGO. The high resolution of TEM also makes it possible to determine the particle size distribution, as shown in the inset of Figure 12i. HR-TEM (high-resolution transmission electron microscopy) can also be used to calculate the *d* spacing between different planes in Cu/Cu$_2$O@C nanoparticles.

Contact angle measurements are performed to evaluate a sample's surface wettability. Graphene and most of its derivatives are hydrophobic, while MOFs are commonly hydrophilic. Graphene@MOF hybrids are usually more stable toward moisture than the parent MOFs because the graphene component makes them more water repellent. Accordingly, the water contact angle (WCA) of ZIF-8 increased substantially after hybridization with HFGO.[128] Pristine ZIF-8 is hydrophilic with a WCA of 56°, whereas HFGO is hydrophobic with a WCA of 125°. The hybridization of these two components yielded the composite HFGO@ZIF-8 whose hydrophobicity (WCA = 162°) exceeded that of both of its parent components (Figure 12j). As a result, the composite exhibited substantially greater moisture stability than ZIF-8. Moreover, it had an oil contact angle (OCA) of 0° and was thus superoleophilic (Figure 12j). The hydrophobicity of a composite of fluorinated graphene (FG) with HKUST-1 was also studied by performing contact angle measurements.[241] Pristine HKUST-1 is superhydrophilic and is readily wetted by water droplets. The functionalization of GO with fluorine moieties significantly increased its hydrophobicity; as a result, the composite obtained by hybridizing FG with HKUST-1 showed both hydrophobic (WCA = 147.3°; probe−*n*-hexadecane) and superoleophilic (OCA = 12.1°) behavior. Finally, contact angle measurements showed that a polyurethane sponge coated with an FG-HKUST-1 composite was hydrophobic (WCA = 130.3°) but slightly less so than the FG-HKUST-1 composite itself.

The pore structure and specific surface area of graphene@MOF hybrids can be determined by recording their N$_2$ physisorption isotherms and applying BET analysis. This method was recently applied to Cu-BTC and graphene-based hybrids with graphene to MOF weight ratios of 1:1, 1:3, 1:5, 1:7, and 1:9.[242] All of the composites exhibited type-1 isotherms, confirming that they contained micropores. However, whereas the isotherms of hybrids with GO:MOF ratios of 1:1 and 1:3 showed no hysteresis loop, those with GO:MOF ratios of 1:5 and 1:7 had hysteresis loops closed at a relative pressure (p/p_0) of 0.41, indicating that these hybrids also contained mesopores and were thus hierarchically porous. To explain this outcome, it was suggested that the mesopores of the 1:1 and 1:3 hybrids

https://doi.org/10.1021/acs.chemrev.2c00270
Chem. Rev. 2022, 122, 17241−17338

were blocked by their high contents of GO. In addition, the BET surface areas calculated from the N_2 physisorption isotherms showed that the Cu-BTC/GO hybrids had lower surface areas than the pristine MOF and that the surface area decreased as the MOF content of the hybrid decreased. Another recent study used N_2 physisorption isotherm measurements to investigate how the covalent hybridization of GA and UiO-66-NH_2 affected the pore structure and surface area of the resulting composite.[76] The N_2 physisorption isotherm of UiO-66-NH_2 at 77 K has a type-I shape characteristic of microporous samples, and BET calculations indicated that the specific surface area of this MOF is 780 m^2 g^{-1}. Conversely, pristine GA has a type-II isotherm, indicating nonporosity; accordingly, it also has a low specific surface area of 25 m^2 g^{-1}. The covalent hybridization of GA with UiO-66-NH_2 yielded the hybrid GA@UiO-66-NH_2, which has a type-IV isotherm and thus contains mesopores (Figure 13a). Interestingly, its calculated BET surface area is 600 m^2 g^{-1}, indicating that the covalent bonding between GA and UiO-66-NH_2 leads to mesopore formation without affecting the micropores of the parent MOF.

Elemental mapping by EDX is usually performed to determine which elements are present in a sample and how they are distributed. Accordingly, EDX analysis has often been used to confirm the homogeneous distribution of MOF particles on the graphene nanosheets of graphene@MOF hybrids. EDX maps of composites of pristine graphene (Gr) with ZIF-8, UiO-66, and HKUS-1 are presented in Figure 13b.[183] As expected, these maps show the presence of Cu, C, and O in Gr-ZIF-8, Zr, C, and O in Gr-UiO-66, and Cu, C, and O in Gr-HKUST. Since the different elements within each MOF are homogeneously distributed in the corresponding hybrids, it follows that ZIF-8, UiO-66, and Cu-BTC are uniformly distributed in Gr-ZIF-8, Gr-UiO-66, and Gr-HKUST-1, respectively. EDX mapping has also been used to determine the elemental weight percent of different elements in graphene@MOF hybrids. For example, a CeO_2/rGO/CeS_2 composite derived from Ce-BTC MOF by a multistep synthetic pathway was characterized by EDX as shown in Figure 13c.[243] On the basis of the intensities of the different elements present in the composite, the elemental weight percent values of C, O, S, and Ce were determined to be 49.7%, 24.33%, 0.35%, and 25.62%, respectively. Finally, EDX has been used to confirm the synthesis of graphene@MOF hybrids.[244]

TGA (thermogravimetric analysis) is mainly used to determine the thermal stability of materials but can also provide additional information. For instance, the thermal decomposition profile of the pillared bilayer MOF (PBM) composite BFG@Cd-PBM shows an initial weight loss at 115 °C that was attributed to the loss of water molecules. The composite showed no further weight loss up to 280 °C, confirming its stability at this temperature.[185] However, its TGA curve showed substantial mass losses above 280 °C, indicating that it is unstable at such high temperatures. TGA analysis can also be used to determine which components of a given hybrid have the greatest effect on its thermal stability and could thus potentially guide the design and synthesis of highly stable hybrids.

PXRD analysis is a valuable technique for evaluating the structural integrity of MOFs within graphene@MOF hybrids. For instance, our research group used it to confirm the structural integrity of UiO-66-NH_2 in the GA@UiO-66-NH_2 composite;[75] Figure 13d shows that the PXRD patterns of the pristine UiO-66-NH_2 MOF are identical with those of the composite, indicating that the sample contains intact UiO-66-NH_2. This technique can also be used to investigate structural changes during composite preparation, as demonstrated by a recent study on a MOF/BFG hybrid[77] in which the PXRD patterns of MOF, GO, MOF/GO, and MOF-5/BFG with BFG contents of 1, 4, and 5 wt % were recorded. The PXRD pattern of MOF-5/BFG showed splitting of a reflex observed at 2θ = 9.7° in the pristine MOF. The new reflex was observed at 8.8°, which was attributed to distortion of the MOF-5 lattice caused by its hybridization with BFG. On the basis of their PXRD patterns, the MOF-5/BFG hybrid with 1 wt % BFG was found to have a monoclinic crystal lattice, whereas the MOF-5/BFG hybrid with 5 wt % BFG had a nanowire-like morphology, which was subsequently verified by TEM and selected area electron diffraction pattern (SAED) studies. The resulting data also allowed the nanowire's diameter to be measured. Another valuable aspect of PXRD analysis is that the grain size of MOF particles can be calculated from the width at half-maximum of the peaks in the PXRD pattern using the Debye−Scherrer equation. Using this relationship, the estimated MOF grain size in the MOF5-BFG composite was estimated to be in the range of 220−260 nm.

The studies discussed in the preceding sections show that graphene@MOF hybrids can be characterized using a wide range of techniques. However, characterization of graphene@MOF hybrids presents some significant difficulties. The major challenges associated with characterizing these hybrids are summarized below.

The thermal stability of graphene@MOF hybrids is usually evaluated by performing a thermogravimetric analysis. An important parameter to consider in such analyses is the heating rate of the graphene@MOF hybrid. For example, when GO is heated, it usually exhibits mass loss around 200 °C due to the conversion of GO into CO and CO_2.[118] However, excessive heating of GO-MOF hybrids at 200 °C causes more substantial mass loss. It is therefore generally advisable to use a low heating rate (<5 °C/min) when performing thermogravimetric analysis of GO-MOF hybrids.[245]

Characterization of GO-MOF hybrids by Raman spectroscopy is also somewhat difficult. The D and G bands observed in the Raman spectra are used to determine the degree of disorder in samples. However, based on a previous report of GO, the observed bands are the superimposition of many bands. Therefore, the degree of disorder cannot be determined simply by determining the intensity ratio of the D and G bands.[246] There have been few published nuclear magnetic resonance (NMR) studies on GO-MOF hybrids, although their pristine GO has been characterized using ^{13}C NMR.[245] The limited use of NMR in this context can be mainly attributed to the low content of NMR-active nuclei (C and H) in GO-MOF hybrids. Because of these issues, it remains quite challenging to accurately determine the quantity of graphene (or a graphene derivative) in graphene@MOF composites or to evaluate the effect of the dispersion of the graphene derivative on the composite's structural features.[245] This problem is exacerbated by the fact that the content of graphene or its derivatives in such hybrids is usually rather low, so its quantification requires the combined application of multiple high-precision characterization techniques.

5. APPLICATIONS

The following sections discuss the various potential applications of MOF-graphene hybrids.

https://doi.org/10.1021/acs.chemrev.2c00270
Chem. Rev. 2022, 122, 17241−17338

5.1. Environmental Applications

Physisorbents based on MOF-graphene hybrids exploit the amenability of MOFs to reticular chemistry[247] (also known as crystal engineering[248]), morphological engineering, interface engineering, and doping. MOF-graphene hybrids are considered to be particularly promising materials for environmental remediation applications because of the synergy resulting from the compositional modularity of MOFs and the high theoretical surface area of graphene derivatives. To satisfy the United Nations (UN) Sustainable Development Goals (SDGs) 6 (clean water and sanitation), 7 (affordable and clean energy), 9 (industry, innovation, and infrastructure), and 13 (climate action) in today's "age of gas",[249] there is an urgent need for translational research on environmental remediation. In particular, there is a need to reduce the high energy footprints of various environmental remediation techniques. One possible way of achieving this would be to design, characterize, and develop a new generation of crystalline (and ideally, porous) graphene@MOF hybrids that could serve as highly efficient adsorbents of pollutants in air and water, enabling the development of new energy-efficient environmental remediation processes. Unfortunately, while many physisorbents are currently available, including over 100 000 MOFs and synthetic zeolites,[250] none are commercially viable because of their poor performance, low stability, or high cost. The instability of these adsorbents in water or harsh chemical environments is largely due to the fact that many of them feature hydrolytically labile metal−ligand bonds. In addition, their performance is often limited by low selectivity for targeted substances, primarily because they interact with adsorbates via weak dispersive forces. The use of hierarchically porous graphene@MOF composites as physisorbents has recently attracted interest because such composites can avoid the limitations that restrict the usefulness of their individual components. For example, the formation of a composite structure in which MOF crystallites are placed between individual graphene layers can prevent restacking of the layered material (and thus creates mesopores) while also protecting the MOF from hydrolytic degradation. This often leads to improved adsorptive performance and/or selectivity, resulting in more efficient separation of targeted adsorbates.[251]

The development of next-generation physisorbents based on MOF-graphene hybrids offers a way to avoid the trade-off between cost and adsorption performance that has restricted the use of MOF-based systems to date.[252,253] No currently known physisorbent is capable of satisfying all of the UN SDGs mentioned above by enabling energy-efficient downstream processing of commodity chemicals,[254] air purification by toxic gas remediation,[255] or trace scavenging of hydrocarbons and fluorocarbons such as persistent mobile organic contaminants (PMOCs) from drinking water.[256,257] Nevertheless, research in this area has thrived over the past decade. Reflecting the focus of this review, the following discussion deals only with the use of MOF-graphene hybrids in these contexts.

5.1.1. Carbon Dioxide Capture. A holy grail of MOF research is the development of a material capable of efficient carbon capture, particularly under conditions that mimic point-source removal during postcombustion and precombustion processes. Not surprisingly, MOF-graphene hybrids have also been studied in this context. Because the even distribution of MOF crystallites across the GO layers of such hybrids creates a dense and dispersive environment for adsorption, MOF/GO composites can form stronger dispersive interactions with adsorbates than the corresponding pristine MOFs. These dispersive interactions may be reinforced by interactions between the adsorbate and the oxygen-containing functional groups introduced by graphite oxidation such as epoxy or hydroxyl groups on the graphitic surfaces or carboxylic acid groups on the edges of graphene sheets.[96] The adsorption selectivity of such composites depends on CO_2-selective molecular interactions and can thus be tuned by adjusting the building blocks of the MOF, i.e., its constituent metallic centers and/or its organic ligands. In addition, the dispersed nature of the GO sheets within the composites maximizes their content of oxygen vacancies and terminal hydroxyl groups, which favors oxidation and reactive CO_2 adsorption.

Despite the high surface areas of MOFs, their open architectures rarely favor strong adsorbate-specific adsorption forces. For trace gas capture (including but not limited to CO_2 capture) and CO_2-selective separation, CO_2 binding sites must be densely arranged within an optimally sized pore environment in which the size and chemical properties of the pores are closely matched to those of the target sorbate. For gas adsorption, this typically requires ultramicropores, i.e., pores with diameters below <7 Å. If the ratios of GO and MOF in a composite are well chosen, the resulting distortion of the graphene sheets may strengthen dispersive interactions with adsorbates, while the composition of the MOFs can be adjusted to control the shapes, sizes, and chemistry of the composite's pores.[96]

To our knowledge, the first nanoporous composite of a MOF with GO was reported in 2013 by Liu et al., who prepared GO@HKUST-1.[258] Hybridization with GO increased the composite's sorption capacity for CO_2 (at 273 K and 1 bar) and H_2 (at 77 K and 42 bar) by around 30% compared to the unhybridized HKUST-1 composite.[180] This improvement was attributed to the presence of nanosized HKUST-1 crystals distributed uniformly across the incorporated GO layers. Epoxy groups on the GO surfaces served as seed sites for crystal growth, while defects in the graphene sheets constrained the size of the resulting crystals. In 2015, a Pickering emulsion strategy was developed to provide easier access to such GO@HKUST-1 composites[208] through in-situ interfacial growth of HKUST-1 nanocrystallites on GO sheets.

The Liu group used the same workflow to synthesize ZIF-8/GO composites (designated ZG-*x*, where *x* denotes the wt % of GO) whose CO_2 storage capacities at 195 K exceeded that of the parent MOF ZIF-8 when *x* was between 4 and 20.[172] This GO-driven improvement was extended by fabricating mixed-matrix membranes (MMMs) in which ZIF-8@GO was embedded in a Pebax (grade 2533) copolymer matrix comprising poly(tetramethylene oxide) and Nylon-12 in a weight ratio of 4:1.[259] An MMM containing 6 wt % of ZIF-8@GO (designated Pebax/ZIF-8@GO-6) exhibited the best performance, achieving a CO_2 permeability of 249 Barrer and a CO_2/N_2 selectivity of 47.6 at 298 K with a feed pressure of 0.1 MPa, close to the Robeson upper bound. The CO_2 permeability and CO_2/N_2 selectivity of the Pebax/ZIF-8@GO-6 MMMs were 191% and 174% higher, respectively, than that of the pure Pebax membrane. Similar results were obtained with the MOF ZIF-301 ($Zn(mim)_{0.67}(mbim)_{1.33}$, where $mbim^-$ = methylbenzimidazolate): interfacial filler−matrix adhesion between GO and ZIF-301 nanocrystals resulted in their even dispersion over a polysulfone (PSF) matrix, yielding water-stable PSF/GO/ZIF-301 MMMs.[260] In 2017, a pure MOF-derived defect-free ZIF-8/GO membrane with a thickness of ca. 100 nm was prepared by Hu et al. using two-dimensional (2D) ZIF-8/GO hybrid nanosheets as seeds.[219] The development of a uniform ZIF-8/

https://doi.org/10.1021/acs.chemrev.2c00270
Chem. Rev. 2022, 122, 17241−17338

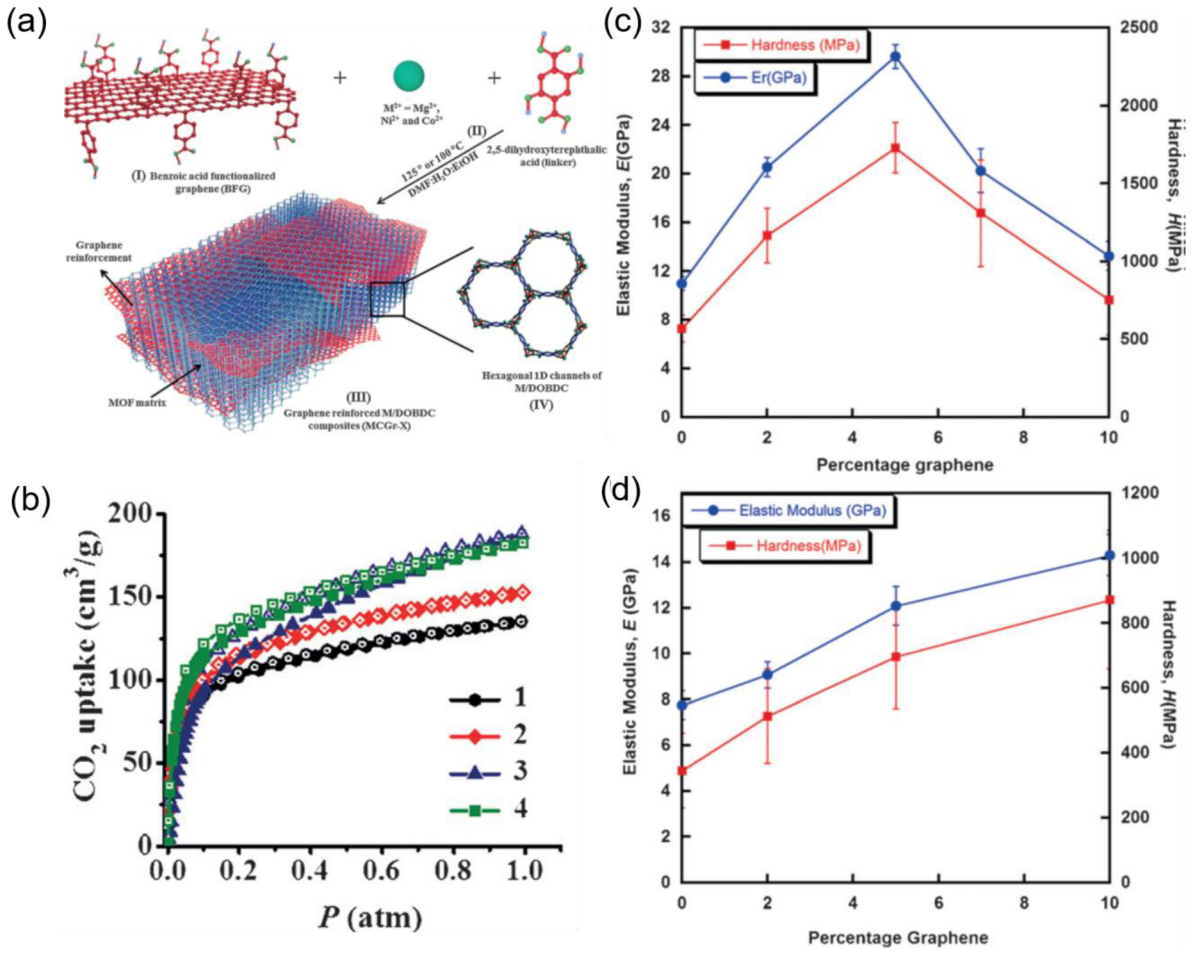

Figure 14. (a) Synthesis of MCGr-*X* composites (*X* = wt % of graphene embedded in the M_2(dobdc) matrix). (b) Ambient-pressure (298 K) CO_2 sorption isotherms of (1) Mg_2(dobdc), (2) MgCGr-2, (3) MgCGr-5, and (4) MgCGr-10 (filled and open symbols denote adsorption and desorption, respectively). Hardness and elastic modulus of (c) MgCGr-*X* and (d) NiCGr-*X*, where *X* = wt % of graphene in M/DOBDC, M = Mg^{2+} and Ni^{2+}. Reproduced with permission from ref 175. Copyright 2016 John Wiley & Sons, Inc.

GO seeding layer facilitated fast crystal intergrowth during formation of the ZIF-8/GO hybrid membrane, which enabled CO_2-selective sieving from a dynamic CO_2/N_2 feed mixture (CO_2/N_2 selectivity ≈ 7). In the same year, the Kang and Park groups improved the CO_2/N_2 selectivity to 57 while keeping a high CO_2 permeability of ca. 163 Barrer[261] using an MMM consisting of ZIF-8/PGO (PGO = porous graphene oxide) grown into a PEBAX1657 polymer matrix (PEBAX = poly ether-*block*-amide). Several similar CO_2-selective MMMs have been reported,[262] including HKUST-1/GO/PVDF (PVDF = poly-(vinylidene fluoride)).[263] However, a few challenges remain to overcome before a practically useful gas separation system can be prepared, giving rise to so-called "separation anxiety".[68]

Nonpolymeric gas separation systems using MOF-graphene hybrids have also been reported. For example, a study on Pt-GO/[La(CPIA)(2H_2O)] ($CPIA^{3-}$ = 5-(4-carboxylato-phenoxy)isophthalate) nanocomposites showed that upon increasing the Pt content of the composites, their CO_2 uptake at 273 K first improved and then declined. This was explained in terms of the interactions between Pt-GO, the CPIA ligands, and the La metal centers.[264] In addition, the Zhang and Xiang groups discovered a high-performance MOF for CO_2 capture known as UTSA-16 (UTSA = University of Texas at San Antonio), [$K(H_2O)_2Co_3$(cit)(Hcit), where cit^{4-} = citrate)] in 2012[265] that was subsequently used to prepare core−shell-type composites with GO such as the prototypical species UTSA-16-GO.[266]

To obtain MOF-based selective CO_2 capture systems with high mechanical strength, Rao et al. investigated a strategy based on covalent bonding between MOFs and graphene.[175] The covalent bonding of 5 wt % of benzoic acid-functionalized graphene (BFG) to be representative of the MOF family M_2(dobdc) ($dobdc^{4-}$ = 2,5-dioxido-1,4-benzenedicarboxylate; M = Mg^{2+}, Ni^{2+}, Co^{2+})[267] yielded composites whose elastic modulus was increased 3-fold relative to the starting materials. Covalent bonding of the MOFs to BFG also increased the composites' surface areas by 200−300 m^2 g^{-1} and their CO_2 capture capacity by ca. 3−5 and 6−10 wt % at 0.15 and 1 bar, respectively (Figure 14). These graphene reinforced-M_2(dobdc) composites were designated MCGr-*X* (M = Mg^{2+}, Ni^{2+}, or Co^{2+}; *X* = wt % of BFG incorporated). Several other covalent graphene@MOF hybrids were subsequently prepared and optimized with respect to their graphene content, including MIL-53(Cr)/GO, ZIF-8/GO, UiO-66-NH_2/GO, MOF-505@GO (MOF-505 = Cu_2(bptc), where $bptc^{4-}$ = 3,3′,5,5′-biphenyltetracarboxylate), MOF-200/GO (MOF-200 = Zn_4O-$(bbc)_2$, where bbc = 4,4′,4′′-(benzene-1,3,5-triyl-tris(benzene-4,1-diyl))tribenzoate), MIL-53(Al)/GNP (GNP = graphene nanoplates), and MIL-101(Cr)/GO.[268−275] In addition, MCGr-*X* analogues containing GO in place of BFG were found to

https://doi.org/10.1021/acs.chemrev.2c00270
Chem. Rev. 2022, 122, 17241−17338

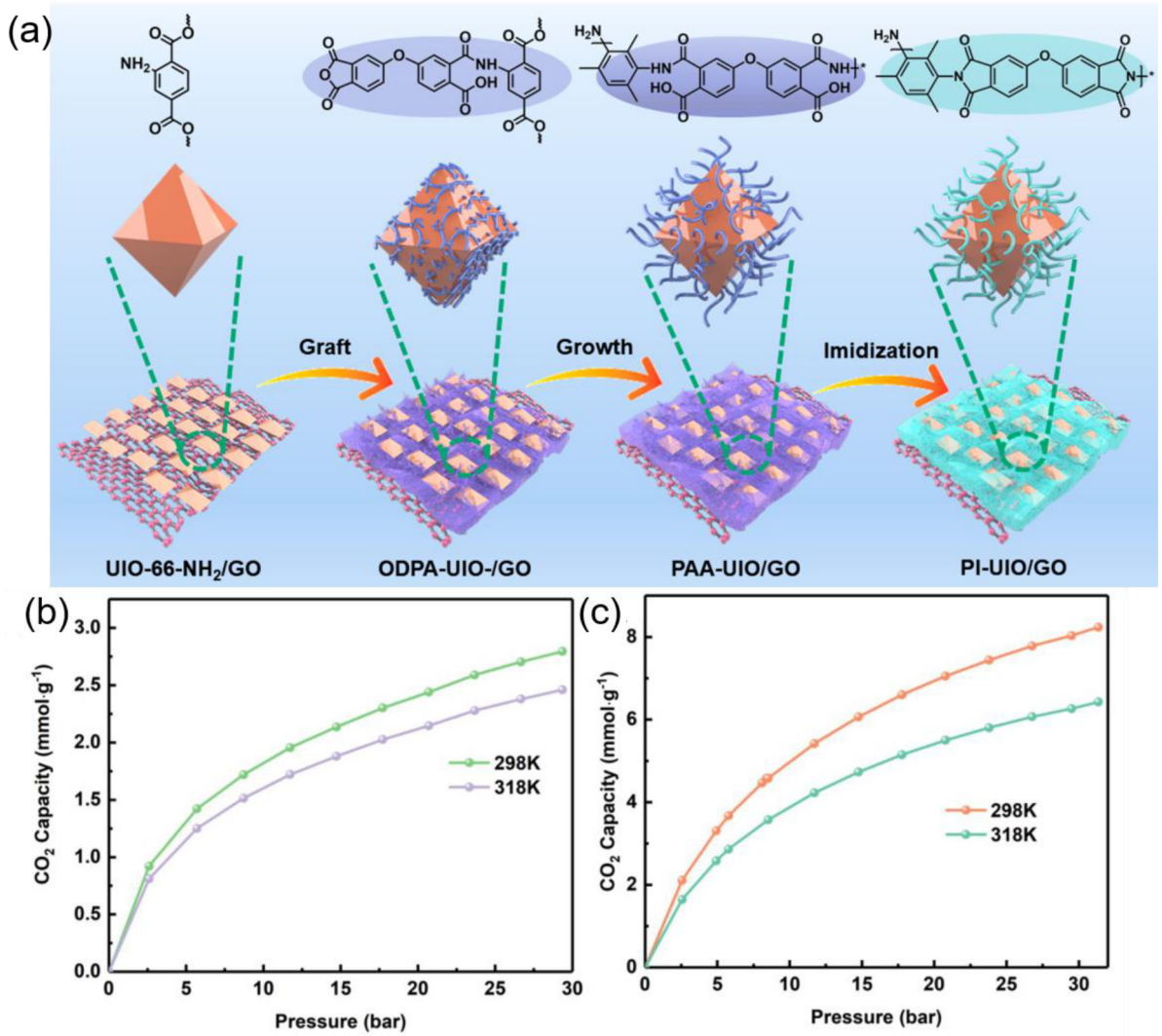

Figure 15. (a) Cross-linked PI-UiO/GO composite sorbents prepared by stepwise reagent grafting; 298 and 318 K CO_2 isotherms (0−30 bar) of (b) UiO-66-NH_2 and (c) PI-UiO-66-NH_2/GO composites. Reproduced with permission from ref 279. Copyright 2021 American Chemical Society.

exhibit similar enhancements in CO_2 sorption,[276] and the CO_2 capture performance of UiO-66/GO hybrids was shown to be 48% higher than that of pristine UiO-66 at ambient temperature and pressure (298 K and 1 bar).[277]

More recently, polypyrrole-derived carbon/GO, polyaniline-derived carbon/GO, and HKUST-1/GO composites were evaluated with respect to their molar (aka ideal) CO_2/N_2 adsorption selectivities.[278] HKUST-1/GO containing ca. 10 wt % of GO had the highest CO_2/N_2 selectivity (15:85) despite not having the highest CO_2 adsorption capacity at 298 K. A new strategy in this area based on the use of in-situ chemical knitting and condensation-based grafting on a GO surface was introduced by Ning et al., who applied polyimide (PI) hyper-cross-linking to a UiO-66-NH_2-graphene (UiO/GO) graphene@MOF hybrid.[279] The PI hyper-cross-linking process uses inexpensive reagents (4,4′-oxidiphthalic anhydride and 2,4,6-trimethyl-1,3-phenylenediamine), and the resulting PIUiO/GO composites have high densities of C−N covalent bonds, secondary amines, and N lone pairs capable of forming N−H···O hydrogen bonds, all of which enhanced their CO_2 selectivity. Consequently, their CO_2 storage capacity and CO_2/N_2 selectivity were three and four times higher, respectively, than those of pristine UiO-66-NH_2, and they also exhibited superior acid and base stability (Figure 15). This demonstrated the potential of combining MOFs (including some of the best performing CO_2 capture agents currently known) with inexpensive polymers such as graphene-imide hybrids.

The incorporation of graphene or GO into MOFs can also increase their H_2 and/or CH_4 selectivity and storage capacity, as demonstrated by a few proof-of-concept reports published around the same time as the carbon capture studies discussed above.[167,280] Both defect-free MOF membranes and MOF-derived MMMs were shown to be capable of H_2/CO_2 separation on the basis of activated CO_2 diffusion.[73,281−283] A few reports have also shown that the CO_2/CH_4 selectivities of these systems can be enhanced by the formation of graphene composites such as MIL-101(Cr)@GO,[271,284] MIL-53(Cr)@GO,[269] MOF-505@GO,[275] and MOF-200(Zn)@GO.[274] Particularly notable are two studies showing that the incorporation of around 5 wt % GO into the MOF MIL-101(Cr) yielded a composite whose CO_2 storage capacity and CO_2/CH_4 adsorption selectivity (determined using ideal adsorbed solution theory, IAST[285]) were both higher than those of the pristine MOF.[271,284] Interestingly, similar effects were observed upon the incorporation of carbon nanotubes (CNTs), including multiwalled MWCNTs.[286−289] The literature on CH_4 storage using

https://doi.org/10.1021/acs.chemrev.2c00270
Chem. Rev. 2022, 122, 17241−17338

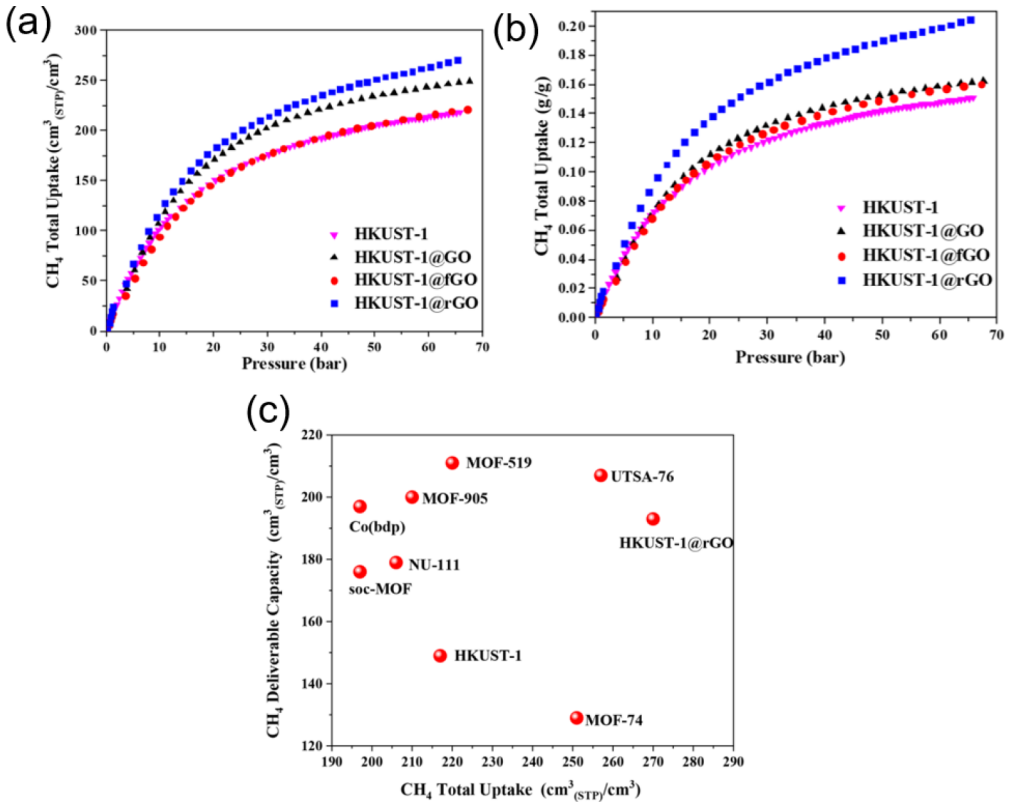

Figure 16. Total volumetric (a) and gravimetric (b) CH_4 adsorption isotherms for three HKUST-1@GO hybrid nanocomposites and pristine HKUST-1 at 298 K. (c) Total high-pressure CH_4 adsorption isotherm-based deliverable capacity versus total uptake for HKUST-1@rGO and selected other MOFs benchmarked for CH_4 storage. Reproduced with permission from ref 292. Copyright 2018 American Chemical Society.

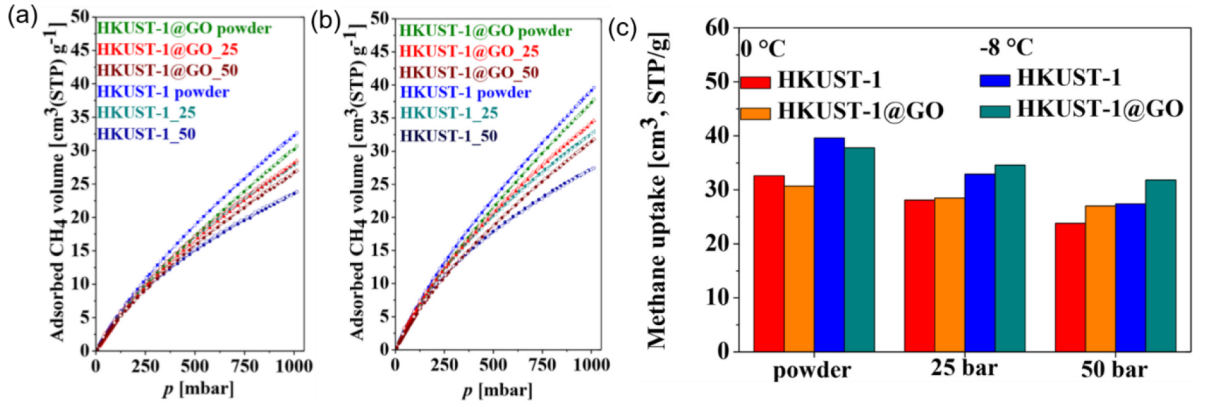

Figure 17. CH_4 adsorption isotherms (up to 1 bar) for powders and pellets of HKUST-1 and HKUST-1@GO recorded at (a) 0 and (b) −8 °C. (c) Comparative CH_4 uptake analysis at 0 and −8 °C at 1, 25, and 50 bar (from left to right). Reproduced with permission from ref 295. Copyright 2021 Elsevier.

graphene@MOF hybrids is reviewed more thoroughly in the following section.

5.1.2. Methane Storage. Only a handful of reports have discussed methane storage in graphene@MOFs hybrids. Recognizing that proper interlayer spacing in graphene and GO-type layered materials can enhance CH_4 adsorption,[290,291] Rezaei's group prepared three MOF@GO hybrids in 2018: (a) HKUST-1/pristine GO, (b) HKUST-1/reduced GO (rGO), and(c) HKUST-1/−COOH-functionalized GO (fGO).[292] High-pressure N_2 adsorption measurements revealed that all three MOF-GO variants had higher BET surface areas and pore volumes than pristine HKUST-1. HKUST-1@rGO with 10 wt % rGO had the highest CH_4 deliverable capacity of 193 $cm^3(STP)/cm^3$ in the pressure range of 5.8−65 bar (298 K), which was around 30% higher than the corresponding value for pristine HKUST-1 (Figure 16a and 16b). The CH_4 deliverable capacities for HKUST-1@GO and HKUST-1@fGO were 181 and 162 cm^3 (STP)/cm^3, respectively. By demonstrating the synergistic effects of MOFs and GO on CH_4 storage and demonstrating the high potential deliverable capacity of MOF@GO nanocomposites, this study suggested that such hybrids could be valuable adsorbed natural gas (ANG) adsorbents (Figure 16c).[293,294]

Building on this discovery and the good CH_4 storage performance of inexpensive HKUST-1, László's group recently valorized this MOF for ANG applications.[295] Commercial

https://doi.org/10.1021/acs.chemrev.2c00270
Chem. Rev. 2022, 122, 17241−17338

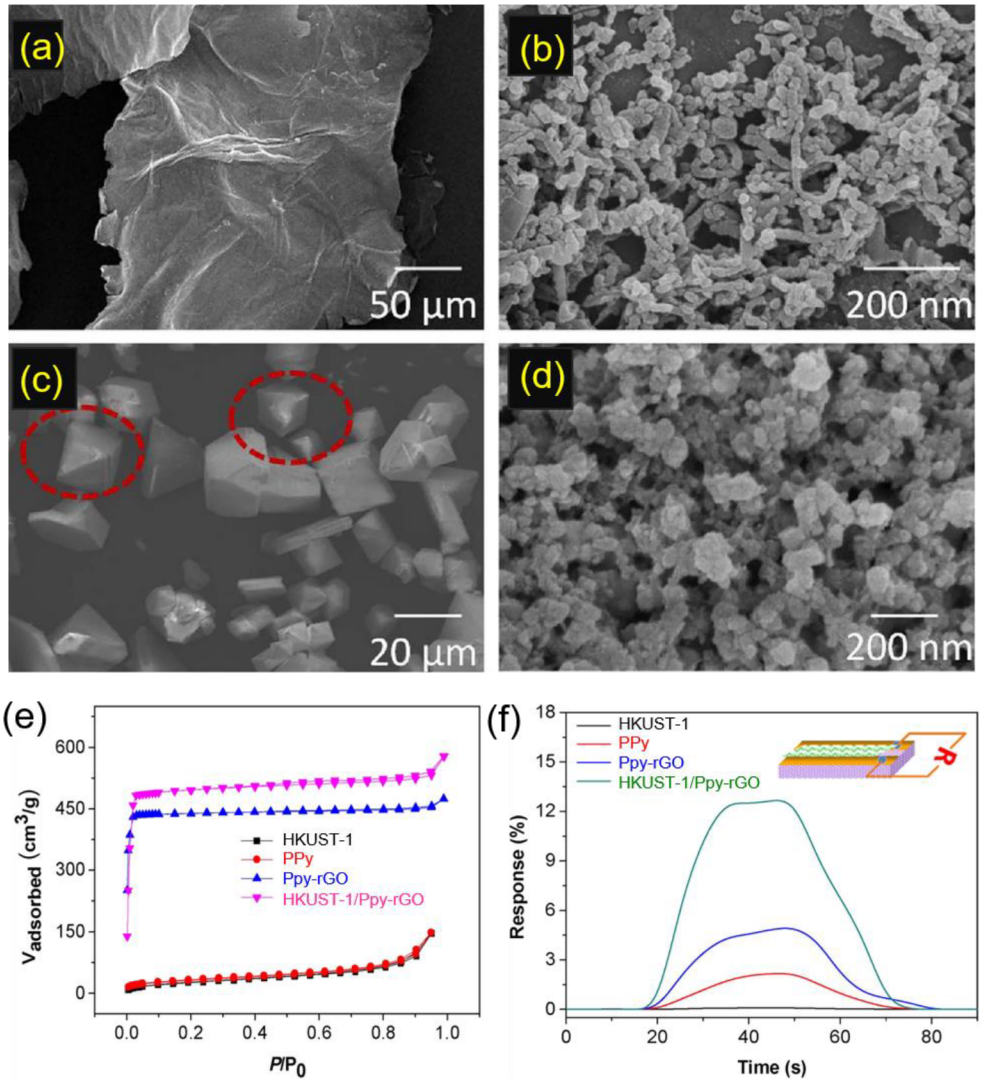

Figure 18. Scanning electron microscopy images of (a) rGO, (b) PPy-rGO, (c) HKUST-1, and (d) HKUST-1/PPy-rGO. (e) N_2 adsorption isotherms recorded at 77 K. (f) Resistive responses of the four thin films to 50 ppm of NH_3 at 298 K. Reproduced with permission from ref 301. Copyright 2018 Elsevier.

HKUST-1 is supplied as a microcrystalline bulk powder with grain sizes of ca. 10−20 μm. However, when compacted into monoliths or pellets (with or without binders), its utility for ANG storage is greatly reduced.[296] The authors discovered that this problem could be avoided by solvothermally incorporating 16% GO by weight and avoiding the use of a binder, which yielded the powdered composite HKUST-1@GO-16. This composite was then compressed into pellets by applying a mechanical pressure of 25 or 50 bar. Whereas the parent MOF HKUST-1 retained only 43% of its initial pore volume and 47% of its initial surface area after compression, the corresponding retention values for HKUST-1@GO-16 were both around 75% (Figure 17). This showed that 2D GO layers could function as compressible fillers between HKUST-1 nanocrystallites, preventing their amorphization. Upon comparing the adsorption properties of the HKUST-1 and HKUST-1@GO powders and pellets, it was discovered that compression adversely affected the structure of the MOF, explaining the reduction in its CH_4 uptake capacity. Further studies are needed to optimize the pelletization pressure to minimize the loss of gas uptake capacity and thereby increase the composite's technological readiness level (TRL).[69] However, the fact that the reduction in CH_4 uptake for the composite was only one-half as strong as that for pristine HKUST-1 demonstrates the effectiveness of GO at increasing the mechanical strength of MOFs and related materials.

5.1.3. Ammonia Adsorption. The use of MOF@GO composites for NH_3 adsorption was first reported by Petit et al. in 2010. Not surprisingly, the composite used in these early studies was HKUST-1@GO.[165] HKUST-1@GO composites were prepared by incorporating 5, 9, or 18 wt % of GO sheets into HKUST-1,[96,297] and the NH_3 adsorption of the resulting materials at 298 K under dry and humid conditions was shown to greatly exceed that of simple physical mixtures of HKUST-1 and GO.[165] Given the compromised stability, in part, under moist air, the presence of the GO layers was found to increase the porosity of the composite and strengthen its dispersive interactions with adsorbed NH_3. This in turn results in a synergistic increase in NH_3 affinity, as revealed by (a) dynamic breakthrough tests and (b) desorption profile analyses. The chemisorption of NH_3 was facilitated by the fact that the HKUST-1 micropores were lined with coordinatively unsaturated Cu^{2+} sites. NH_3 chemisorption led to the formation of $Cu(OH)_2$ and $(NH_4)_3BTC$ and thus caused a colorimetric response.

https://doi.org/10.1021/acs.chemrev.2c00270
Chem. Rev. 2022, 122, 17241−17338

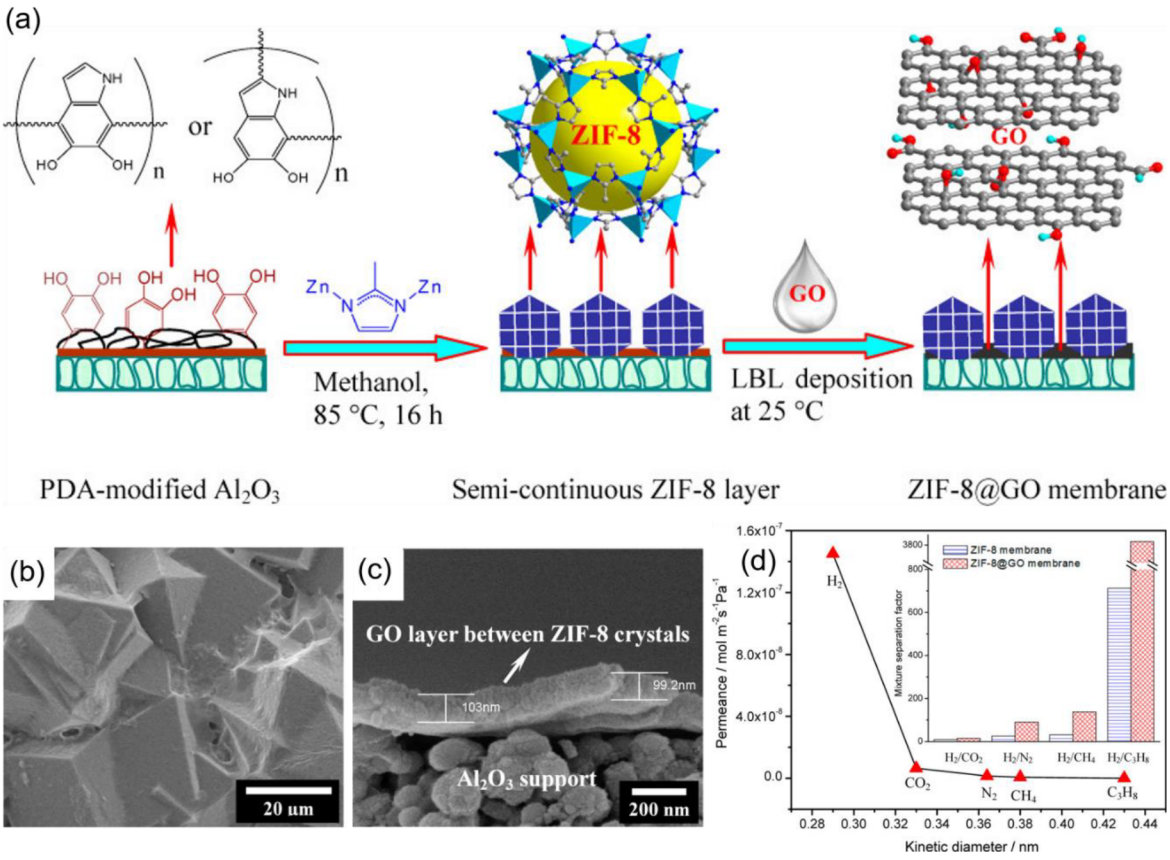

Figure 19. (a) Schematic illustration detailing the preparation of bicontinuous ZIF-8@GO membranes through layer-by-layer deposition of graphene oxide onto a ZIF-8 semicontinuous layer cast on a polydopamine-modified Al_2O_3 disk (PDA = polydopamine). Top-view (b) and cross-section (c) field-emission scanning electron microscopy (FE-SEM) images of the bicontinuous ZIF-8@GO membrane fabricated on a porous Al_2O_3 disk. (d) Single gas permeances of H_2, CO_2, N_2, CH_4, and C_3H_8 through the ZIF-8@GO membrane at a permeation temperature of 250 °C as a function of the kinetic diameter. (Inset) Two-gas mixture separation factors for H_2/CO_2, H_2/N_2, H_2/CH_4, and H_2/C_3H_8. Reproduced with permission from ref 167. Copyright 2014 American Chemical Society.

Building on this discovery and a couple of follow-up studies,[96,165,297−299] Bandosz et al. reported low-concentration electrochemical NH_3 sensing using HKUST-1@GO.[300] HKUST-1@GO chips were episodically exposed to three continuous cycles of NH_3, resulting in distinct but irreversible responses in resistance. Increased carrier mobility upon NH_3 exposure was confirmed by resistance measurements despite an apparent transition to a poorly characterized amorphous hybrid phase. The electrochemical response of the HKUST-1@GO sensor chips was found to be linearly related to the trace NH_3 concentration.

In 2018, Yin et al. reported a follow-up study in which in-situ oxidative polymerization-grown polypyrrole (PPy) nanofiber-coated rGO (PPy-rGO) was hydrothermally embedded into HKUST-1 nanoparticles using a simple and inexpensive thin-film fabrication protocol to afford a HKUST-1/PPy-rGO thin film that was used as an ammonia sensor under ambient conditions.[301] This composite has two-in-one sensing capabilities because it combines the permanent porosity of HKUST-1 with the electrical conductivity of PPy-rGO. The microporous HKUST-1/PPy-rGO thin film accordingly exhibited improved NH_3 sensing with higher sensitivity and faster response times than bare PPy-rGO thin films. The HKUST-1 nanocrystallites enabled affinity-driven NH_3 adsorption, while the PPy-rGO film enhanced the electrochemical signal induced by NH_3 binding. Studies on the selectivity and stability of the HKUST-1/PPy-rGO thin film before and after NH_3 adsorption confirmed its robustness and suitability for crafting practical MOF-based sensing devices (Figure 18).

These two studies are notable because NH_3 overexposure is common in chemical plants[64] but also because by demonstrating that the NH_3 affinity signatures of HKUST-1@GO hybrids can be used to generate NH_3-responsive electrical signals, they revealed new ways of synergistically leveraging two properties (conductivity and porosity) in sensing devices.

5.1.4. Hydrocarbon Storage/Separation. To our knowledge there have been no published studies on the selective adsorption-driven separation of higher hydrocarbons (saturated, C_nH_{2n+2}; unsaturated, C_nH_{2n}; or aromatic) from CH_4 using MOF-graphene hybrids. The following discussion therefore focuses on studies exploring the selective exclusion of CH_4 due to preferential H_2 adsorption. The first foray into this field was made in 2014 by Caro's group, who casted GO onto a ZIF-8 layer using a layer-by-layer (LBL) deposition technique[302] to prepare a bicontinuous ZIF-8@GO membrane (Figure 19a−c). The combined effects of covalent bonding and capillary action ensured that only H_2 molecules could permeate through the ZIF-8 ultramicropores (ca. 3.4 Å), giving these membranes high H_2/CH_4 and H_2/C_3H_8 selectivities (Figure 19d). At a high permeation temperature of 250 °C and ambient pressure (1 bar), H_2/CH_4 and H_2/C_3H_8 separation factors of 139.1, and 3816.6 were obtained for the studied ZIF-8@GO membrane with H_2 permeances of ca. 1.3×10^{-7} mol·m^{-2}·s^{-1}·Pa^{-1}. Such H_2

https://doi.org/10.1021/acs.chemrev.2c00270
Chem. Rev. 2022, 122, 17241−17338

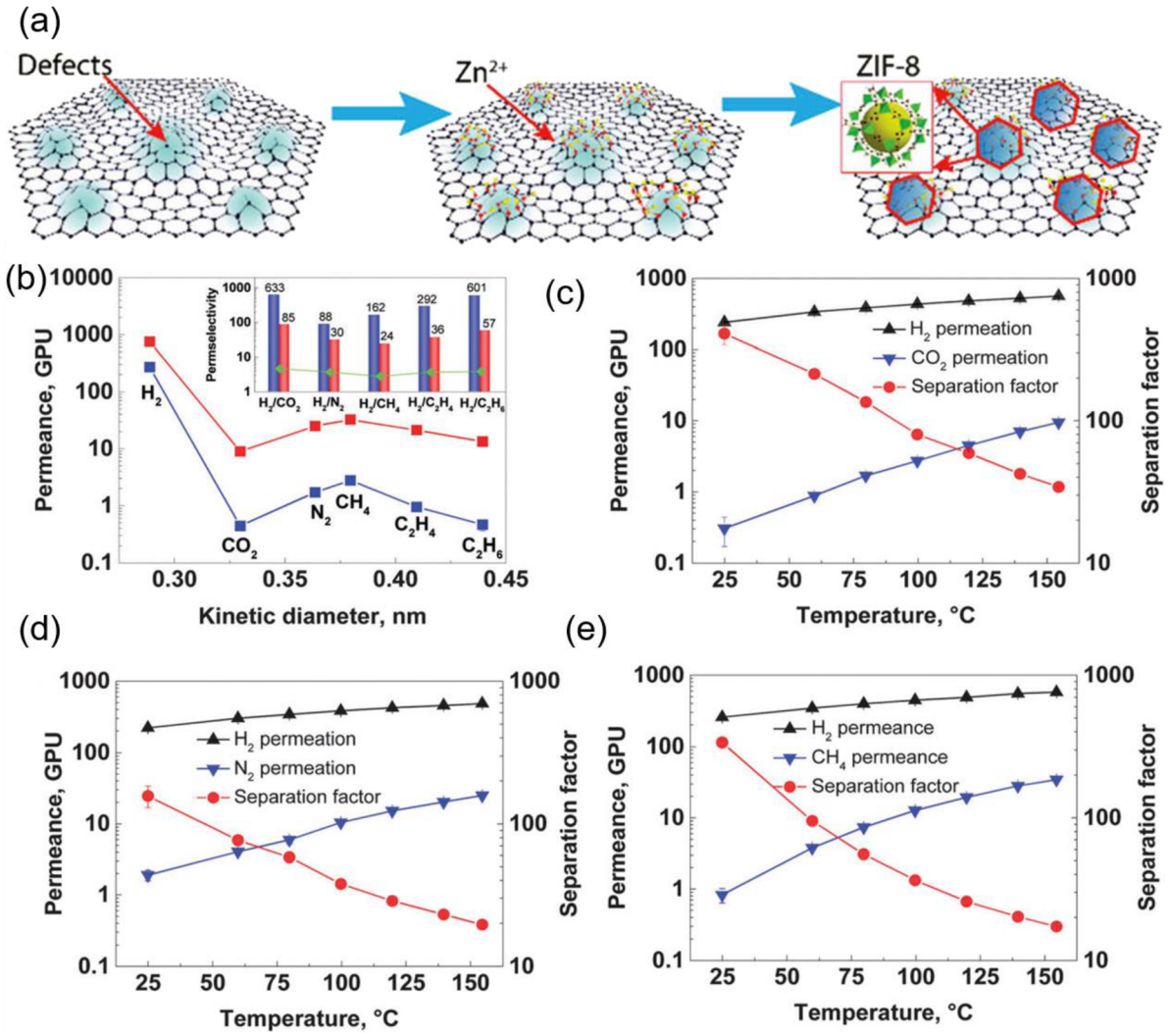

Figure 20. (a) Schematic depiction of the ZIF-8@GO membrane fabrication process. Upon soaking the Zn^{2+}-anchored membrane in a solution of the ligand 2-methylimidazole, ZIF-8 crystals nucleated and grew on the adsorbed Zn^{2+}. (b) Permeance of single gases through the ZIF-8@GO membrane as a function of the kinetic diameter at RT (blue line) and 155 °C (red line). Green line in the inset shows the Knudsen factor of H_2 over other studied gases. (c–e) Gas separation performance of the ZIF-8@GO membrane for binary H_2/CO_2, H_2/N_2, and H_2/CH_4 mixtures at temperatures plotted on the *X* axis. *Y* axis unit is the gas permeation unit, GPU; 1 GPU = 10^{-6} cm^3(STP)/(cm^2 s cm Hg). Reproduced with permission from ref 303. Copyright 2014 Royal Society of Chemistry.

permeance is highly attractive for hydrocarbon purification by H_2 sieving.

In 2016, shortly after this discovery's publication, Zhao's group reported a three-in-one H_2-selective ZIF-8@GO membrane capable of H_2/CO_2, H_2/N_2, and H_2/CH_4 separation.[303] In this system, the ZIF-8 nanochannels were constricted by the strategic intergrowth of ZIF-8 crystals on ultrathin (ca. 20 nm) GO membranes. This caused selective nucleation that reduced the content of nonselective defects in the ultrathin GO membranes while also controlling intercrystalline ZIF-8 growth at the defect sites (Figure 20a). In single-gas permeation tests, this ZIF-8@GO membrane demonstrated excellent H_2/CO_2, H_2/N_2, and H_2/CH_4 separation signatures (Figure 20b); its permselectivities for H_2/CO_2, H_2/N_2, and H_2/CH_4 at 298 K were 633, 88, and 162, respectively, all of which are above the corresponding Knudsen separation factors for H_2 over these gases (green line, Figure 20b inset). These results together with the separation factors determined at 298 K (406 for H_2/CO_2, 155 for H_2/N_2, and 335 for H_2/CH_4; see Figure 20c–e) support the hypothesis that interweaving ZIF-8 crystals into GO membranes simultaneously blocks nonselective defects in the GO membranes and reduces the ZIF-8 pore size. As a result, the ZIF-8@GO membrane could offer a practical way of separating H_2 from hydrocarbon mixtures and synthesis gas, which is a mixture of CO (30–60%), CO_2 (5–15%), CH_4 (0–5%), and H_2 (25–30%).

Another method for fabricating ZIF-8/GO nanosheets based on size- and distribution-selective plasma etching was developed shortly afterward in 2018.[304] An "assembly-and-intergrowth" approach was used to assemble nanosheets comprising mechanically tough nacre-mimetic microstructures of the 2D hybrid ZIF-8/MGO (MGO = mesoporous GO). The resulting hybrid ZIF-8/MGO membrane was ca. 430 nm thick and had a high H_2/C_3H_8 separation factor of 2409 with a H_2 permeance of 1.17×10^{-6} mol m^{-2} s^{-1} Pa^{-1}, making it one of the best-performing H_2/hydrocarbon (gas) separating membranes of its time.[304] At around the same time, introduction of a new hydrothermal interfacial contradiffusion synthesis method enabled Li et al. to prepare a defect-free ZIF-8/rGO composite-based hollow fiber membrane.[283] The resulting

https://doi.org/10.1021/acs.chemrev.2c00270
Chem. Rev. 2022, 122, 17241–17338

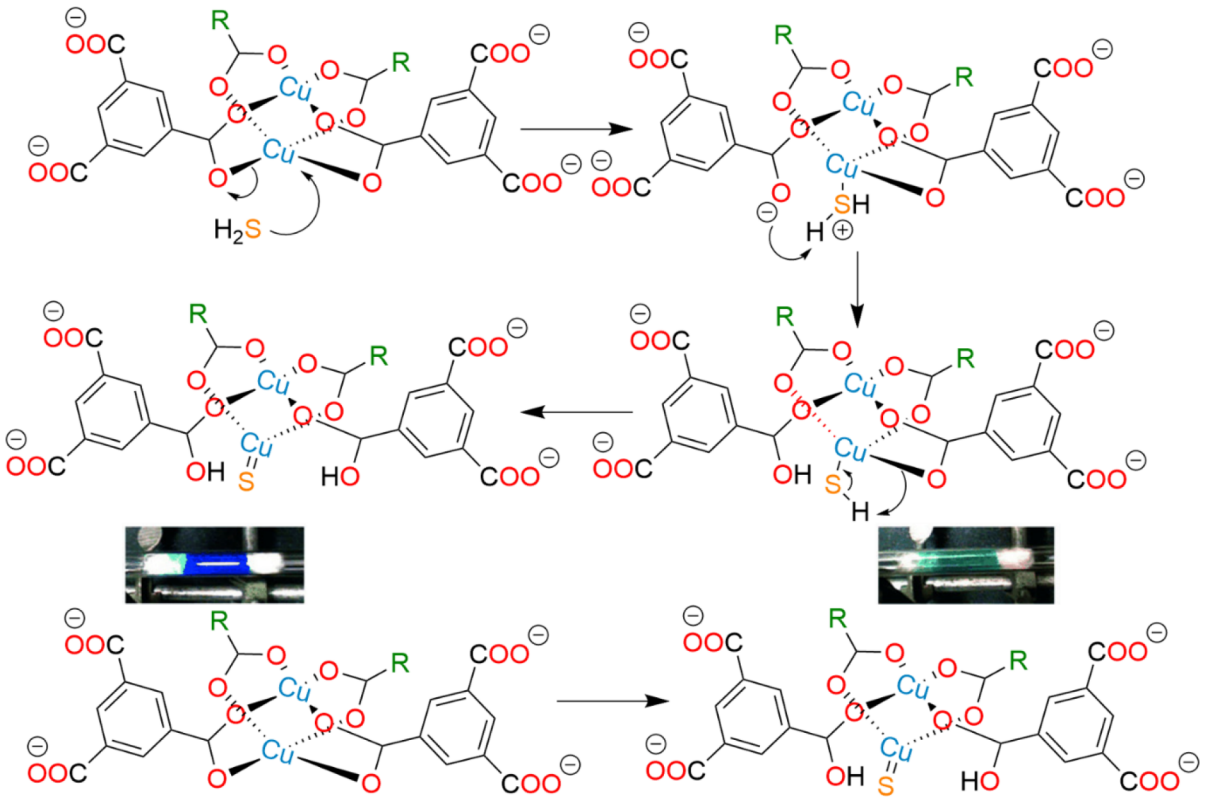

Figure 21. Plausible mechanism of H_2S adsorption in HKUST-1@GO by irreversible reactive adsorption in which H_2S reacts with coordinatively unsaturated Cu(II) sites to release a carboxylic acid and CuS; this process is accompanied by a color change from blue to black (left bottom). Reproduced with permission from ref 307. Copyright 2010 John Wiley & Sons, Inc.

ultrathin (thickness = ca. 150 nm) ZIF-8/rGO composite membrane achieved a benchmark H_2 permeance of $>60 \times 10^{-8}$ mol m^{-2} s^{-1} Pa^{-1}, and its H_2/CO_2, H_2/N_2, and H_2/CH_4 selectivities were as high as 25.3, 70.4, and 90.7, respectively. Shortly after this report was published, the ZIF-8/GO prototype membrane was improved by adding the polyelectrolyte branched polyethylenimine (PEI) to the composite.[305] PEI served as an interfacial modifier, strengthening the interactions between ZIF-8 and the GO nanosheets. This allowed the GO layers to act as isolating layers that extended the gas diffusion pathway, while ZIF nanocrystals enabled H_2 permselectivity from a H_2/CH_4 mixture based on size sieving. The resulting membrane achieved a H_2/CH_4 selectivity of 43 with a H_2 permeance of 6.3×10^{-8} mol m^{-2} s^{-1} Pa^{-1}. These results suggest that MOF@GO hybrids could have very wide ranging applications in sensors and detection devices.[306]

5.1.5. Hydrogen Sulfide Adsorption. As with NH_3 adsorption (section 5.1.3), the early studies of Petit et al. on HKUST-1@GO in 2010 were foundational in the field of adsorptive H_2S removal using MOF@GO hybrids.[307] When studying NH_3 adsorption, these authors discovered a general limitation of pristine MOFs: weak dispersive interactions are insufficient for strong retention of adsorbates like NH_3 in the void spaces of MOFs under ambient conditions. This prompted the preparation of composites of HKUST-1 with nonporous and layered GO.[96,165,297−299] Following a similar logic, HKUST-1/GO composites were tested for H_2S removal under ambient conditions.[307] The composites adsorbed H_2S more strongly than pristine HKUST-1 and GO, partly because of enhanced physisorption in its micropores but mostly because of reactive adsorption leading to the formation of CuS and an accompanying change in color from blue to black (Figure 21).

Huang, Liu, and Kang followed up on this report but used $Zn_4O(bdc)_3$,[308] aka MOF-5, as the composite precursor in place of HKUST-1. A solvothermal process was used to prepare glucose-modified Zn(II)-based microporous MOF-5/GO composites (Figure 22a), and their H_2S adsorption performance was evaluated[309] by performing fixed-bed dynamic breakthrough tests. The authors also proposed a desulfurization mechanism for this system similar to that previously described by Petit et al.[307] As the GO loading increased, the surface area and pore volume of the composites initially increased to a maximum at the optimal GO loading of 5.25% and fell thereafter. The composite with the optimal GO loading achieved a high H_2S uptake of 130.1 mg/g (Figure 22b). Although increasing the GO loading strengthened the dispersive interactions between the adsorbate and the composite, a trade-off arose because it also increased the crystal distortion of the MOF. The inclusion of glucose counteracted this structural collapse by limiting the distortion of MOF-5. These opposing effects explained why H_2S uptake and stability were maximized when the GO loading was 5.25% (MG-G3), culminating in high uptake and stability by leveraging two factors in one: dispersion-driven physisorption and reactive adsorption.

More recent work in this area led to the introduction of HKUST-1@GO-PEI (PEI = polyethylenimine)[310] and γ-Fe_2O_3/rGO composites featuring highly dispersed γ-Fe_2O_3 octahedrons derived from MIL-88B on rGO.[311] In the former case, HKUST-1 grown in situ on GO prefunctionalized with PEI was shown to have a H_2S adsorption capacity that was 1.8 times (i.e., 80%) greater than that of pristine HKUST-1 while also

https://doi.org/10.1021/acs.chemrev.2c00270
Chem. Rev. 2022, 122, 17241−17338

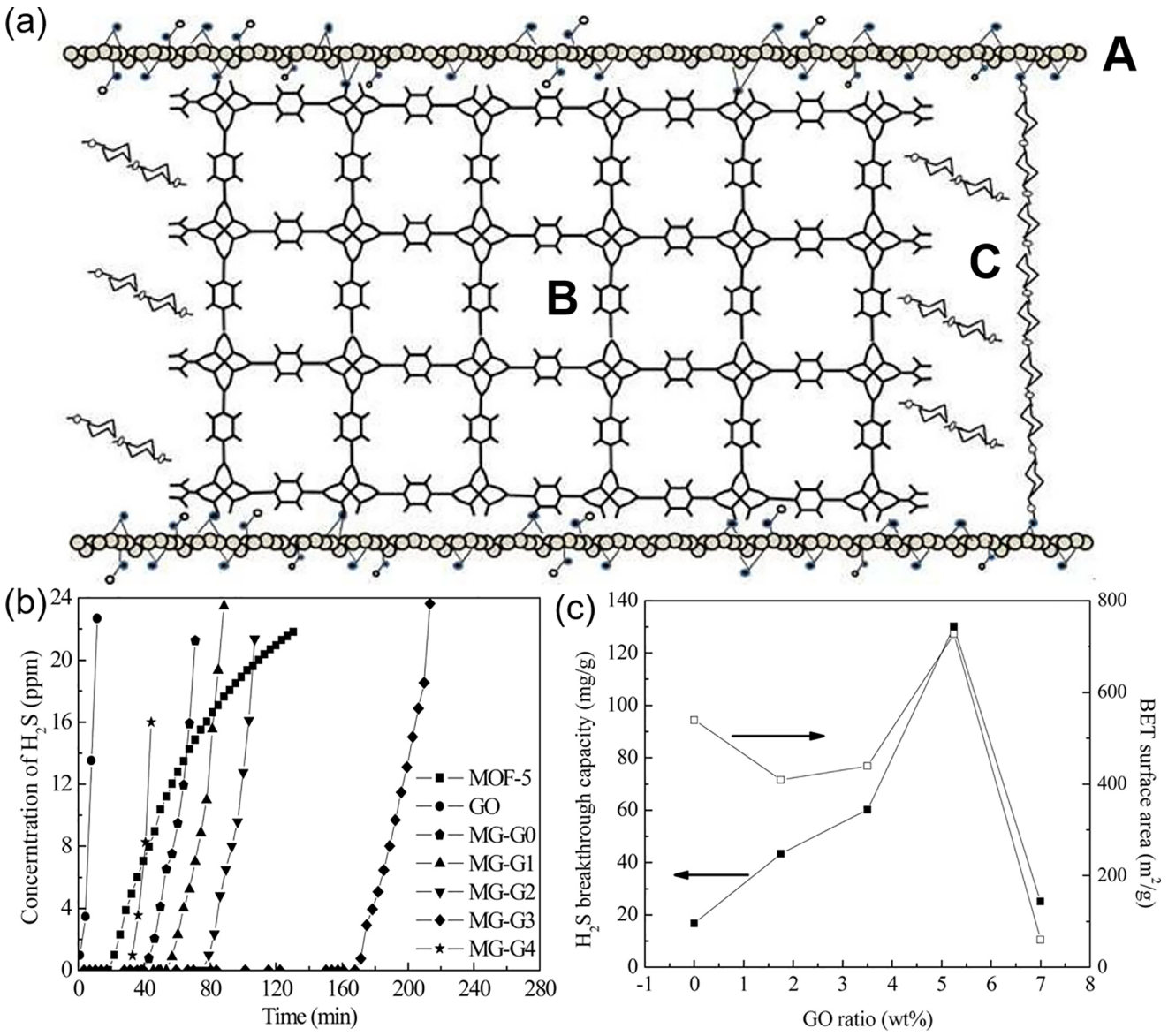

Figure 22. (a) Schematic depiction of the glucose-modified MOF-5/GO composite (A, GO layer; B, MOF-5; C, glucose polymer). (b) H_2S dynamic breakthrough curves for MOF-5, GO, and MG-G*i* composites (i = 0, 1, 2, 3, and 4 corresponding to GO loadings of 5.25, 1.75, 3.5, 5.25, and 7 wt %, respectively). (c) Relationship of GO loading and the H_2S breakthrough capacity and surface area at 298 K. Reproduced with permission from ref 309. Copyright 2012 American Chemical Society.

having more favorable adsorption kinetics.[310] Conversely, Zhang et al. discovered that embedding GO in the well-known (solvothermally synthesized) Fe^{3+} MOF MIL-88B template[312] affords ordered γ-Fe_2O_3/rGO composites that function as H_2S-selective electrochemical sensors.[311] Importantly, the combination of bulk resistance originating from γ-Fe_2O_3 and surface-controlled resistance originating from rGO enabled efficient H_2S-selective electrochemical sensing (R_{air}/R_{gas} = 520.73, 97 ppm) with negligible responses to NH_3, $CHCl_3$, NO, SO_2, and HCHO. These findings have revealed new and currently underexplored ways of using MOF-derived metal oxide semiconductors as H_2S-specific electrochemical sensors.

5.1.6. Oil Spill Clean up from Water. In 2015, Jayaramulu et al. intercalated ZIF-8 crystallites between highly fluorinated graphene oxide (HFGO) sheets using an easily scalable method.[128] Static water contact angle (WCA) measurements showed that the resulting hierarchical HFGO@ZIF-8 composites were superhydrophobic (WCA ≈ 162°) and superoleophilic (oil contact angle, OCA ≈ 0°). In addition to paving the way for the use of graphene@MOF hybrids in oil−water separation, this report was the first published example of fluorographene being used as a scaffold for immobilizing MOF crystallites. The low surface energy of C−F bonds in HFGO, the methyl-functionalized imidazole groups of ZIF-8, and the composite's nanoscale surface roughness and micro/mesoporous hierarchical structure all contribute to its superhydrophobicity, which causes it to reject water and strongly absorb polar and nonpolar organic (oil-constituent) solvents from water (Figure 23a). The oil uptake capacity of HFGO@ZIF-8 was further improved by preparing another application-friendly hybrid composite, Sponge@HFGO@ZIF-8 (Figure 23b). The buoyancy of the sponge together with the high organic solvent absorption capacities of the HFGO@ZIF-8 composite enabled efficient extraction of oil and organic solvents from water in a simple and cost-efficient manner.[128]

https://doi.org/10.1021/acs.chemrev.2c00270
Chem. Rev. 2022, 122, 17241−17338

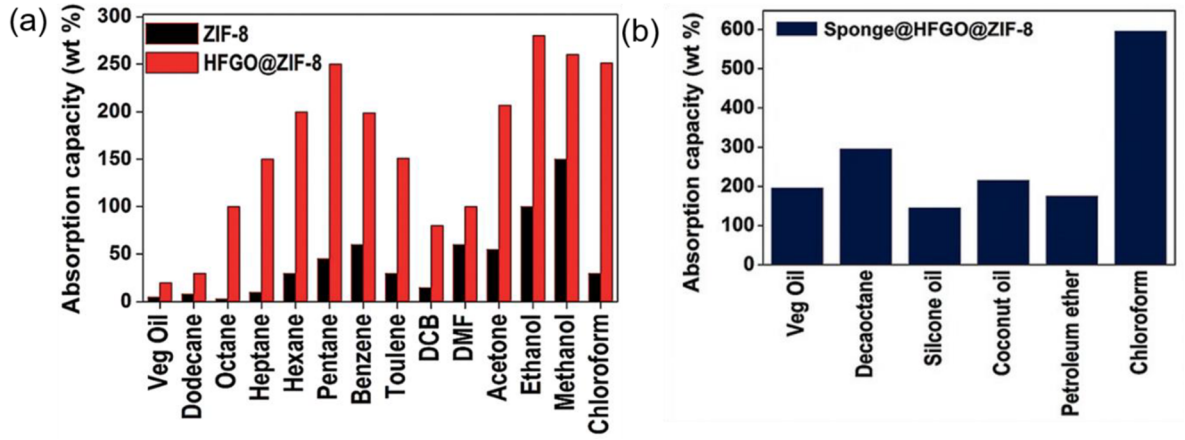

Figure 23. (a) Absorption of oil and oil-constituent organic solvents with ZIF-8 (black bars) and the HFGO@ZIF-8 composite (red bars) (DCB = dichlorobenzene; DMF = *N*,*N*-dimethylformamide). (b) Oil absorption with Sponge@HFGO@ZIF-8. Reproduced with permission from ref 128. Copyright 2015 John Wiley & Sons, Inc.

The next major advance in the use of graphene@MOF hybrids for oil spill cleanup came 4 years later and made use of Mg_2(dobpdc) MOFs (dobpdc = 4,4′-dioxidobiphenyl-3,3′-dicarboxylate; the M_2(dobpdc) isostructural series[313] consists of expanded analogues of M_2(dobdc), aka the M-MOF-74 family of MOFs[267]).

It was shown that postcoordination modification of Mg_2(dobpdc) MOFs with monoamines having different alkyl chain lengths enabled facile tuning of surface wettability.[315] While the octylamine-appended MOF (OctA) demonstrated efficient oil/water separation, its composite with reduced graphene oxide aerogel (OctA/rGA) achieved benchmark absorption capacities for oil and organic liquids while also offering good absorption recyclability. Around the same time, the Fan and Meng groups collaborated to develop novel three-dimensional microspherical superhydrophobic and superoleophilic ZIF-8@rGO composites.[314]

These materials were prepared by growing ZIF-8 nanocrystallites between layered rGO nanosheets and then performing high-temperature reduction-driven self-assembly to obtain micro/nanohierarchical architectures (Figure 24a). In essence, these hybrids consist of crumpled rGO nanosheets intercalated with well-dispersed MOF nanoparticles, which gives them the rare combination of superhydrophobicity (superwettability with oil) and meso/microporosity. Consequently, the ZIF-8@rGO microspheres had ultrafast absorption rates and high absorption selectivities for organic solvents and oils in water. Of particular importance was the preparation of the ZIF-8@rGO@Sponge (Figure 24b) using a commercial, macroporous polyurethane (PU) sponge. This coated sponge achieved good performance in recyclable oil−water separation, largely because of the composite's high absorption capacities for oil and organic solvents (Figure 24c). Two other reports on oil−water separation using graphene@MOF hybrids surfaced in 2019.[316,318] One described a hierarchically structured stainless steel mesh (SSM) decorated with UiO-66-NH_2 crystallites on GO nanosheets, SSM/UiO-66-NH_2/GO.[318] This hierarchical structure is both superhydrophilic (WCA ≈ 2°) and superoleophobic (OCA ≈ 163°), resulting in excellent oil resistance-guided oil/water separation performance. The second report described a rather conventional method for fabricating superhydrophobic (i.e., superoleophilic) UiO-66-F4@rGO composites on filter paper (FP) and a melamine sponge (MS) as substrates. UiO-66-F4 denotes the MOF $Zr_6O_4(OH)_4(F_4\text{-bdc})_6$,[323] where F_4-bdc^{2-} = 2,3,5,6-tetrafluoro-1,4-benzenedicarboxylate.[316] With a high WCA of 169.3 ± 0.6°, both UiO-66-F4@rGO/MS and UiO-66-F4@rGO/FP were capable of separating several water-in-oil emulsions with high fluxes and separation efficiencies.

Several other papers in this area have been published in the last 2 years; in 2020, graphene@MOF hybrids reported as being useful for oil−water separation included ZIF-8@GSH/PI,[317] UiO-66-NH_2@GO-PAA,[320] and FG-HKUST-1-PU,[241] while in 2021, PRGO@UiO-66-NH_2-laden MFs[322] were described. Table 1 briefly lists the properties and capabilities of these systems as well as those of the composites discussed above.

5.1.7. Removal of Water Pollutants. Water is ubiquitous, but potable water is scarce in many parts of the world. Rather precariously, a global population of >2 billion drink contaminated water, while a larger population of 4 billion faces water scarcity.[324] Therefore, both the 2025 World Health Organization (WHO) forecast[106] and the United Nations (UN) Sustainable Development Goal 6 (SDG6)[105] state that there is an urgent need for new ways of reducing or removing water pollution. This is not just a problem for developing countries; many organic and inorganic anthropogenic contaminants are present in Europe's water bodies, prompting the introduction of stringent water purity targets in the European Economic Area (EEA) briefing "Urban waste water treatment for 21st century challenges".[108] Many of these contaminants are recalcitrant and can have severe ecotoxicological effects despite generally being present at $\mu g\ L^{-1}$ to $ng\ L^{-1}$ concentrations.[109] Next-generation porous solids such as MOF@GO hybrids that can efficiently capture (and/or sense) water contaminants are considered promising for the removal of such contaminants because of their many favorable properties, which include high surface areas, tunable pore environments, stability, and amenability to inexpensive bulk-scale synthesis.[256]

This is perhaps the most popular area of research using graphene@MOF hybrids; one could use the expression "a dime a dozen" to describe the proliferation of papers on this topic. As might be expected given this flurry of activity, it is hard to identify any one report that established the field. For clarity, we classify the publications in this area based on the nature of the pollutants targeted for removal (organic or inorganic) and restrict our focus to papers published in the last 5 years. Papers

https://doi.org/10.1021/acs.chemrev.2c00270
Chem. Rev. 2022, 122, 17241−17338

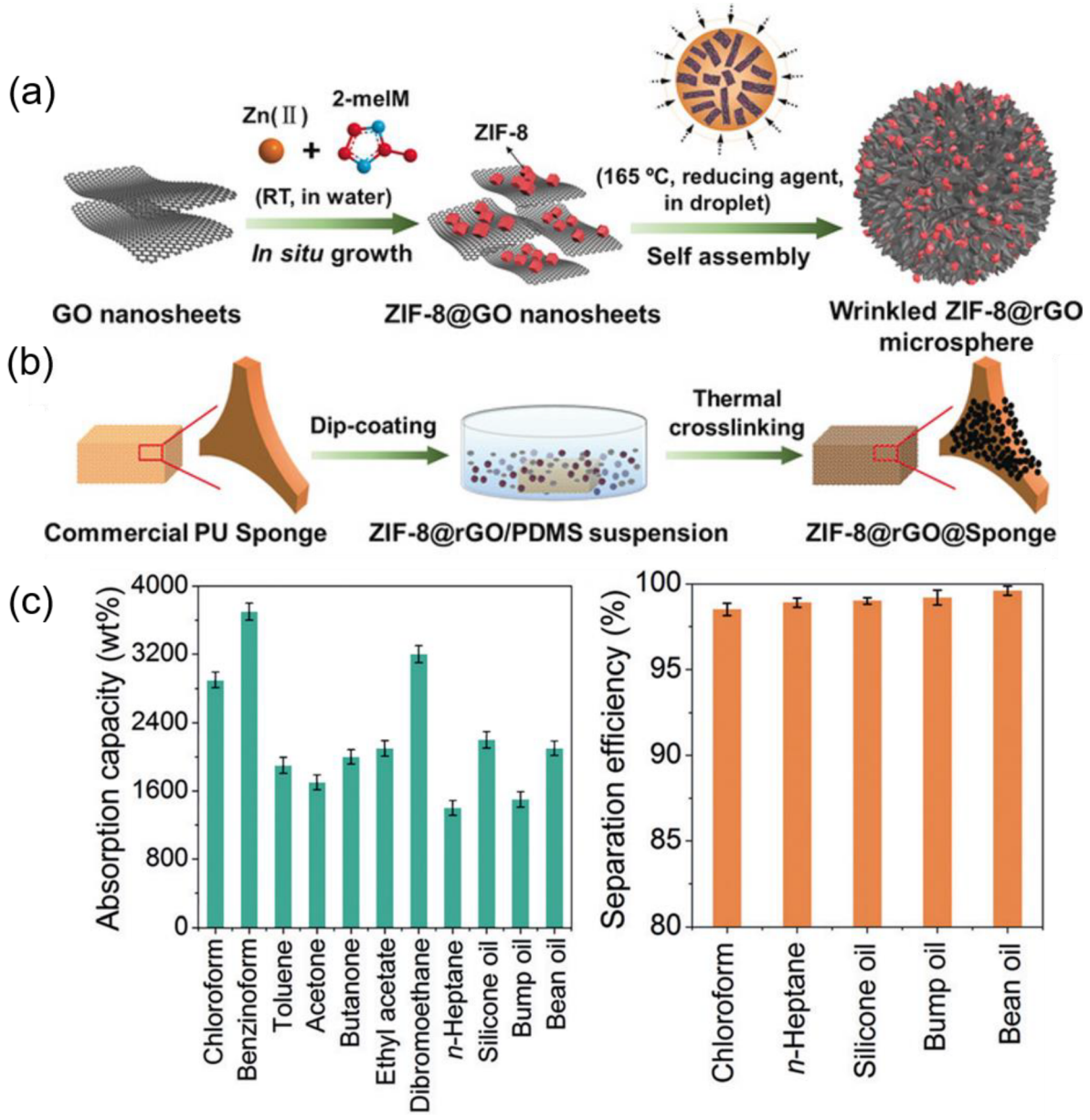

Figure 24. (a) Synthesis and composition of wrinkled ZIF-8@rGO microspheres. (b) Synthesis of the composite ZIF-8@rGO@Sponge. (c) Oil and organic solvent absorption capacities and separation efficiencies determined for the ZIF-8@rGO@Sponge. Reproduced with permission from ref 314. Copyright 2019 John Wiley & Sons, Inc.

on this topic published within this time window are listed in chronological order in Tables 2, 3, and 4 along with brief descriptions of the composites that were studied, the pollutants that were targeted, and the properties of the composite that facilitated removal. Table 2 lists composites used to remove inorganic pollutants, Table 3 deals with removal of organic toxic dyes, and Table 4 lists composites used to remove other organics.

In addition to the applications listed above, MOF@GO composites continue finding new uses; for example, chemoresistive hybrids have been put forward as electrochemical sensors of VOC (volatile organic compounds) biomarkers and toxins, both of which are relevant to water purification.[183,379,380] Tunable electrochemical sensors appear primed to become a leading practical application of MOF@GO hybrids, and efforts to develop these applications will bring such composites to higher TRLs as they move toward commercialization.[70]

5.2. Catalysis

5.2.1. Heterogeneous Catalysis. Catalysts play vital roles in the production of bulk and fine chemicals and value-added products; various catalysts are used in the synthesis of almost 10 000 products per year that collectively account for 15% of the world's gross domestic product (GDP).[381] Heterogeneous catalysts are preferred to homogeneous catalysts in large-scale industrial production because of their easy separation and recovery and lower operating costs.[382] MOFs are interesting materials for heterogeneous catalysis due to their well-defined porosity, organic−inorganic hybrid nature, structural diversity, and content of potentially catalytically active metals sites.[147] However, their usefulness in this area is limited by their low thermal stability; prolonged use of MOF-based catalysts leads to their structural degradation and thus a loss of catalytic performance.[383] It has been suggested that this problem could

https://doi.org/10.1021/acs.chemrev.2c00270
Chem. Rev. 2022, 122, 17241−17338

Table 1. MOF@GO Composites Used for Oil/Water Separation[a]

graphene@MOF composite	WCA (deg)	origin of oil/water separating surface property	porosity	ref
ZIF-8@rGO@Sponge	171	micro/nanohierarchical architecture; in situ and postsynthetic functionalization	micro- and meso-P ZIF-8@rGO embedded in macro-P sponge	314
UiO-66-F4@rGO/FP	169	micro/nanohierarchical architecture	micro- and meso-P UiO-66-F4@rGO embedded in macro-P FP	316
HFGO@ZIF-8 composite	162	low surface energy of C−F bonds in HFGO, methyl-functionalized imidazolate ligand, nanoscale surface roughness, and micro/mesoporous hierarchical structure	micro- and meso-P	128
ZIF-8@GSH/PI membrane	153.2	hydrophobicity of ZIF-8 and GSH, methyl-functionalized imidazolate ligand nanoscale roughness and hierarchical structure	micro- and meso-P ZIF-8@GSH embedded in macro-P PI	317
SSM/UiO-66-NH_2/GO	2	amine, carboxyl, and hydroxyl groups of UiO-66-NH_2/GO hierarchical structure inducing strong H_2O affinity	NM	318
UiO-66-F4@rGO/FP and UiO-66-F4@rGO/MS	169.3 (FP); 155.1 (MS)	superhydrophobicity of UiO-66-F4@rGO composite (from F4-bdc ($^-OOC-C_6F_4-COO^-$) ligand), micro/nanohierarchical structural roughness	micro- and meso-P UiO-66-F4@rGO embedded in macro-P FP and MS	316
prGO@cHKUST-1	31.5	surface roughness	NM	319
UiO-66-NH_2@GO-PAA	<5	carboxyl groups assisted high H_2O affinity in UiO-66-NH_2; micro/nanostructures' ability to trap H_2O, eliciting a robust hydration layer	NM	320
FG-HKUST-1-PU	147	low surface energy of C−F bonds originating from FG layers,[321] and dispersion of HKUST-1 crystallites over FG	micro- and meso-P FG-HKUST-1 embedded in macro-P PU	241
PRGO@UiO-66-NH_2-laden MFs	154	high hydrophobicity of PRGOs	micro- and meso-P PRGO@UiO-66-NH_2 embedded in macro-P MF	322

[a]Abbreviations: NM, not mentioned; UiO, University of Oslo; FG, fluorinated graphene; micro-P, microporous; meso-P, mesoporous; macro-P, macroporous; PDMS, polydimethylsiloxane; HFGO, highly fluorinated graphene oxide; GSH, thiolated graphene; PAA, poly(acrylic acid); SSM, stainless steel mesh; FP, filter paper; MS, melamine sponge; PU, polyurethane sponge, commonly denoted as sponge; MFs, melamine foams; PRGO, partially reduced graphene oxides.

https://doi.org/10.1021/acs.chemrev.2c00270
Chem. Rev. 2022, 122, 17241−17338

Table 2. MOF@GO Composites for Remediation of Inorganic Water Pollutants[a]

graphene@MOF composite	removed pollutant	key property contributing to pollutant remediation	porosity	ref
IRMOF-3/GO	Cu(II)	GO incorporation improves dispersive forces facilitating higher Cu(II) adsorption	micro-P	325
GO-COOH/UiO-66	U(VI) (ppb and ppm level removal)	chelation and ion exchange of U(VI) ions with GO-COOH/UiO-66	micro-P	326
ZIF-8/rGA	Pb(II), Cd(II)	high specific surface area	micro- and macro-P	193
Cu(bdc)GO	Mn(II), Cu(II), Zn(II), Cd(II), Pb(II), and Fe(III) from AMD wastewater	chemical interactions between the metal ion toxins and the π-conjugated MOF functional groups	NM	327
GO/2D-Co-MOF-60 membrane	Cs^+ (192.14 mg g^{-1})[c]	chemical adsorption and electrostatic interaction (Cs^+ forming surface complexation with C═O and C−O)	micro-P[d]	194
GO−CS@MOF [Zn(BDC)(DMF)]	Cr(VI)	strong electrostatics	micro-P	328
MIL-53(Al)-GO	As(III)	electrostatic affinity between the δ^+ 3%-MIL-53(Al)-GO and δ^- arsenates[e]	micro-P	329
P^+GO-anchored HKUST-1 sandwiched between polymer[b] and a commercial RO membrane	Na(I), Ca(II), and Mg(II)	synergistic charge- and pore-based sieving	micro-P	330
dpGNS-encapsulated DMOF-1	As(III) and Pb(II)	electrostatic interactions and DMOF-1 porosity	micro-P	331
$[Co_2(btec)(bipy)(DMF)_2]_n$ (Co−MOF) on the surface of rGO	CrO_4^{2-}	rGO provides electric conductivity; hydrated ion size relative to the Co−MOF pore size, intermolecular H bonds, and charge interactions with $-NH_2$ groups	micro-P	332
La-mof-1 GO membrane	total phosphorus	monolayer chemisorption	NM	333
Fe_3O_4@HKUST-1/GO	U(VI) (in the speciation of UO_2^{2+} at pH 3−5)[f]	interactions with HKUST-1 and GO	meso-P	334

[a]Abbreviations: NM, not mentioned; micro-P, microporous; meso-P, mesoporous; macro-P, macroporous; rGA, reduced graphene-oxide aerogel; tpa, terephthalate; AMD, acid mine drainage; CS, chitosan; BDC, 1,4-benzenedicarboxylate; DMF, *N*,*N*-dimethylformamide; P^+GO, phosphonium-conjugated graphene oxide. [b]Synthesized by RAFT, reversible addition−fragmentation chain transfer; dpGNS, dithiophosphonated graphene nanoscrolls; btec, 1,2,4,5-benzenetetracarboxylate; bipy, 4,4′-bipyridine. [c]Under a contact time of 4 h and an adsorbent dose of 2 mg. [d]Pore diameter ≈ 10 Å based on the single-crystal structure. [e]In the range of 9 < pH < 11. [f]In the speciation of $(UO_2)_3(OH)_7$ and $UO_2(CO_3)_2^{2-}$ in the pH scope of 6−10 at pH 3−5.

be overcome by using MOF-based hybrid materials in place of pristine MOFs because such hybrids have greater thermal stability and the synergic effects of hybridization can give rise to unique properties.[384] Graphene@MOF hybrids are particularly interesting in this context. Because pristine graphene lacks functional groups capable of forming strong interactions with MOFs, catalytically active graphene@MOF hybrids are generally prepared using graphene derivatives.[385] In addition to stabilizing the MOF, hybridization alters the properties of the graphene layers by preventing their stacking. In addition to pristine MOFs, MOF-derived porous materials have been used in composites with graphene derivatives. The hierarchically porous structure of such MOF-derived materials together with their high surface areas and exposed active sites make them very interesting as hybrid catalysts.[386] Combining MOFs with graphene derivatives thus offers a useful route to heterogeneous catalysts with good stability and high performance. Table 5 lists all of the studies on graphene@MOF hybrid-based heterogeneous catalysts that were found while preparing this review.

5.2.1.1. Pollutant Removal. The catalytic degradation of toxic and harmful pollutants is seen as a promising strategy for reducing environmental pollution. Previous reports have shown that graphene@MOF hybrids can strongly promote the catalytic degradation of dyes (methyl orange), organic pollutants (bisphenol A and sulfamethoxazole), drugs (4-aminobenzoic acid ethyl ether), chlorinated phenol (trichlorophenol), and other organic pollutants.[386−390]

Shao et al. recently prepared a 2D porous catalyst-designated C-ZIF-67@ZIF-8@GO-900 by carbonizing dual-MOF-coated graphene oxide (ZIF-67@ZIF-8@GO) at 900 °C.[391] This resulted in the formation of carbon nanotubes with codoped nanocrystalline Co and Co−N_x sites without requiring the use of chemical vapor deposition. The fabricated catalyst had Fenton-like activity after activation by peroxymonosulfate, a conductive framework, a micro/mesoporous structure, and Co/Co−N_x/pyridinic-N active sites. On the basis of these properties, its performance in the degradation of benzene derivatives such as phenol, bisphenol A, biphenyl, naphthalene, and poly(sodium 4-styrene sulfonate) (PSS) was investigated. Figure 25a shows the percentage degradation of bisphenol A by various catalysts and confirms that all of the different components of C-ZIF-67@ZIF-8@GO-900 are required to obtain a composite that effectively degrades bisphenol A. Because this degradation process is initiated by ROS (reactive oxygen species), Figure 25a indicates that C-ZIF-67@ZIF-8@GO-900 produces more ROS than the other catalysts shown in the figure. In addition, the degradation activity of C-ZIF-67@ZIF-8@GO-900 exceeded that of some more well-known catalysts, as shown in Figure 25b, and it efficiently degraded a range of other benzene derivatives (Figure 25c). The excellent catalytic activity of C-ZIF-67@ZIF-8@GO-900 makes it suitable for wastewater treatment. Another report on bisphenol A degradation was presented by Zhu and co-workers, who prepared the CoS@GN catalyst from the ZIF-67@GN hybrid.[389] The as-synthesized ZIF-67@GN hybrid was used as a template for the synthesis of Co_3S_4@GN by a ligand exchange strategy, after which a phase transformation was induced to obtain CoS@GN. Because of the unique structural features of CoS@GN, it was used to catalyze the oxidation of bisphenol A. Whereas the above-mentioned C-ZIF-67@ZIF-8@GO-900 catalyst induced only 75.4% degradation of bisphenol A in 40 min, CoS@GN achieved 100% degradation in 8 min. Furthermore, whereas ROS were the main active species for C-ZIF-67@ZIF-8@GO-900, the degradation of bisphenol A was caused by sulfate radicals ($SO_4^{\bullet-}$) in the case of CoS@GN; as shown in Figure 25d, the fastest degradation was seen in the presence of peroxymonosulfate (PMS), which is a

https://doi.org/10.1021/acs.chemrev.2c00270
Chem. Rev. 2022, 122, 17241−17338

Table 3. Summary of MOF@GO Composites Used To Remediate Toxic Organic Dyes[a]

graphene@MOF composite	removed pollutant	key property contributing to pollutant remediation	porosity	ref
Fe_3O_4/HKUST-1@GO	methylene blue	hydrophobic and/or $\pi-\pi$ as well as charge−charge interactions	micro-P	335
ZIF-8/rGA	methylene blue	high specific surface area	micro- and macro-P	193
Fe-MIL-88B/GO	reactive red dye (RR195)	synergistic effect between Fe-MIL-88B and GO to photocatalytically degrade RR195	meso-P	336
NH_2-MIL-68(Al)/RGO	Congo red	electrostatic and $\pi-\pi$ interactions, intermolecular H bonds	micro- and meso-P	337
UiO-66@GO/PES membrane	methyl orange, direct red 80[b]	pores fit for water-selective molecular sieving	NM	338
ZIF-8@GO	malachite green	enhanced dispersive interactions, restricted aggregation, high surface area, optimal pore size	meso-P	339
Ni BTC@GO	congo Red	acid−base interaction between active metal sites (Lewis acid) and $-NH_2$ (Lewis base)	meso-P	340
GO-TMU-23[c]	methylene blue	electrostatic and/or acid−base interactions, MB physisorption on GO layers, $\pi-\pi$ interactions between the MB aromatic rings and the organic ligands affording TMU-23	NM	341
6% GO/Ni-BTC	methylene blue	electrostatic (negative charged surface of GO/MOF and the cationic dye) and acid−base interactions	meso-P	342
MIL-101/GO	azo dyes: amaranth, sunset yellow, carmine	hydroxyl group in each azo dye, interacting with −OH and carboxyl groups of MIL-101/GO	NM	343
MIL-100(Fe)/graphene hybrid aerogel (MG-HA)	methylene blue	large surface area and pore volume of MG-HA facilitating (a) electrostatic interaction, (b) H-bonding, and (c) hydrophobic interactions	meso-P	344
PDA/rGO/HKUST-1 membrane	methylene blue, Congo red	electrostatic interactions: high rejection of cationic dye at high pH, high rejection of anion dye at low pH	NM	345
NENU/GO	basic red 46	hydrophobic interactions (between cationic dye and GO), $\pi-\pi$ interactions	meso-P	346
Pseudomonas putida GA/MIL-100(Fe)	acid orange 10	combination of adsorption and biodegradation	macro-P	347
MIL-100(Fe)/GO[d]	methylene blue and methyl orange	$\pi-\pi$ interactions and electrostatic interactions	micro- and meso-P	348
UiO-66@GO-CS membrane	methylene blue, methyl orange, direct red 80	UiO-66 can expand its channel opening, eliciting molecular sieving of water; coated chitosan layer increases the surface hydrophilicity	NM	349
$BiVO_4$/MIL-53 (Fe)/GO	rhodamine B	adequate active sites; energy levels of the $BiVO_4$/MIL-53(Fe)/GO reduce the electron−hole recombination rate to enable RhB photodegradation	meso-P	350
AIF/GO, AIF/rGO	Congo red	$\pi-\pi$ stacking, electrostatic, and intermolecular H-bonding interactions	micro-P	351
Ni-BDC@GO	methylene blue	hydrophobic and/or $\pi-\pi$ interactions	NM	352
GO/In-MOFs-*i* (i = 1, 2)	Congo red	electrostatic and acid−base interactions, intermolecular H-bonding and $\pi-\pi$ stacking interactions	meso-P	353
$Fe_3O_4/Co_3(BTC)_2$@GO	methylene blue	increased dispersive forces, inhibition of GO sheet stacking to increase content of MB adsorption sites	NM	354
MOF-1/GO/Fe_3O_4[e]	methylene blue	GO addition prevented recombination of photogenerated electron−hole pairs, thus boosting MB photodegradation	meso-P	355
Sm-MOF/GO[f]	rhodamine B, methylene blue	regular membrane skeleton caused by the facilitated stacking of the GO layers	NM	356
UiO-66/MIL-101(Fe)-GOCOOH[g]	methylene blue	high surface area, $\pi-\pi$ interactions, residual negative charge on the adsorbent surface interacting with the positively charged MB dye molecules; highly dispersed nature of GOCOOH	NM	357
UiO-66-$(OH)_2$/GO	methylene blue	high surface area, strong chemical affinity between Zr(IV) and MB, electrostatic interactions, intermolecular H-bonding and $\pi-\pi$ interactions	micro-P	358
MOF-5@GO	rhodamine B	unsaturated bonds (C═C, O−C=O) in MOF-5, δ^- nature of GO surface, and δ^+ nature of RhB eliciting ionic interactions; $\pi-\pi$ interactions between RhB and MOF-5	meso-P	359
GrO/MIL-101(Cr) (GrO@MCr)	methyl orange; reactive blue 198	electrostatic attractive forces and pore/size-selective adsorption	micro- and meso-P	360

[a]Abbreviations: NM, not mentioned; micro-P, microporous; meso-P, mesoporous; macro-P, macroporous; BDC, 1,4-benzenedicarboxylate; PES, poly(ether sulfone). [b]Rejection ratio determination experiments conducted, based on single-crystal structure. [c]TMU stands for the MOF $[Zn_2(oba)_2(bpfb)]\cdot(DMF)_5$; oba, 4,4′-oxybisbenzoate, bpfb, *N*,*N*′-bis(4-pyridylformamide)-1,4-benzenediamine; DMF, *N*,*N*-dimethylformamide; PDA, polydopamine; NENU, Northeast Normal University. [d]Composite containing 5% (ww) GO showed the best performance in MB and/or MO uptake; CS, chitosan; AIF, aluminum fumarate. [e]MOF-1, $[Nd_2(TCPB)_2(DMF)(H_2O)]_n$ (H_3TCPB, 1,3,5-tris(4-carbon(phenoxy)benzene)). [f]Prepared by hydrothermal treatment of GO dispersion, 1,4-bis(4-carboxylatopyridinium-1-methylene)benzene dichloride, isonicotinic acid, and Sm_2O_3; RhB, rhodamine B; MB, methylene blue. [g]GOCOOH, carboxylated graphene oxide; GrO, graphite oxide; MO, methyl orange; RB198, reactive blue 198.

source of $SO_4^{\bullet-}$. The synthesis of CoS@GN caused Co^{2+} ions to move out from the ZIF-67 framework to form a shell with active sites that can activate PSM for $SO_4^{\bullet-}$ generation.

The degradation of sulfamethoxazole (SMX) was achieved by Ye et al. using a 2D bimetal sulfide and N-doped rGO-based hybrid CoFeS@N-rGO.[387] The synthesis of CoFeS@N-rGO first involved the solvothermal preparation of Fe−Co−BTC@GO, which was then converted to FeCo-*x*/N-rGO (x = Fe^{3+}/Co^{2+} molar ratio, which can be 2, 4, and 8) by calcination at 650 °C. CoFeS@N-rGO was then obtained by solvothermal treatment of FeCo-*x*/N-rGO in the presence of thioacetamide. The main active species in the degradation reaction catalyzed by FeCo-*x*/N-rGO were ROS ($OH^{\bullet}$, $^1O_2$, and $O_2^{\bullet-}$), but various sulfur-containing species (S^0, S^{2-}, S_n^{2-}, SO_3^{2-}, and SO_4^{2-}) were also involved, so PMS was required to achieve optimal degradation performance. Figure 25e shows the degradation of

https://doi.org/10.1021/acs.chemrev.2c00270
Chem. Rev. 2022, 122, 17241−17338

Table 4. Summary of MOF@GO Composites Used To Remediate Organic Water Pollutants Other than Dyes[a]

graphene@MOF composite	removed pollutant	key property contributing to pollutant remediation	porosity	ref
MIL-68(Al)/reduced graphene oxide (MA/RG) composite	*p*-nitrophenol	improvement of porosity, intermolecular H bonds and $\pi-\pi$ dispersion interactions	meso-P	361
UiO-67/GO	glyphosate	surface/inner complexation with functional groups of UiO-67/GO	NM	362
ZIF-8/rGA	phthalic acid	GO incorporation improves dispersive forces facilitating higher Cu(II) adsorption	micro-P	325
Fe_3O_4-GO-β-CD	neonicotinoid insecticides[b]	superparamagnetism, high surface area, hydrophobic inner cavities, and supramolecular recognition	micro- and macro-P	363
GNP/MIL-101[c]	naphthalene	$\pi-\pi$ interactions between naphthalene and terephthalate	meso-P	364
MIL-101/GrO	CCl_4	high surface area, GrO induced dispersion interactions, and crystal surface defects	micro- and meso-P	365
TGO@UiO-66[d]	pesticides: paraoxon (POX) and chlorpyrifos (CPF)	high surface area and conductivity facilitated electron transfer between the analytes (POX or CPF) and the TGO@UiO-66 electrode surface	meso-P	366
MIL-53-NH_2@fabric (cotton and wool)	indole, quinoline	fabrics' binding sites interact with intermolecular spaces; indole and quinoline adsorbed on single active sites, producing one adsorbed layer	NM	367
GnO/MIL-101	AIDs, naproxen (NAP), and ketoprofen (KTP)	H bonding with NAP as H acceptor	micro-P	368
MGO-ZnCB[e]	chiral drug intermediates (racemic), 1,1′-bi-2-naphthol, and 2,2′-furoin	$\pi-\pi$ and H-bonding interactions, homochiral pore environment	meso-P	369
Fe_3O_4@SiO_2-GO-MOFs	imidacloprid, carbendazim, metalaxyl, myclobutanil, tebuconazole, and cyfluthrin	$\pi-\pi$ interactions, hydrophobic interaction and hydrogen bonds	micro-P	370
Cu-BTC@GO	toluene	metal$-\pi$ interaction; interaction with organic ligands stems from cooperative effect of $\pi-\pi$ bond and H bond	micro- and meso-P	371
MIL-101(Cr)@GO	sulfonamides (sulfadiazine, sulfadoxine, and sulfamethoxazole)	$-NH_2$ of sulfonamides forming coordination bonds with unsaturated Cr(III) sites, intermolecular H bonds, hydrophobic interactions, $\pi-\pi$ interactions, van der Waals interactions	NM	372
GNP/UiO-66[f]	polyphenols; oleuropein and hydroxytyrosol	$\pi-\pi$ stacking interactions of GNP, adsorbate size selectivity	meso-P	373
Cu-BDC@GrO	bisphenol A	$\pi-\pi$ interaction and H bonding	NM	374
UiO-66/GPNPs[g]	β-carotene	endothermic and nonspontaneous chemisorption concerning kinetics, equilibrium, and thermodynamics	micro-P	375
UiO-66-$(COOH)_2$/GO	tetracycline hydrochloride antibiotics	$\pi-\pi$ interactions, chemical coordination, and weak electrostatic interactions	meso-P	376
Mn-PBA/GO[h]	ciprofloxacin	intermolecular hydrogen bonding, hydrophobic affinity, electrostatic interaction, and acid–base interaction	meso-P	377
$Zr(OH)_4$/GO	nerve agent soman (GD)	hydrolytic degradation of GD under high-humidity air (80% RH) and/or water	meso-P	378

[a]Abbreviations: NM, not mentioned; micro-P, microporous; meso-P, mesoporous; macro-P, macroporous; CD, cyclodextrin. [b]Thiamethoxam, imidacloprid, acetamiprid, nitenpyram, dinotefuran, clothianidin, and thiacloprid. [c]GNP, graphene nanoplatelet. [d]TiO_2-functionalized graphene oxide@UiO-66; GNO, graphene oxide. [e]ZnCB, $[Zn_2(D\text{-Cam})_2(4,4'\text{-bpy})]_n$; D-Cam, D-(+)-camphoric acid; MGO, magnetic graphene oxide. [f]GNP, graphene nanoplatelet; GrO, graphene oxide. [g]GPNPs, graphene nanoplatelets. [h]PBA, Prussian blue analogue.

https://doi.org/10.1021/acs.chemrev.2c00270
Chem. Rev. 2022, 122, 17241−17338

Table 5. Graphene@MOF Hybrids Used in Heterogeneous Catalysis

graphene@MOF hybrid	MOF	form of graphene	name of pollutant	application	performance	ref
MIL-100(Fe)/GO	MIL-100(Fe)	GO	methyl orange	pollutant removal	degradation time: 240 min	390
CoS@GN	ZIF-67	GO	bisphenol A		degradation time: 8 min	389
NMC-50/PMS	NH_2-MIL-53(Fe)	graphitic C_3N_4	4-aminobenzoic acid ethyl ether (ABEE) and sulfamethoxazole (SMX)		% degradation: 87.37% (SMX) and 100% (ABEE) in 60 min	386
rGO/MIL-101(Fe)	MIL-101(Fe)	rGO	trichlorophenol		% degradation: 92% in 180 min	388
FeCoS@NGC membrane	Fe-Co-BTC	GO	sulfamethoxazole (SMX)		% degradation: 92% in 60 min	387
MCG/PMS	ZIF-67	GO	acid yellow (AY)		% degradation: ∼100% in 60 min	188

graphene@MOF hybrid	MOF	form of graphene	name of substrate	application	performance	ref
AuPd-MnO_x/ZIF-8-rGO	ZIF-8	rGO	formic acid	hydrogen evolution	TOF[a] = 382.1 mol $mol_{cat.}^{-1}$ h^{-1}	395
PdAg NPs@ZrO_2/C/rGO	UiO-66	rGO	formic acid		TOF = 4500 h^{-1}	394
Pt-Ni NPs@ZrO_2/C/rGO	UiO-66	GO	hydrous hydrazine		TOF = 1920 h^{-1}	396

graphene@MOF hybrid	MOF	form of graphene	name of reactant	application	performance	ref
MCG-*x*	ZIF-67	GO	benzyl alcohol	oxidation	% conversion: 89.5%	383
N-G(D), N-G(M), and N-G(U)	MIL-100(Fe)		*p*-hydroxybenzoic acid		degradation time (min): 20, 30, and 90 for N-G(D), N-G(M), and N-G(U)	397
Ru/GA-HK-150	HKUST-1	GO	CO		% conversion: 100% at 150 °C	398
GO/Fe-MOF	Fe-MIL-88NH2	GO	3,3′,5,5′-tetramethylbenzidine			402
Pt/ZrO_2-GA-MOF-5	MOF-5	GO	formaldehyde		% conversion: 100% at 100 °C	400
GO/HKUST-1	HKUST-1	GO	phenol		% conversion: 99% in 30 min	401
3D Cu/rGO/PDS	Cu-BTC	rGO	2,4-dichlorophenol		% conversion: 98.5% in 120 min	399

graphene@MOF hybrid	MOF	form of graphene	name of reactant	application	performance	ref
UiO66@rGO-Pd	UiO66	rGO	nitroaromatic compounds	reduction	% yield: 86−98% at 25 °C	384
rGO@Fe_3O_4@MIL-100/Au	MIL-100	rGO	4-nitrophenol		% conversion: ∼100%	392
Cu/Cu_2O@C-rGO	HKUST-1	rGO	4-nitrophenol		% conversion: 100% in 90 s	240
Pt@UiO-66@GO and Pt@UiO-66@rGO	UiO-66	GO and rGO	nitrophenol and nitrobenzene			393

graphene@MOF hybrid	MOF	form of graphene	name of reactant	other applications	performance	ref
Pd/PRGO/Ce-MOF	Ce-MOF	partially reduced graphene oxide (PRGO)	vanillin	hydrodeoxygenation	% conversion: 100% at 100 °C in 240 min	385
Cu_2O-rGO	Cu(BDC-NH_2)	rGO	C(sp^2)−H bond (benzene)	hydroxylation	% conversion: ∼24% (benzene)	406
GO@MOF-5	MOF-5	GO	ammonium perchlorate	degradation	% degradation: 100% at ∼322 °C	409
ZIF-8/rGO hydrogel	ZIF-8	rGO	cellulose		% degradation and yield: 100% and 94%	410
Pd/UiO-66@SGO	UiO-66	sulfonated graphene oxide (SGO)	glucose and fructose	synthesis of 2,5-dimethylfuran	% yield: 70.5 mol % (fructose), 45.3 mol % (glucose) in 3 h	403
Cu-Pd/UiO-66(NH_2)@SGO	UiO-66-NH_2	SGO	sucrose, cellobiose, starch, and cellulose		% yield: 73.4% in 3 h	410
ZIF-8@SO_3H-GO	ZIF-8	GO	1,3-cyclohexane-dione and α,β-unsaturated aldehydes	[3 + 3] formal cycloaddition	% conversion: 94% in 24 h	405
Cu/Cu_2O NPs@GR	Cu(bdc)$_2$	rGO	phenylacetylene with iodobenzene	Sonogashira cross-coupling	% yield: 91% in 8 h	404
Pd@MIL-101@SGO	MIL-101	SGO	styrene	epoxidation and hydroxymethoxylation	% yield: 38.05% and ∼100% for epoxidation and hydroxymethoxylation	411
MIL-101-GH-TS-1	MIL-101	GO	olefins	epoxidation	% yield: 15% in 12 h at 60 °C	412
lys@GO/ZIF, lys@GO/CaBDC	ZIF-8 and CaBDC	GO	*Micrococcus lysodeikticus* cell	bacterial cell degradation		408
Cyt c@ZIF-8/GO	ZIF-8	GO	hydrogen peroxide	degradation	% conversion: 100%	407

[a]TOF = Turn over frequency.

SMX over time in the presence of various catalysts, revealing that the FeCo-*x*/N-rGO/PMS catalyst with an Fe^{3+}/Co^{2+} molar ratio of $x = 4$ had the highest activity. To further improve the performance of FeCo-*x*/N-rGO catalysts and enable their real-time use, a FeCo-*x*/N-rGO and graphitic carbon nitride (g-CN)-based membrane was prepared using a polydopamine-modified poly(vinylidene fluoride) (PVDF) membrane support. The resulting hybrid membrane (FeCoS-4@NGC) showed self-cleaning behavior, which was evaluated by measuring its methylene blue (MB) removal efficiency. As shown in Figure 25f, the cyclic MB removal efficiency of FeCoS-4@NGC increased from the first cycle to the fifth cycle while the flux of the aqueous MB solution through the membrane decreased. This was attributed to the accumulation of MB on the surface of the FeCoS-4@NGC membrane, which caused it to gradually take on a blue color. The SMX degradation efficiency of the FeCoS-4@NGC membrane increased from ∼8% to 92% (60 min) upon introducing PMS into the system. Adding PMS also

https://doi.org/10.1021/acs.chemrev.2c00270
Chem. Rev. 2022, 122, 17241−17338

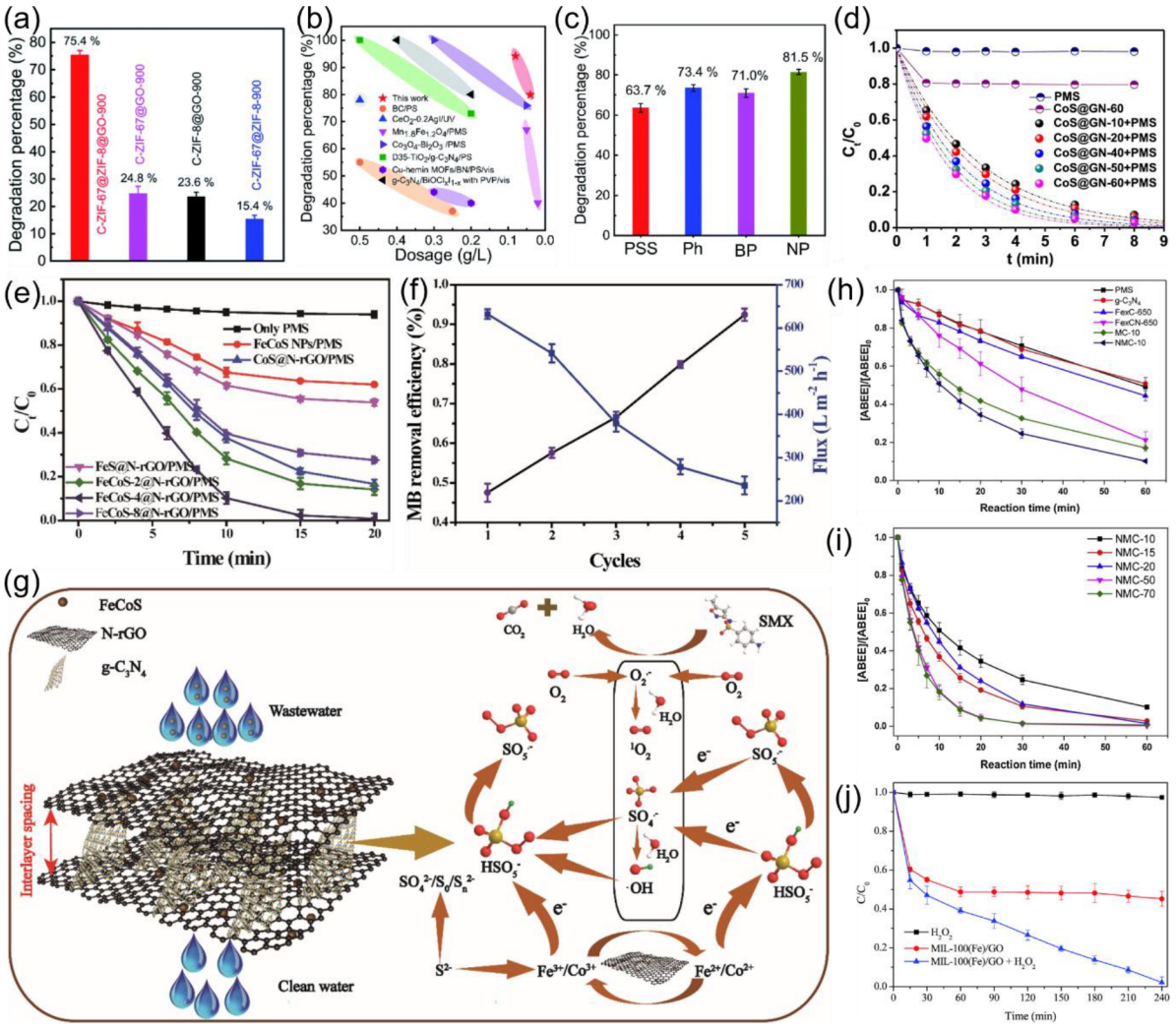

Figure 25. (a) Rates of bisphenol A degradation by different catalysts over 40 min. (b) Bisphenol A degradation rates of C-ZIF-67@ZIF-8@GO-900 and other Fenton-like catalysts at various catalyst loadings. (c) Degradation rates of different pollutants over 50 min when using the C-ZIF-67@ZIF-8@GO-900 catalyst. Reproduced with permission from ref 391. Copyright 2020 Royal Society of Chemistry. (d) Bisphenol A removal activity of different catalysts. Reproduced with permission from ref 389. Copyright 2019 Elsevier. (e) Degradative sulfamethoxazole (SMX) removal activity of various catalysts. (f) Methylene blue (MB) removal performance and permeation flux of the FeCoS@NGC membrane. (g) Illustrative representation of the self-cleaning activity of FeCoS@NGC membrane and the activation of peroxymonosulfate (PMS) for SMX degradation. Reproduced with permission from ref 387. Copyright 2021 Elsevier. (h) Variation in the 4-aminobenzoic acid ethyl ether (ABEE) removal efficiency of various catalysts over time. (i) ABEE degradation curves of NMC catalysts with different g-C_3N_4 contents. Reproduced with permission from ref 386. Copyright 2019 Elsevier. (j) methyl orange degradation curves observed under various catalytic systems. Reproduced with permission from ref 390. Copyright 2017 Royal Society of Chemistry.

caused the removal of the MB layers on the membrane's surface and thus restored the flux through the membrane, confirming that PMS increases the catalytic performance of FeCoS-4@NGC. The membrane showed good cycling performance, achieving >90% SMX removal in 20 min even during the fifth cycle. Importantly, only minor quantities of Fe and Co leached from the catalytic membrane, indicating that it should retain catalytic activity during prolonged use; the total leached concentrations of Co and Fe were 0.086−0.168 and 0.122−0.234 mg/L, respectively. The mechanism of SMX degradation by the FeCoS-4@NGC membrane is shown in Figure 25g, which also illustrates the membrane's self-cleaning activity and the involvement of both ROS and sulfur-based species in the degradation of SMX to CO_2 and H_2O.

Pharmaceuticals and waste from the pharmaceutical industry are also known environmental hazards, so their removal is of prime importance. To this end, Liu and co-workers synthesized Fe@N-doped graphene-like carbon (NMC-*x*, where *x* is the wt % of g-C_3N_4 which could be 10%, 15%, 20%, 50%, or 70%) by subjecting g-C_3N_4 and the precursors of the MOF NH_2-MIL-53(Fe) ($FeCl_3 \cdot 6H_2O$ and NH_2-bdc) to an in-situ solvothermal process followed by carbonization of the resultant hybrid at 650 °C in a tube furnace.[386] For comparative purposes, control catalysts without bdc (MC-*x*) or g-C_3N_4 (FexCN-650) or with NH_2-bdc but without g-C_3N_4 (FexC-650) were also prepared. The catalytic activity of the synthesized hybrids was evaluated by studying its ability to degrade SMX and 4-aminobenzoic acid ethyl ester (ABEE) following PMS activation. Figure 25h shows that the maximum degradation of ABEE was achieved with NMC-10. The content of g-C_3N_4 in the synthesized hybrid was found to affect its catalytic activity, so ABEE degradation was studied with NMC having different contents of g-C_3N_4. This revealed that activity was highest for NMC containing 50 wt % of g-C_3N_4 (Figure 25i). SMX degradation using NMC was also

https://doi.org/10.1021/acs.chemrev.2c00270
Chem. Rev. 2022, 122, 17241−17338

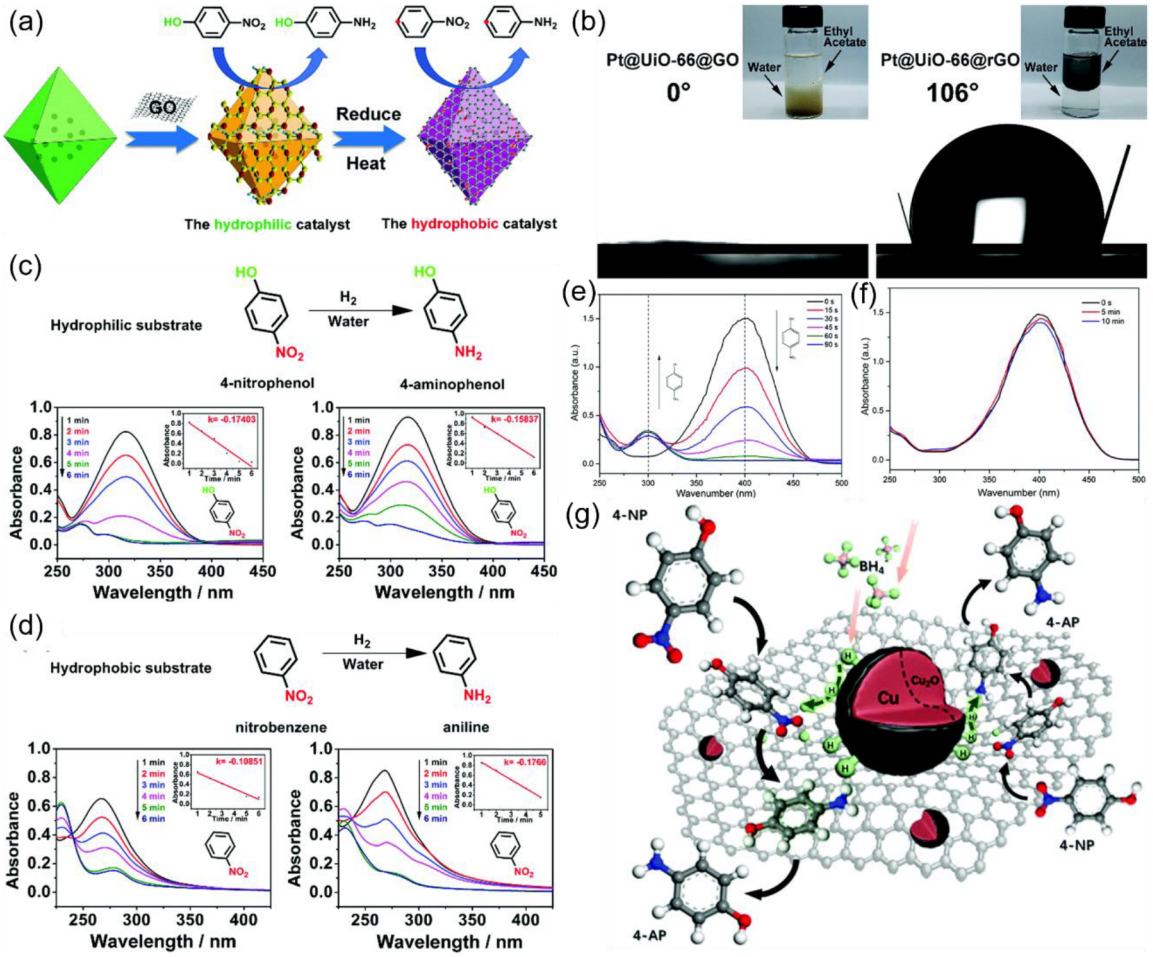

Figure 26. (a) Synthesis of hydrophilic and hydrophobic Pt@UiO-66@GO/rGO composites for the selective reduction of *p*-nitrophenol and nitrobenzene. (b) Water contact angles of Pt@UiO-66@GO and Pt@UiO-66@rGO, and optical images showing the hydrophilic nature of Pt@UiO-66@GO and the hydrophobic nature of Pt@UiO-66@rGO. UV−vis spectra for (c) *p*-nitrophenol reduction and (d) nitrobenzene by (left) Pt@UiO-66@GO and (right) Pt@UiO-66@GO. (Insets) Rate constants for the different reactions catalyzed by each catalyst. Reproduced with permission from ref 393. Copyright 2018 Royal Society of Chemistry. UV−vis spectra of a pure 4-nitrophenol solution and its conversion to 4-aminophenol in the presence of (e) the Cu/Cu_2O@C-rGO composite and (f) the same catalyst without Cu. (g) Mechanistic pathway for the reduction of 4-nitrophenol to 4-aminophenol by the Cu/Cu_2O@C-rGO catalyst. Reproduced with permission from ref 240. Copyright 2018 Royal Society of Chemistry.

tested; in these experiments, degradation products of both SMX and ABEE were detected in the product stream. SMX and ABEE degradation was shown to occur via PMS activation and involved $^1O_2$ and radical species such as $SO_4^{\bullet-}$ and $^\bullet$OH. The degradation efficiencies of NMC-50 for SMX and ABEE in the presence of PMS over 60 min were 87.37% and 100%, respectively. The degradation of SMX is lower than that achieved with the previously discussed FeCoS-4@NGC catalyst, but NMC-50 removed ABEE as well as SMX, which is a major advantage. The degradation activity of NMC-*x* decreased after each cycle, which was attributed to iron leaching into the reaction mixture. The concentrations of leached Fe^{3+} and Fe^{2+} ions were found to be 1.89 and 0.19 mg/L, respectively, and the total leached iron amounted to 12.8% of the catalyst's initial iron content. However, the amount of leached iron was lower than that reported for Fe_xCo_y nanocages, Fe@N-doped carbon, and Fe@porous carbon, indicating that NMC-*x* represents a notable advance in catalyst durability. Dyes are other important water pollutants, so Tang et al. designed the MIL-100(Fe)/GO catalyst for their degradation.[390] The MIL-100(Fe)/GO hybrid was synthesized by a hydrothermal process and was shown to degrade methyl orange (MO) via a Fenton-type mechanism. The catalyst showed high performance in MO degradation in the presence of H_2O_2, which served as a source of OH$^\bullet$ radicals (the main active species in the reaction), as shown in Figure 25j. The degradation process took 240 min for completion when using 3−5 g L^{-1} of the catalyst. Although MIL-100(Fe)/GO was a good heterogeneous catalyst, it showed some leaching of iron into the reaction mixture, which reduced its lifetime. The amount of leached iron increases with the number of cycles, but the catalyst's performance did not change much over the first three cycles. However, given the apparent rate of leaching, this catalyst seems to require further optimization.

5.2.1.2. Reduction of Nitroaromatic Compounds. Nitroaromatic compounds are nonbiodegradable and toxic chemicals that pollute waterways and the environment while also causing diseases including cancer in humans.[384] Graphene@MOF hybrids have therefore been investigated as heterogeneous catalysts for reductively converting nitroaromatic compounds into less harmful products.[240,392,393]

Supported catalysts based on nanoparticles of noble metals have great potential, but their usefulness is limited by the nontailorable features of the support material. Because MOFs have tunable properties, they have been employed as effective

https://doi.org/10.1021/acs.chemrev.2c00270
Chem. Rev. 2022, 122, 17241−17338

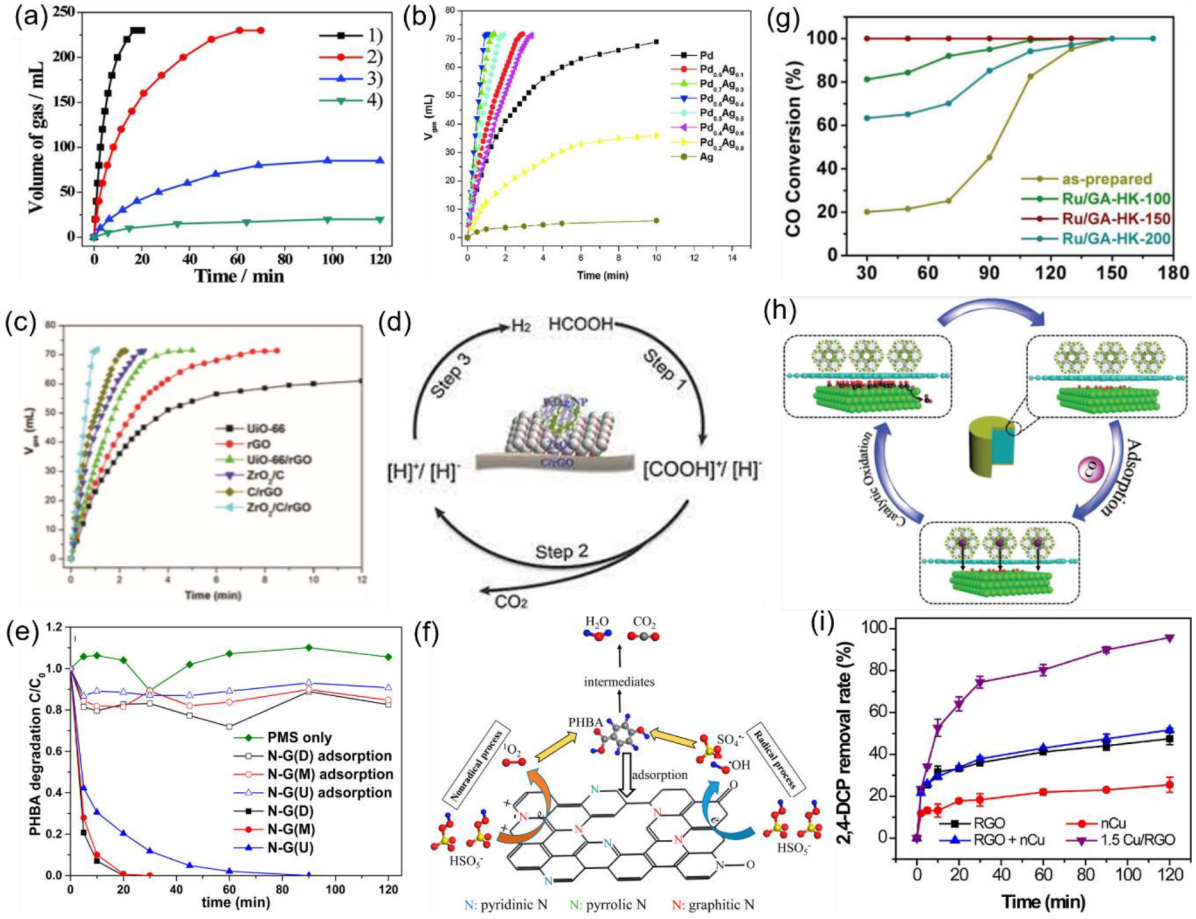

Figure 27. (a) Volumes of hydrogen gas generated over time at 298 K by formic acid dehydrogenation catalyzed by (1) AuPd−MnO_x/ZIF-8-rGO, (2) AuPd−MnO_x/rGO, (3) free AuPd−MnO_x nanoparticles, and (4) AuPd−MnO_x/ZIF-8. Reproduced with permission from ref 395. Copyright 2015 John Wiley & Sons, Inc. Mixed gas (H_2 + CO_2) evolution volume curves obtained at different time points at 323 K (b) in the presence of Pd_xAg_{1-x}@ZrO_2/C/rGO catalysts ($0 \leq x \leq 1.0$) and (c) in the presence of catalysts containing $Pd_{0.6}Ag_{0.4}$ nanoparticles and different supports. (d) Schematic depiction of the mechanism of formic acid dehydrogenation catalyzed by $Pt_{0.6}Ni_{0.4}ZrO_2$/C/rGO. Reproduced with permission from ref 394. Copyright 2018 John Wiley & Sons, Inc. (e) Degradative removal of *p*-hydroxybenzoic acid (PHBA) over various catalysts. (f) Illustrative representation of PHBA degradation to H_2O and CO_2 over N-doped graphene. Reproduced with permission from ref 397. Copyright 2017 American Chemical Society. (g) CO oxidation at different reaction temperatures in the presence of Ru/GA-HK catalysts synthesized at different temperatures. (h) Mechanism of CO oxidation over Ru/GA-HK catalysts. Reproduced with permission from ref 398. Copyright 2018 John Wiley & Sons, Inc. (i) Removal of 2,4-dichlorophenol (2,4-DCP) by peroxydisulfate (PDS) with different catalytic systems over time. Reproduced with permission from ref 399. Copyright 2021 Elsevier.

alternative supporting materials.[384] However, the performance of these catalysts is limited by the instability of MOFs and the difficulty of catalyst regeneration. Liu et al. therefore investigated noble-metal catalysts supported on hybrids of MOFs with rGO.[384] A UiO-66@rGO-Pd hybrid for the reduction of various nitroaromatic compounds was prepared by a two-step hydrothermal process. The synergistic interactions between this hybrid's components made it a very active catalyst for the reduction of nitroaromatics, giving moderate to high reduction product yields (86−98%) with a wide range of substrates. A similar study was reported by Chen et al., who also prepared a composite hybrid for the reduction of nitroarenes (specifically nitrophenol and nitrobenzene) using the same MOF but with Pt nanoparticles instead of Pd.[393] The surface wettability of this hybrid catalyst was controlled by covering the MOF surface with either GO (for hydrophilicity) or rGO (for hydrophobicity). In this way, the hybrid catalyst's selectivity could be tuned to favor the reduction of either hydrophilic (4-nitrophenol) or hydrophobic (nitrobenzene) nitroarenes. Figure 26a shows the preparation of GO- and rGO-coated Pt@UiO-66 hybrid MOFs and their capacity to selectively reduce hydrophilic and hydrophobic reactants. Their selectivity is due to the fact that Pt@UiO-66@GO/rGO is a core−shell hybrid with a UiO-66 core and GO or rGO acting as the outer shell of the composite. GO is enriched with polar functional groups such as −OH and −COOH, so Pt@UiO-66@GO is hydrophilic and effectively reduces hydrophilic reactants. The reduction of GO reduces its hydrophilicity, so the Pt@UiO-66@rGO selectively reduces hydrophobic reactants. The results of wettability studies on Pt@UiO-66@GO/rGO are presented in Figure 26b, which shows the water contact angles (WCAs) of both hybrid catalysts. The catalyst with GO is hydrophilic (WCA = 0°) and dissolves ethyl acetate in water to some extent. Conversely, Pt@UiO-66@rGO is hydrophobic (WCA = 106°) and completely separates ethyl acetate from water, as shown in Figure 26c. The catalytic hydrogenation of 4-nitrophenol and nitrophenol with Pt@UiO-66@GO/rGO was also studied by UV−vis spectroscopy, giving the results shown in Figure 26d. This revealed that the rate of 4-nitrophenol reduction with Pt@UiO-66@GO exceeds that of nitrobenzene, whereas the opposite is true for Pt@UiO-66@

https://doi.org/10.1021/acs.chemrev.2c00270
Chem. Rev. 2022, 122, 17241−17338

rGO. The rate constants of these reduction processes (inset of Figure 26d) explain their observed kinetics.

Catalysts derived from graphene@MOF hybrids have also been used for the reduction of nitroaromatic compounds. For example, a recent publication reported the design of a Cu/Cu_2O@C core−shell hybrid anchored to a rGO surface (Cu/Cu_2O@C-rGO), which was obtained by carbonizing HKUST-1/GO at 500 °C under nitrogen.[240] The performance of this catalyst in the reduction of 4-nitrophenol to the corresponding aminophenol was investigated, revealing that its activity was sufficient to bring the reduction to 100% completion in 90 s. Analysis of the reduction process by UV−vis spectroscopy showed that the presence of the reducing agent $NaBH_4$ without the substrate did not cause any color change or shift in the intensity or position of the observed signals in the UV spectrum of the substrate even after 3 h. However, upon adding Cu/Cu_2O@C-rGO, the 4-nitrophenol signal at 400 nm disappeared and a 4-aminophenol signal at 298 nm appeared within 90 s, as shown in Figure 26e. The main active species in this reduction process were Cu/Cu_2O nanoparticles because treatment of the Cu/Cu_2O@C-rGO catalyst with nitric acid (which would convert the nanoparticles to bulk copper) greatly reduced its catalytic activity (see Figure 26f). In addition, the HKUST-1 derivative (which contains Cu in an agglomerated form) was unable to completely reduce 4-nitrophenol even in 10 min, confirming that the Cu nanoparticles were responsible for the observed activity. A mechanistic study of the reduction process (see Figure 26g) showed that a hydride transfer from Cu/Cu_2O@C-rGO to 4-nitrophenol was responsible for its conversion to 4-aminophenol. Briefly, 4-nitrophenol binds to rGO via $\pi-\pi$ interactions, while the interaction of BH_4^- with the Cu/Cu_2O core forms a hydride complex. The conductivity of rGO then facilitates hydride transfer from the Cu/Cu_2O core to 4-nitrophenol molecules bound to the rGO surface.

5.2.1.3. Hydrogen Evolution. Hydrogen gas is a versatile energy carrier whose stored energy can be released via a number of useful processes, one of which is the production of electricity using polymer electrolyte membrane fuel cells.[394] The industrial-scale production of hydrogen may thus play a vital role in meeting society's energy requirements in the future. Dehydrogenation is a useful process that allows hydrogen to be released from organic chemicals known as liquid hydrogen carriers, which include methanol and other hydrogen-rich small molecules. Graphene@MOF hybrids have recently been used to catalyze the dehydrogenation of various liquid hydrogen carriers including hydrous hydrazine and formic acid.[394−396]

Yan et al. developed a strategy for room-temperature hydrogen production by formic acid dehydrogenation.[395] For this purpose, an AuPd−MnO_x/ZIF-8-rGO hybrid was synthesized by a wet chemical method in which ZIF-8-rGO acted as a biphasic support for AuPd−MnO_x, which was the main active species responsible for the composite's catalytic activity. The ZIF-8-rGO support is very important for the hybrid's stability and activity because the confining effect of ZIF-8 controls the size of the metal nanoparticles and prevents their agglomeration, while rGO alters the electronic structure of the metal nanoparticles and thereby increases their catalytic activity. The activity of the composite in hydrogen production by dehydrogenation of formic acid (FA) was enhanced by the combined effects of the ultrasmall size of the Pd nanoparticles, the modification of their electronic structure resulting from their interactions with rGO (which were confirmed by XPS studies), their uniform distribution within the composite, and the strong interaction between the biphasic support and AuPd−MnO_x. Each component of the AuPd−MnO_x/ZIF-8-rGO hybrid catalyst thus made a distinct contribution to its high overall catalytic activity. This is demonstrated by the results presented in Figure 27a, which shows the volume of hydrogen obtained in FA dehydrogenation reactions catalyzed by AuPd−MnO_x/ZIF-8-rGO and variants of this catalyst lacking one component. The reactions were conducted at 298 K with no additive. Under these conditions, the highest volume of hydrogen (230 mL) and the highest conversion of formic acid (94% in 16.7 min) were achieved using AuPd−MnO_x/ZIF-8-rGO. The catalyst's turnover frequency (TOF) in this process was 382.1 mol H_2 mol_{cat}^{-1} h^{-1}, exceeding the TOFs of other heterogeneous catalysts in FA dehydrogenation reactions under comparable conditions. Gas chromatographic analyses showed that CO_2 was the only gaseous product other than H_2; no CO was detected in the synthesized gas mixture. Moreover, the catalyst was stable for three cycles, indicating that it is quite robust.

Some time thereafter, Song et al. conducted further studies on hydrogen production by FA dehydrogenation using a catalyst support derived from a graphene@MOF hybrid.[394] The catalyst in this case contained Pd and Ag nanoparticles, which were loaded onto a ZrO_2/C/rGO support formed by heat treatment of a UiO-66/GO hybrid. The ZrO_2/C/rGO support ensured a uniform dispersion of the loaded nanoparticles and improved the overall catalytic activity of the composite hybrid. Because of the synergistic interactions between the metal nanoparticles and the ZrO_2/C/rGO support, the hybrid catalyst had a high TOF of 4500 h^{-1} for FA dehydrogenation at 333 K. To optimize the catalyst's composition, the molar ratio of the Pd/Ag nanoparticles and the mass ratio of UiO-66 to GO were optimized. Since the total nanoparticle content of the catalyst was kept constant at 1 M, the hybrids studied in the optimization process were designated Pd_xAg_{1-x}@ZrO_2/C/rGO, where $0 \le x \le 1.0$. The optimal value of x was found to be 0.6, and the catalytic activity was highest when the mass ratio of UiO-66 to GO was 10%. The influence of the supporting material on the hybrid catalyst's activity was investigated by measuring the volumes of H_2 and CO_2 produced by hybrid catalysts containing the same nanoparticle mixture ($Pd_{0.6}A_{g0.4}$) but different supports, as shown in Figure 27b. The $Pd_{0.6}Ag_{0.4}ZrO_2$/C/rGO catalyst had the highest catalytic activity and produced the largest volume of gas (70 mL) in these experiments. As in the systems studied by Yan et al., the support affected the electronic structure of the nanoparticles and thereby influenced the hybrid catalyst's activity. Specifically, a catalyst variant without ZrO_2 was less active than the catalyst with ZrO_2 (see Figure 27c), indicating that ZrO_2 altered the electronic structure of the Pd and Ag nanoparticles. The mechanism of hydrogen evolution by $Pd_{0.6}Ag_{0.4}ZrO_2$/C/rGO is presented in Figure 27d. In the first step, FA binds to the PdAg nanoparticles to form PdAg−formate. CO_2 is then released from this intermediate via β-hydride elimination. The Pd-hydride species forming during this process transfers hydride to H^+, releasing hydrogen. The $Pd_{0.6}Ag_{0.4}ZrO_2$/C/rGO catalyst is less active than AuPd−MnO_x/ZIF-8-rGO in terms of the volume of gas produced but is more durable because it could be used for five cycles without severe loss of activity rather than three.

The Song research group also recently demonstrated that hydrous hydrazine is a suitable substrate for dehydrogenative hydrogen evolution.[396] The catalyst designed for this process was similar to PdAgZrO_2/C/rGO but featured PtNi nanoparticles dispersed over a ZrO_2/C/rGO support rather than

https://doi.org/10.1021/acs.chemrev.2c00270
Chem. Rev. 2022, 122, 17241−17338

PdAg nanoparticles. Its synthesis was very similar to that of $PdAgZrO_2/C/rGO$. In addition, like the $PtNiZrO_2/C/rGO$ hybrid, its activity depended on its relative content of Pt and Ni nanoparticles; a hybrid catalyst with a Pt:Ni ratio of 3:2 gave the highest TOF ($1920\ h^{-1}$ at 323 K). This value is less than one-half of the TOF observed for $Pd_{0.6}Ag_{0.4}ZrO_2/C/rGO$ at 333 K. The dehydrogenation of hydrazine (N_2H_4) generates a mixture of H_2 and N_2 $[2n(H_2) + n(N_2)]$, so the support's effect on the catalytic activity was evaluated by measuring the molar ratio of the H_2 + N_2 mixture to N_2H_4. As in the case of the PdAg system, the activity of the PtNi hybrid was highest when using $ZrO_2/C/rGO$ as the support because the $[n(H_2) + n(N_2)]/[n(N_2H_4)]$ ratio was highest for the $Pt_{0.6}Ni_{0.4}ZrO_2/C/rGO$ catalyst. Once again, ZrO_2 altered the electronic structure of the nanoparticles; hybrid catalysts without ZrO_2 exhibited low activity. Other factors contributing to the high performance of the $Pt_{0.6}Ni_{0.4}ZrO_2/C/rGO$ catalyst were the ultrasmall size of the PtNi nanoparticles, their strong coupling with ZrO_2, and the use of an alkaline medium. Like the $PdAgZrO_2/C/rGO$ catalyst, $Pt_{0.6}Ni_{0.4}ZrO_2/C/rGO$ could be used in five consecutive cycles without appreciable loss of catalytic activity.

5.2.1.4. Oxidative Pollutant Degradation and Chemical Production. Oxidative degradation and conversion are two important pathways for removing pollutants and minimizing environmental, water, and agricultural pollution. In addition, catalytic oxidation reactions are important in the production of various bulk chemicals. Graphene@MOF hybrids have therefore been investigated as potential catalysts for the oxidative degradation of pollutants such as *p*-hydroxybenzoic acid (PHBA), CO, formaldehyde, phenol, and 2,4-dichlorophenol.[397−401] Hybrids of this type have also been used to catalyze the oxidation of benzyl alcohol to the industrially important chemical benzaldehyde.[383]

The catalytic degradation of highly toxic *p*-hydroxybenzoic acid (PHBA) using MOF-derived N-doped graphene was demonstrated by Liang et al.[397] This catalyst was prepared by a one-pot reaction between MIL-100(Fe) and dicyandiamide (DCDA) followed by solvent evaporation and pyrolysis of the resulting composite at 800 °C under nitrogen to obtain N-doped graphene, N-G(D). N-G(U) and N-G(M) were prepared by similar processes using urea and melamine as the nitrogen source, respectively. The oxidative degradation of PHBA was performed using peroxymonosulfate (PMS) activation. Figure 27e shows the activity of these three catalysts for PHBA degradation; almost 100% degradation was achieved using N-G(D), N-G(U), and N-G(M) in 20, 90, and 30 min, respectively. These catalysts were also tested for phenol degradation, which showed the same trend: N-G(D) and N-G(U) were the most and least active catalysts, respectively. The poor catalytic performance of N-G(U) was because it had a lower content of doped nitrogen than the other two catalysts. The carbonyl groups and sp^2 carbon centers within the catalysts were responsible for PMS activation, which released $^{\bullet}OH$ and $SO_4^{\bullet-}$ radicals that were detected by electron paramagnetic resonance (EPR). The intensity of the $SO_4^{\bullet-}$ radicals was less than that of the $^{\bullet}OH$ radicals. Another reactive oxygen species important for PHBA degradation, $^1O_2$, was generated by the doped N atoms. Studies on the mechanism of degradation revealed that PHBA was first converted into dihydroxybenzoic acid, which then underwent aromatic ring opening. The ring-opened products were in turn converted into various carboxylic acids, which were finally degraded into H_2O and CO_2 (see Figure 27f).

The oxidative conversion of CO to CO_2 is an important process for destroying toxic CO gas. Qu and co-workers designed a hybrid catalyst for this reaction by stepwise coating of HKUST-1 on a ruthenium (Ru)-loaded graphene aerogel (Ru/GA).[398] The as-synthesized catalyst (Ru/GA-HK) combines the high CO adsorption capacity of HKUST-1 with the macroporous structure of the graphene aerogel (GA) and is highly active for CO oxidation. The CO adsorption capacity of HKUST-1 strongly increases the catalyst's activity because Ru/GA-HK was 48.4% more catalytically efficient than Ru/GA. Moreover, at same weight hourly space velocity, the % CO conversion of Ru/GA was 0.5% lower than that of Ru/GA-HK, confirming that HKUST-1 greatly improves the catalytic activity of pristine Ru/GA. The effect of the synthesis temperature on the catalytic activity of Ru/GA-HK was also analyzed, as shown in Figure 27g. The most active catalyst was Ru/GA-HK-150, which completely oxidized CO at the low temperature of 30 °C; the other studied catalysts required higher temperatures for complete oxidation. Figure 27h shows the proposed mechanism of the CO oxidation process. Briefly, CO molecules are adsorbed on HKUST-1 from where they diffuse to the graphene surface and get trapped between the graphene layers. The Ru surfaces then convert these molecules to CO_2, which leave the catalyst surface and thus regenerate the catalyst.

A similar system was studied by Tan et al., whose work focused on Pt- and GO-based composite gels coated with MOF-5.[400] Briefly, SBA-15-OH (hydroxyl-modified Santa Barbara Amorphous Type Material-15, mesoporous silica) was used as a template for the synthesis of Pt-supported zirconium oxide (Pt/ZrO_2) by a surface-casting technique. Pt/ZrO_2 was then converted into the Pt/GA aerogel via a self-assembly reaction with GO followed by freeze drying. Finally, Pt/GA was coated with MOF-5 in a stepwise process. Benefiting from the high adsorption capacity of MOF-5 and the mesoporous structure of the graphene aerogel, Pt/ZrO_2-GA-MOF-5 was used for oxidative degradation of formaldehyde (HCHO) in which complete substrate degradation was achieved even at the low temperature of 100 °C. Studies on the relationship between the catalyst's composition and its activity showed that the optimal Pt loading was 7 wt %. Pt/ZrO_2-GA-MOF-5 is also highly stable; after 24 h of continuous use at 100 °C, it retained over 99% of its catalytic efficiency and exhibited no detectable changes in its XRD pattern. The mechanism of CO oxidation involved the generation of reactive O atoms at the Pt centers, which then interacted with formaldehyde adsorbed on the catalyst via hydrogen bonding. This resulted in the formation of dioxymethylene species that were in turn converted into H_2O and CO via formate salt formation. Finally, the obtained CO was oxidized to CO_2 by oxygen. Another report on the oxidative degradation of harmful chemicals was presented by Liu et al., who investigated the role of Cu(III) species in the degradation of 2,4-dichlorophenol (2,4-DCP).[399] A solvothermal reaction between GO, $Cu(NO_3)_2$, and BTC was performed to prepare a hybrid material that was then heat treated at 650 °C under argon gas to obtain the main catalyst, 3D Cu/rGO. Optimization of the content of Cu nanoparticles in this catalyst system revealed that the best-performing catalyst (designated 1.5Cu/rGO) was obtained by reacting 0.1875 g of Cu salt with 0.105 g of BTC. This catalyst achieved a higher 2,4-DCP removal rate than other catalytic systems previously used in this reaction, as shown in Figure 27i. Cu atoms were the main active sites, activating peroxydisulfate (PDS) to release $^{\bullet}OH$ and $SO_4^{\bullet-}$ radicals. Further studies showed that Cu^{3+} was formed during PDS

https://doi.org/10.1021/acs.chemrev.2c00270
Chem. Rev. 2022, 122, 17241−17338

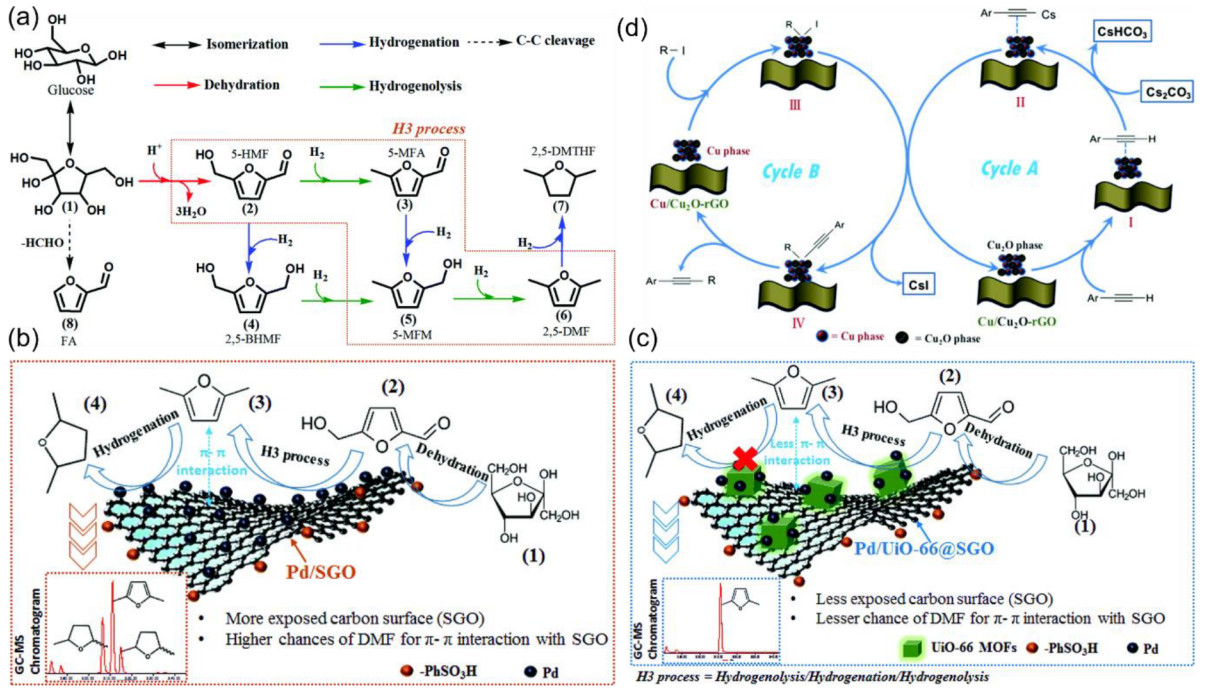

Figure 28. (a) Synthesis of 2,5-dimethylfuran (2,5-DMF) from glucose via the H3 process (hydrogenolysis−hydrogenation−hydrogenolysis) and the interactions of 2,5-DMF with the (b) Pd@SGO and (c) Pd/UiO-66@SGO catalysts. Reproduced with permission from ref 403. Copyright 2017 Royal Society of Chemistry. (d) Illustrative catalytic cycle of the Sonogashira coupling promoted by Cu/Cu_2O-rGO. Reproduced with permission from ref 404. Copyright 2018 Royal Society of Chemistry.

activation and was primarily responsible for the degradation of 2,4-DCP, which occurred via a single-electron-transfer pathway. Studies on the practical utility of the 1.5Cu/rGO catalyst showed that it tolerated the presence of the Cl^- and $H_2PO_4^-$ ions, both of which are commonly present in water, but the HCO_3^- ion reduced its activity. This catalyst could thus be used to treat water samples containing 2,4-DCP in real time.

A recent publication by Ruan et al. showed that graphene@MOF hybrids can exhibit enzyme-like activity.[402] Specifically, a nanoenzyme based on a composite of Fe-MOF (Fe-MIL-88B-NH_2) and GO was prepared. This system was described as a Nanozyme Nest and exhibited peroxidase-like activity that was demonstrated by oxidizing 3,3′,5,5′-tetramethylbenzidine (TMB) to the corresponding diimine. The catalytic reaction proceeded via a Fenton-like mechanism that required the presence of H_2O_2 as an $^{\bullet}OH$ radical source. Importantly, the GO/Fe-MOF catalyst was much more stable under harsh pH and temperature conditions than the enzyme horseradish peroxidase (HRP). The GO/Fe-MOF catalyst also exhibited greater peroxidase-like activity for TMB oxidation than HRP at high H_2O_2 concentrations and was more water stable than Fe-MOF, enabling its long-term use. In addition, its Michaelis constant for TMB oxidation was lower than those of both HRP and Fe-MOF. GO/Fe-MOF thus bound TMB more strongly than either HRP or Fe-MOF, explaining its greater activity.

5.2.1.5. Other Catalytic Applications. The catalytic potential of graphene@MOF hybrids has also been investigated in a wide range of other reactions. However, these remaining reactions have little in common with one another, and each one has only been examined in a few studies. This section focuses on these miscellaneous processes, which include cycloadditions, the degradation of ammonium perchlorate and cellulose, the synthesis of 2-methoxy-4-methyl phenol and 2,5-dimethylfuran, Sonogashira coupling, hydroxylation, hydroxymethoxylation, epoxidation, and biocatalysis.

Cycloaddition reactions are important for the preparation of cyclic and heterocyclic compounds in organic synthesis. Wei et al. presented a report on the catalysis of [3 + 3] formal cycloaddition reactions using a hybrid catalyst based on ZIF-8- and SO_3H-functionalized GO.[405] These reactions involved the formation of pyranyl heterocycles via Knoevenagel-like condensations followed by electrocyclic ring formation. Various catalytic systems were prepared by an in-situ synthetic approach using 50, 100, and 150 mg of GO, yielding samples that were designated ZIF-8@SO_3H-GO-1, ZIF-8@SO_3H-GO-2, and ZIF-8@SO_3H-GO-3, respectively. These hybrids exhibited high catalytic activity in the formal [3 + 3] cycloaddition, which was attributed to their content of SO_3^{2-}, Zn^{2+}, imidazole moieties, and CO_2^- species. Studies on the reaction between 3-methyl-2-butenal and 1,3-cyclohexanedione showed that ZIF-8@SO_3H-GO-2 was the most active catalyst of the three that were prepared, giving a conversion of 94%. The ZIF-8@SO_3H-GO hybrids were almost twice as active as ZIF-8 alone, which was attributed to the formation of mesopores at the interface of GO nanosheets and ZIF-8 nanoparticles. The catalyst also displayed high durability: it showed no appreciable loss of activity after 10 successive cycles. Recognizing the utility of biomass conversion for the synthesis of value-added chemicals and biofuels, Insyani et al. designed a Pt-loaded UiO-66@SGO (SGO = sulfonated graphene oxide) catalyst for the conversion of fructose and glucose into the biofuel 2,5-dimethylfuran (2,5-DMF).[403] The catalyst is prepared by loading Pd onto UiO-66 and adding an ethanolic solution of SGO to the reaction mixture. Fructose is converted into 2,5-DMF via three distinct reactions: dehydration to 5-hydroxymethylfurfural (5-HMF), hydrogenolysis, and finally hydrogenation of 5-HMF. The intermediates produced during these transformations were identified by gas

https://doi.org/10.1021/acs.chemrev.2c00270
Chem. Rev. 2022, 122, 17241−17338

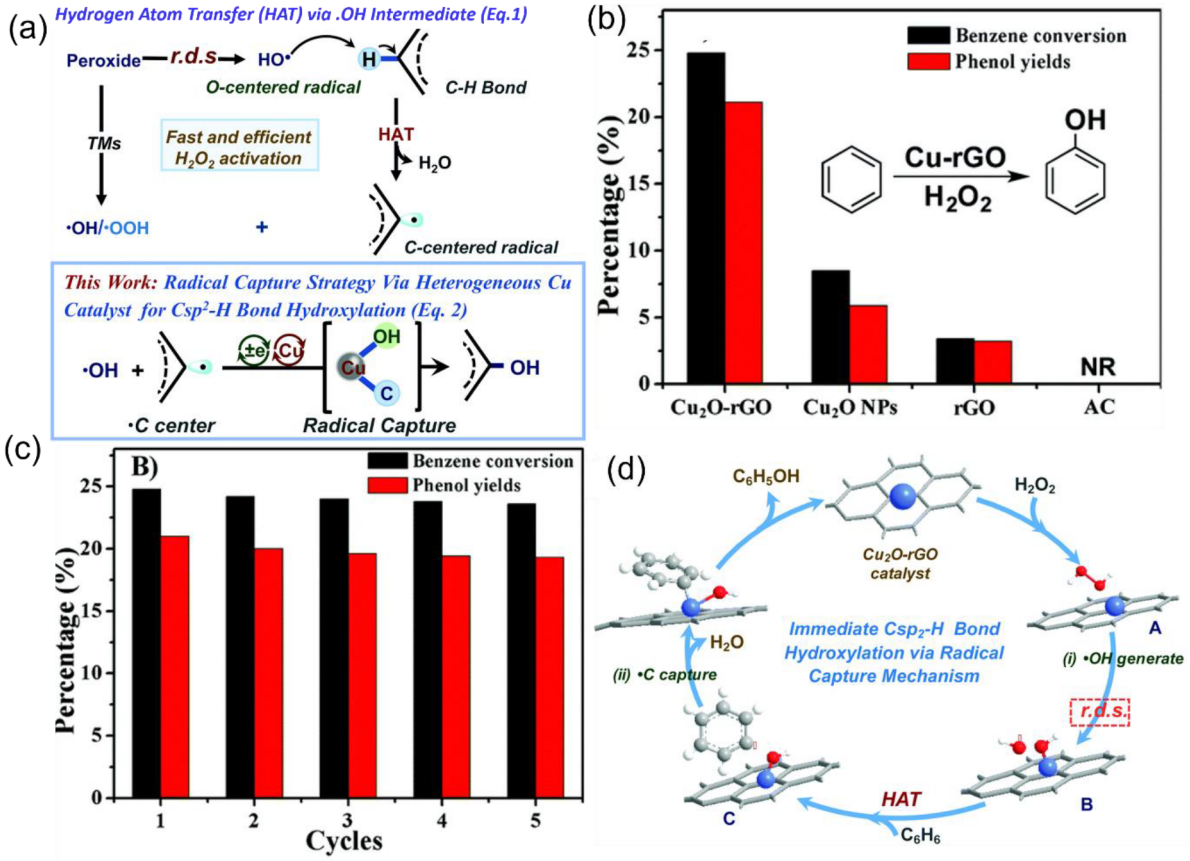

Figure 29. (a) Generation of carbon-centered radicals and their hydroxylation by a radical capture process. (b) Percent conversion of benzene and yield of phenol in the hydroxylation of benzene catalyzed by Cu_2O-rGO. (c) Cyclic performance of the Cu_2O-rGO catalyst in benzene hydroxylation. (d) Catalytic cycle of hydroxylation mediated by Cu_2O-rGO. Reproduced with permission from ref 406. Copyright 2019 Royal Society of Chemistry.

chromatography-time-of-flight mass spectroscopy, which made it possible to propose a mechanism for the overall process that is shown in Figure 28a. Pd can catalyze the hydrogenation of unsaturated bonds, but UiO-66 nanocrystals on the GO surface weaken the $\pi-\pi$ interactions between the 2,5-DMF and the C═C bonds of GO and thus suppress its undesired hydrogenation, as shown in Figure 28b and 28c. The maximum yields of 2,5-DMF were 45.3% from glucose and 70.5% from fructose, which were achieved by allowing the reaction to proceed at 160 °C for 3 h.

Aryl iodides can be cross-coupled with terminal acetylenes via the Sonogashira reaction, which can be catalyzed by a graphene@MOF hybrid. The Cu/Cu_2O-rGO catalyst for this reaction has a MOF-derived jacket structure and was prepared using a strategy involving sequential "take" and "off" steps.[404] The starting material for the synthesis was MOF-2(Cu), in which the copper centers are protected by a "jacket" formed by the organic component of the MOF. The MOF was then combined with GO in a reductive solvothermal process during which interactions between the jacket and the faces of the GO sheets allowed the latter to "take" the MOF onto their surfaces while also being reduced to rGO, leading to the formation of an intermediate composite material designated MOFs-Cu_2O-rGO. Annealing was then performed to take "off" the jacket, and the resulting hybrid (Cu_2O-rGO) was treated with Cu(I) ions and $NaBH_4$ to obtain the final Cu nanoparticle-loaded Cu/Cu_2O-rGO catalyst. This catalyst was highly active in Sonogashira coupling, providing a 91% yield of 1,2-diphenylethyne in the reaction of iodobenzene with phenylacetylene. Its high activity was attributed to reversible oxidation and reduction of Cu species by rGO-facilitated electron transfer between Cu^0 species and Cu_2O (Cu^+) phases. The catalytic cycle of this Sonogashira coupling is presented in Figure 28d, which shows that intermediate I is formed by coordination of the alkyne to Cu_2O. Deprotonation by Cs_2CO_3 then produces intermediate II. In cycle B, the Cu^0 phase reacts with the aryl iodide to form intermediate III, which then reacts with II to form IV. The final product is then formed by a reductive elimination process with concomitant regeneration of the Cu nanoparticles. A similar Cu_2O-rGO catalyst was used by Sun et al. to catalyze the hydroxylation of $C(sp^2)-H$ bonds through a radical capture mechanism.[406] This catalyst was prepared via a solvothermal reaction between MOF-2(Cu)-NH_2 ($Cu_2(NH_2\text{-bdc})_2$) and GO followed by annealing of the resulting MOF-Cu_2O-rGO hybrid at 500 °C under nitrogen. C−H bonds are relatively inert, but they can be activated by •OH radicals, which have a strong tendency for hydrogen-atom abstraction. The generation of •OH radicals is the rate-determining step (rds) of this C−H activation process, which is based on hydrogen transfer to form carbon-centered radicals (Figure 29a). As shown in Figure 29a, the Cu_2O-rGO catalyst converts carbon-centered radicals into hydroxyl compounds by enabling •OH radical attack. The substrate conversion, yield, and cycling performance achieved when using this catalyst in the hydroxylation of benzene are shown in Figure 29b and 29c, and the complete mechanism for the hydroxylation of benzene is shown in Figure 29d. Briefly, the Cu(I) centers of the Cu_2O-rGO catalyst are the main catalytic sites; they are oxidized to Cu(II)−OH by H_2O_2, releasing •OH

https://doi.org/10.1021/acs.chemrev.2c00270
Chem. Rev. 2022, 122, 17241−17338

radicals that then abstract hydrogen atoms from benzene to form carbon-centered radicals that are captured by Cu(II)−OH, forming Ar−Cu(III)−OH adducts that finally undergo reductive elimination to regenerate the catalyst and release the product. The good performance of this catalyst demonstrates the potential of Cu_2O-rGO composites for $C(sp^2)$−H bond oxidation.

Biocatalysis is a relatively new area of application for graphene@MOF hybrids. Enzymes catalyze a very wide range of reactions with high activity and selectivity, but their catalytic potential is limited by their low stability, reusability, and organic solvent tolerance.[407] To overcome these drawbacks, graphene@MOF hybrids have been used as supporting materials for enzyme immobilization. For example, Zhu et al. recently immobilized the enzyme cytochrome c (Cyt c) on a ZIF-8/GO hybrid[407] using an in-situ process involving stirring a methanolic solution of PVP, 2-methylimidazole, $Zn(NO_3)_2 \cdot 6H_2O$, GO, and Cyt c. The enzymatic activity of the resulting Cyt c@ZIF-8/GO catalyst was evaluated by measuring its performance in H_2O_2 decomposition. Optimization of the catalyst preparation parameters revealed that the highest activity was achieved when the enzyme concentration during catalyst preparation was 5 mg/mL and the enzyme was added after stirring the other catalyst components for 7 h. In addition, the rate of H_2O_2 decomposition was highest when the H_2O_2 concentration was 1 mM. The Cyt c@ZIF-8/GO system also suffered no appreciable loss of activity after being stored in buffer for 11 days, which is important because the practical utility of immobilized enzymes depends strongly on their stability. Finally, immobilization in the ZIF-8/GO hybrid enhanced both the enzyme's organic solvent tolerance and its reusability; the immobilized enzyme retained 100% of its catalytic activity after four cycles. In another report, Farmakes et al. immobilized the enzyme T4 lysozyme on the surface of ZIF-8@GO using the same one-pot synthetic strategy.[408] This allowed the enzyme to be immobilized without chemical modification and thus minimized its perturbation, which often reduces the activity of enzymes immobilized through covalent linkages. The catalytic activity of the enzyme immobilized on the graphene@MOF hybrid (lysMOF@GO) was then studied by testing its ability to degrade bacterial cells, which was measured by monitoring the optical density of cells at 450 nm (OD450). This revealed that the activity of lysMOF@GO greatly exceeded that of the same enzyme immobilized on ZIF-8 alone (lys@MOF). In denaturation experiments with urea, sites at both the C terminus (131R1 and 151R1) and the N terminus (44R1) of the immobilized enzyme were unfolded, indicating that both termini are surface exposed. However, the enzyme's long helix (72R1) was largely unaffected by urea treatment, indicating that it was inside the GO/ZIF-8 composite. Interestingly, lysMOF@GO exhibited poor activity at pH < 7. This was ascribed to the low stability of ZIF-8 in acidic media, which caused degradation of its structure and leaching of the encapsulated enzyme. Subsequent experiments showed that the immobilized enzyme performed well in reactions with various large substrates, suggesting that immobilization on graphene@MOF hybrids is a promising general strategy for improving enzymes' activity in biocatalytic applications.

5.2.2. Electrocatalysis. Electrocatalysis has become increasingly important in recent years because of its potential role in the transition from fossil fuels to green energy; it could serve as an enabler for the wider and more efficient exploitation of intermittent energy sources, such as wind or sunlight, by allowing molecules such as N_2 and CO_2 to be converted into valuable chemicals and fuels.[413] Great efforts are therefore being made to identify inexpensive and efficient electrocatalytic materials.

MOFs have several qualities that are advantageous for electrocatalytic applications, including high surface areas, high porosity, and a high density of catalytic sites. Importantly, these properties can be easily tuned by changing the metal ions of the MOF, the linker, or both.[414] However, bulk MOFs are generally not electrically conductive, which precludes their direct use as electrocatalysts. Strategies for overcoming their poor intrinsic electrical conductivity are therefore needed. One such strategy involves using thin 2D MOF nanosheets that allow charge transfer across MOF-modified electrode−electrolyte interfaces.[415,416] Such ultrathin nanosheets can be obtained by mechanical exfoliation.[417,418] Another strategy uses highly conductive catalyst supports, typically carbon materials such as graphene, to construct high-performance hybrid materials.[91] The greatest challenge of using pristine molecular MOFs for electrocatalysis is their instability in high- and low-pH electrolytes. Moreover, there have been few studies on their stability at the high temperatures relevant to practical applications. To circumvent their low intrinsic conductivity and inherent instability in low- and high-pH electrolytes and at high temperature, MOFs have been used as precursors and scaffolds for the fabrication of more stable catalyst materials consisting of highly dispersed catalytic sites embedded in a carbon matrix.[414] Unfortunately, however, this is often achieved at the expense of the MOF's structural integrity. Controlled pyrolysis[250] and electrochemical treatment[419] are among the most commonly used methods of transforming molecular MOFs into more active derivatives. Both MOFs and graphene@MOF hybrids can be used in these processes to fabricate derivatives with high performance in electrocatalytic applications. In particular, metal oxides, metal sulfides, and metal phosphides have shown promising catalytic properties in various important electrocatalytic reactions and can be prepared by heat treatment of MOFs and graphene@MOF hybrids in the presence of a suitable source of the corresponding heteroatom.[89] Another approach involves using MOFs with heteroatom-containing organic linkers as precursors for the preparation of graphene@MOF hybrids and their derivatives.[91] A third powerful strategy for enhancing the catalytic activity of graphene@MOF derivatives is heteroatom doping of their carbon matrices, particularly with P or S, which disrupts the electroneutrality of the matrix and thus causes charge redistribution.[91] A study on oxygen reduction catalyzed by S-doped graphene showed that this can weaken O−O bonds.[420]

The following subsections highlight important advances in the design and use of graphene@MOF hybrids and their derivatives as electrocatalysts for reactions important in electrochemical energy conversion and environmental applications. For further information on the electrochemical applications of graphene@MOF hybrids, we refer the reader to specialized reviews.[87,91,421]

5.2.2.1. Hydrogen Evolution Reaction (HER). Hydrogen is considered the ideal fuel in terms of sustainability because of its high specific energy and the fact that it generates only water as a byproduct when consumed for the production of electricity.[422] It is also an important reagent in the refining and chemical industries, thus demand for hydrogen is increasing continuously.[423] At present, it is mainly produced using methods that rely on fossil fuels and thus emit greenhouse gases. Water

https://doi.org/10.1021/acs.chemrev.2c00270
Chem. Rev. 2022, 122, 17241−17338

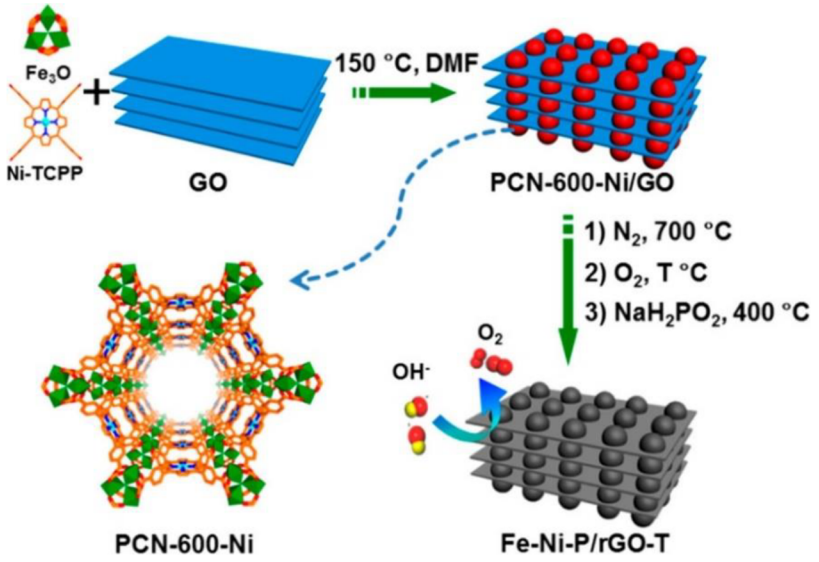

Figure 30. Stepwise fabrication of an Fe−Ni−P/rGO-T composite. Reproduced with permission from ref 443. Copyright 2017 American Chemical Society.

electrolysis, i.e., the electrocatalytic splitting of water into hydrogen and oxygen, would be a more environmentally friendly way of producing this fuel.[424]

Volcano-type plots are commonly used to identify potential metal-based catalysts for the hydrogen evolution reaction (HER), i.e., the cathode reaction during electrochemical water splitting.[425,426] Pt group-based materials are currently the benchmark catalysts for the HER, but their scarcity and prohibitive cost make their large-scale use unattractive. The HER is also catalyzed by a family of enzymes known as hydrogenases, and a range of artificial hydrogenase mimics and analogues have been developed. MOF-based HER catalysts have been designed using these systems as models. This strategy takes advantage of the molecular nature and tunable structure of MOFs. Three different approaches to the design of MOF-based HER catalysts have been explored: (1) mimicking the active sites of natural HER catalysts, (2) optimizing the precious metal loading in MOF-derived composites, and (3) fabricating MOF-derived catalysts based on inexpensive and earth-abundant components.[427] Strategies of the second type have been implemented using a wide variety of precious metal-containing MOF/graphene hybrids,[428] and systems containing Pt,[429] Pd,[430,431] and Ru[432] have all shown good activity in the HER. Strategies of the third kind make use of materials containing nonprecious metals, particularly Ni, Fe, Cu, Mo, and Co, as low-cost HER catalysts. For example, Makhafola et al. synthesized the Cu-based MOF HKUST-1 via a hydrothermal route and combined it with GO by impregnation to obtain a GO/MOF composite that displayed higher HER activity than the same GO-free MOF in acidic media.[433]

Among nonprecious-metal-based derivatives, metal sulfides and phosphides have attracted increasing attention due to their remarkable HER activity, which is generally attributed to high intrinsic activity and corrosion resistance.[91] Xu et al. reported the fabrication of a MOF-74(Co/Ni)-derived $NiCo_2S_4$@$NiCo_2O_4$ deposited onto rGO. The obtained material exhibited remarkable activity and stability during HER in alkaline media, which was attributed to strong synergies between the oxide and the sulfide components, as well as the increased electrical conductivity provided by rGO.[434] Mo-based materials are seen as particularly promising precious-metal-free HER catalysts, and MOF/graphene hybrids containing molybdenum have therefore also been examined as potential HER electrocatalysts. For instance, nanosized MoS_2 was incorporated into a Cu-MOF based hybrid, HKUST-1/rGO,[435] via a solvothermal process, yielding a composite that benefited from the high activity of MoS_2, the high surface area and porosity of the MOF, and the high electrical conductivity of rGO.[436] Similarly, MoP encapsulated in P-doped C nano-octahedrons supported on rGO, fabricated by carbonizing polyoxometalate-based MOFs with subsequent phosphidization, exhibited the advantages of all its different components and achieved excellent HER performance and stability in acidic media.[437]

5.2.2.2. Oxygen Evolution Reaction (OER). During water electrolysis, the cathodic HER is necessarily balanced by a parallel anodic reaction: the oxygen evolution reaction (OER). The OER is currently seen as the main barrier to the development of water electrolysis technologies due to its sluggish kinetics (which reduce the efficiency of the overall process) and the high cost of state-of-the-art precious-metal-based electrode materials.[438] There is thus an urgent need for inexpensive and highly active catalysts that can efficiently drive the OER.

The high porosity and surface area of graphene@MOF hybrids and their derivatives are advantageous in gas-evolving reactions like the OER because they increase the accessibility of catalytic sites and the rate of oxygen diffusion in addition to having high electrical conductivity. Moreover, the possibility of varying the chemical composition and structural characteristics of these composites allows their catalytic properties to be fine tuned.[439] Co- and Ni-containing hybrids have demonstrated particularly promising performance in the OER. For instance, Xie et al. reported a composite consisting of an Ni-based MOF mounted on graphene (3D Gr/Ni-MOF) that exhibited high OER activity after optimization of its synthesis and outperformed the graphene-free Ni-MOF.[440] A strong synergy between graphene and a MOF leading to enhanced OER performance was also demonstrated by Yaqoob et al.,[441] who used a solvothermal route to prepare a Co^{2+} BTC MOF/rGO composite that had an OER overpotential (η_{OER}) of just 290 mV

https://doi.org/10.1021/acs.chemrev.2c00270
Chem. Rev. 2022, 122, 17241−17338

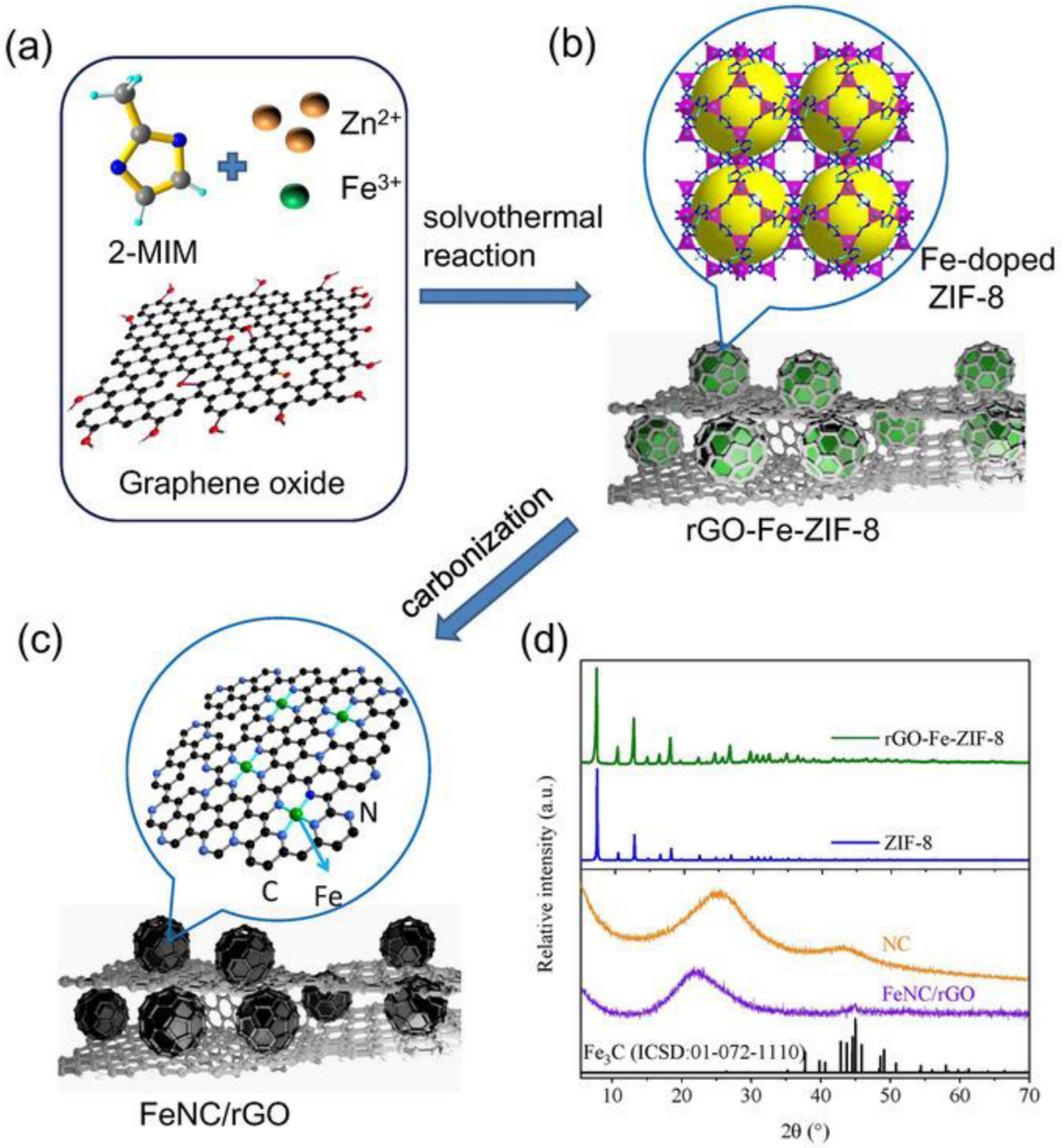

Figure 31. Starting materials, intermediates, and final product in the synthesis of FeNC/rGO: (a) metal ions, linker, and graphene oxide; (b) Fe-doped ZIF-8 (inset: crystallographic structure of ZIF-8); (c) FeNC/rGO (inset: structure of FeNx-doped carbons). (d) PXRD patterns of the precursor rGO-Fe-ZIF-8 (top) and FeNC/rGO (bottom). Reproduced with permission from ref 459. Copyright 2020 John Wiley & Sons, Inc.

at the benchmark current density of 10 mA cm^{-2}. Huang et al.[442] presented another example in which a series of sandwich-like $Co(OH)_2$ nanoarrays was derived from ZIF-67 grown on GO. These composites showed high OER activity, with the most active catalyst in the series achieving a η_{OER} of 259 mV. DFT calculations indicated that synergistic effects between the Co-containing component and GO in this material enhanced its OER performance.

MOF-graphene hybrids containing two or more metals have also shown promising catalytic activity and stability. This is generally ascribed to strong synergistic interactions between the metal components together with synergistic interactions between the metal centers and the graphene derivative. In particular, bimetallic NiFe systems exhibit remarkable OER activity in alkaline media.[444,445] For instance, PBA-derived (PBA = Prussian blue analogue; $Ni[Fe(CN)_6]$) metal NiFe nanocrystals encapsulated in N-doped few-layer graphene, fabricated via a microwave-assisted CVD-like synthesis route, exhibited a η_{OER} of just 261 mV.[446] An even lower η_{OER} of 240 mV was observed for a sheet-like NiFeP/rGO composite fabricated by pyrolysis and phosphidation of a porphyrinic MOF (Figure 30; PCN-600-Ni, $(Fe_3O(OH))_2$Ni-$TCPP_3$ with PCN = porous coordination network)[443] and a lamellar NiFe MIL-53 encapsulated in graphene aerogel-grafted Ni foam.[447] Other bimetallic hybrids have also shown promising OER performance, including CoNi,[448] FeCo,[449] CoCu,[450] and CeCu systems.[451] The exploitation of synergistic interactions between the different components of multimetallic graphene@MOF

https://doi.org/10.1021/acs.chemrev.2c00270
Chem. Rev. 2022, 122, 17241−17338

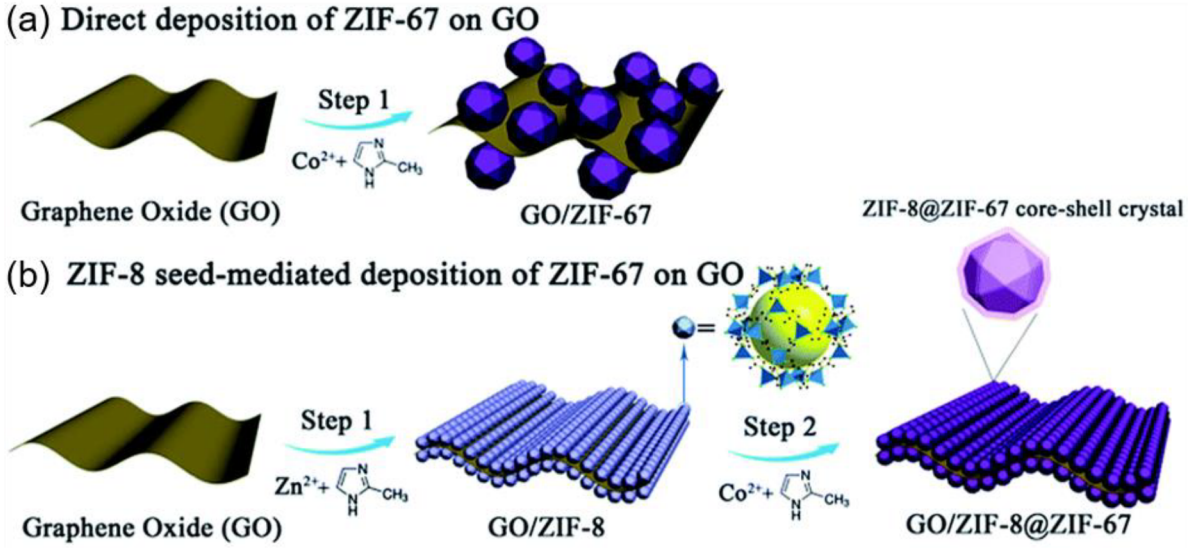

Figure 32. Methods for the synthesis of MOF/GO composites: (a) direct deposition of ZIF-67 on GO sheets; (b) ZIF-8 seed-mediated deposition of ZIF-67 on GO sheets. Reproduced with permission from ref 462. Copyright 2017 Royal Society of Chemistry.

hybrids is thus clearly a powerful strategy for designing high-performance OER catalysts.[452]

5.2.2.3. Oxygen Reduction Reaction (ORR). The oxygen reduction reaction (ORR) is the reverse of the OER and is typically the cathode reaction in fuel cells where oxygen reacts with protons and electrons from the anode to form water and generate electricity. The ORR can proceed via (1) a direct pathway, producing H_2O or OH^- in acidic or alkaline media, respectively, with the transfer of 4 electrons or (2) an indirect pathway, producing peroxide species as intermediates with the transfer of 2 electrons followed by either a second 2-electron-transfer reduction step or chemical disproportionation of the peroxide.[453] The direct pathway is generally preferred due to its higher energy efficiency, so ORR selectivity is an important criterion to consider when evaluating electrocatalysts for this reaction together with their catalytic activity and stability. The fabrication of ORR catalysts using MOFs and graphene as precursors enables control of the hybrid's size, morphology, and composition while providing high electrical conductivity and surface area. In addition, heteroatom-doped carbon-based systems can be obtained through graphene functionalization[454] and/or MOF pyrolysis,[455] offering further possibilities for fine tuning the properties of the composites including their morphology, defect content, electrical conductivity, and catalytic activity in the ORR.[456] Materials containing Fe−N−C and Co−N−C sites have emerged as the most promising noble-metal-free ORR catalysts in terms of activity and selectivity.[457,458] In a work by Lv and co-workers, ions in ZIF-8 were substituted by Fe^{3+} and the resulting bimetallic MOF was modified with GO to obtain a sandwich-like heterostructure.[459] Upon heat treatment, highly active FeNxC moieties embedded in rGO were obtained (Figure 31). The ORR activity of the resulting hybrid was comparable to that of the benchmark catalyst Pt/C (20 wt %) with a half-wave potential ($E_{1/2}$) of 0.88 V vs RHE. The composite also proved to be superior to Pt/C in terms of stability. On the basis of control experiments, the authors ascribed its high performance to synergistic interactions between FeNx sites and graphene. An interesting Fe-containing ORR catalyst was reported by Sohrabi et al., who first modified graphene nanosheets with pyridinium groups and then combined them with the MOF PCN-222 ($Zr_6(\mu_3\text{-}OH)_8(OH)_8(Fe\text{-}TCPP)_2$) via coordination of the pyridine nitrogen centers with the iron centers of the porphyrin units of the Fe-TCPP linker. This yielded a hybrid with high catalytic activity that was partly attributed to fast electron transfer facilitated by the pyridine groups.[460] Other noteworthy Fe-based hybrids for ORR electrocatalysis include a core−shell hybrid comprising Fe/Fe_3C@N-doped C decorated on graphene that has an $E_{1/2}$ value of 0.88 V vs RHE[461] and an assembly consisting of an Fe-porphyrin framework (Fe_2(Fe-TCPP)) and pyridine-functionalized rGO that exhibits remarkable ORR selectivity in favor of the 4-electron-transfer pathway over a wide potential range.[162]

Various Co-based graphene@MOF hybrids have also been reported as catalysts for the ORR.[462−465] An interesting example comprising GO and two MOF structures was prepared by Wei et al.[462] using a synthetic strategy that involved first depositing ZIF-8 seeds on GO to obtain a sandwich-like ZIF-8/GO/ZIF-8 structure and then depositing ZIF-67 crystals on this material to form ZIF-8@ZIF-67 core−shell crystals while preserving the sandwich-like structure. This synthetic strategy proved superior to direct deposition of ZIF-67 on GO (Figure 32) in terms of control over crystal size and uniform distribution of ZIF-67 on GO. Pyrolysis of this core−shell hybrid at 900 °C yielded a composite containing highly ORR-active and well-distributed Co-Nx-C sites that outperformed Pt/C in terms of overpotential and showed preferential selectivity for the direct 4-electron-transfer pathway.[462] Other highly ORR active Co-containing core−shell-type hybrids have also been reported. For instance, Co@CoO nanoparticles supported on N-doped graphene, fabricated by pyrolysis of GO-anchored ZIF-67, exhibited an $E_{1/2}$ value similar to that of Pt/C (40 wt %) for alkaline ORR.[463] In addition, ultrasmall Co nanodots wrapped with 2−5 layers of graphene codoped with Co and N were derived from 2D $Co_xZn_{2-x}(bmim)_4$ to provide a hybrid that showed high activity in both alkaline and neutral media along with high durability and favorable ORR selectivity after optimization.[464]

Combining cobalt and iron into a single composite has proven to be an effective strategy for improving the catalysis of oxygen conversion by various systems[466−468] including graphene@

https://doi.org/10.1021/acs.chemrev.2c00270
Chem. Rev. 2022, 122, 17241−17338

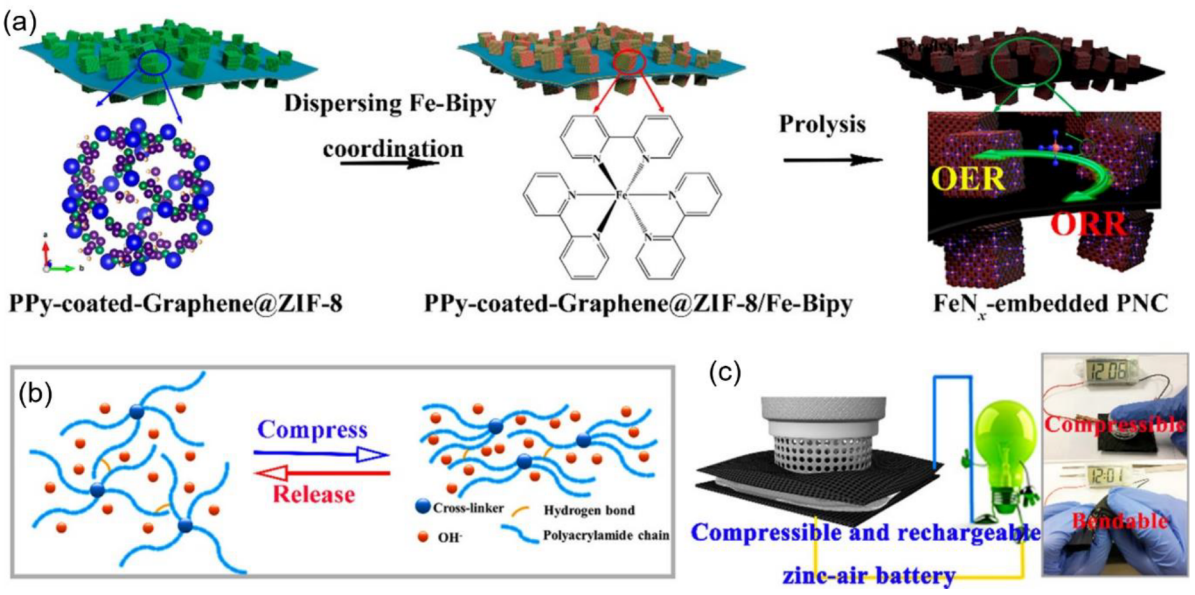

Figure 33. (a) Synthesis of FeN_x embedded in 2D porous nitrogen-doped carbon. Local amplification shows the structure of ZIF-8, coordination of (iron ion)-(2,2-Bipy), and FeN_x dispersed on the porous nitrogen-doped carbon surface. (b) Compressible polyacrylamide hydrogel, and (c) compressible, bendable, rechargeable zinc−air battery. Reproduced with permission from ref 485. Copyright 2018 American Chemical Society.

MOF hybrids. For instance, Li et al. synthesized FeCo-containing N-doped graphene/tubular graphene composites using a cage-containing Co-based MOF, dicyandiamide, and iron acetate as precursors.[469] Pyrolysis of these composites at 1000 °C yielded hybrids whose ORR performance was evaluated in acidic and alkaline media, giving $E_{1/2}$ values of 0.76 and 0.88 V vs RHE, respectively, and outperforming Pt/C in the latter case.

Graphene@MOF-based hybrids containing less commonly used metals such as Cu[160,470] or Zn[471−473] have also been reported as ORR catalysts. For instance, the synthesis of HKUST-1 in the presence of rGO forms a system featuring highly dispersed Cu NPs assembled on the graphene sheets.[160] This Cu/rGO hybrid displays higher activity and more favorable ORR selectivity than its individual components (MOF and rGO), demonstrating a strong synergy between them.[474] In a work by Zhuang et al., ZIF-8 was modified with N-doped graphene by nanoscale high-energy wet ball milling, forming N-G/MOF composites with ORR activity and selectivity comparable to Pt/C.[471] While these results are intriguing, some caution is needed when evaluating the catalytic properties of graphene@MOF hybrids featuring unconventional metals because metal impurities could strongly influence their activity.[475]

5.2.2.4. Bifunctional Electrocatalysis. Bifunctional electrocatalysts (BEs) can promote two different electrocatalytic reactions on decoupled electrodes or a single reversible electrode. Common examples include full water splitting BEs, which exhibit high activity in both the HER (cathode) and the OER (anode), or so-called bifunctional reversible oxygen electrodes (BOEs) that can efficiently drive both the ORR and the OER. BEs provide some important practical advantages: they eliminate the issue of incompatibility between different catalysts that have to be integrated into the same device[476] and may enable economies of scale that reduce the cost of fabricating and using complex electrode materials.[477] BOEs may have applications in regenerative energy conversion systems such as rechargeable metal−air batteries, which require that the OER and the ORR take place at the same electrode during charging and discharging, respectively.[478] The main challenge in the design of BEs is that they must be both highly active and highly stable under the conditions of the two different reactions.[479]

BEs typically contain active sites for the two reactions of interest integrated into a hybrid material that is usually derived from carbon- and/or transition-metal-based components.[478] MOF/graphene-derived catalysts are therefore considered to have outstanding potential in bifunctional electrocatalysis. In particular, high bifunctional performance has been achieved using heteroatom-containing composites that take advantage of synergistic interactions between different types of active centers.[317] For instance, a recent report described the fabrication of bimetallic FeNi-based oxides supported by few-layer N-graphene polyhedrons via pyrolysis of Ni_xFe_{1-x} MOFs with various Ni/Fe ratios. By optimizing the metal composition of these hybrids, a candidate BE for water splitting benefiting from synergistic interactions was obtained.[480] In a work by Jayaramulu et al., a composite consisting of nanoporous N-doped GO and Ni_7S_6 was prepared from a MOF (MOF-74(Ni)) via solvothermal synthesis and identified as a bifunctional HER/OER catalyst whose properties could be tuned by varying the level of N doping.[238] Metal phosphide-based composites derived from graphene/MOF hybrids have also shown remarkable performance as HER/OER catalysts.[89] For example, Bu et al. reported the microwave-assisted thermal conversion of FeNi-based Prussian blue analogues/GO in the presence of NaH_2PO_2 as the phosphorus source to form FeNiP/graphene composites with adjustable heterostructures. One such composite, FeNiP supported on P-doped graphene, showed promising HER/OER performance that benefited strongly from P doping and was proposed as a catalyst for a symmetric water electrolysis cell.[481]

Strong catalytic synergies can also be realized using only trace quantities of one of the synergistic components,[482,483] as recently demonstrated by Parkash: a MOF-derived composite containing graphene-wrapped Pt and Cu nanoparticles exhibited outstanding bifunctional ORR/OER activity despite having a Pt loading of less than 0.5 wt %.[484]

https://doi.org/10.1021/acs.chemrev.2c00270
Chem. Rev. 2022, 122, 17241−17338

Table 6. Activity Descriptors of Bifunctional ORR/OER Catalysts Derived from Heteroatom-Containing MOF/Graphene Hybrids Investigated in KOH Solutions

catalyst	precursors	KOH concentration	E_{OER}/V[a]	$E_{1/2}$/V[b]	ΔE/V[c]	ref
Pt/Cu/NPC-900	Zn-MOF-74; Pt NPs; Cu NPs	0.1 M	1.48	0.89	0.59	484
CuCo/N-rGO	metal nitrates; H_3BTC; GO	0.1 M (ORR) 1.0 M (OER)	1.52	0.86	0.66	488
S-$Co_{9-x}Fe_xS_8$@rGO	CoFe-ZIF; GO	0.1 M	1.52	0.84	0.68	489
N-doped CoC_x/FeCo@C/rGO	Fe-doped $Co_3[Co(CN)_6]_2$; GO	0.1 M	1.62	0.92	0.70	490
GNCNTs-4	ZIF-67; GO	0.1 M (ORR) 1.0 M (OER)	1.58	0.85	0.73	486
N-GC/Co@CoO/rGO	ZIF-67; rGO	0.1 M (ORR) 1.0 M (OER)	1.59	~0.87	~0.73	491
Co_3Fe_7@Fe_2N/rGO	Fe^{3+}- and Co^{2+}-coordinated H_3BTC; rGO	0.1 M	1.60	~0.85	~0.75	332
Fe-MOF@CNTs-G	MIL-53; $(NH_4)_2S_2O_8$; melamine	0.1 M	1.65	0.87	0.78	492
FeN_X-embedded PNC	ZIF-8; PPy-coated graphene	0.1 M	1.64	0.86	0.78	485
i-CoNC@GF	metal nitrates; 2-methylimidazole; GO	0.1 M	1.66	0.87	0.79	493
CoNi-MOF/rGO	TCPP; $M_2(COO)_4$ paddlewheel motif; rGO	0.1 M (ORR) 1.0 M (OER)	1.55	0.73	0.83	494
$Ni_xCo_yO_4$/Co-NG	ZIF-67; GO	0.1 M	1.63	0.80	0.83	495
MnBDC@rGO	Mn benzene-1,4-dicarboxylate; GO	0.1 M (ORR) 1.0 M (OER)	1.84	0.98	0.86	496
Co@N-CNT/rGO	2D ZIF-L; GO	0.1 M	1.69	0.82	0.87	497
CoO@Co3O4/NSG-650	ZIF-67; GO; $Na_2S{\cdot}9H_2O$	0.1 M	1.69	0.79	0.90	487
ZnCo-ZIF@GO	ZIF-67; GO	0.1 M (ORR) 1.0 M (OER)	1.66	0.76	0.90	498

[a]E vs RHE at 10 mA cm^{-2}. [b]Half-wave potential vs RHE. [c]$E_{OER} - E_{1/2}$

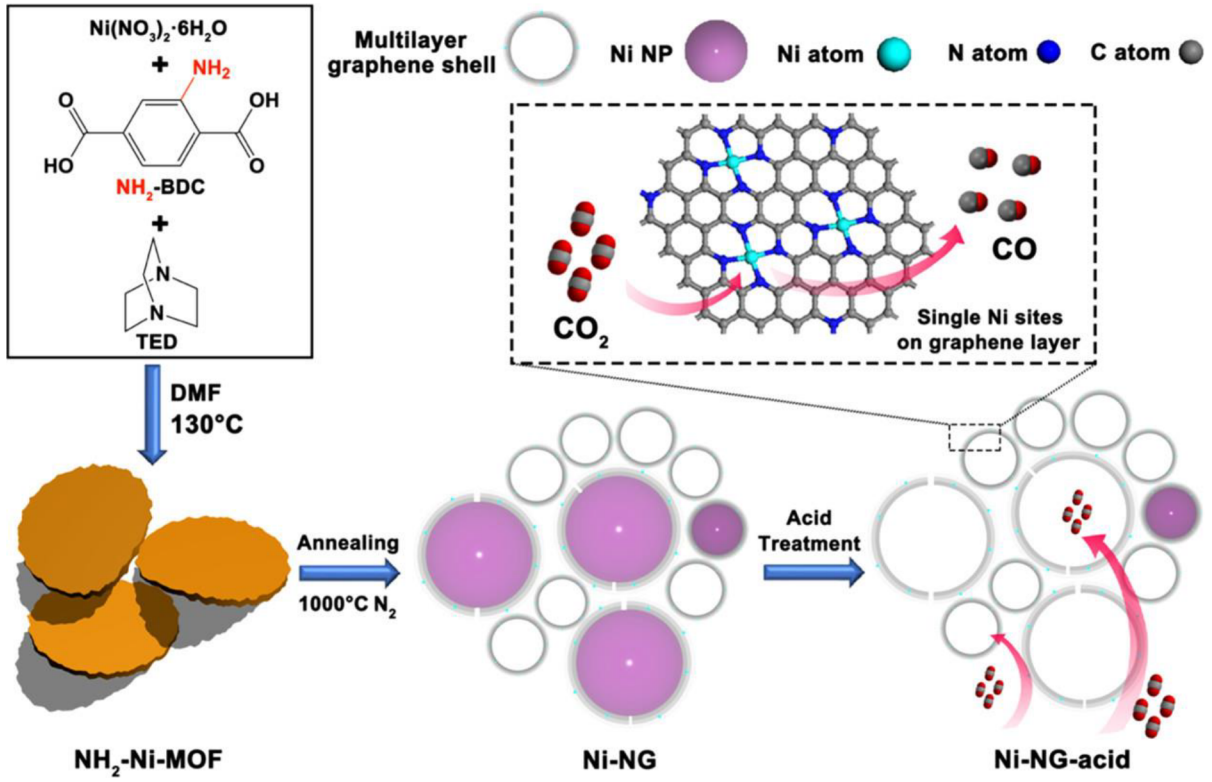

Figure 34. Preparation of Ni-NG-acid. Reproduced with permission from ref 500. Copyright 2021 American Chemical Society.

MOF/graphene-derived materials have attracted great interest in the field of rechargeable air−metal batteries, demonstrating high performance as BOEs for air electrodes. In a study by Xu et al., a 2D N-doped CNTs/graphene hybrid was synthesized by annealing ZIF-67 nanocrystals supported on GO in a reductive atmosphere to obtain a high-performance BOE with good ORR/OER activity and outstanding stability for rechargeable Zn−air battery applications.[486] In the same field, Ma et al. reported the synthesis of FeN_x embedded in highly graphitic 2D porous N-doped carbon using polypyrrole-coated graphene, ZIF-8, and Fe-coordinated 2,2-bipyridine as precursors; the resulting materials were used as bendable high-

https://doi.org/10.1021/acs.chemrev.2c00270
Chem. Rev. 2022, 122, 17241−17338

performance BOEs (Figure 33).[485] The functionalization of graphene with nitrogen and a second heteroatom has also been explored as a strategy to enhance the activity of graphene/MOF derivatives. For instance, $CoO@Co_3O_4$ supported on N,S-codoped graphene was synthesized by growing ZIF-67 in the presence of GO and $Na_2S{\cdot}9H_2O$ followed by carbonization at different temperatures. The obtained derivatives exhibited ORR activity and selectivity comparable to Pt/C, while their OER performance matched that of IrO_2. Their high performance was attributed to the electrical conductivity provided by the graphene derivative as well as the enhancement of ORR and OER activity resulting from the presence of nitrogen and sulfur dopants.[487] Table 6 describes the activity descriptors of bifunctional ORR/OER catalysts derived from heteroatom-containing MOF/graphene hybrids.

The structural and functional flexibility of graphene@MOF hybrids also enables the preparation of multifunctional materials capable of catalyzing three or more reactions. For example, Jahan et al. showed that a hybrid of a Cu-based MOF and GO is a trifunctional catalyst of the HER, OER, and ORR.[163] The authors also demonstrated that the presence of GO in the composite increased its stability in acidic media relative to that of the GO-free MOF.[163] Similarly, cobalt nitride anchored on N-doped graphene aerogel was proposed as a trifunctional HER/OER/ORR catalyst by Zou et al.[499] This composite was fabricated by annealing ZIF-67 under an ammonia atmosphere in the presence of graphene aerogel and was used as a catalyst in a device for self-driven water splitting comprising a water electrolyzer and two Zn−air batteries.[499] These results clearly show that graphene@MOF hybrids have great potential as multifunctional catalysts for diverse electrochemical applications.

5.2.2.5. Electrochemical CO_2 Reduction. The emission of greenhouse gases due to human activities has tremendous negative environmental impact. Consequently, there is an urgent need to curb their emissions and reduce their atmospheric concentrations, particularly in the case of carbon dioxide. The electrocatalytic CO_2 reduction reaction (CO_2RR) is a very attractive way of removing atmospheric CO_2 because it allows this pollutant to be converted into useful fuels and chemicals.[501] However, the conversion involves several electron-transfer steps that occur in competition with less complex reactions that form CO and H_2. Achieving high selectivity for valuable products is thus a major challenge in the development of CO_2RR technologies.[501]

Carbon-based electrocatalysts derived from MOFs have been widely studied for the CO_2RR because it is easy to vary their dopants, metal composition, and textural characteristics.[502] In particular, graphene@MOF hybrids have shown promising capabilities as CO_2RR catalysts. For instance, Ni−N−C sites embedded in multilayer N-doped graphene fabricated by annealing an amino-functionalized Ni-based MOF (Figure 34) demonstrated a Faradaic efficiency above 90% in the conversion of CO_2 to CO at relatively low potentials.[500] A composite with similar active sites was prepared by Pan et al.[503] via thermal decomposition of Ni-doped ZIF-8. The resulting material had Ni−N−C moieties located in the carbon basal plane and at the edges of two layered graphene planes, allowing it to achieve a Faradaic efficiency of 96% for the reduction of CO_2 to CO at an overpotential of 570 mV.

Selective reduction of CO_2 to hydrocarbons has also been achieved using composites based on graphene@MOF hybrids. For example, Zhang et al. reported a composite prepared by vertical growth of ZIF-L on GO nanosheets followed by carbonization in the presence of a Cu precursor. Ethanol was formed with a Faradaic efficiency of 70.52% when this material was used to catalyze the CO_2RR.[504] Similarly, Hwang et al. evaluated the CO_2RR performance of Cu-MOF (H-KUST-1) grown via a hydrothermal method in the presence of GO. The reaction was studied in a range of electrolytes, and formic acid was the main product obtained in all cases. The highest Faradaic efficiency (58%) was achieved using a mixture of tetrabutylammonium bromide and dimethylformamide as the electrolyte.[505]

Although CO_2RR electrocatalysis using graphene@MOF hybrids is a new field of research, interest in this area is expected to increase rapidly because the vast diversity of possible catalyst compositions and properties enables the use of a very wide range of material design strategies.

5.2.2.6. Electrochemical Nitrogen Reduction. Ammonia is an important bulk chemical that is used as a fertilizer, a precursor for the synthesis of N-containing compounds, and an energy carrier. Unfortunately, the Haber−Bosch process by which it is produced industrially generates very high greenhouse gas emissions.[506] Electrocatalytic ammonia production via the nitrogen reduction reaction (NRR) powered by renewable energy could be a more sustainable alternative to the Haber−Bosch process. However, current state-of-the-art NRR catalysts have very low efficiencies, so the development of highly active NRR catalysts that are selective for ammonia formation will be needed to enable energy transition and decarbonization.[507]

Several groups have investigated the use of MOF-based catalysts in the NRR. For example, Cui et al. recently presented DFT studies on a series of 2D MOFs consisting of hexaaminobenzene and various transition metals (Mo, Co, Ni, and Cu). The molybdenum-containing MOF was predicted to have potentially useful electrocatalytic activity with high selectivity for the NRR over the HER.[508] A separate DFT study on 2D MOFs consisting of pyrenetetraone and octaamino-derived phthalocyanine with diverse transition metals (Sc, Ti, V, Cr, Mn, Fe, Co, Ni, Cu, Zn, Nb, Mo, Ru, Rh, Pd, Ag, W, Ir, Pt, and Au) similarly identified an Mo-containing MOF as the most promising candidate for experimental investigation.[509] Accordingly, experimental studies on Mo-containing MOFs have shown that these species can drive the NRR toward NH_3 production. An MoFe catalyst supported on P-doped C was prepared by coupled pyrolysis−phosphation of a bimetallic Mo−Fe MOF precursor and achieved a Faradaic efficiency of 16.83% in the NRR experiments, giving an ammonia yield of 34.23 $\mu g\ h^{-1}\ mg^{-1}$ at −0.5 V vs RHE.[510] MOF-derived materials based on other transition metals have also shown promising performance in ammonia synthesis. For example, Zhao et al. reported a Cu-based MOF (JUC-1000) that acts as a bifunctional catalyst capable of driving the NRR and sodium gluconate oxidation at the cathode and anode of an electrolysis cell, respectively, achieving a Faradaic efficiency of 11.90% for ammonia formation and an ammonia yield of 24.7 $\mu g\ h^{-1}\ mg^{-1}$ at a cell voltage of just 0.4 V.[511] In addition, Bi-doped CeO_2 nanorods derived from a Ce-MOF yielded 6.29 $\mu g\ h^{-1}\ mg^{-1}$ of ammonia with a Faradaic efficiency of 8.56% at −0.5 V vs RHE.[512] Other studies have shown that MOFs can be used as precursors of NRR-active M-N-C materials with similar rates of NH_3 production.[513−517]

Graphene-based hybrids containing transition metals have also been reported to drive the NRR toward ammonia formation under ambient conditions:[518] experimental and DFT studies

https://doi.org/10.1021/acs.chemrev.2c00270
Chem. Rev. 2022, 122, 17241−17338

conducted by Wang et al.[519] showed that MoO_2 nanoparticles supported on rGO exhibited a Faradaic efficiency of 6.6% at −0.35 V vs RHE for ammonia formation, achieving a yield of 37.4 $\mu g\ h^{-1}\ mg^{-1}$. Thus, although there have not yet been any published studies describing NRR catalysis using graphene@MOF hybrids, the observation of NRR catalysis by both MOFs and graphene-supported transition metals suggests that these materials have great potential in this area.

5.2.3. Photocatalysis. Sunlight-driven photocatalysis is a promising strategy with many potential environmental-, industrial-, and energy-based applications. Because it enables almost complete conversion of reactants into products without generating secondary pollution, it is environmentally friendly.[520] Moreover, it is driven by earth-abundant sunlight and is therefore energy and cost efficient.[521] However, the development of effective solar photocatalysts is challenging and requires careful optimization of both structure and composition. Semiconductor-like TiO_2-based photocatalysts have been studied but generally suffer from problems including poor light-harvesting ability, rapid electron−hole recombination, a nonoptimal band gap for emerging applications of photocatalysis, and catalytic sites with relatively low activity.[522,523] MOF-based photocatalysts have also been investigated,[524,525] but their usefulness is limited by the low conductivity, poor solar-light conversion ability, and moisture sensitivity of pristine MOFs.[526−529] It has been suggested that photocatalysts based on graphene@MOF hybrids could avoid these problems because of the synergistic effects arising from the high porosity and large specific surface area of MOFs together with the high conductivity of graphene and its derivatives.[530,531] These hybrid photocatalysts have potential applications in environmental remediation, which has been demonstrated by testing their ability to catalyze the degradation of dyes and the removal of various other pollutants.[532−535] Such photocatalysts have also been used to catalyze oxidation and reduction processes and other chemical transformations.[536−539] Table 7 summarizes the performance of graphene@MOF hybrids for various photocatalytic applications. In addition, their ability to catalyze hydrogen evolution reactions has been studied because of hydrogen's potential use as a solar fuel and energy carrier.[540−542]

5.2.3.1. Dye Degradation. Organic dyes are important pollutants because they are both toxic and stable enough to be persistent. A range of techniques have therefore been used to remove dyes from water including ultrafiltration, absorption, electrocoagulation, photodegradation, and ozonation.[533] Because light-assisted degradation is seen as a particularly effective technique for this purpose, a large variety of graphene- and MOF-based hybrids have been designed for the photocatalytic degradation of dyes like rhodamine B (RhB), methylene blue (MB), methyl orange (MO), triphenylmethane, gentian violet, reactive yellow 145, rhodamine 6G, and malachite green.[531,532,543−547]

Zhang et al. reported the solvothermal synthesis of a hybrid photocatalyst based on graphene (GR) and microrods of MIL-53(Fe) (MIL-Materials Institute Lavoisier).[527] The low rate of recombination of charge carriers in the resulting composite GR/MIL-53(Fe) was attributed to good interfacial contact between the graphene and the MOF resulting from the in-situ reduction of graphene oxide during the synthetic process. The photocatalytic performance of GR/MIL-53(Fe) was improved by adding H_2O_2 to form the GR/MIL-53(Fe)−H_2O_2 system. UV−vis spectroscopic data on the photocatalytic degradation of RhB catalyzed by this system are presented in Figure 35a. The main reactive species in the photocatalytic system were $^{\bullet}OH$ radicals released by the decomposition of H_2O_2. Figure 35b compares the RhB degradation activities of various photocatalysts with and without light, showing that the most active catalyst was GR/MIL-53(Fe) in the presence of H_2O_2 under visible light. Optimization studies showed that the photocatalytic activity of this composite varied with its content of GR; the best performance was achieved with the hybrid having 5 wt % GR, which was designated GR/MIL-53(Fe)-5. Electrochemical impedance spectroscopy confirmed that GR/MIL-53(Fe)-5 separated photogenerated charge carriers more efficiently than hybrids with GR contents of 0, 7, or 10 wt %. The complete process leading to the photocatalytic degradation of RhB is shown in Figure 35c; briefly, excitation by incident light produces charge carriers in MIL-53(Fe), after which electrons in the conduction band (CB) of MIL-53(Fe) are transferred to GR and react with H_2O_2 to generate $^{\bullet}OH$ radicals. Additional radicals are generated by the interaction of surface-exposed iron species in the composite with H_2O_2, which initiates the degradation of RhB. Another graphene@MOF hybrid photocatalyst used for dye degradation was based on MOF-5 ($Zn_4O(BDC)_3$, where BDC^{2-} = 1,4-benzodicarboxylate) and reduced graphene oxide (rGO).[533] The MOF-5@rGO composite was prepared via a hydrothermal process in which rGO bound to MOF-5 through electrostatic interactions between the positively charged metal ions of MOF-5 and the negatively charged oxygen functional groups of rGO. Photoluminescence analysis confirmed that the synergic combination of MOF-5 and rGO reduced the recombination rate of photogenerated charge carriers, explaining the composite's good photocatalytic performance. Experimental measurements of this composite's activity in the photocatalytic degradation of MB, MO, and RhB revealed that it outperformed several other photocatalysts in the degradation of MB, as shown in Figure 35d. Specifically, MOF-5@rGO caused 93% degradation of MB after 20 min, leading to a clear reduction in the dye's absorption intensity and decoloration of the aqueous MB solution (Figure 35e). This composite also achieved degradation efficiencies of 97% and 92% after 20 min for RhB and MO, respectively. A mechanistic analysis of the degradation pathway indicated that reactive oxygen species (ROS) such as superoxide radicals, hydroperoxyl radicals, and hydroxyl radicals were responsible for the dye degradation ability of MOF-5@rGO.

5.2.3.2. Pollutant Removal. Industrialization, population growth, and the concomitant rising demand for food have all resulted in severe pollution problems around the world. Many different pollutants with adverse effects on plant, animal, and human life now exist in various environments. Graphene@MOF hybrid photocatalysts have proven to be effective at removing certain pollutants by photocatalytic degradation. Specifically, hybrid photocatalysts of this type have been designed for the degradative removal of herbicides (atrazine), drug pollutants (amoxicillin, norfloxacin, diclofenac, and tetracycline), and insecticides (malathion).[534,548−551]

Wu et al. recently designed a three-component hybrid photocatalyst for the photocatalytic degradation of the antibiotic norfloxacin (NOR).[550] MIL-53(Fe) acts as a photocatalyst by itself, but it suffers from rapid electron−hole recombination. To overcome this limitation, ultrasmall nanoparticles (NPs) of γ-Fe_2O_3 were incorporated into MIL-53(Fe) particles, which improved its light absorption ability and formed many heterojunctions within the MOF. These heterojunctions prevented the recombination of photogenerated charge carriers

https://doi.org/10.1021/acs.chemrev.2c00270
Chem. Rev. 2022, 122, 17241−17338

Table 7. Known Graphene@MOF Hybrids and Their Photocatalytic Applications

graphene@MOF hybrid	MOF	form of graphene	name of dye	application	performance	ref
MIL-88(Fe)@GO	MIL-88(Fe)	GO	methylene blue (MB) and rhodamine B (RhB)	dye degradation	degradation time: 20 and 30 min for MB and RhB	543
Pd/MIL-101/rGO	MIL-101	rGO	brilliant green (BG) and acid fuchsin (AF)		degradation time: 15 min for BG and 20 min for AF	531
GR/MIL-53(Fe)H_2O_2	MIL-53(Fe)	graphene (GR)	rhodamine B (RhB)		degradation t time: 60 min	527
Ag/rGO/MIL-125(Ti)	MIL-125(Ti)	rGO	rhodamine B (RhB)		% degradation: 95.7 (50 min)	544
rGO/NH_2-MIL-125(Ti)	MIL-125(Ti)	rGO	methylene blue (MB)		degradation time: 60 min	521
MIL-88A(Fe)/GO	MIL-88A(Fe)	GO	rhodamine B (RhB)		degradation time: 80 min	545
NH_2-MIL-88B(Fe)@rGO	NH_2-MIL-88B(Fe)	rGO	rhodamine B (RhB) and methylene blue (MB), rhodamine 6G (R6G), malachite green (MG), methyl orange (MO), and gentian violet (GV)		% degradation: 98.5% (RhB), 99.2% (MB), 88.7% (R6G), 92.8% (MG), 79.1% (MO), and 86.3% (GV) in 60 min	547
GO-CS@$Cu_3(btc)_2$	$Cu_3(btc)_2$	GO	methylene blue (MB)		% degradation: 98% (60 min)	546
MOF-5@rGO	MOF-5	rGO	methylene blue (MB), rhodamine B (RhB), and methyl orange (MO)		% degradation: 93% (MB), 97% (RhB), and 92% (MO)	533
Fe-BTC/GO	Fe-BTC	GO	reactive yellow 145 (RY-145)		% degradation: 98.18% (60 min)	532
UiO-66-rGO/TiO_2, Cu-BTC-rGO/TiO_2, and ZIF-8-rGO/TiO_2	UiO-66, Cu-BTC, and ZIF-8	rGO	rhodamine B (RhB)			535

graphene@MOF hybrid	MOF	form of graphene	name of pollutant	application	performance	ref
Ag_3PO_4/$BiPO_4$/Cu(tpa)·GR	Cu(tpa)	graphene (GR)	atrazine herbicide	pollutant removal	degradation time: 120 min	548
MIL-68(In)-NH_2/rGO	MIL-68(In)-NH_2	rGO	amoxicillin		% degradation: 93% (120 min)	549
γ-Fe_2O_3-MIL-53(Fe)-GO	MIL-53(Fe)	GO	norfloxacin		% degradation: 92.8% (90 min)	550
$AgFeO_2$/GR@$Cu_2(BTC)_3$	$Cu_2(BTC)_3$	graphene (GR)	diclofenac (DCF) and amoxicillin (AMX)		% degradation: 92.9% AMX, 91.4% DCF in 150 min	551
UiO-66@WO_3/GO	UiO-66	GO	tetracycline (TC) and malathion (MA)		% degradation: 84% (TC) and 100% (MA) in 70 min	534

graphene@MOF hybrid	MOF	form of graphene	name of gas	application	performance	ref
UiO-66/CdS/1%rGO	UiO-66	rGO	hydrogen	gas evolution	H_2 evolution rate: 13.8 mmol g_{CdS}^{-1} h^{-1}	530
SiW_{12}@UiO-67/MoS_2/rGO-CdS	UiO-67	rGO			H_2 evolution rate: 1.27 mmol h^{-1}	542
MoS_2 QDs/UiO-66-NH_2/GO	UiO-66-NH_2	GO			H_2 evolution rate: 62.12 μmol h^{-1}	552
rGO/UiO-66/Co-Mo-S	UiO-66	rGO			H_2 evolution rate: 70 μmol h^{-1}	528
CdS@NU-1000/rGO	NU-1000	rGO			H_2 evolution rate: 12 μmol h^{-1}	541
GR-wrapped UiO-66-NH_2	UiO-66-NH_2	graphene (GR)			H_2 evolution rate: 41.4 mmol h^{-1} g^{-1}	554
NH_2-MIL-125(Ti)@rGO	NH_2-MIL-125(Ti)	rGO			H_2 evolution rate: 90 μmol g_{cat}^{-1} h^{-1}	169
TiO_2/UiO-66-NH_2/GO	UiO-66-NH_2	GO			H_2 evolution rate: 0.27 mmol h^{-1}	553
GOPt@UiO-66-NH_2	UiO-66-NH_2	GO			H_2 evolution rate: 18.15 mmol h^{-1} g^{-1}	529
rGO/UiO-66/Ni_4S_3	UiO-66	rGO			H_2 evolution rate: 56 μmol h^{-1}	540
FeO_x-carbon	MIL-88B	GO			H_2 evolution rate: 318.0 μmol h^{-1} g^{-1}	555
(MoS_2, γ-Fe_2O_3)/GR	MIL-101(Fe)	graphene (GR)	oxygen		4400 μmol g^{-1} h^{-1}	557

graphene@MOF hybrid	MOF	form of graphene	name of reactant	application	performance	ref
GR/Ce-UiO-66	UiO-66	GR	nitrobenzene and derivatives	reduction reactions	conversion: 70% in 5 h for nitrobenzene	562
3DGR/NC@Co	ZIF-67	graphene (GR)	4-nitrophenol		4-aminophenol production rate constant: 1.5 × 10^{-2} s^{-1}	538
NH_2-rGO/Al-PMOF	Al-PMOF	NH_2-rGO	CO_2		$HCOO^-$ production rate: 685.6 μmol $g_{cat.}^{-1}$ h^{-1}	558
O-ZnO/rGO/UiO-66-NH_2	UiO-66-NH_2	rGO			evolution rate: 6.41 μmol g^{-1} h^{-1} ($HCOO^-$) and 34.83 μmol g^{-1} h^{-1} CH_3OH	561
rGO@NH_2-MIL-125	NH_2-MIL-125	rGO			methyl formate production rate: 1116 μmol·g^{-1}·h^{-1}	565

https://doi.org/10.1021/acs.chemrev.2c00270
Chem. Rev. 2022, 122, 17241−17338

Table 7. continued

graphene@MOF hybrid	MOF	form of graphene	name of reactant	application	performance	ref
GQD/MIL-101(Fe) (G/M101)	MIL-101(Fe)	GQDs		CO production rate: 224.71 μmol h^{-1} g^{-1}		559
rGO/NH_2-MIL-125(Ti)	NH_2-MIL-125(Ti)	rGO		CH_3OH production rate: 1.96 mmol h^{-1} g^{-1}		539
graphene@MOF hybrid	MOF	form of graphene	name of reactant	application	performance	ref
rGO/NH_2-MIL-125(Ti)	NH_2-MIL-125(Ti)	rGO	benzyl alcohol	oxidation reactions	% conversion: 18.6% in 8 h	566
MIL@GO	MIL-LIC-1(Eu)	GO	benzyl alcohol		% conversion: 85.4% in 3 h	563
Pd@UiO-66/rGO	UiO-66	rGO	benzyl alcohol		% conversion: 76% in 6 h	537
GO/NH_2-MIL-125(Ti)	NH_2-MIL-125(Ti)	GO	nitric oxide (NO) and acetaldehyde		% conversion: 50% in 80 min (NO) and 65% (acetaldehyde)	485
rGO@$ZnCo_2O_4$	ZnCo-ZIF	rGO	nitric oxide (NO)		% conversion: 92.6%	536

by facilitating their separation. The photocatalyst was further improved by forming a hybrid with functionalized graphene oxide (GO), which improved the dispersibility of the MOF particles and reduced their size to 100−200 nm.

The electrical conductivity and large surface area of GO also increased the abundance of active photocatalytic sites in the hybrid photocatalyst. As a result, the hybrid photocatalysts (designated *x*-MMIL-GO-*y*, where *x* and *y* denote the mass ratios of γ-Fe_2O_3 and GO with respect to MIL-53(Fe), respectively) degraded NOR very efficiently with a maximum removal rate of 92.8% over 90 min. Figure 36a shows that 0.6-MMIL-GO-50% had the highest NOR removal rate of the tested photocatalysts. Importantly, these catalysts were easily removed and regenerated after use because of their magnetic nature, allowing 0.6-MMIL-GO-50% to be recycled 5 times, achieving an NOR removal rate of 89.8% on the fifth cycle (Figure 36b). Adding H_2O_2 improved the photocatalytic performance of MMIL-GO because it facilitated the separation of photogenerated electrons and holes by capturing electrons and generating $^{\bullet}OH$ radicals. The degradation of NOR was primarily attributed to ROS (particularly $^{\bullet}OH$ radicals) and was proposed to occur through three pathways (see Figure 36c): defluorination and decarboxylation, piperazine ring cleavage, and quinoline group conversion. In addition to graphene@MOF hybrids, photocatalysts derived from these hybrids have been used for the degradative removal of various pollutants.

5.2.3.3. Hydrogen Production. Environmental concerns and the prospect of a global energy crisis have prompted extensive research on hydrogen production processes that could provide clean and environmentally friendly energy to replace conventional energy sources such as fossil fuels. Photocatalytic water splitting stands out as a promising way of producing hydrogen fuel. Consequently, several hybrid photocatalysts have been designed by hybridizing graphene and its derivatives with MOFs.[552−555]

Cadmium sulfide (CdS) is a photocatalyst whose photocatalytic activity for hydrogen production is limited by a low density of catalytically active sites and a high recombination rate of photogenerated charge carriers.[556] To overcome these issues, Lin et al. introduced a three-component hybrid catalyst UiO-66/CdS/1%rGO, which contains CdS, the MOF UiO-66, and 1 wt % rGO.[530] Neither rGO nor UiO-66 has photocatalytic activity in the hybrid photocatalyst; instead, they improve the performance of CdS. Due to the high surface area of UiO-66, CdS is uniformly distributed in the hybrid catalyst, which increases its density of catalytically active sites while also preventing its agglomeration. Meanwhile, the high electrical conductivity of rGO facilitates the transfer of photogenerated electrons to suppress charge carrier recombination. As a result, UiO-66/CdS/1%rGO achieved a higher rate of photocatalytic hydrogen evolution than a set of alternative photocatalysts, as shown in Figure 37a. In particular, this catalyst's hydrogen production activity exceeded that of commercial CdS by a factor of 13.1 because of the synergistic interactions between UiO-66, rGO, and CdS. Another CdS-based ternary hybrid photocatalyst was prepared by Bag et al. using the MOF Nu-1000 (NU = Northwestern University, $Zr_6(\mu_3\text{-}O)_4(\mu_3\text{-}OH)_4(-OH)_4(-OH_2)_4(PyTBA)_2$, PyTBA = 4,4′,4″,4‴-(pyrene-1,3,6,8-tetrayl)tetrabenzoate) and rGO.[541] The photocatalytic activity of the resulting hybrid, CdS@NU-1000/rGO, was 12.1 times that of commercial CdS and was thus slightly lower than that of the previously discussed UiO-66/CdS/1% rGO (Figure 37b). Wang et al. further improved the H_2

https://doi.org/10.1021/acs.chemrev.2c00270
Chem. Rev. 2022, 122, 17241−17338

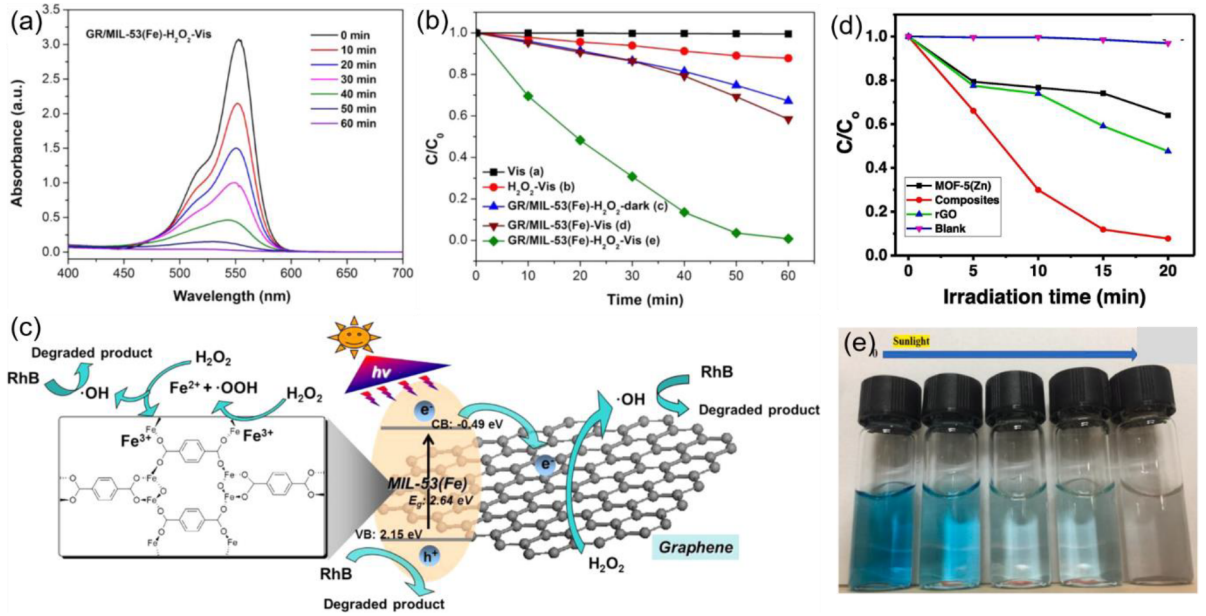

Figure 35. (a) UV−vis spectra showing the removal of RhB from water over time using GR/MIL-53(Fe). (b) Changes in the concentrations of aqueous RhB solutions in the presence of different photocatalysts under different conditions. (c) Mechanism of photocatalytic RhB degradation catalyzed by GR/MIL-53(Fe). Reproduced with permission from ref 527. Copyright 2015 American Chemical Society. (d) Methylene blue degradation profiles for rGO, MOF-5(Zn), and MOF-5@rGO. (e) Optical image showing the color change of an aqueous solution of methylene blue after irradiation with sunlight for 20 min in the presence of the MOF-5@rGO photocatalyst. Reproduced with permission from ref 533. Copyright 2020 Elsevier.

evolution rate of graphene@MOF hybrids by wrapping graphene around UiO-66-NH_2 octahedra. Three different graphene-UiO-66-NH_2 hybrids designated RCGO/U6N, RDGO/U6N, and RGOWU6N were synthesized by single-face interaction, simple mixing, and multiface interaction pathways, respectively.[554] Water splitting was performed in solutions containing triethanolamine (TEOA) as a sacrificial electron donor and the erythrocin B (ErB) as a photosensitizer. Under these conditions, the hybrid prepared by the multiface interaction pathway gave a higher rate of H_2 evolution (41.4 mmol h^{-1} g^{-1}) than the other two hybrids because it caused graphene to be wrapped around the UiO-66-NH_2 octahedra in a way that accelerated the separation of photogenerated charge carriers. The rate of H_2 evolution by these hybrids was further improved by treatment with a H_2PtCl_6 solution to induce the incorporation of cocatalytic Pt particles. As shown in Figure 37c, the evolution of H_2 by RGOWU6N is initiated by the generation of electrons from ErB (adsorbed on UiO-66-NH_2) upon visible-light irradiation. These electrons are then transferred to the graphene, either via the MOF or directly, enabling catalysis of H_2 production by the Pt nanoparticles. The multiface interaction between graphene and the MOF in RGOWU6N suppressed charge carrier recombination, leading to better performance than was achieved with the RCGO/U6N and RDGO/U6N hybrids.

Photocatalysts derived from graphene@MOF hybrids without CdS are also known. For example, Liu et al. reported that irradiating 10 mg of a rGO/UiO-66/Co-Mo-S hybrid with visible light for 5 h led to a very high H_2 production of 339 μmol.[528] This was attributed to the formation of charge transmission channels between rGO and the MOF resulting from their modification with Co-Mo-S; the H_2 production of the modified catalyst was 226 times that achieved with the unmodified rGO/UiO-66 photocatalyst. Recognizing that iron oxide is nontoxic with a narrow band gap and a valence band (VB) that is well positioned for photocatalytic hydrogen production, Li et al. fabricated photocatalytic iron oxide-GO composites by using the graphene@MOF hybrid MIL-88B/GO as a template.[555] Specifically, MIL-88B/GO was carbonized at 300 and 600 °C to obtain maghemite (γ-Fe_2O_3)- and magnetite (Fe_3O_4)-based carbonaceous Fe_2O_3/GO composites, respectively. The position of the conduction band (CB) of the Fe_2O_3 particles was altered by their interaction with GO, improving their ability to catalyze the reduction half-reaction in H_2 formation. The synergic interaction between γ-Fe_2O_3 and GO also increased the flat band potential of the γ-Fe_2O_3 composite, allowing it to achieve a hydrogen evolution rate of 318 μmol h^{-1} g^{-1}. Another report described a photocatalytic composite of rGO and NH_2-MIL-125(Ti) in which the graphene derivative and MOF are bound by noncovalent interactions: Karthik et al. fabricated the NH_2-MIL-125(Ti)/rGO hybrid via $\pi-\pi$ interaction-assisted loading of rGO onto NH_2-MIL-125(Ti).[169] The strong interaction between rGO and NH_2-MIL-125(Ti) led to efficient separation of photogenerated electrons and holes; consequently, this hybrid's photocatalytic hydrogen evolution activity was 9.1 times that of pristine NH_2-MIL-125(Ti). Although the rate of H_2 production (91 μmol h^{-1} g_{cat}^{-1}) achieved in this case was lower than that for the hybrid photocatalysts discussed above, this was the first report focusing on a hybrid photocatalyst based on NH_2-MIL-125(Ti) rather than UiO-66.

In addition to H_2 production by graphene@MOF hybrids, some reports have examined the photocatalytic evolution of oxygen. For instance, Li et al. recently reported the design of a MoS_2/MIL-101(Fe)-derived (MoS_2, γ-Fe_2O_3)/graphene composite with Z-scheme heterojunctions.[557] Because Z-scheme heterojunctions are very effective at separating photogenerated charge carriers, the oxygen evolution rate achieved with this hybrid (4400 μmol g^{-1} h^{-1}) was twice that for γ-Fe_2O_3/graphene. Effective electron−hole separation was confirmed by

https://doi.org/10.1021/acs.chemrev.2c00270
Chem. Rev. 2022, 122, 17241−17338

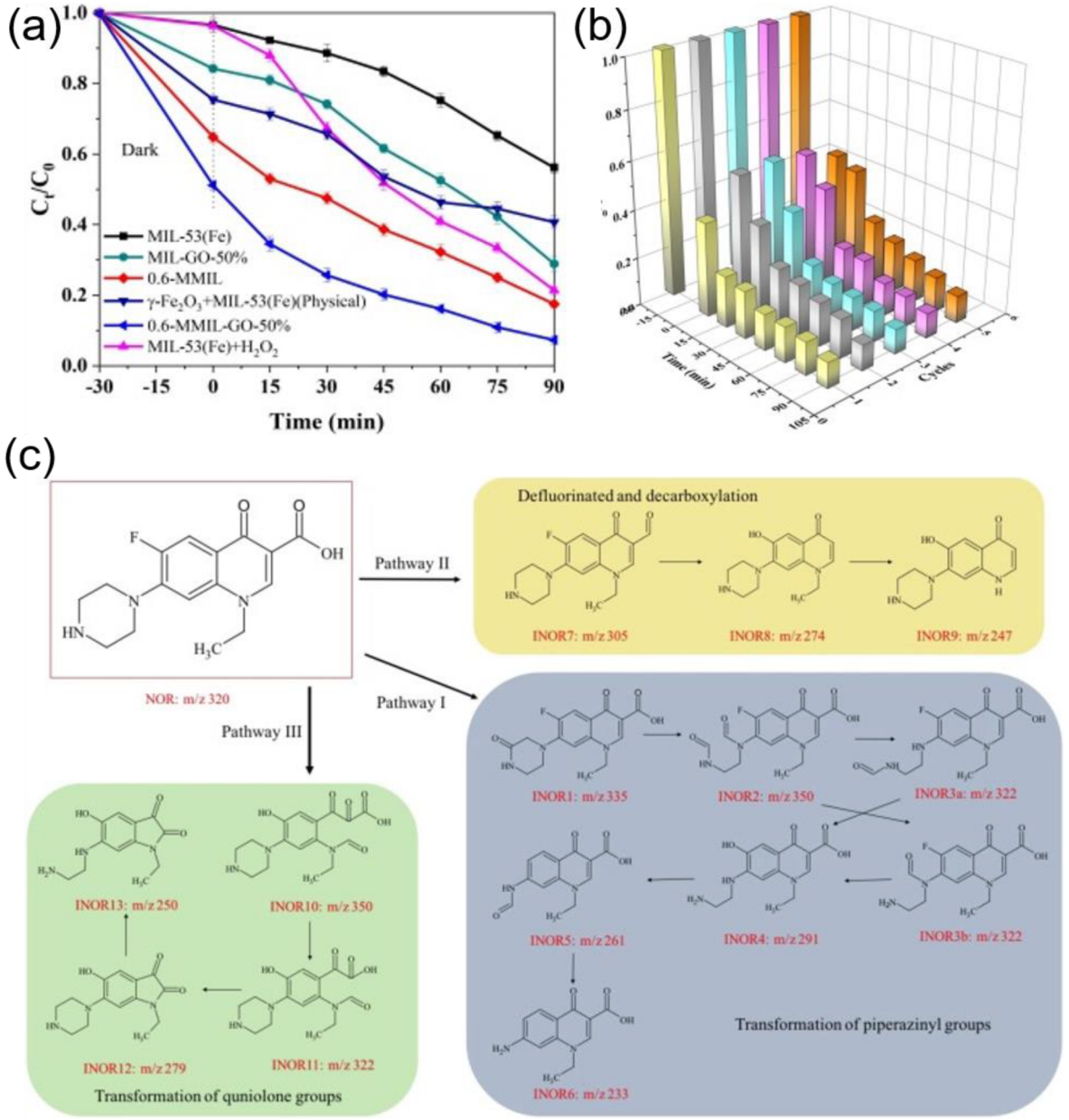

Figure 36. (a) Changes in NOR concentration over time in the presence of various photocatalysts. (b) NOR degradation performance of MMIL-GO in five successive cycles. (c) Three different pathways of NOR photodegradation in the presence of the MMIL-GO photocatalyst. Reproduced with permission from ref 550. Copyright 2020 Elsevier.

ultraviolet photoelectron spectrometry, photoluminescence spectroscopy, and photocurrent measurements, which showed that the electron transport channels created by conductive graphene facilitated the transfer of photogenerated electrons from the CB of γ-Fe_2O_3 to the VB of MoS_2. Electron transfer from the CB of MoS_2 to the CB of γ-Fe_2O_3 was not possible due to the absence of conductive graphene pathways, so electrons are instead transferred to the VB of MoS_2 from the VB of γ-Fe_2O_3 via the conductive graphene pathway.

5.2.3.4. CO_2 Reduction. The sunlight-driven reduction of CO_2 to useful products such as CH_4, HCOOH, and CH_3OH could be a powerful tool for reducing global warming.[559] The first publication on this topic was presented in 1979 by Inoue et al., who used the semiconductor TiO_2 as a photocatalyst for CO_2 reduction.[560] This report led to several efforts to prepare more active photocatalysts. However, the activity of most photocatalysts for CO_2 reduction is limited by rapid recombination of charge carriers and inefficient CO_2 conversion.[539] It has been suggested that graphene@MOF hybrids could be designed to overcome these problems by combining the photocatalytic activity of MOFs with the electrical conductivity of graphene derivatives. Consequently, several graphene@MOF hybrid photocatalysts for CO_2 reduction have been prepared.

The first report on CO_2 photoreduction with a graphene@MOF hybrid was presented by Sadeghi et al., who designed hybrids of amine-functionalized rGO (NH_2-rGO) and a tetrakis(4-carboxyphenyl)porphyrin (TCPP) ligand-based Al-porphyrin MOF (Al-PMOF).[558] NH_2-rGO/Al-PMOF hybrids were prepared with varying NH_2-rGO contents (5, 15, and 25 wt %) and used to catalyze CO_2 reduction with TEOA serving as a sacrificial electron source (see Figure 37d). The function of the NH_2 groups in this photocatalyst is to covalently link the

https://doi.org/10.1021/acs.chemrev.2c00270
Chem. Rev. 2022, 122, 17241−17338

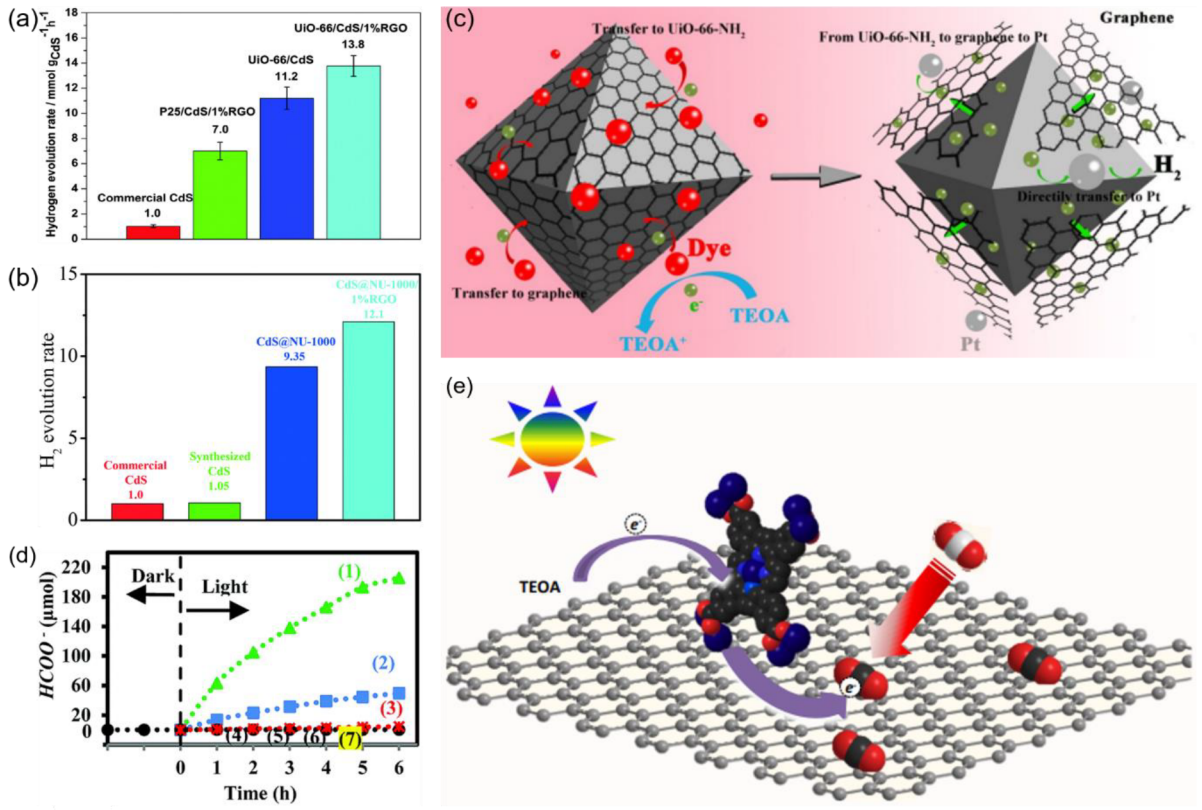

Figure 37. (a) Photocatalytic hydrogen production rates achieved with various photocatalysts. Reproduced with permission from ref 530. Copyright 2014 Royal Society of Chemistry. (b) Hydrogen evolution rates of different photocatalysts under visible-light irradiation. Reproduced with permission from ref 541. Copyright 2017 Royal Society of Chemistry. (c) Electron-transfer mechanism leading to photocatalytic hydrogen evolution catalyzed by RGOWU6N. Reproduced with permission from ref 554. Copyright 2017 Royal Society of Chemistry. (d) Formate ion production under visible-light irradiation catalyzed by NH_2-rGO (5 wt %)/Al-PMOF (1), Al-PMOF (2), and TCPP (3); 4−7 show formate ion production with no added catalyst (4), without TEOA (5), without CO_2 (6), and with N_2 over NH_2-rGO (7). (e) Diagrammatic representation of the electron-transfer process during CO_2 reduction catalyzed by NH_2-rGO(5 wt %)/Al-PMOF. Reproduced with permission from 558. Copyright 2018 Royal Society of Chemistry.

graphene to the PMOF and thereby enable electron transfer from the excited state of the PMOF to the graphene. The NH_2 groups are also capable of light absorption, which facilitates the electron-transfer process. Because of these features, NH_2-rGO/Al-PMOF showed high activity in the photoreduction of CO_2 to $HCOO^-$; 205.6 μmol of $HCOO^-$ was obtained in 6 h when using this catalyst, whereas only 49.6 μmol was obtained with the same quantity of pristine Al-PMOF. Moreover, XRD and FTIR studies showed that NH_2-rGO/Al-PMOF could be reused for 5 cycles without major loss of activity and is thus highly recyclable. Mechanistic studies (see Figure 37e) on its photocatalytic activity revealed that the binding of the TCPP ligands to the PMOF via C−O−M (M = metal) bonds enabled electron transfer from the ligand to graphene via metal nodes. When the hybrid is in a CO_2 atmosphere, the graphene surface is covered with CO_2 molecules because graphene adsorbs CO_2 quite well. The electrons transferred to the graphene from the TCPP can then be transferred further to the adsorbed CO_2, causing its transformation into $HCOO^-$ in the presence of TEOA. In this system, TEOA provides the basic environment needed to support photocatalytic CO_2 reduction.

In addition to binary hybrid photocatalysts, three-component hybrid photocatalysts have been studied. A Z-scheme ternary heterostructure (O-ZnO/rGO/UiO-66-NH_2) for the photoreduction of CO_2 to HCOOH and CH_3OH was prepared by Meng et al. via a solvothermal pathway.[561] UiO-66-NH_2 and oxygen-defective ZnO (O-ZnO) are the active species responsible for this hybrid catalyst's photocatalytic activity, while rGO acts as a conductive medium that enables facile electron transport. The O-ZnO/rGO/UiO-66-NH_2 photocatalyst performed better than the corresponding catalyst prepared with ZnO lacking oxygen defects because the oxygen defects facilitated CO_2 adsorption and the separation of photogenerated charge carriers. Figure 38a compares the CO_2 reduction activity of O-ZnO/rGO/UiO-66-NH_2 to that of selected other photocatalysts, showing that pristine O-ZnO and UiO-66-NH_2 by themselves lack CO_2 reduction activity, but their hybrids with rGO both exhibit some photoreduction activity. This was attributed to the formation of Z-scheme heterojunctions in the hybrid photocatalysts, which enabled the effective separation of charge carriers. The ability of O-ZnO/rGO/UiO-66-NH_2 to effectively separate charge carriers was confirmed by its low photoluminescence intensity (see the photoluminescence spectra presented in Figure 38b). In addition, the photocurrent intensity of O-ZnO/rGO/UiO-66-NH_2 (Figure 38c) was greater than that of both O-ZnO and UiO-66-NH_2, again indicating that charge separation is enhanced in this graphene@MOF hybrid system. The rGO content of the hybrid photocatalyst was optimized to 1.5 wt %; higher quantities of rGO competed with the light-absorbing activity of the catalyst's other two components and thus reduced its activity (see Figure 38d). The optimal hybrid photocatalyst achieved CO_2 photoreduction rates of 6.41 and 34.83 μmol g^{-1} h^{-1} for the formation of $HCOO^-$ and CH_3OH, respectively.

https://doi.org/10.1021/acs.chemrev.2c00270
Chem. Rev. 2022, 122, 17241−17338

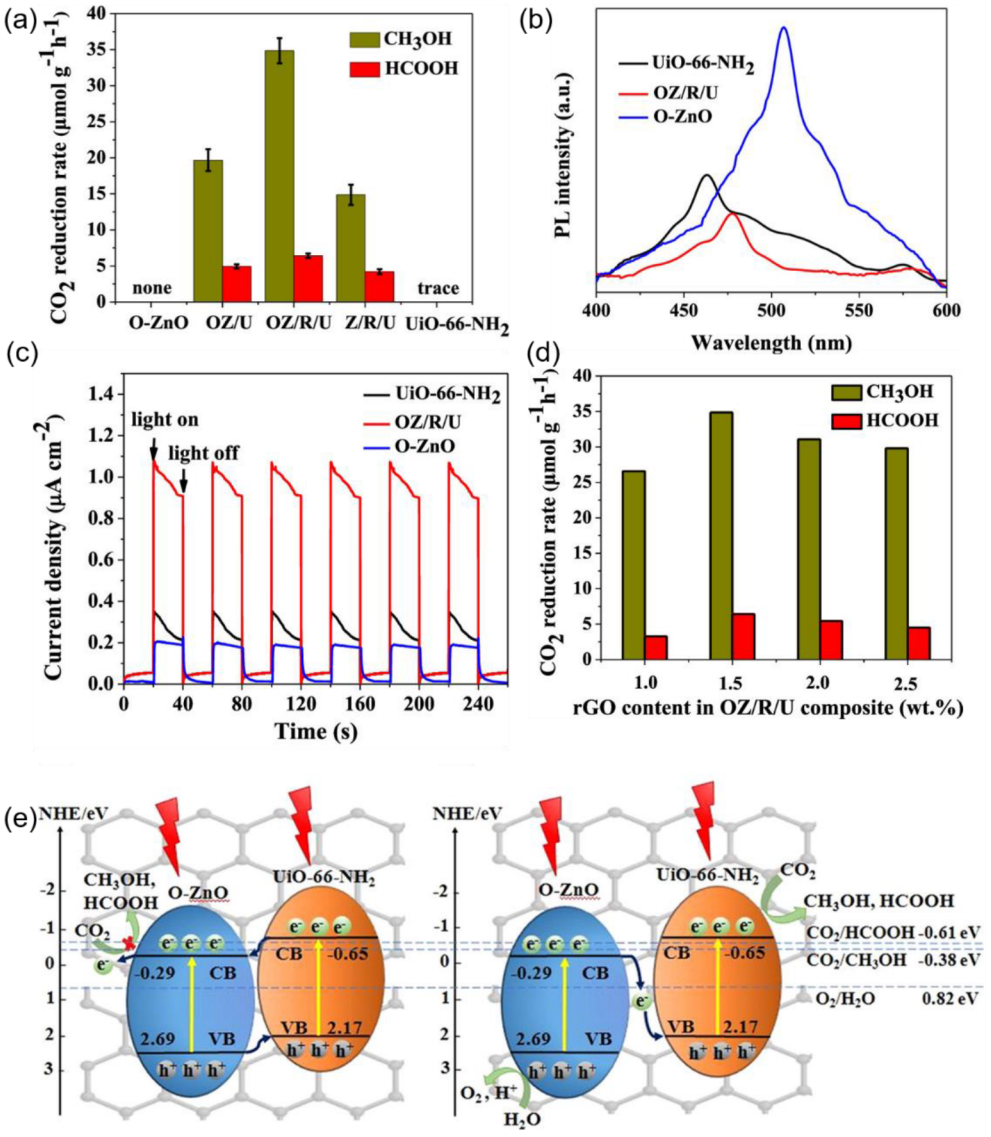

Figure 38. (a) Photocatalytic CO_2 reduction rate of the O-ZnO/rGO/UiO-66-NH_2 photocatalyst for HCOOH and CH3OH production. (b) Photoluminescence intensities and (c) photocurrent responses of the O-ZnO/rGO/UiO-66-NH_2 (OZ/R/U) photocatalyst, UiO-66-NH_2, and O-ZnO. (d) CO_2 production rates of O-ZnO/rGO/UiO-66-NH_2 photocatalysts with different rGO contents. (e) Type-II (left) and Z-scheme (right) heterojunction mechanisms for the photocatalytic CO_2 reduction by the O-ZnO/rGO/UiO-66-NH_2 photocatalyst. Reproduced with permission from ref 561. Copyright 2019 American Chemical Society.

Although the rate of $HCOO^-$ evolution for O-ZnO/rGO/UiO-66-NH_2 is lower than that achieved with the previously discussed NH_2-rGO/Al-PMOF (6.41 vs 685.6 μmol g^{-1} h^{-1}), the O-ZnO/rGO/UiO-66-NH_2 catalyst is notable because it can produce CH_3OH as well as $HCOO^-$. Photocatalytic CO_2 reduction by O-ZnO/rGO/UiO-66-NH_2 could occur via either a Z-scheme or a type-II heterojunction mechanism (Figure 38e). The former is more likely because the type-II pathway would involve the use of electrons from the CB of O-ZnO, which is implausible since the CB potential of O-ZnO is more positive than the reduction potential of CO_2.

CO_2 reduction is the most commonly studied reductive application of photocatalysts based on graphene@MOF hybrids. However, hybrids of this class have also been used to catalyze nitroarene reduction.[562] Yang et al. designed a graphene/Ce-UiO-66 hybrid for this purpose[538] and showed that Ce increased the system's photocatalytic activity by acting as an electron-transfer-facilitating mediator between graphene and UiO-66. Another photocatalyst derived from a graphene@MOF hybrid was fabricated specifically for the reduction of *p*-nitrophenol (*p*-NP) to *p*-aminophenol (*p*-AP). This system was obtained by hydrothermal synthesis of 3Dgraphene/NC@Co followed by annealing at 600 °C under an argon atmosphere to obtain graphene loaded with N-doped carbon-coated metallic NPs (3DGraphene/NC@Co). Upon irradiating this photocatalyst with a spectrum of UV, visible, and infrared radiation, free/hot electrons are released from the 3DGraphene, enabling the reduction of *p*-NP to *p*-AP.

5.2.3.5. Oxidation. Photocatalytic oxidation is a useful process with various industrial and environmental applications. Oxidation by graphene@MOF hybrid photocatalysts has been used to synthesize industrially relevant chemicals and to remove harmful gases from environment.[485,487,537,563]

The synthesis of ketones and aldehydes by the oxidation of alcohols is important in the food, pharmaceutical, and perfume-based industries. Cai et al. therefore designed MIL@GO, a

https://doi.org/10.1021/acs.chemrev.2c00270
Chem. Rev. 2022, 122, 17241−17338

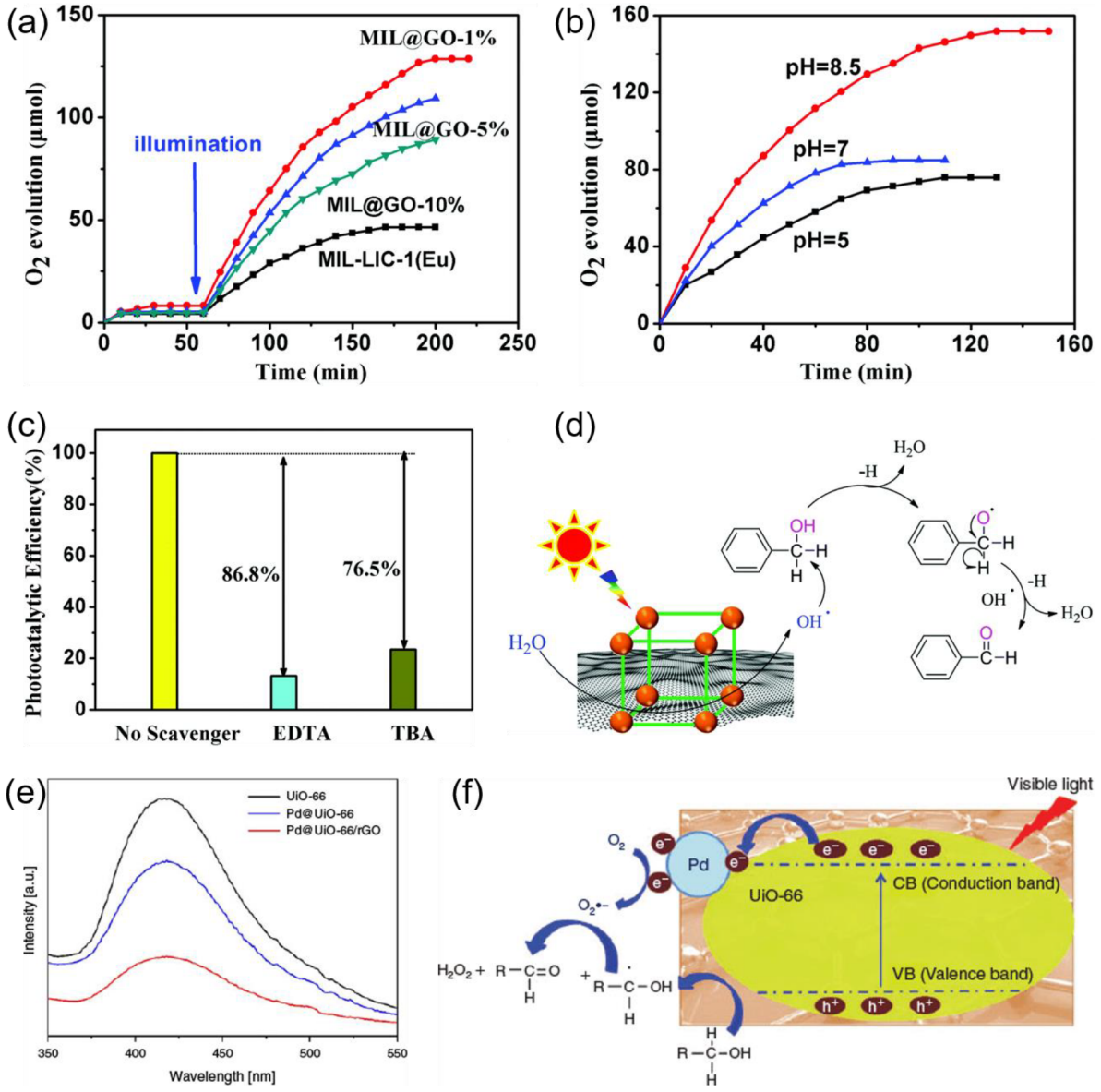

Figure 39. (a) Photocatalytic O_2 production by pristine MIL-LIC-1(Eu) and MIL@GO with varying GO loadings using a LED as the light source. (b) Effect of pH on the photocatalytic O_2 production activity of MIL@GO-1%. (c) Photocatalytic efficiency of the MIL@GO-1% photocatalyst in the presence of different scavengers. (d) Mechanistic pathway for the photo-oxidation of benzyl alcohol using MIL@GO-1%. Reproduced with permission from ref 563. Copyright 2017 Royal Society of Chemistry. (e) Photoluminescence spectra of UiO-66, Pd@UiO-66, and Pd@UiO/rGO. (f) Proposed mechanism of photocatalytic benzyl alcohol oxidation by Pd@UiO-66/rGO. Reproduced with permission from ref 537. Copyright 2018 CSIRO Publishing.

hybrid photocatalyst for the oxidation of benzyl alcohol to benzaldehyde.[563] MIL@GO is based on the MOF MIL-LIC-1(Eu), which was chosen because Eu^{3+} is easily reduced and then reoxidized. The oxygen source in this photo-oxidation was H_2O, which was confirmed by the finding that the yield of the oxidized product was only 2.3% under anhydrous conditions. The photocatalytic activity of the MIL-LIC-1(Eu)@GO hybrid was highest when the loading of GO relative to MIL-LIC-1(Eu) was 1 wt %, as shown in Figure 39a; the catalyst's activity was reduced when the content of GO was above this level because the excess GO reduced its light-absorbing ability. The pH of the reaction mixture also significantly affected the O_2 production activity of MIL-LIC-1(Eu)@GO and was therefore optimized, revealing that O_2 evolution peaked at pH 8.5, as shown in Figure 39b. Radical scavenging studies showed that $^{\bullet}OH$ and holes were the key active species in alcohol oxidation because adding scavengers such as *tert*-butyl alcohol (for $^{\bullet}OH$) and ethylenediamine tetraacetate (for holes) reduced the hybrid's photocatalytic efficiency (see Figure 39c). The oxidation of benzyl alcohol was studied in detail, and a mechanism was proposed based on the results mentioned above (see Figure 39d). Briefly, irradiation of the photocatalyst with a light-emitting diode (LED) lamp excites $Eu^{3+}-O$ to the $[Eu^{2+}-O]^*$ state, leading to the generation of electron−hole pairs. The holes then react with H_2O to form O_2 or $^{\bullet}OH$ radicals that in turn oxidize benzyl alcohol. During this process, $[Eu^{2+}-O]^*$ is converted back to $Eu^{3+}-O$ via its reaction with O_2 or $^{\bullet}OH$ radicals. GO facilitated the photocatalytic oxidation by capturing the photoinduced electrons and thereby reducing the rate of charge carrier recombination. Another study on the photocatalytic oxidation of

https://doi.org/10.1021/acs.chemrev.2c00270
Chem. Rev. 2022, 122, 17241−17338

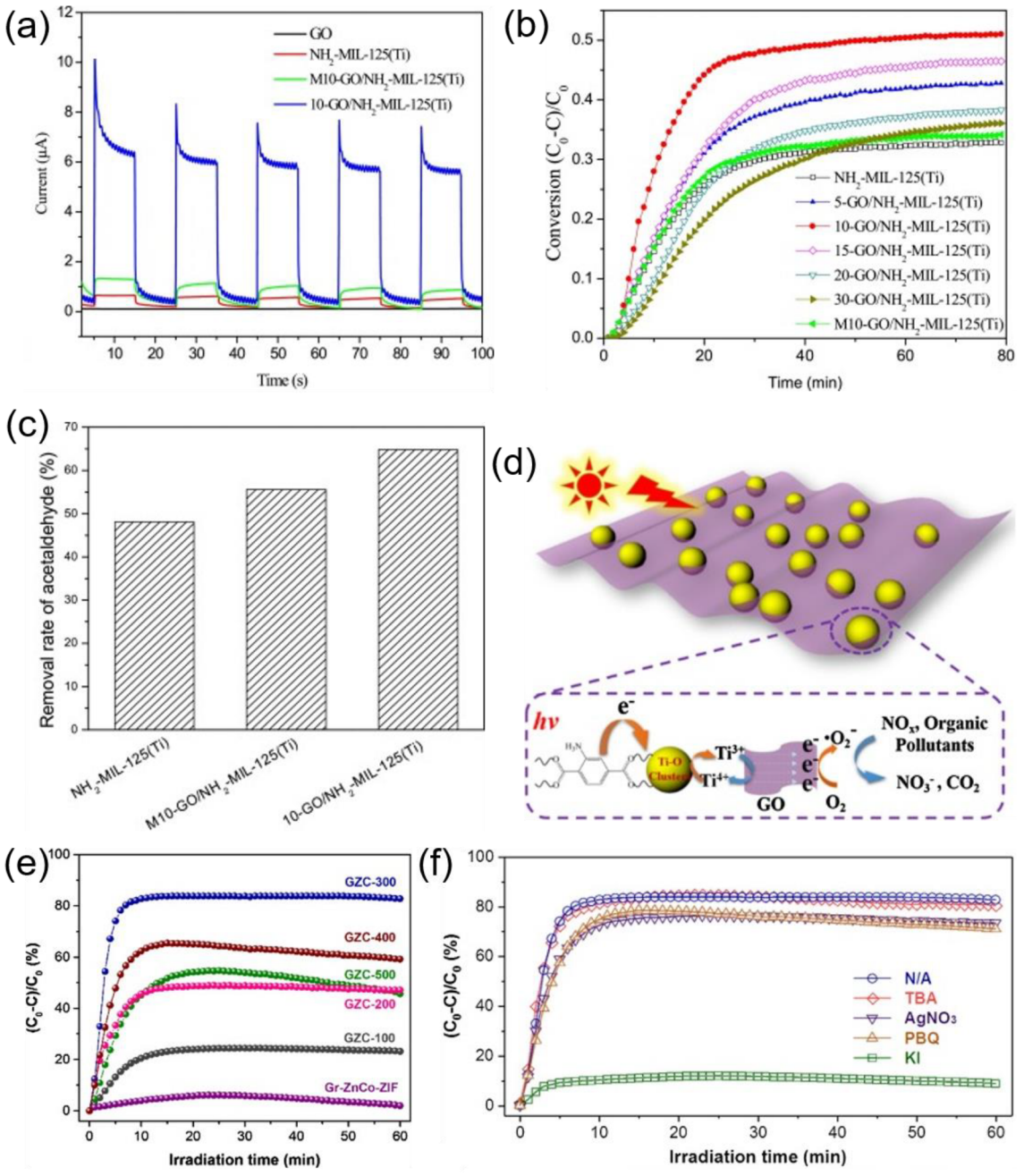

Figure 40. (a) Photocurrent responses of GO, NH_2-MIL-125(Ti), M10-GO/NH_2-MIL-125(Ti), and 10-GO/NH_2-MIL-125(Ti). Visible-light-assisted (b) conversion of NO and (c) percent removal of acetaldehyde by photo-oxidation using different photocatalysts. (d) Mechanism of photo-oxidation of NO and acetaldehyde by GO/NH_2-MIL-125(Ti). Reproduced with permission from ref 564. Copyright 2018 Elsevier. (e) Percentage conversion of NO oxidation by rGO@$ZnCo_2O_4$ (GZC-x), where x = 100, 200, 300, 400, and 500. (f) Photocatalytic NO oxidation activity of GZC-300 in the presence of various trapping agents. Reproduced with permission from ref 536. Copyright 2018 Elsevier.

benzyl alcohol using oxygen as the oxidant was recently reported by Li et al., who used a ternary hybrid photocatalyst based on rGO, Pd NPs, and the MOF UiO-66. The synthesized photocatalyst Pd@UiO-66@rGO was active enough to give a high conversion efficiency of 76% with 99% selectivity in benzyl alcohol oxidation. The optimal concentration of Pd NPs in the catalyst was found to be 0.8%; higher concentrations restricted contact between the active species, the substrate, and UiO-66. The effective separation of photoinduced charge carriers in this hybrid was confirmed by the fact that the intensities of the peaks in its photoluminescence spectrum were lower than those in the spectra of its individual components, as shown in Figure 39e. The hybrid was completely inactive under an argon atmosphere, indicating that the main active species involved in benzyl alcohol oxidation were holes and $O_2^{\bullet-}$. A mechanism was proposed based on these findings (see Figure 39f) in which electron−hole pairs are formed upon visible-light irradiation of UiO-66. The electrons are then transferred to Pd, which reduces molecular oxygen to $O_2^{\bullet-}$. Meanwhile, the holes activate benzyl alcohol by transforming it into the corresponding cation radical, which in turn reacts with $O_2^{\bullet-}$ to form benzaldehyde. During this process, rGO captures photogenerated electrons to prevent their recombination with holes.

https://doi.org/10.1021/acs.chemrev.2c00270
Chem. Rev. 2022, 122, 17241−17338

The presence of harmful gases in the air is a serious problem that could be resolved by converting them into species that are less harmful or, ideally, harmless. This can be achieved through photocatalytic oxidation of gases such as nitric oxide (NO) and acetaldehyde using graphene@MOF hybrid photocatalysts.[489,536] A recent report on photocatalytic oxidation of NO and acetaldehyde was presented by Li et al., who hybridized the amine-functionalized MOF NH_2-MIL-125(Ti) with GO via a solvothermal process to obtain GO/NH_2-MIL-125(Ti).[564] As in other cases, GO improved the photocatalytic activity of the resultant hybrid, which was also shown to have a very low charge-transfer resistance (indicated by a small semicircle radius in a Nyquist plot). Samples of this hybrid photocatalyst prepared with 10 mg of GO (10-GO/NH_2-MIL-125(Ti)) showed a good photocurrent response and had a photocurrent density exceeding that of both their precursors and hybrid photocatalyst samples prepared by mechanical grinding of GO and NH_2-MIL-125(Ti) in the same proportions used in the solvothermal process (see Figure 40a). On the basis of these observations, GO/NH2-MIL-125(Ti) was tested in the photocatalytic oxidation of NO and acetaldehyde. Figure 40b shows the conversion of NO to NO_3^- by hybrid photocatalysts with different GO contents, revealing that the 10-GO/NH_2-MIL-125(Ti) photocatalyst outperformed the hybrid prepared by mechanical grinding. This highlights the strong interaction between GO and NH_2-MIL-125(Ti) in the solvothermal hybrid. The 10-GO/NH_2-MIL-125(Ti) was also used to catalyze the oxidative degradation of acetaldehyde; Figure 40c compares its activity in this reaction to that of various other photocatalysts. A mechanistic study revealed that the photo-oxidation of acetaldehyde and NO by 10-GO/NH_2-MIL-125(Ti) is mediated by holes and $^{\bullet}O_2^-$, as shown in Figure 40d. Visible-light irradiation of 10-GO/NH_2-MIL-125(Ti) causes the generation of electrons from 2-aminoterephthalic acid, leading to the reduction of Ti^{4+} to Ti^{3+}. These electrons are then transferred from Ti−O clusters to GO before reacting with O_2 to generate $^{\bullet}O_2^-$. The oxidation process is accelerated in the presence of water vapor, which enables the formation of $^{\bullet}OH$ radicals through the reaction of water with holes. Another study on NO oxidation examined rGO@$ZnCo_2O_4$ (GZC-x) hybrids formed by annealing rGO@ZnCo-ZIF (x represents the annealing temperature, which was 100, 200, 300, 400, or 500 °C).[536] In comparison to the previously discussed 10-GO/NH2-MIL-125(Ti) photocatalyst, 300-rGO@$ZnCo_2O_4$ was highly active for NO oxidation, achieving a conversion of 83.8% (see Figure 40e); only 50% conversion was achieved with 10-GO/NH_2-MIL-125(Ti) under same light source. The high activity of 300-rGO@$ZnCo_2O_4$ is due to the high energy of its VB and the low energy of its CB, which facilitated the separation of electrons and holes. Experiments using trapping agents such as KI for holes, *tert*-butyl alcohol (TBA) for $^{\bullet}OH$, $AgNO_3$ for electrons, and *p*-benzoquinone (*p*-BQ) for $^{\bullet}O_2^-$ confirmed that holes and O_2^- are the active species during NO oxidation because the conversion of NO to NO_3^- was reduced in the presence of KI and *p*-BQ (Figure 40f). Interestingly, the conversion of NO by rGO@$ZnCo_2O_4$ increased to 92.6% when simulated sunlight was used as the light source.

5.3. Energy Storage/Conversion

Nanocarbons, particularly graphene-based composites, enjoy prime importance in myriad applications. In particular, they are seen as very promising materials for energy storage because they have many properties that are beneficial in this context such as high specific surface areas, porosity, and the exceptional mechanical and thermal properties of graphene. Although MOFs[567] and graphene-based materials[568] have been studied as electrode materials individually, their energy storage performance is limited by a few factors. For example, graphene-based materials are prone to aggregation, while MOFs are inherently poor conductors. As discussed in the preceding sections, nanographene@MOF composites and their derivatives can synergistically combine the benefits of both material types while minimizing their drawbacks, enabling the fabrication of MOF-based materials with improved electrical conductivity or electrode materials with unique designs and architectures.[569−571] Other benefits that can be achieved through the formation of such composites include improved charge transfer and electrochemical redox reaction kinetics. As such, these materials could potentially offer solutions to longstanding problems in electrode design and energy storage and conversion. Many MOF-graphene composites have been successfully prepared and tested as active materials for these purposes,[571,572] drawing on the large and growing library of known MOF-based structures. The following sections review the uses of such composites in supercapacitors and various battery chemistries.

5.3.1. Supercapacitors. Supercapacitors (SCs) use Faradaic and non-Faradaic processes to store energy. As energy storage systems, they have several unique characteristics including high power density, rapid charge/discharge rates, long cycle lives, and a wide working temperature range.[573,574] Graphene@MOF composites can enhance these properties by combining physical and charge storage mechanisms in a single electrode. In other words, the electric double-layer capacitance (EDLC) originating from graphene-based materials and the pseudocapacitance originating from the MOFs (metal-based) could help deliver an optimal combination of energy and power density.[76,568,575] Although few unmodified MOFs can be used in electrochemical devices due to their poor electrical conductivity and low chemical stability, metal−carbon nanostructures can improve the electrochemical performance by enabling more extensive contact between the electrode and the electrolyte while also being highly porous and having many active sites to improve ion diffusion.[164] In addition, when MOFs are compounded with graphene-based materials, the latter act as valuable nanostructured fillers and supporting structures, as discussed in the preceding sections.

The carbon material may also form bonds with the MOF, changing its coordination chemistry and thereby increasing the composite's conductivity. This in turn can create new pathways for charge conductance within the composite. Accordingly, pioneering studies conducted by Yaghi et al. showed that many nanocrystalline MOFs (nMOFs) with multiple organic functionalities and metal ions could be doped with graphene sheets and used as supercapacitor electrodes.[164] Coin-cell-type supercapacitor devices constructed with such composite thin-film electrodes soaked in 1 M tetraethylammonium tetrafluoroborate electrolyte exhibited high capacities for ion storage during charging and discharging. Although good capacitance was achieved with several nMOFs, a zirconium-based MOF (a composite of MOF 867 and graphene) yielded the highest stack and areal capacitance while also being sufficiently robust to exhibit no appreciable loss of performance after 10 000 charge/discharge cycles. This was attributed to the composite's high porosity and open structure. Notably, the composite's capacitance was around six times that of supercapacitors made

https://doi.org/10.1021/acs.chemrev.2c00270
Chem. Rev. 2022, 122, 17241−17338

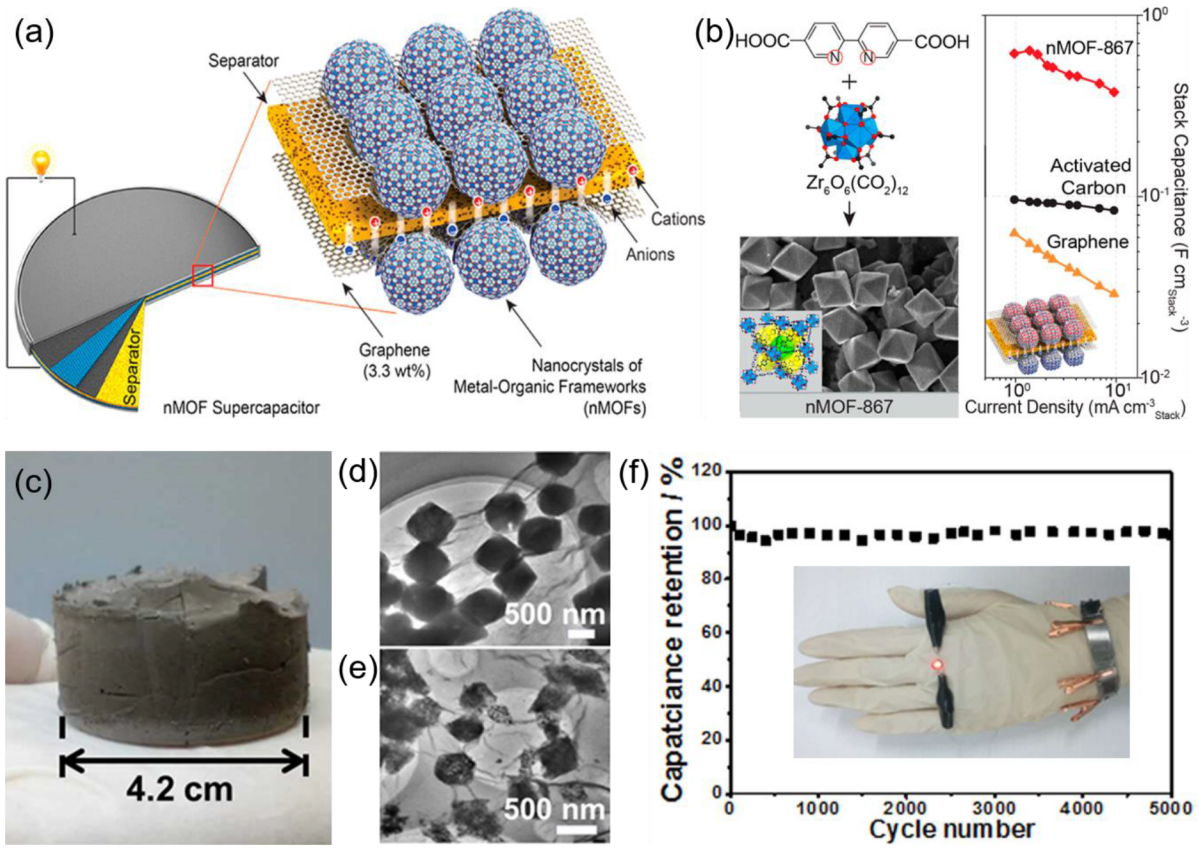

Figure 41. (a) Schematic depiction of nMOF/graphene supercapacitors, and (b) nMOF 867 along with the stack capacitance of nMOF-867/graphene, activated carbon, and pristine nMOF-867. Reproduced with permission from ref 164. Copyright 2014 American Chemical Society. (c) Photograph of GO/Fe-MOF aerogel, demonstrating the scalability of its synthesis. (d and e) TEM images of GO/Fe-MOF and rGO/Fe_2O_3 composite aerogel, respectively. (f) Long-term cycle life of the rGO/Fe_2O_3 electrode at 50.4 mA/cm^3 for 5000 cycles with practical demonstration (inset). Reproduced with permission from ref 232. Copyright 2017 American Chemical Society.

from commercial activated carbon, which was taken as a benchmark (Figure 41a and 41b).

MOFs based on transition metals (Fe, Co, Ni) have also shown promising electrochemical performance owing to their large surface areas, low cost, and high mass density. Several studies have therefore investigated the doping of such MOFs with graphene-based materials to construct composite supercapacitor electrodes.[576] For example, Zhou et al.[577] grew Ni-MOFs directly on graphene sheets to obtain a GO@MOF structure with excellent electrochemical properties including long-term cycling stability (3000 CD cycles), a good rate capability (85% of the initial capacitance was retained upon raising the current density from 1 to 10 A/g), and high capacitance (2192.4 F/g at 1 A/g). A major challenge in preparing high-performance electrodes using graphene@MOF composites is in preparing the composite in a scalable manner while controlling its surface characteristics. It is therefore notable that Xu et al.[232] achieved the large-scale synthesis of 3D graphene/MOF composites using a simple "mixing" strategy with several different MOFs including MOF-5, ZIF-8, ZIF-67, $K_2Sn_2(1,4\text{-bdc})_3$, and an Fe-MOF prepared from $FeCl_3$ and H_2bdc for which no structural data was provided. The GO/Fe-MOF composite was subsequently used as a precursor for the fabrication of rGO/Fe_2O_3 aerogels by freeze drying and calcination. Figure 41c shows a photograph of a large quantity of the GO/Fe-MOF composite, demonstrating the scalability of its synthesis. In addition, TEM images of the GO/MOF composite and the derived rGO/Fe_2O_3 aerogels showed that their graphene sheets were homogeneously coated with nanocrystals of the MOF and Fe_2O_3, respectively (see Figure 41d and 41e). When used as an electrode, the rGO/Fe_2O_3 hybrid delivered capacitances of 869.2 and 289.6 F/g at current densities of 1 and 20 A/g, respectively, as well as a long cycle life without obvious capacitive decay after 5000 cycles (Figure 41f). A flexible all-solid-state SC based on the rGO/Fe_2O_3 aerogel assembled to investigate its practical utility achieved a volumetric capacitance of 250 mF/cm^3 at 6.4 mA/cm^3 and retained 96.3% of its initial capacity after 5000 cycles when measured at 50.4 mA/cm^3. Benefiting from the synergistic interactions between rGO and MOF-derived nanostructures as well as their unique 3D framework, the rGO/Fe_2O_3 aerogels thus delivered outstanding supercapacitive performance. Similarly, Majumdar and co-workers synthesized Ni-doped MOF/rGO (reduced graphene oxide) composites in gram-scale quantities. Their strategy involved partially substituting Zn metal clusters with Ni, which can participate in reversible redox reactions in alkaline electrolytes. Interestingly, the presence of Ni-doped MOF-5 also circumvented the restacking issue associated with graphene sheets. An electrode based on MOF-5 supported on rGO (with equal contents of Ni and rGO) had an energy density of 37.8 W h kg^{-1} at 226.7 W kg^{-1} with low charge transfer resistance.[578] Li et al. used the ball-milling method followed by calcination to prepare an rGO/Mn_3O_4 composite.[579] The starting material in this case was a porous rGO aerogel prepared by hydrothermal and freeze-drying processes, which was then ball milled with an Mn-based MOF.

https://doi.org/10.1021/acs.chemrev.2c00270
Chem. Rev. 2022, 122, 17241−17338

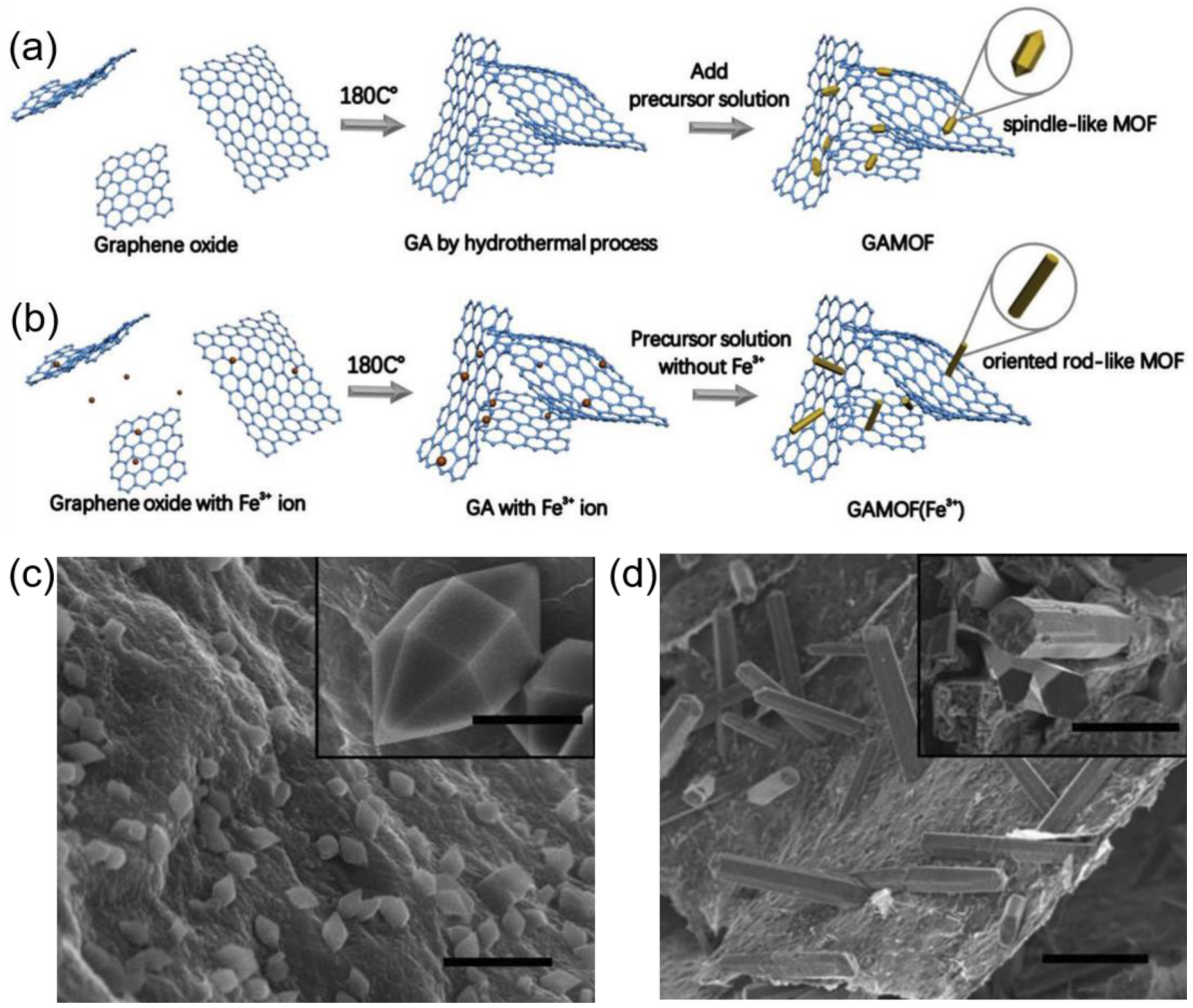

Figure 42. (a) Schematic representation of the synthesis of MIL-88(Fe) grown on graphene with two different nanostructures: (a) spindle-like MOF@GA and (b) rod-like MOF@GA. SEM images of (c) spindle-like MOF@GA and (d) rod-like MOF@GA hybrid. Reproduced with permission from ref 580. Copyright 2018 John Wiley & Sons, Inc.

The optimized rGO/Mn_3O_4 electrode delivered a capacitance of 420 F/g at 0.5 A/g with good cycling stability (89.6% capacitance retention after 5000 cycles). An all-solid-state symmetric SC based on rGO/Mn_3O_4 was subsequently constructed, which had an energy density of 22.1 Wh/kg and a power density of 3.0 kW/kg with good cycling stability (90.1% capacitance retention after 5000 cycles). In this system, ion/electron transport is facilitated by the integration of Mn_3O_4 with rGO to form a hierarchically porous matrix.

Another efficient way of increasing an electrode material's redox activity involves using synergistic activation to obtain a material whose performance exceeds that of its individual components. In one study using this approach, it was discovered that the morphology and crystal structure of MIL-88(Fe) MOF nanocrystals on graphene could be tuned simply by varying the order of addition of Fe^{3+} ions:[580] a dispersion of spindle-like nanocrystals (spindle-like MOF@GA) on graphene sheets was obtained if the Fe^{3+} and organic ligand were added simultaneously (see Figure 42a and 42c), whereas oriented rod-like nanocrystals (rod-like MOF@GA) were obtained when GO was heated with Fe^{3+} before adding the organic ligand (see Figure 42b and 42d). The controlled growth of spindle-like MOF crystals was attributed to the coupling of electrophilic Fe^{3+} ions with graphene via p−π interactions to form uniformly scattered seeds that nucleated crystal growth upon adding the organic ligand. SCs constructed using spindle-like MOF@GA had a capacitance of 353 F/g at 20 A/g, while SCs made with rod-like MOF@GA had faster charge/discharge rates, greater cycling stability, and remarkable capacitance retention (74.4% after 10 000 cycles). This study showed that MOFs' morphology and growth patterns on aerogel matrices significantly affect their electrochemical properties. In addition to the surface morphology, the size of the nanoparticles (nanostructures) in such composites is important because short ionic and electronic pathways enable efficient electrochemical processes. To maximize the benefit of small particle sizes, Xiao et al.[581] developed a graphene-supported Co-based MOF with ultrasmall (<5 nm) nanocrystals whose decomposition temperature was raised by coating with a polymer, causing the formation of significantly smaller MOF crystals than would otherwise be obtained. While a graphene support can mitigate losses in performance arising from longer ionic/electronic pathways, the best performance is generally observed when the active materials are less than 10 nm in size.

The interesting properties of graphene@MOF hybrids arise partly from the fact that the MOF component prevents stacking of the graphene sheets. However, this often depends on comparatively weak π−π interactions and hydrogen bonds

https://doi.org/10.1021/acs.chemrev.2c00270
Chem. Rev. 2022, 122, 17241−17338

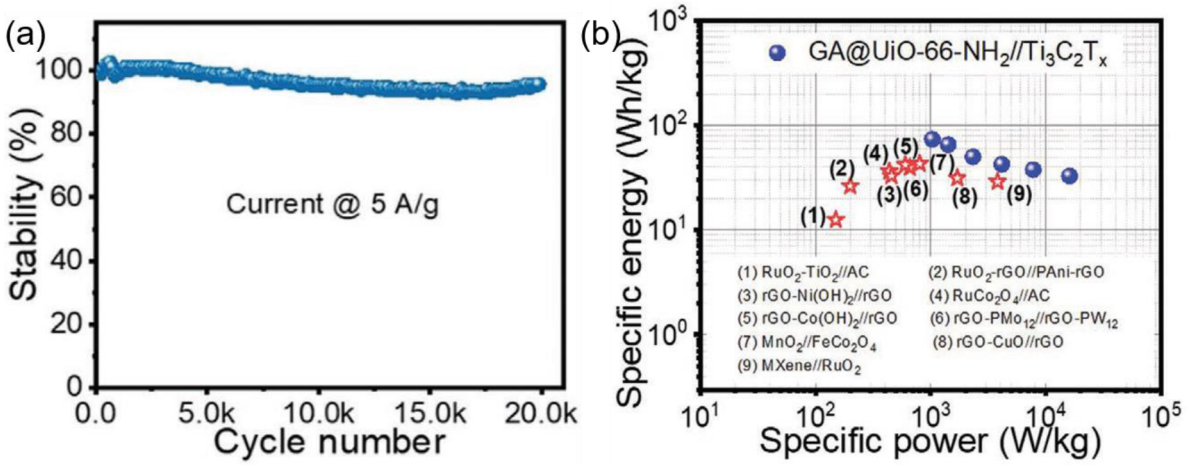

Figure 43. (a) Cycling stability of GA@UiO-66-NH_2 at 5 A g^{-1} over 20 000 cycles. (b) Ragone plot for a GA@UiO-66-NH_2//MXene device. Reproduced with permission from ref 76. Copyright 2021 John Wiley & Sons, Inc.

between the MOF and the graphene derivative, which may limit the mechanical stability of the resulting composites. This problem can be avoided by forming composites with functionalized graphene derivatives that allow MOFs to be grown selectively at the locations of specific functional groups and to be covalently attached to the graphene, providing stronger binding and greater stability. Kolleboyina et al.[76] demonstrated this concept by covalently linking the amine-functionalized MOF UiO-66-NH_2 to carboxylate-functionalized graphene (graphene acid, GA). The resulting amide-linked GA@UiO-66-NH_2 hybrid had a high specific surface area, a hierarchical pore structure, and an interconnected conductive network. Electrochemical testing showed that GA@UiO-66-NH_2 is as an effective charge storing material with a capacitance of 651 F/g at 2 A/g and good cycling stability; it retained 94% of its initial capacitance after 20 000 cycles, as shown in Figure 43a. Its amide linkages enable the formation of a π-conjugated structure that facilitates charge transfer, explaining these outcomes. An innovative asymmetric SC was subsequently constructed using GA@UiO-66-NH_2 as the positive electrode and $Ti_3C_2T_x$ MXene as the negative electrode. This cell achieved power densities of up to 16 kW/kg and an energy density of up to 73 Wh/kg (Figure 43b) with 88% cycling stability over 10 000 cycles. In general, electrode materials for SCs should have high contact areas and high conductivity to enable rapid transport of ions and/or electrons. A material with these qualities was prepared by growing vertically aligned Ni−Zn hydroxide nanosheets on rGO to form a sandwich-like structure, providing abundant electrolyte-accessible contact sites.[582] The heterogeneous doping of Zn into the Ni-based hydroxide of this composite altered its electronic structure and greatly increased its conductivity. Because of these properties, the Ni−Zn hydroxide/rGO composite delivered a reasonably high capacitance (615.4 C/g at 1 A/g), good stability (87.5% after 8000 cycles), and excellent capacity rate performance (62.3% capacity retention when the current was increased from 1 to 30 A/g).

To demonstrate the composite's practical utility, it was used to manufacture a hybrid SC with an activated carbon (AC) negative electrode. The resulting NiZn−OH/rGO//AC SC had an energy density of 53.7 Wh/kg at a power density of 825.1 W/kg. Moreover, at its maximum power density of 8276.7 W/kg, it retained an energy density of 24.6 Wh/kg. The cell also retained 89.7% of its initial capacity after 10 000 cycles when measured at 5 A/g. Another polymetallic graphene@MOF hybrid electrode material was studied by Ashourdan et al.,[583] who prepared nanocomposite electrodes made from a trimetallic (nickel−cobalt−manganese) MOF and high-quality graphene (HQG) obtained by graphite peeling in the liquid phase. The as-prepared G-HQG@NiCoMn-MOF hybrid contained several functional groups at the graphene surface and had a fairly high surface area (140 m^2/g). As a supercapacitive electrode, the composite delivered a capacity of 1263.6 C/g at a current density of 1 A/g with 89.2% capacity retention after 5000 consecutive charge/discharge cycles. A hybrid SC was constructed using positive and negative electrodes consisting of this composite and AC, respectively. The SC was successfully cycled at working voltages up to 1.6 V and delivered a specific energy of 69.9 Wh/kg at a power of 1217.9 W/kg. It also had an excellent rate capability, retaining 74.1% of its initial capacitance when the current density was increased from 1 to 10 A/g and had an outstanding cycle life (85.2% capacity retention after 5000 cycles).

In addition to growing MOFs on the graphene surface, graphene sheets can be used as wrapping layers. Zhang et al. demonstrated this wrapping strategy by synthesizing a composite of graphene, carbon nanotubes, and cobalt derivatives (Gr-CNT@Co).[584] The innovative design of this material and its highly interconnected porous structure gave it a high surface area (253.9 m^2/g), resulting in a capacitance of 1108 F/g at 1 A/g with high cycling stability (75% after 6000 cycles). Accordingly, an all-solid-state asymmetric Gr-CNT@Co//N-doped rGO device delivered an energy density of 36.55 Wh/kg at 685.3 W/kg and an excellent capacitance retention of 78% after 6000 cycles at 1.5 A/g. At a high power of 9.4 kW/kg, the device delivered an energy density of 7.6 Wh/kg. Cao et al.[585] similarly reported that graphene could be wrapped around an Mo-based MOF simply by stirring a mixture of the two components. The resulting composite had an excellent rate capability (~61% of its initial capacitance was retained after raising the current density from 1 to 10 A/g) and cycling stability (~87.5% over 6000 cycles when recorded at 6 A/g). These remarkable electrochemical properties can be attributed to the graphene wrapping layers, which increased the material's electronic conductivity while preventing aggregation of the active MoO_3 nanoparticles. Wu et al. reported another

https://doi.org/10.1021/acs.chemrev.2c00270
Chem. Rev. 2022, 122, 17241−17338

Table 8. Graphene@MOF Hybrids Used in Electrodes for Supercapacitors and Batteries[a]

graphene@MOF hybrids used in electrodes for supercapacitors					
active material	surface area (m^2/g)	electrolyte	capacitance	cycling stability	ref
GA@UiO-66-NH_2	780	1 M Na_2SO_4	615 F/g at 1 A/g	94% over 2000 cycles at 5 A/g	76
ZIF-8-supported 3D graphene	352.8	1 M H_2SO_4	238 F/g at 1 A/g	72% over 3000 cycles at 7 A/g	609
rGO-wrapped MoO_3	79.9	1 M H_2SO_4	617 F/g at 1 A/g	87.5% over 6000 cycles at 6 A/g	585
MOF-derived B/N-doped carbon-coated graphene	798	1 M H_2SO_4	288 F/g at 1 A/g		610
		1 M TEA BF_4/AN	126 F/g at 1 A/g		
PEDOT-GO/(UiO-66-CNT)	623	3 M KCl	102 mF/cm^2 at 10 mV/s		611
MOF-derived Mn_3O_4@N-doped carbon/graphene	326	1 M Na_2SO_4	456 F/g at 1 A/g	98.1% after 2000 cycles at 5 A/g	612
rGO-$NiCo_2S_4$ MOF		6 M KOH	972 F/g at 1 A/g	94.1% after 2000 cycles at 3 A/g	613
MOF-derived (Ni-Co-LDH)/rGNS		6 M KOH	2179 F/g at 1 A/g	88% after 3000 cycles at 1 A/g	614
G-HQG@NiCoMn-MOF	140	3 M KOH	1263.6 C/g at 1 A/g	89.2% after 5000 cycles at 7 A/g	583
MOF-derived rGO/CoS_x		1 M KOH	460 F/g at 1 A/g	85.1% after 5000 cycles at 5 A/g	615
NiCo-MOFs/GO	89.68	2 M KOH	413.61 C/g at 0.5 A/g	85.89% after 5000 cycles at 7 A/g	616
Ni-MOF-derived NiO/rGO		6 M KOH	435.25 F/g at 1 A/g	no loss after 25 000 cycles at 50 mV/s	617
N-ZIF-67/rGO	1367	2 M KOH	962 F/g at 20 mA/cm^2	97% after 1000 cycles at 20 mA/cm^2	618
GO/Zn-Co-Ni LDHs	178.2	1 M KOH	843 C/g at 1 A/g	97.71% after 5000 cycles at 10 A/g	619
Mn_3O_4@C/rGO		0.5 M Na_2SO_4	328.4 F/cm^3 at 0.5 A/cm^3	85% after 10 000 cycles at 4 A/cm^3	620
NbOF-GO		3 M KOH	489 F/g at 1 A/g	88% after 5500 cycles at 5 A/g	621
rGO@C/Fe_3C	154.9	6 M KOH	95.3 mAh/g at 1 A/g	81.5% after 5000 cycles at 5 A/g	622
conductive Cu-MOF/rGO	540	1 M KCl	44.6 mF/cm^2 at 5 mV/s	69% after 1000 cycles at 0.04 mA/cm	623
CoS_2/GO	214.81	6 M KOH	842 F/g at 0.5 A/g	95% after 2000 cycles at 10 A/g	624
Ni/ZIF-67/rGO	369.1	1 M H_2SO_4	304 F/g at 1 A/g	98.9% after 1000 cycles at 10 A/g	625
$Co_2V_2O_7$/graphene		1 M KOH	276.5 C/g at 1 A/g	93% after 10 000 cycles at 10 A/g	626
$Co_{1-x}S/CoFe_2O_4$@rGO	290	2 M KOH	2202 F/g at 1 A/g	90% after 20 000 cycles at 10 A/g	627
(Ni,Co)Se_2@rGO	36.79	3 M KOH	649.1 C/g at 1 A/g	90.5% after 5000 cycles at 10 A/g	628
Co_3O_4-NiO/graphene	54.04	2 M KOH	766 F/g at 1 A/g	83% after 5000 cycles at 1 A/g	629
rGO@NiCoAl-LDHs		2 M KOH	2202 F/g at 1 A/g	92% after 2000 cycles at 10 A/g	630
Na/Zn-bimetallic MOF/rGO	83.62	0.5 M Na_2SO_4	435.2 F/g at 1.6 A/g	100% after 4000 cycles at 40 A/g	631
Cu-MOF/rGO		1 M KOH	1871 F/g at 0.5 A/g	89% after 5000 cycles at 4 A/g	38
N-GQD@cZIF-8/CNT	520	1 M H_2SO_4	540 F/g at 1 A/g	90.9% after 8000 cycles at 0.5 A/g	632
α-NiS nanorods/graphene		2 M KOH	744 C/g at 1 A/g	89% after 20 000 cycles at 20 A/g	633
rGO−Co_3O_4 hexagons	98	0.1 M KOH	1300 F/g at 4 A/g	80.5% after 5000 cycles at 4 A/g	634
rGO/Co_9S_8		1 M KOH	575.9 F/g at 2 A/g	92% after 9000 cycles at 4 A/g	635
Ni-Co LDH/graphene	218.9	1 M KOH	1265 F/g at 1 A/g	92.9% after 2000 cycles at 3.33 A/g	636
$Ni_xCo_{3-x}O_4$/G		2 M KOH	2870.8 F/g at 1 A/g	81% after 5000 cycles at 4 A/g	637
(CoBTC MOF/G)	577.1	1 M KOH	608.2 F/g at 0.25 A/g	94.9% after 2000 cycles at 0.25 A/g	638
rGO/Ni_2P	524.6	6 M KOH	890 F/g at 1 A/g	61.1% after 4000 cycles at 8 A/g	639
rGO/ZIF8 Ni-nanocone		1 M KOH	336 F/g at 1 A/g	96% after 10 000 cycles at 1 A/g	640

graphene@MOF hybrids used in electrodes for batteries					
active material	battery type	operating voltage window	initial discharge capacity	cycling stability	ref
MIL-101(Cr)@rGO/S	Li−S	1.5−3 V	1228 mAh/g at 0.2 C at 1st cycle	66.6% over 50 cycles at 0.2 C	641
GS-S/C_{ZIF8-D}	Li−S	1.0−3 V	∼1171 mAh/g at 168 mA/g at 1st cycle	48% over 120 cycles at 168 mA/g	642
graphene/chromium-MOF (MIL-101(Cr))	Li−S	1.0−3 V	∼1192 mAh/g at 0.1 C at 1st cycle	95% over 134 cycles at 0.8 C	643
Co_9S_8-3DGF/S	Li−S	1.8−2.8 V	∼736 mAh/g at 1 C after 500 cycles	84.9% after 200 cycles at 0.1 C	644
				77.2% after 500 cycles at 1 C	
N-Co_3O_4@N-C/rGO	Li−S	1.5−3 V	∼1223 mAh/g at 0.2 C at initial cycle	77% over 300 cycles at 0.2 C or ∼945 mAh/g at 0.2 C after 300 cycles	645
				∼611 mAh/g at 2 C after 1000 cycles	
graphene-like (analogue) $Ni_3(HITP)_2$	Li−S	1.7−2.8 V	∼1302 mAh/g at 0.2 C at initial cycle	∼848.9 mAh/g at 0.2 C after 100 cycles	646
				∼65% over 100 cycles at 0.2 C	
S-in-MIL-53-on-rGO	Li−S	1.8−2.7 V	∼1250 mAh/g at 0.1 C at initial cycle	67% after 100 cycles at 0.5 C	647

https://doi.org/10.1021/acs.chemrev.2c00270
Chem. Rev. 2022, 122, 17241−17338

Table 8. continued

graphene@MOF hybrids used in electrodes for batteries					
active material	battery type	operating voltage window	initial discharge capacity	cycling stability	ref
MOF-808@S/GEC	Li−S	1.6−2.9 V	~688 ± 56 mAh/g at 0.5 C at 1st cycle	59% after 100 cycles at 0.5 C	648
S/LDH/rGO	Li−S	1.7−2.8 V	~958 mAh/g at 0.2 C at 1st cycle	~60% over 100 cycles at 0.2 C	649
RGO/$ZnCo_2O_4$-ZnO-C/Ni	Li ion	0.01−3 V	~930 mAh/g at 0.1 A/g at 1st cycle	>100% discharge capacity at 0.1 A/g due to electrode activation	650
Fe-MOF/RGO	Li ion	0.01−3 V	~2259 mAh/g at 500 mA/g at 1st cycle	44% over 200 cycles at 500 mA/g	651
N-doped porous carbon-coated rGO	Li ion	0.01−3 V	~1391 mAh/g at 0.5 A/g at 1st cycle	74% over 200 cycles at 0.5 A/g	652
3DGN/CuO	Li ion	0.01−3 V	~569 mAh/g at 100 mA/g at 1st cycle	~72% over 50 cycles at 100 mA/g	653
$Co_2(OH)_2$BDC/CGr	Li ion	0.01−3 V	~2566 mAh/h at 100 mA/g at 1st cycle	~53% over 100 cycles at 100 mA/g	654
SnO_2@N-RGO	Li ion	0.01−3 V	~2217 mAh/g at 200 mA/g at initial cycle	~51% over 100 cycles at 200 mA/g	655
Ni-Co-BTC MOF (flower-like $NiCo_2O_4$)	Li ion	0.01−3 V	~1544 mAh/g at 200 mA/g at initial cycle	~75% over 100 cycles at 200 mA/g	656
FePatNC@rGO	Li ion	0.005−3 V	~1442 mAh/g at 100 mA/g at initial cycle	~57% over 100 cycles at 100 mA/g	657
Fe_2O_3/Co_3O_4/rGO from MIL-88-Fe/ZIF-67/GO	Li ion	0.01−3 V	~1110 mAh/g at 1 A/g at initial cycle	~72% over 110 cycles at 1 A/g	658
Ni@NC-rGO	Li ion	0.01−3 V	~1977 mAh/g at 0.2 A/g at initial cycle	~67% over 120 cycles at 0.2 A/g	659
Al-MOF/graphene composite	Li ion	0.01−3 V	~481 mAh/g at 100 mA/g at initial cycle	~85% over 100 cycles at 100 mA/g	660
Ni_7S_6/graphene nanosheet	Li ion	0.01−2.5 V	~1596 mAh/g at 0.12 A/g at initial cycle	~97% over 2000 cycles at 1 A/g	593
C@GQD	Li ion	0.1−3 V	~708 mAh/g at 100 mA/g at 1st cycle	~62% over 200 cycles at 100 mA/g	661
SnO_2@MOF/graphene composite	Li ion	0.01−3 V	~660 mAh/g at 100 mA/g at 1st cycle	~75% over 100 cycles at 100 mA/g	662
hollow SiO_x@N-doped graphene aerogel (HSiOx@N-GA)	Li ion	0.01−2 V	~2670 mAh/g at 0.1 C at 1st cycle	~86% over 500 cycles at 10 C	663
3D hollow porous carbon/graphene composites	Li ion	0−3 V	~1237 mAh/g at 100 mA/g at first cycle	highly stable for 1000 cycles at 5 A/g	664
Fe_3O_4 QDs@C/rGO	Li ion	0.01−3 V	~1445 mAh/g at 100 mA/g	~92% over 300 cycles at 500 mA/g	665
Co-TCPP MOF/rGO composite	Li ion	0.01−3 V	~2316 mAh/g at 100 mA/g	~45% over 100 cycles at 100 mA/g	31
FeS@carbon (FeS@C)-graphene	Na ion	0.01−3 V	~507 mAh/g in the initial cycle at 0.1 A/g	~97% over 300 cycles at 1 A/g	666

[a]Abbreviations: G, glucose; HQG, high-quality graphene; rGO, reduced graphene oxide; LDH, layered double hydroxides; Ni-CAT, Ni-catecholate; LSG, laser scribed graphene; N-GQDs, N-doped graphene quantum dots; GA, graphene aerogel; NG-A, N-doped graphene aerogels; CoBTC, cobalt-benzene tricarboxylic acid; PET, polyester fabric.

innovative electrode design using the rGO/CoSx-rGO/rGO composite, which was prepared from a nanocomposite designated ZIF-GO obtained by mixing ZIF-67 nanocubes with a GO solution. During this process, the ZIF-67 nanocubes underwent a morphological change and were converted into 2D nanoflakes. A sandwich-like GO/ZIF-GO/GO hybrid film was then fabricated by the successive vacuum membrane filtration of GO, ZIF-GO, and GO solutions followed by a hydrothermal sulfidation/reduction process. The resulting freestanding rGO/CoS_x-rGO/rGO hybrid film demonstrated good electrochemical performance due to the Faradaic (battery-like) properties of CoS_x and the good conductivity and EDL capacitance of rGO. An all-solid-state hybrid SC with the rGO/CoSx-rGO/rGO film as the positive electrode and a negative AC electrode had an energy density of 10.56 Wh/kg and a power density of 2250 W/kg while retaining 92.8% of its initial capacitance after 10 000 cycles. Building on these findings, many other graphene-MOF hybrids have been prepared using diverse strategies and tested in supercapacitors; these systems are listed in Table 8.

Overall, it is clear that graphene@MOF hybrids are promising electrode materials for SCs due to their outstanding electrochemical properties, which include high energy storage capacity, high power, and excellent cycling stability. These exciting features can be attributed to their unique architectures, which typically confer high specific surface areas, an abundance of active sites, favorable pore size distributions, and good conductivity. However, it should be noted that despite the promising performance of these graphene-based materials, considerable improvements will be needed to obtain practically useful supercapacitors. Therefore, more research is needed to investigate graphene@MOF composites featuring various new MOFs (e.g., conducting MOFs and 2D-MOFs) and different forms of graphene including heteroatom-doped, functionalized, and 3D porous sponge-like graphene.

5.3.2. Li-Ion Batteries (LIBs). Since they were introduced into the market by Sony in 1991, LIBs have found applications in a vast array of commercial products ranging from small portable electronics to large electric vehicles and grid-scale energy storage systems.[586] In general, the power and capacity of a LIB is

https://doi.org/10.1021/acs.chemrev.2c00270
Chem. Rev. 2022, 122, 17241−17338

dictated by the properties of its electrode materials. Unfortunately, current LIBs suffer from low rate performance, sluggish lithium diffusion, and poor cycle lives due to the low electrical conductivity and poor structural stability of intercalation-based electrode materials. Therefore, great efforts have been devoted to developing new electrode materials with higher theoretical capacities and greater long-term cycling stability. Several studies have identified MOF/graphene-based composites as promising materials in this context.

Solvothermal methods are commonly used to synthesize graphene@MOF composites for battery electrodes. For instance, a flower-like Co-TCPP MOF/rGO composite was prepared by combining cobalt *meso*-tetrakis(4-carboxyphenyl)-porphyrin (Co-TCPP MOF) with rGO in a one-pot process.[587] Both Co-TCPP MOF and Co-TCPP MOF/(15 wt %)rGO performed well as anode materials in LIB. The flower-like Co-TCPP MOF delivered a capacity of 854 mAh/g after 100 cycles, which was significantly boosted to 1050 mAh/g at 100 mA/g by the formation of a composite with rGO (15 wt %). The introduction of rGO effectively prevents the stacking of MOF nanoparticles and facilitates the formation of a continuous conductive framework with entangled graphene that enables rapid transport of electrons and ions. Interestingly, the composite retained a specific capacity of 650 mAh/g after 300 cycles even at 1000 mA/g, which was attributed to its 3D ultrathin lamellar structure, which exposes an abundance of electroactive sites, reduces the diffusion distance of Li^+ to the internal electroactive sites, and improves the overall electrical conductivity. Fe-MOF/rGO was also reported to be a promising LIB anode material. Pristine Fe-MOF undergoes various irreversible reactions when used as an anode material, resulting in a poor Coulombic efficiency (35.5%). However, the incorporation of rGO (5 wt %) improved the electrode's Coulombic efficiency to 43.3% while also increasing the rate capability and cyclic stability. Accordingly, electrochemical impedance analysis showed that incorporating 5 or 10 wt % rGO reduced the resistance of Fe-MOF and thus facilitated ion transfer at the electrochemical interface. A particularly important parameter for LIB electrode materials is the cycling life, which depends strongly on the structural stability of the electrode material. It is thus notable that Gao et al.[588] developed an Al-MOF/graphene hybrid that can serve as a highly stable LIB anode material. An Al-based MOF (MIL-53) was synthesized using a hydrothermal method in water and combined with GO to form an Al-MOF/GO composite, after which the GO was reduced to graphene with vitamin C. When used as a LIB anode, the resulting Al-MOF/graphene composite demonstrated significantly better electrochemical performance than the pristine Al-MOF. Interestingly, it was found that Li intercalation and deintercalation induced a structural change in Al-MOF/GO that manifested as an order−disorder transition, leading to more open channels for Li diffusion and storage.

The above discussion shows that growing MOFs with graphene-based materials can improve their electrochemical performance to a degree. However, their poor electrical conductivity (due to the nonconductivity of their organic linkers) still restricts their rate performance and cycle life when used as LIB electrodes. To overcome this problem, several researchers have transformed MOFs into carbon materials and combined them with graphene derivatives to obtain new LIB anode materials.[589] For instance, a carbon-on-carbon composite was prepared by combining a porous carbon material derived from the MOF ZIF-8 with graphene quantum dots (GQDs) using an in-situ self-assembly method.[64] The resulting composite exhibited an excellent SSA of 668 m^2/g with tailored micro- and mesopores. When used as a LIB anode, this composite delivered promising reversible capacity and outstanding cycle stability (493 mAh/g at 100 mA/g after 200 cycles). These exciting properties were attributed to its hierarchical pore structure and high surface area, both of which facilitate ion diffusion and thus accelerate Li insertion/deinsertion. Similarly, N-doped porous carbon-coated graphene (NPC@graphene) was synthesized by carbonizing in-situ grown ZIF-8 on GO.[590] The N doping, rich porosity, and high electrical conductivity of this carbon-on-carbon hybrid created synergies that resulted in outstanding performance when used as a LIB anode: its initial discharge and charge capacities were 1391 and 873 mAh/g, respectively, with an initial Coulombic efficiency of around 62.7%. These results are far better than those for graphite-based anodes, which have a theoretical maximum capacity of 372 mAh/g. The composite also exhibited a reversible capacity of 1040 mAh/g after 200 cycles at 0.5 A/g with excellent rate performance.

Anode materials based on metal chalcogenides (oxides/carbide/phosphides) are attractive for LIBs due to their high energy storage capacity and power output. However, most of them suffer from poor electrical conductivity and structural instability, which reduces their rate performance and cycling stability. An emerging solution to these problems is to combine porous metal oxides with conducting supports such as graphene. MOFs with tailored porosity were recently proposed as ideal precursors for highly porous metal oxides/sulfides with uniform pore distribution. For instance, Wang et al.[591] proposed an innovative double-buffering strategy in which the MOF MIL-100(Fe) was grown on graphene oxide and then calcinated to obtain ultrafine and well-dispersed mesoporous carbon-coated Fe_3O_4 QDs (4 nm) embedded in rGO (Fe_3O_4 QDs@C/rGO). In this composite, the graphene and the mesoporous carbon serve as a conductive scaffold for homogeneous anchoring of the Fe_3O_4 QDs that provides confined double buffering to accommodate and control cyclic changes in volume resulting from Li intercalation and deintercalation. This unique electrode architecture with a hierarchically porous structure gives the composite a high reversible lithium-ion storage capacity with excellent long-term cyclic stability after 2000 cycles (505 mAh/g at 2 A/g). In terms of rate performance, the Fe_3O_4 QDs@C/rGO composite achieved capacities of 878 and 234 mAh/g at 0.1 and 5 A/g, respectively. Moreover, when the current density was returned to 0.1 A/g, its measured capacity was 890 mAh/g (100% retention after 60 cycles at various current densities), indicating that the introduction of GO and the composite's well-designed layered array architecture conferred good structural stability and Li^+ storage reversibility. Similarly, Li et al.[592] synthesized ultrafine MnO nanoparticles on graphene-interconnected N-doped 3D carbon frameworks (MnO@NC-G) by pyrolyzing a GO-wrapped Mn(II)-MOF composite and used the resulting material in cathodes for Li-CO_2 batteries. Benefiting from the combined merits of its individual components, the MnO@NC-G composite delivered an unprecedentedly high discharge capacity of 25021 mAh/g between 2.0 and 4.5 V with a Coulombic efficiency of 95.6%. In rate-performance tests, these electrodes completed 10 reversible cycles with a cutoff capacity of 5000 mAh/g (1.33 mAh/cm^2) when measured at 400 mA/g. In addition, at 1 A/g, the electrode could complete over 200 cycles with a capacity limit of 1000 mAh/g and was able to complete another 176 cycles without loss

https://doi.org/10.1021/acs.chemrev.2c00270
Chem. Rev. 2022, 122, 17241−17338

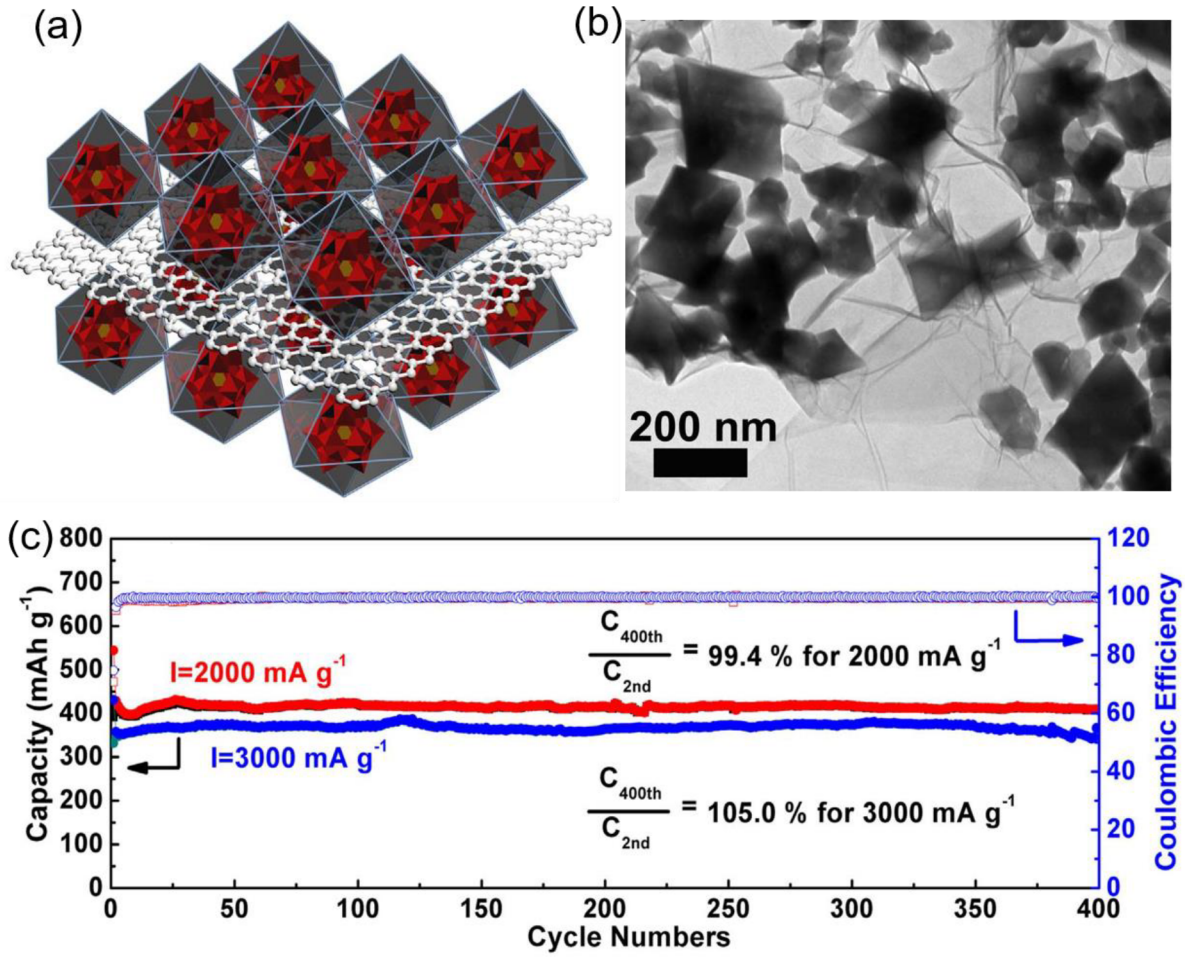

Figure 44. (a) Fabrication of POMOF/rGO composite with Keggin's-type $H_5PMo_{10}V_2O_{40}$ ($PMo_{10}V_2$)-POM, Cu-MOF, and GO. (b) SEM image of POMOF/rGO hybrid. (c) Stability test of POMOF/rGO hybrid over 400 cycles at current densities of 2 and 3 A/g. Reproduced with permission from ref 597. Copyright 2017 Elsevier.

of performance after replacing the lithium anode and electrolyte. This indicates that its cycle life within a battery is limited by ineffective anode protection. These results suggest that effective cathode materials for Li-CO_2 batteries should have (1) dispersed catalytic species, (2) fast electron transport, and (3) robust interconnected networks. Similarly, a polymer-templated strategy was used to synthesize a Ni_7S_6/graphene composite.[191,593] The first step in this composite's preparation involved hydrothermal treatment of a 2D nickel-based metal framework $[Ni(C_4O_4)(H_2O)_2]_n$ obtained from $Ni(OH)_2$ and squaric acid ($H_2C_4O_4$) in the presence of the structure-directing agent polyvinylpyrrolidone (PVP). The resulting 2D Ni-MOF sheets were then mixed with graphene and transformed into Ni_7S_6/graphene by in-situ sulfidation using thiourea as the sulfur source. Spectroscopic and microscopic measurements showed that the hybrid consisted of nickel sulfide layers intercalated between graphene sheets. The Ni_7S_6/graphene composite showed a reversible capacity of 1010 mAh/g at 0.12 A/g with a Coulombic efficiency of 98%. Moreover, when used as an anode material, it exhibited remarkable cycle stability (~95% capacity retention after 2000 cycles). Ex-situ characterization of the electrode demonstrated that its charge storage is based on a conversion mechanism, and the material exhibited good structural stability even after many charge/discharge cycles. These outstanding electrochemical features were ascribed to the synergistic effects of Ni_7S_6 and graphene: graphene acts as a conducting matrix, while Ni_7S_6 offers Faradaic charge storage. Gao et al.[594] prepared a doubly carbon-coated FeP composite (FeP@NC@rGO) by in-situ phosphorization of a Prussian blue@GO (PB@GO) precursor. SEM images showed that FeP nanocrystals were embedded in the nitrogen-doped porous carbon matrix of the resulting material. When tested in LIBs, FeP@NC anodes delivered a poor specific capacity of 89 mAh/g after 100 cycles, but a significantly better capacity (830 mAh/g) was achieved upon adding rGO. In addition, the FeP@NC@rGO electrode had reversible capacities of 751 and 359 mAh/g at 0.1 and 5 A/g, and its reversible capacity returned to 737 mAh/g upon reducing the current density to 0.1 A/g after 60 cycles at 5 A/g. It thus exhibits remarkable reversibility with around 99.25% capacity retention. These results show that the conductivity of FeP nanoparticles is greatly enhanced by graphene coating and being embedded in porous carbon and that the resulting material can accommodate their large changes in volume during cycling.

Unlike transition-metal oxides/sulfides, graphene@MOF hybrids have also been investigated in conjunction with polyoxometalates (POM). POMs are an exceptional group of inorganic redox-active materials consisting of multiple metal oxide ions that are linked by oxygen atoms to form nanoclusters within an ordered three-dimensional framework.[595,596] Their rapid and highly reversible redox activity gives them remarkable electrochemical properties. Wei et al.[597] prepared POMOF/

https://doi.org/10.1021/acs.chemrev.2c00270
Chem. Rev. 2022, 122, 17241−17338

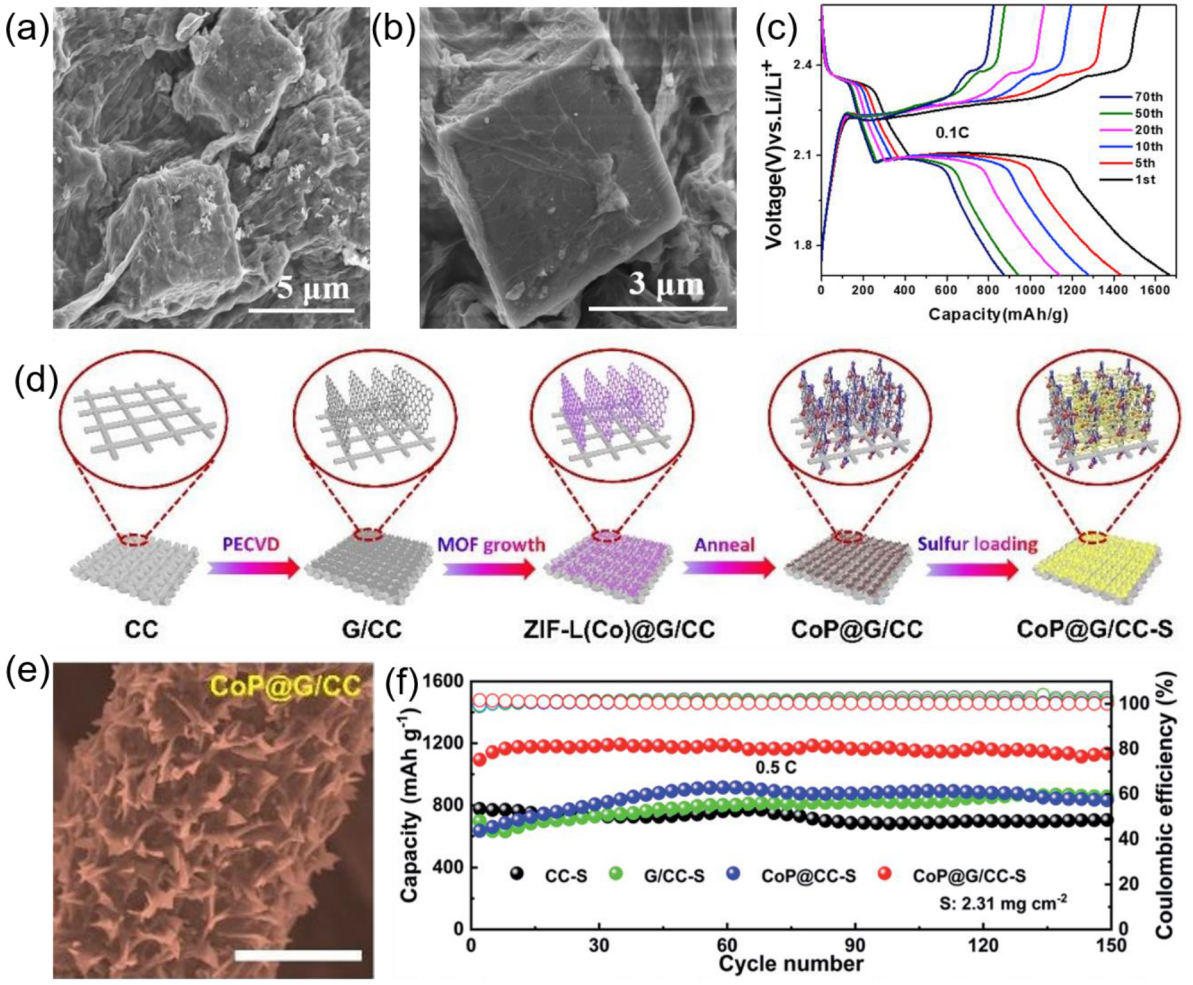

Figure 45. (a and b) SEM images of Fe-soc@GO at two different magnifications. (c) Galvanostatic charge/discharge profiles for the S/Fe-soc@rGO hybrid over 70 cycles at 0.1 C. Reproduced with permission from ref 598. Copyright 2020 Elsevier. (d) Synthesis of self-supported CoP@G/CC-S cathode. (e) SEM image of self-supported CoP@G/CC-S. (f) Cycling performance of CoP@G/CC-S, CC-S, G/CC-S, and CoP@CC-S cathodes at 0.5 C. Reproduced with permission from ref 599. Copyright 2020 Royal Society of Chemistry.

rGO using $H_5PMo_{10}V_2O_{40}$, which is a Keggin-type POM designated ($PMo_{10}V_2$)-POM, together with HKUST-1 (Cu-MOF) and GO, as shown in Figure 44a. In the resulting POMOFs/rGO hybrid, the heteropolyanions of ($PMo_{10}V_2$)-POM provide multiple redox-active species while the MOF HKUST-1 serves as a porous scaffold with a suitable size and shape for POM adsorption, and the rGO films provide electrical conductivity for ion transportation while preventing aggregation of the nano-POMOFs particles. The POM-loaded MOF was uniformly dispersed on the surface of rGO, as shown in Figure 44b. The resulting composite demonstrated remarkable electrochemical performance as a LIB anode, with a reversible capacity of 1075 mAh/g after 100 cycles and good rate performance with 100% capacity retention at both 2000 and 3000 mA/g after more than 400 cycles (Figure 44c). Combining the multielectron redox capabilities of POMs with the high conductivity of rGO and the open structure of the MOF thus buffers the volume expansion of the POMs during cycling and thereby delivers good cycling stability.

Owing to their high crystallinity, large surface area, and hierarchical porosity, graphene@MOF hybrids have also been proposed as potential host materials for sulfur in Li−S batteries. Although Li−S batteries are an attractive energy storage technology due to their high theoretical capacity and energy density, sluggish reaction kinetics and rapid capacity decay have obstructed their commercial use. To address these issues, Yao et al.[598] developed a sulfur host in which the MOF Fe-soc is wrapped with rGO. SEM images (Figure 45a and 45b) demonstrated uniform wrapping of the MOF, and the as-prepared S/Fe-soc@rGO composite achieved an initial discharge capacity of 1634.3 mAh/g with a stable capacity retention of 865.3 mAh/g after 80 cycles (Figure 45c). The composite also delivered discharge capacities of 638.8 and 334.3 mAh/g after 200 cycles at 0.5 and 1 C, respectively. In this system, the unsaturated metal sites of Fe-soc efficiently adsorb both elemental sulfur and polysulfides. At the same time, the stable porous structure of the MOF facilitates fast ion transport and thus increases the ion diffusion rate while also constraining volume changes during charge/discharge cycling. Several MOF-derived metal phosphides, carbides, and sulfides have also been used as immobilizing agents and electrocatalysts to overcome the shuttling effect.[599,600] For instance, Jin et al.[599] prepared a composite of MOF-derived CoP anchored on vertical graphene on a carbon cloth (CC) support (CoP@G/CC) as a freestanding hybrid sulfur host (Figure 45d).

This material was obtained by growing 3D porous graphene vertically on CC, which offers a conductive network for carrier transport and electrolyte penetration while also enabling the

https://doi.org/10.1021/acs.chemrev.2c00270
Chem. Rev. 2022, 122, 17241−17338

adsorption of sulfur species and accommodating the associated volume changes to ensure a high loading of active material. MOF-derived CoP nanostructures were then grown on the vertical graphene surface where they can efficiently immobilize and participate in electrocatalytic interactions with Li-polysulfides, thereby suppressing the shuttle effect and promoting fast redox processes (Figure 45e). This made it possible to attain large capacities at high rates with low voltage polarization. Accordingly, CoP@G/CC-S cathodes delivered a capacity of 1195 mAh/g at 0.5 C and retained a capacity of 1135 mAh/g after 150 cycles, outperforming CC-S, G/CC-S, and CoP@CC-S cathodes (Figure 45f). Cells using these cathodes also retained a capacity of 1044.9 mAh/g after 500 cycles at high rates of 2 C. Even at a high sulfur loading of 10.83 mg/cm^2, CoP@G/CC-S cathodes retained a high areal capacity of 8.81 mAh/cm^2 at 0.05 C. Importantly, the authors also prepared flexible Li−S pouch cells with self-supported CoP@G/CC-S cathodes that offered impressive rate and cycling performance when subjected to various mechanical deformations. Similarly, Xu et al.[601] prepared Ni−Co LDH-wrapped rGO using ZIF-67 as an effective sulfur host. The high specific surface area of LDH/rGO (324 m^2/g) allows easy polysulfide adsorption, and the excellent conductivity of rGO facilitates electron transfer between LDH and the insulating sulfur. When tested as a cathode, S/LDH/rGO had an initial discharge capacity of 958 mAh/g at 0.2 C with a Coulombic efficiency of 99% and also showed good rate capability with a capacity of 730 mAh/g at a high current density of 1 C. In another study, a separator coated with catalytic and conductive Fe_3C nanoparticles dispersed over conductive N-doped graphene was prepared using the bimetallic MOF Fe/Zn-bio-MOF-100 to suppress the shuttle effect.[600] At low mass loadings (1 mg/cm^2), the composite delivered a capacity of 1248.1 mAh/g. Moreover, after 300 cycles, cells with Fe_3C/NG-coated separators retained a capacity of 1020.6 mAh/g and had a Coulombic efficiency of almost 100%, implying that no shuttle effect occurred during cycling. Even at a high current density of 6 C, Li−S cells with Fe_3C/NG-coated separators showed a capacity of 954.5 mAh/g in the first cycle, which was reduced to 439.9 mAh/g after 500 stable cycles.

5.3.3. Beyond LIBs. Although LIBs currently outperform alternative battery technologies, the limited and uneven distribution of lithium resources and the high cost of raw materials are barriers to their further development. Moreover, the energy storage capabilities of LIBs are insufficient for emerging applications such as the electrification of vehicles and energy grids. Consequently, there is a clear need for another leap in battery technology that will enable the production of safe, inexpensive, and high-energy devices. Because they could potentially be made using inexpensive and abundant resources while offering greater safety than LIBs, Na-, K-, and Zn-ion batteries have received considerable attention recently. Graphene@MOF composites have many potential applications in these battery types.

The major challenge in developing high-performance Na-ion batteries (SIBs) is to find suitable electrode materials to host relatively large Na ions. Composites of several MOFs and their derivatives with graphene have therefore been explored as anode materials for SIBs. For example, Wei et al.[602] synthesized a hollow urchin-like F-doped Co-MOF on rGO using a solvothermal method and used it as a SIB anode. When tested at current densities of 0.1, 0.2, 0.5, 1, and 2 A/g, the F-Co-MOF/rGO electrode achieved average capacities of 354.5, 264.3, 218.9, 174.8, and 128.9 mAh/g, respectively. It also demonstrated good cycling stability, retaining a capacity of 181.6 mAh/g at 0.1 A/g after 100 cycles with a Coulombic efficiency of 99.98%. MOF-derived metal chalcogenides are promising electrode materials for SIBs due to their tunable porous structure, which provides easy access to electrochemically active sites and short diffusion lengths. An $FeSe_2$@rGO composite was therefore prepared using a template-assisted method with GO/Fe-MOF (MIL-88-Fe) as the precursor.[603] MIL-88-Fe was formed by mixing ferric chloride and fumaric acid under heating, then the MOF was stirred with a suspension of GO, and the resulting material was subjected to selenization to provide the $FeSe_2$@rGO hybrid. In this material, the $FeSe_2$ particles are tightly wrapped with GO, which limits their growth and causes $FeSe_2$ to inherit the morphology of the precursor. When used as a SIB anode, $FeSe_2$@rGO exhibited 2−3-fold better electrochemical performance than either $FeSe_2$ or rGO with a capacity of 392 mAh/g at 5000 mA/g (vs 172 and 98.6 mAh/g, respectively). Because of its small nanoparticles and high surface area, the $FeSe_2$@rGO composite exhibits a high reversible capacity of 350 mAh/g after 600 cycles at 5000 mA/g as well as excellent rate performance as indicated by its discharge specific capacities of 558.5 mAh/g at 0.1 A/g and 390.5 mAh/g at 5 A/g (corresponding to the retention of 70% of the initial capacity). In-situ structural characterization confirmed that the electrode's charge−discharge reactions were highly reversible, indicating that the electrode material possesses excellent structural stability. Tin-based materials are also seen as suitable anode candidates with promising sodium-ion storage capacity for rechargeable batteries due to their special alloying/dealloying-type storage mechanism. An MOF-derived SnSe/C composite wrapped with N-doped graphene (NG@SnSe/C) was therefore designed for Na-ion storage.[604] A Sn-MOF was prepared by a simple wet chemistry method and then subjected to thermal selenization to form SnSe/C, which was wrapped with N-doped graphene using direct plasma-enhanced chemical vapor deposition (PECVD). The resulting NG@SnSe/C composite exhibited good electrical conductivity and structural stability due to its "inner" carbon framework formed by thermal treatment of the MOF together with its "outer" graphitic cage from the PECVD synthesis. Consequently, NG@SnSe/C anodes had a reversible capacity of 650 mAh/g at 0.05 A/g, a favorable rate performance of 287.8 mAh/g at 5 A/g, and good cycle stability with a negligible capacity decay of 0.016% per cycle over 3200 cycles at 0.4 A/g. Their sodium-ion storage properties were systematically investigated using first-principles simulations, while the electrode's structural stability was confirmed by in-situ XRD and ex-situ TEM analysis. To determine the practical utility of these electrodes, Na-ion capacitor full cells were constructed using NG@SnSe/C anodes and AC cathodes, delivering energy and power densities of 115.5 Wh/kg and 5742 W/kg, respectively. These cells also exhibited stable cycling for 1100 cycles. Potassium is seen as another promising alternative to lithium for batteries because its reserves are effectively unlimited and its intercalation chemistry is similar to that of lithium. The low standard reduction potential of K^+/K (−2.93 V versus E^0, which is close to the Li^+/Li reduction potential of −3.03 V versus E^0) allows high energy densities and fast ion transport kinetics in electrolytes. Graphene@MOF composites have therefore been evaluated as potential electrode materials capable of reversibly hosting large K^+ ions.[605−607] For example, rGO-wrapped MOF-derived FeS_2 hollow nanocages (FeS_2@rGO) were tested in KIB anodes.[608] This material was obtained by using Prussian blue (PB) as a source of Fe and

https://doi.org/10.1021/acs.chemrev.2c00270
Chem. Rev. 2022, 122, 17241−17338

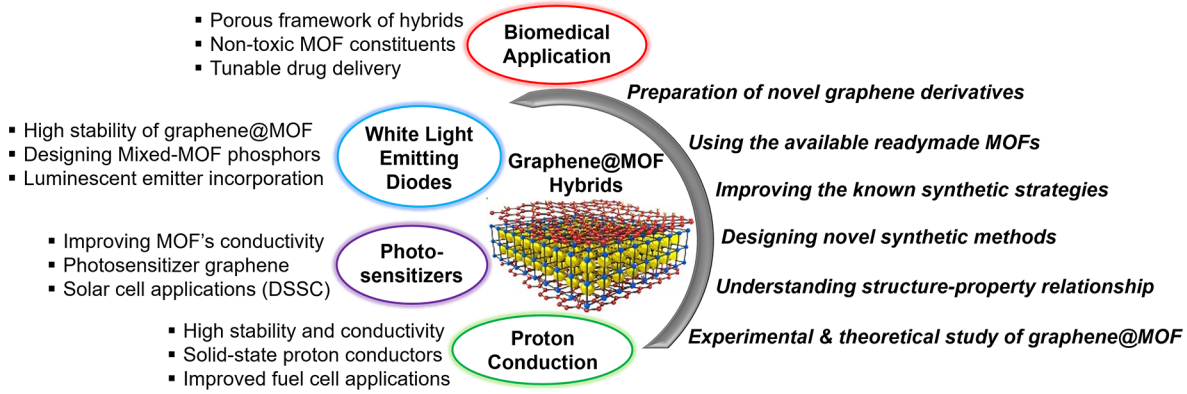

Figure 46. Directions for future research on graphene@MOF hybrids.

mixing it with a GO solution followed by thermal reduction to obtain Fe@rGO, which was then transformed into FeS_2@rGO 3D hollow nanocages via a sulfidation process. Owing to the synergistic interaction between the FeS_2 nanocages and rGO shells, the FeS_2@rGO hybrid exhibited superior electrochemical performance; it had a high capacity of 264 mAh/g after 50 cycles at 50 mA/g and 123 mAh/g after 420 cycles at 500 mA/g, implying 47% retention of its initial capacity.

The above discussion clearly shows that combining graphene and its derivatives with a MOF matrix can improve the electrical properties of the MOF and establish a conductive network in the electrode. The resulting hybrids can significantly increase the cycling stability of Li−S batteries by confining the polysulfide species. In addition, unique electrode architectures such as porous MOFs and conductive graphene scaffolds shorten the diffusion paths for electrolyte ions and accelerate phase-transfer reactions, resulting in enhanced rate performance and cycling stability. Despite the advances that have been made in the field of graphene@MOF composites for battery applications, several challenges remain to be addressed. For instance, very few solvothermal, hydrothermal, or direct mixing methods have been used to prepare graphene@MOF hybrids. Newer synthesis methods such as self-assembly and layer-by-layer fabrication should also be investigated because they could provide composites with novel morphologies and surface features. Similarly, combinations of graphene derivatives with new MOFs such as conductive MOFs should be explored to identify materials with exceptional electrochemical performance.

6. FUTURE DIRECTIONS AND CONCLUDING REMARKS

Graphene@MOF hybrids are a very interesting and extensively studied class of MOF hybrids. While the pristine components of these hybrids, i.e., graphene derivatives and MOFs, possess useful properties, they also have distinct limitations that have prompted researchers to shift their attention to the fabrication of graphene@MOF hybrids. MOFs are fascinating functional porous materials that have attracted great interest over the last few decades because of their remarkable features, which include high tunability, porosity, and large surface areas together with low densities, giving them applications in diverse fields. However, their instability under harsh and humid conditions seriously limits their potential uses. One way of avoiding these problems is to synthesize hybrids of MOFs with other materials. Out of the different types of MOF hybrids, the graphene@MOF hybrids are most interesting nowadays.

This review is based on a critical analysis, deep understanding, and in-depth study of graphene@MOF hybrids and covers almost all issues relating to these materials, ranging from their synthesis to their applications. We have clarified the motivation for synthesizing and studying graphene@MOF hybrids by describing how the properties of pristine MOFs can be enhanced or modified through hybridization with graphene and its derivatives, expanding their potential range of applications. Properties of pristine MOFs that can be modified by hybridization with graphene derivatives include their texture, morphology, stability, electronic properties, and surface properties as well as the accessibility, abundance, and characteristics of their active sites. Moreover, the way in which these properties are modified can be controlled by varying the content of the graphene derivative in the graphene@MOF hybrid or by varying the nature of the graphene derivative that is used. It is thus possible to tune the properties of these hybrids for specific purposes. The properties and applications of graphene@MOF hybrids are also influenced by the synthetic methods used in their fabrication. Several different synthetic methods have been used to prepare graphene@MOF hybrids, ranging from the very commonly used in-situ synthetic approach to the much rarer in-situ polymerization approach. General protocols for all of these methods have been presented, and their capabilities have been illustrated by discussing the graphene@MOF hybrids obtained in each case. These examples provide useful insights into strategies that can be used to design graphene@MOF hybrids for various applications.

In accordance with the main objective of this review, we have also discussed the applications of graphene@MOF hybrids in environmental remediation, catalysis, and energy storage and conversion. Like pristine MOFs, graphene@MOF hybrids have porous structures that make them suitable for gas adsorption applications. These hybrids have thus emerged as capable adsorbents of gases including CO_2, CH_4, NH_3, and H_2S. Because of their permanent porosity, controllable pore size distributions, and high surface areas, they have also been used in separation applications including hydrocarbon separation, pollutant removal from water, and oil−water separation.

The successful hybridization of graphene derivatives with MOFs ensures uniform distribution of MOFs within the hybrids, increasing the exposure of their catalytic active sites. Consequently, such hybrids have also been used extensively as heterogeneous catalysts for organic transformations and also as photocatalysts and electrocatalysts in various photocatalytic and electrocatalytic processes. Some MOFs have interesting photocatalytic activity, but their practical usefulness is often limited by

https://doi.org/10.1021/acs.chemrev.2c00270
Chem. Rev. 2022, 122, 17241−17338

issues such as poor conductivity, facile recombination of charge carriers, and limited production of photogenerated charge carriers, which cause them to suffer from poor efficiency. Graphene@MOF hybrids can avoid these limitations and thus offer superior photocatalytic efficiency. Similarly, graphene@MOF hybrids can offer better electrocatalytic properties than pristine MOFs, making them suitable for various electrocatalytic applications. These hybrids also show fascinating performance in energy storage/conversion applications because hybridization with graphene derivatives yields materials that have greater conductivity than pristine MOFs but also retain a porous framework that allows fast diffusion of electrons and ions, enabling outstanding performance in energy storage and conversion devices such as supercapacitors and batteries. In addition to graphene@MOF hybrids, materials derived from these hybrids by controlled degradation of the MOF component to obtain new carbon materials have shown great promise in energy storage and conversion applications. As a result, graphene@MOF hybrids and their derivatives have been used to improve the performance of supercapacitors, lithium-ion batteries, and batteries with alternative chemistries.

6.1. Future Perspectives

Given the remarkable advances that have been made in the field of graphene@MOF hybrids, it might seem difficult to identify directions for future research in this area. However, we are confident that there remain several unexplored directions of research on graphene@MOF hybrids. These directions are illustrated in Figure 46 and discussed in more detail below.

(1) Graphene@MOF hybrids have found practical applications in many fields, but their use in biomedical science has been very limited. However, given the biomedical applications of pristine MOFs, it is very likely that graphene@MOF hybrids will also show high performance in various biomedical applications, particularly in drug delivery. Since these hybrids have larger surface areas than pristine MOFs while retaining a highly porous framework, graphene@MOF hybrids based on nontoxic biocompatible MOFs could be powerful vehicles for drug delivery. Importantly, the ability to tune the properties of such hybrids by varying their content of graphene derivatives could enable tunable drug delivery.

(2) MOFs with the ability to function as solid-state proton conductors (SSCs) have recently been investigated as solid electrolytes for fuel cell applications. MOF-based SSCs have high proton conductivity resulting from an extensive H-bonding network. Because hybridizing MOFs with graphene derivatives can improve their stability and conductivity, it should be possible to develop SSCs based on graphene@MOF hybrids for fuel cell applications. The high conductivity of graphene@MOF hybrids will enable rapid proton conduction, while their high stability should enable their long-term use.

(3) Dye-sensitized solar cells (DSSCs) use photosensitizing dyes to generate electricity. Although MOFs have been used in DSSCs, their poor conductivity and inferior light-harvesting ability yielded uninspiring performance.[224] However, graphene and its derivatives have been successfully used as photosensitizers in diverse applications.[667] These observations strongly suggest that photosensitizers based on graphene@MOFs could have excellent performance. Indeed, one such hybrid was recently used as a photosensitizer in a DSSC.[224] This represents a relatively new direction for graphene@MOF hybrids, and we anticipate that further studies on their photosensitizing capabilities will markedly improve the performance of MOF-based DSSCs and related devices.

(4) Like proton conduction, the fabrication of light-emitting diodes is a relatively new application of MOFs. Luminescent MOFs have been used to prepare phosphor-converted white-light-emitting diodes (pc-LEDs),[668] and mixed-MOF phosphors can be prepared by incorporating luminescent emitters (e.g., metal complexes, organic dyes, or quantum dots) into the MOF framework; carbon dots have also recently been used for this purpose.[668] However, the limited stability of the MOF pore structure restricts their range of potential applications in this area. Because graphene@MOF hybrids have stable and conductive architectures, they could be used to prepare more robust mixed-MOF phosphors with interesting performance in white-light emission applications.

6.2. Perspectives on Designing Graphene@MOF Hybrids

On the basis of interwoven structures and bespoke properties thereof, we summarize the following design principles.

(1) Currently, most synthetic approaches rely upon the self-assembly of MOFs and graphene (or its derivatives), and for that reason, controlling the electronic properties of the resulting hybrids has been challenging. In the future, we expect that with the advances in atomically precise design of nanographenes and graphene nanoribbons as well as with progress in the design of layer-defined van der Waals heterostructures, the tunability of the electronic band structure of graphene@MOF hybrids will be further increased.[669−675] There are already examples where nanographenes and graphene nanoribbons have been used as coordinating linker molecules to construct MOFs or framework architectures, whereas functionalized bulk graphenes have been used to covalently build up more precise hybrid structures. A lot of promise lays in such materials, since they are atomically/molecularly precise and they enable the observation of new electronic phenomena or may allow one to improve the usability of graphene@MOF hybrids in previously discussed applications, particularly if synthetically controlled band structure tuning is beneficial. The design of graphene@MOF van der Waals heterostructures is closely intertwined with the progress of MOF nanosheets. In recent years, publications on conductive layered metal−organic frameworks have surged like never before, and such framework assembly (in a layer-by-layer fashion via the Langmuir−Blodgett method or the Langmuir−Schaefer method) seems promising to prepare layer-precise graphene/MOF heterostacks.

(2) Water-stable MOFs are a natural choice to afford water-stable graphene@MOF hybrids, and in general, it is highly unlikely that compositing water-labile MOFs, such as HKUST-1, with graphenes will enable amenability to function in aqueous media. X-ray diffractogram-based stability claims for such graphene@water-unstable MOFs notwithstanding, exhaustive stability evaluation, such as adopting accelerated stability tests (a benchmark in pharmaceutical industry), should be a common practice in this area.[676]

https://doi.org/10.1021/acs.chemrev.2c00270
Chem. Rev. 2022, 122, 17241−17338

To conclude, graphene@MOF hybrids are an important class of hybrid MOFs with several fascinating properties that have been exploited in a wide range of applications. We anticipate that this review will help accelerate the ongoing research on graphene@MOF hybrids and encourage further development of this class of hybrid materials.

AUTHOR INFORMATION

Corresponding Authors

Kolleboyina Jayaramulu − *Department of Chemistry, Indian Institute of Technology Jammu, Jammu and Kashmir 181221, India; Regional Centre of Advanced Technologies and Materials, Czech Advanced Technology and Research Institute (CATRIN), Palacký University Olomouc, Olomouc 783 71, Czech Republic;* orcid.org/0000-0003-4923-5065; Email: jayaramulu.kolleboyina@iitjammu.ac.in

Radek Zbořil − *Regional Centre of Advanced Technologies and Materials, Czech Advanced Technology and Research Institute (CATRIN), Palacký University Olomouc, Olomouc 783 71, Czech Republic; Nanotechnology Centre, CEET, VŠB-Technical University of Ostrava, Ostrava-Poruba 708 00, Czech Republic;* orcid.org/0000-0002-3147-2196; Email: radek.zboril@upol.cz

Roland A. Fischer − *Inorganic and Metal−Organic Chemistry, Department of Chemistry and Catalysis Research Centre, Technical University of Munich, Garching 85748, Germany;* orcid.org/0000-0002-7532-5286; Email: roland.fischer@tum.de

Authors

Soumya Mukherjee − *Inorganic and Metal−Organic Chemistry, Department of Chemistry and Catalysis Research Centre, Technical University of Munich, Garching 85748, Germany;* orcid.org/0000-0003-2375-7009

Dulce M. Morales − *Analytical Chemistry, Center for Electrochemical Sciences (CES), Faculty of Chemistry and Biochemistry, Ruhr-Universität Bochum, Bochum D-44780, Germany; Nachwuchsgruppe Gestaltung des Sauerstoffentwicklungsmechanismus, Helmholtz-Zentrum Berlin für Materialien und Energie GmbH, Berlin 14109, Germany;* orcid.org/0000-0002-9420-2724

Deepak P. Dubal − *School of Chemistry and Physics, Queensland University of Technology (QUT), Brisbane, Queensland 4001, Australia;* orcid.org/0000-0002-2337-676X

Ashok Kumar Nanjundan − *School of Chemistry and Physics, Queensland University of Technology (QUT), Brisbane, Queensland 4001, Australia;* orcid.org/0000-0001-6502-0844

Andreas Schneemann − *Lehrstuhl für Anorganische Chemie I, Technische Universität Dresden, Dresden 01067, Germany;* orcid.org/0000-0001-6801-2735

Justus Masa − *Max Planck Institute for Chemical Energy Conversion, Mülheim an der Ruhr D-45470, Germany;* orcid.org/0000-0002-8555-5157

Stepan Kment − *Regional Centre of Advanced Technologies and Materials, Czech Advanced Technology and Research Institute (CATRIN), Palacký University Olomouc, Olomouc 783 71, Czech Republic; Nanotechnology Centre, CEET, VŠB-Technical University of Ostrava, Ostrava-Poruba 708 00, Czech Republic;* orcid.org/0000-0002-6381-5093

Wolfgang Schuhmann − *Analytical Chemistry, Center for Electrochemical Sciences (CES), Faculty of Chemistry and Biochemistry, Ruhr-Universität Bochum, Bochum D-44780, Germany;* orcid.org/0000-0003-2916-5223

Michal Otyepka − *Regional Centre of Advanced Technologies and Materials, Czech Advanced Technology and Research Institute (CATRIN), Palacký University Olomouc, Olomouc 783 71, Czech Republic; IT4Innovations, VŠB-Technical University of Ostrava, Ostrava-Poruba 708 00, Czech Republic;* orcid.org/0000-0002-1066-5677

Complete contact information is available at: https://pubs.acs.org/10.1021/acs.chemrev.2c00270

Author Contributions

[‖]K.J. and S.M.: These authors contributed equally. CRediT: **Kolleboyina Jayaramulu** supervision, visualization, writing-original draft, writing-review & editing; **Soumya Mukherjee** writing-original draft; **Dulce M. Morales** writing-original draft; **Deepak Prakash Dubal** writing-original draft; **Ashok Kumar Nanjundan** writing-original draft; **Andreas Schneemann** supervision; **Justus Masa** supervision, writing-original draft; **Stepan Kment** supervision; **Wolfgang Schuhmann** supervision, writing-original draft; **Michal Otyepka** supervision, writing-original draft; **Radek Zbořil** supervision; **Roland A. Fischer** supervision.

Notes

The authors declare no competing financial interest.

Biographies

Kolleboyina Jayaramulu (Ram) Assistant Professor at Department of Chemistry, Indian Institute of Technology Jammu, India and visiting professor at CATRIN-RCPTM Palacký University in Olomouc, Czech Republic. He received a B.Sc. from Andhra Loyola College, Vijayawada and a M.Sc. in Chemistry from Banaras Hindu University. He earned a PhD in Materials Chemistry at Jawaharlal Nehru Centre for Advanced Scientific Research in 2014, Bangalore, India. He had an opportunity to work with Prof. CNR Rao, ICMS Bangalore and Prof. Daniel Maspoch, ICN2 Barcelona, Spain followed by Alexander von Humboldt postdoctoral Fellow with Prof. Roland A. Fischer at Ruhr-University Bochum, Germany. He worked as combined senior researcher at CATRIN-RCPTM, Palacký University in Olomouc, Czech Republic and Technical University Munich, Germany. His research expertise is in the design and development, structure-property relationship of various advanced hybrid (2D) porous materials for application like water purification, water harvesting, clean energy conversion and storage technology.

Soumya Mukherjee received his Chemistry Honours Bachelor's degree and Master's degree in Chemistry at the University of Calcutta. As a Ph.D. student, he studied metal−organic chemistry at the Indian Institute of Science Education and Research (IISER) Pune under the tutelage of Sujit K. Ghosh. He did postdoctoral research at Bernal Institute, University of Limerick for 3 years in Mike Zaworotko's group. As an Alexander von Humboldt research fellow, he next moved to Roland A. Fischer's AMC chair at the Technical University of Munich. Thanks to an SFI-IRC Pathway Award from the Science Foundation Ireland, he began his independent research career and established his own research group (NanoSorbUL) at the Department of Chemical Sciences, University of Limerick in 2022. NanoSorbUL, as a growing team, is making headway into the development of energy-efficient nanoporous adsorbents, particularly those fostering environmental sustainability.

Dulce M. Morales is currently Deputy Head of the research group led by Marcel Risch at Helmholtz-Zentrum Berlin. She has a degree in Industrial Chemical Engineering from Instituto Politécnico Nacional in

https://doi.org/10.1021/acs.chemrev.2c00270
Chem. Rev. 2022, 122, 17241−17338

Mexico City and received her Ph.D. degree in Chemistry in 2019 mentored by Wolfgang Schuhmann at Ruhr Universität Bochum. Her research focuses on the development of multimetallic composites as electrocatalysts for sustainable energy conversion and storage applications and presently aims for their study under industrial-relevant conditions.

Deepak P. Dubal is currently working as Full Professor at the Queensland University of Technology (QUT), Australia. He is a prolific, well-cited, and multiple-fellowship-winning scientist. He has received several prestigious fellowships such as the Brain Korea-21 Fellowship (South Korea, 2011), Alexander von Humboldt Fellowship (Germany, 2012), Marie Curie Fellowship (Spain, 2014), and Australian Future Fellowship (Australia, 2018). His research expertise is in the design and development of multifunctional materials for clean energy conversion and storage technologies with a special focus on supercapacitors, lithium-ion batteries, lithium-ion capacitors, and electrochemical flow cells. In addition, his team is extending their research area in biomass valorization and battery recycling, aiding the circular economy and sustainable practices.

Ashok Kumar Nanjundan received his Doctor of Engineering degree in Materials Chemistry in 2010. He is a recipient of several prestigious fellowships, namely, the Marie Curie Fellowship, the Japanese Society for the Promotion of Science (JSPS) Fellowship, and the UQ Fellowship. He is currently the Chief Scientific Officer at Graphene Manufacturing Group Ltd., Australia and holds Adjunct Associate Professor positions at the School of Chemical Engineering at The University of Queensland and the Queensland University of Technology. With over 20 years of combined academic and industrial experience, his expertise lies in synthesizing carbon-based nanostructured materials for emerging energy storage applications, particularly lithium- and postlithium-based batteries.

Andreas Schneemann grew up in Sprockhövel, a small town in the Ruhr-Valley on the west side of Germany. In 2016, he obtained his Ph.D. degree in Inorganic Chemistry from Ruhr University Bochum under the guidance of Roland A. Fischer, working on flexible metal−organic frameworks. Afterward, he was a staff scientist at Technische Universität München. In 2017, he joined Mark D. Allendorf and Vitalie Stavila at Sandia National Laboratories in Livermore, CA, on a DFG Postdoctoral Fellowship to tinker with the thermodynamics and kinetics of hydrogen release from metal hydrides. In 2019, he returned to Germany on a Liebig Fellowship to become an independent young investigator at Technische Universität Dresden. He is involved in the DFG Collaborative Research Centre 1415 "Chemistry of Synthetic 2D Materials", and his primary research focuses on the development of low-dimensional covalent−organic frameworks with novel bonding situations.

Justus Masa is a staff scientist at the Max Planck Institute for Chemical Energy Conversion and coordinator of activities in the area of Materials Electrochemistry. He received his B.Sc. degree in Industrial Chemistry in 2003 and M.Sc. degree in Chemistry in 2008 from Makerere University. He earned his Ph.D. degree in Chemistry under the supervision of Wolfgang Schuhmann at Ruhr University Bochum in 2012. He was a Visiting Scholar at Oxford University in 2013 and a group leader (2015−2019) for Electrocatalysis and Energy Conversion in the Department for Analytical Chemistry and Centre for Electrochemical Sciences (CES), Ruhr University Bochum.

Stepan Kment received his PhD in solid state physics and photoelectrochemistry in 2010 from Czech Technical University in Prague, Czech Republic. He then spent one year as a postdoctoral research fellow at Department of Electrical Engineering, University of Nebrasca − Lincoln, Lincoln, NE, USA. Since 2011 he has been working at Palacky University, Olomouc, Czech Republic as a group leader of Photoelectrochemistry. He has been also working at VSB - Technical University of Ostrava, Czech Republic. His research is focused on development of new materials and nanostructures for PEC water splitting application mainly via advanced plasma deposition methods.

Wolfgang Schuhmann studied chemistry at the University of Karlsruhe and completed his Ph.D. degree in 1986 at the Technical University of Munich. After finishing his habilitation at Technical University of Munich in 1993, he was appointed Professor for Analytical Chemistry at the Ruhr University Bochum in 1996. His research interests cover a broad spectrum of different fields of electrochemistry, including biosensors, biofuel cells, batteries, photoelectrochemistry, electrocatalysts for energy conversion including high-entropy materials, scanning electrochemical microscopy, scanning electrochemical cell microscopy, in-situ electrochemistry−spectroscopy techniques, micro- and nanoelectrochemistry, among others.

Michal Otyepka is Head of CATRIN-RCPTM, a research division at Palacký University in Olomouc. He is a member of the Scientific Board of the Czech Grant Agency and LUMI Supercomputer (Finland). His research interests cover physical−chemical properties and reactivity of graphene derivatives and 2D materials, noncovalent interactions to 2D materials, and photoluminescent properties of carbon dots (CDs). He has been developing the chemistry of fluorographene (2D chemistry) toward graphene derivatives, which can be applied in (bio)sensing, catalysis, and energy storage. He specializes also in modeling of biomolecules, nanomaterials, and complex molecular systems and development of force fields, multiscale methods, and their applications.

Radek Zboril is a Founding Director of the Regional Centre of Advanced Technologies and Materials (RCPTM) at Palacky University in Olomouc, Czech Republic (http://www.rcptm.com). After finishing his Ph.D. study, he underwent several short-term stays, e.g., at the University of Delaware and University of Tokyo. Currently, he works as the head of the group at VSB Technical University Ostrava and a Scientific Director of Czech Advanced Technology and Research Institute (CATRIN) − RCPTM in Olomouc. He is a co-author of more than 500 publications and many books published by Springer, Wiley, and the American Chemical Society. He was awarded as a Highly Cited Researcher in 2018, 2019, 2020, and 2021 as announced by Clarivate Analytics. He is a member of the editorial boards of many journals published by the Nature family, Elsevier, and Wiley. He received the Prize of Minister of Education of the Czech Republic for his extraordinary scientific results. His works have been cited 56 000+ times with an H index of 106 (according to Google Scholar).

Roland A. Fischer holds the Chair of Inorganic and Metal−Organic Chemistry at the Technical University Munich (TUM) and is Director of the TUM Catalysis Research Centre (CRC). Previously, he was Professor of Inorganic Chemistry at Ruhr University Bochum (1997−2015) and Heidelberg University (1996 and 1997). He was elected Vice President of the Deutsche Forschungsgemeinschaft (DFG) in 2016. He is member of the European Academy of Sciences. His research interests focus on functional molecular materials, in particular, on metal−organic frameworks and on intermetalloid, superatomic clusters for advanced applications in energy conversion, catalysis, gas storage and separation, chemical sensing, photonics, and microelectronics.

ACKNOWLEDGMENTS

K.J.R. acknowledges support from the Indian Institute of Technology Jammu for providing a seed grant SGT-100038 and SERB SRG/2020/000865. Financial support by MEYS of the Czech Republic (projects CZ.02.1.01/0.0/0.0/16_019/0000754 and LM2018124) and ERC Consolidator Grant (No.

https://doi.org/10.1021/acs.chemrev.2c00270
Chem. Rev. 2022, 122, 17241−17338

683024) from Horizon 2020. Further, Operational Programme Research, Development and Education-European Regional Development Fund, project no. CZ.02.1.01/0.0/0.0/15_003/0000416 is gratefully acknowledged. S.K. and R.Z. acknowledge the funding from the Czech Science Foundation, project GA CR−EXPRO no.19-27454X. This work was supported by the German Research Foundation (DFG) within e-conversion (Fundamentals of Energy Conversion Processes, EXC 2089). S.M. is thankful for the generous fellowship grant from the Alexander von Humboldt foundation. A.S. gratefully acknowledges the Fonds der Chemischen Industrie for a Liebig Fellowship.

REFERENCES

(1) Rowsell, J. L. C.; Yaghi, O. M. Metal-Organic Frameworks: a New Class Of Porous Materials. *Microporous Mesoporous Mater.* **2004**, *73*, 3−14.
(2) Allendorf, M. D.; Bauer, C. A.; Bhakta, R. K.; Houk, R. J. T. Luminescent Metal-Organic Frameworks. *Chem. Soc. Rev.* **2009**, *38*, 1330−1352.
(3) Kurmoo, M. Magnetic Metal-Organic Frameworks. *Chem. Soc. Rev.* **2009**, *38*, 1353−1379.
(4) Lee, J. Y.; Farha, O. K.; Roberts, J.; Scheidt, K. A.; Nguyen, S. B. T.; Hupp, J. T. Metal-Organic Framework Materials as Catalysts. *Chem. Soc. Rev.* **2009**, *38*, 1450−1459.
(5) Murray, L. J.; Dinca, M.; Long, J. R. Hydrogen Storage in Metal-Organic Frameworks. *Chem. Soc. Rev.* **2009**, *38*, 1294−1314.
(6) Horcajada, P.; Gref, R.; Baati, T.; Allan, P. K.; Maurin, G.; Couvreur, P.; Ferey, G.; Morris, R. E.; Serre, C. Metal-Organic Frameworks in Biomedicine. *Chem. Rev.* **2012**, *112*, 1232−1268.
(7) Yoon, M.; Srirambalaji, R.; Kim, K. Homochiral Metal-Organic Frameworks for Asymmetric Heterogeneous Catalysis. *Chem. Rev.* **2012**, *112*, 1196−1231.
(8) Furukawa, H.; Cordova, K. E.; O'Keeffe, M.; Yaghi, O. M. The Chemistry and Applications of Metal-Organic Frameworks. *Science* **2013**, *341*, 1230444.
(9) Hu, Z.; Deibert, B. J.; Li, J. Luminescent Metal-Organic Frameworks for Chemical Sensing and Explosive Detection. *Chem. Soc. Rev.* **2014**, *43*, 5815−5840.
(10) Farha, O. K.; Hupp, J. T. Rational Design, Synthesis, Purification, and Activation of Metal-Organic Framework Materials. *Acc. Chem. Res.* **2010**, *43*, 1166−1175.
(11) Li, J.-R.; Ma, Y.-G.; McCarthy, M. C.; Sculley, J.; Yu, J.-M.; Jeong, H.-K.; Balbuena, P. B.; Zhou, H.-C. Carbon Dioxide Capture-Related Gas Adsorption and Separation in Metal-Organic Frameworks. *Coord. Chem. Rev.* **2011**, *255*, 1791−1823.
(12) Wei, Y.-S.; Zhang, M.; Zou, R.; Xu, Q. Metal-Organic Framework-Based Catalysts with Single Metal Sites. *Chem. Rev.* **2020**, *120*, 12089−12174.
(13) Alhumaimess, M. S. Metal-Organic Frameworks and their Catalytic Applications. *J. Saudi Chem. Soc.* **2020**, *24*, 461−473.
(14) Pascanu, V.; González Miera, G.; Inge, A. K.; Martín-Matute, B. Metal-Organic Frameworks as Catalysts for Organic Synthesis: A Critical Perspective. *J. Am. Chem. Soc.* **2019**, *141*, 7223−7234.
(15) Li, D.; Xu, H.-Q.; Jiao, L.; Jiang, H.-L. Metal-Organic Frameworks for Catalysis: State of the Art, Challenges, and Opportunities. *EnergyChem.* **2019**, *1*, 100005.
(16) Xu, W.; Yaghi, O. M. Metal-Organic Frameworks for Water Harvesting from Air, Anywhere, Anytime. *ACS Cent. Sci.* **2020**, *6*, 1348−1354.
(17) Hanikel, N.; Prévot, M. S.; Yaghi, O. M. MOF Water Harvesters. *Nature Nanotechnl.* **2020**, *15*, 348−355.
(18) Nemiwal, M.; Kumar, D. Metal Organic Frameworks as Water Harvester From Air: Hydrolytic Stability And Adsorption Isotherms. *Inorg. Chem. Commun.* **2020**, *122*, 108279.
(19) Kalmutzki, M. J.; Diercks, C. S.; Yaghi, O. M. Metal-Organic Frameworks for Water Harvesting from Air. *Adv. Mater.* **2018**, *30*, 1704304.
(20) Li, H.-Y.; Zhao, S.-N.; Zang, S.-Q.; Li, J. Functional Metal-Organic Frameworks as Effective Sensors of Gases and Volatile Compounds. *Chem. Soc. Rev.* **2020**, *49*, 6364−6401.
(21) Koo, W.-T.; Jang, J.-S.; Kim, I.-D. Metal-Organic Frameworks for Chemiresistive Sensors. *Chem.* **2019**, *5*, 1938−1963.
(22) Fang, X.; Zong, B.; Mao, S. Metal-Organic Framework-Based Sensors for Environmental Contaminant Sensing. *Nano-Micro Lett.* **2018**, *10*, 64.
(23) Devaraj, M.; Sasikumar, Y.; Rajendran, S.; Ponce, L. C. Metal Organic Framework Based Nanomaterials for Electrochemical Sensing of Toxic Heavy Metal Ions: Progress and Their Prospects. *J. Electrochem. Soc.* **2021**, *168*, 037513.
(24) Zhang, L.-T.; Zhou, Y.; Han, S.-T. The Role of Metal-Organic Frameworks in Electronic Sensors. *Angew. Chem., Int. Ed.* **2021**, *60*, 15192−15212.
(25) Zhu, C.; Gerald, R. E.; Huang, J. Metal-Organic Framework Materials Coupled to Optical Fibers for Chemical Sensing: A Review. *IEEE Sens. J.* **2021**, *21*, 19647−19661.
(26) Jayaramulu, K.; Geyer, F.; Schneemann, A.; Kment, Š; Otyepka, M.; Zboril, R.; Vollmer, D.; Fischer, R. A. Hydrophobic Metal-Organic Frameworks. *Adv. Mater.* **2019**, *31*, 1900820.
(27) Xu, B.; Zhang, H.; Mei, H.; Sun, D. Recent Progress in Metal-Organic Framework-Based Supercapacitor Electrode Materials. *Coord. Chem. Rev.* **2020**, *420*, 213438.
(28) Gao, H.; Shen, H.; Wu, H.; Jing, H.; Sun, Y.; Liu, B.; Chen, Z.; Song, J.; Lu, L.; Wu, Z.; Hao, Q. Review of Pristine Metal-Organic Frameworks for Supercapacitors: Recent Progress and Perspectives. *Energy Fuels* **2021**, *35*, 12884−12901.
(29) Baumann, A. E.; Burns, D. A.; Liu, B.; Thoi, V. S. Metal-Organic Framework Functionalization and Design Strategies for Advanced Electrochemical Energy Storage Devices. *Commun. Chem.* **2019**, *2*, 86.
(30) Cherusseri, J.; Pandey, D.; Sambath Kumar, K.; Thomas, J.; Zhai, L. Flexible Supercapacitor Electrodes Using Metal-Organic Frameworks. *Nanoscale* **2020**, *12*, 17649−17662.
(31) Mohanty, A.; Jaihindh, D.; Fu, Y.-P.; Senanayak, S. P.; Mende, L. S.; Ramadoss, A. An Extensive Review on Three Dimension Architectural Metal-Organic Frameworks Towards Supercapacitor Application. *J. Power Sources* **2021**, *488*, 229444.
(32) Mehek, R.; Iqbal, N.; Noor, T.; Amjad, M. Z. B.; Ali, G.; Vignarooban, K.; Khan, M. A. Metal-Organic Framework Based Electrode Materials for Lithium-Ion Batteries: A Review. *RSC Adv.* **2021**, *11*, 29247−29266.
(33) Ye, Z.; Jiang, Y.; Li, L.; Wu, F.; Chen, R. Rational Design of MOF-Based Materials for Next-Generation Rechargeable Batteries. *Nano-Micro Lett.* **2021**, *13*, 203.
(34) Wang, Z.; Tao, H.; Yue, Y. Metal-Organic-Framework-Based Cathodes for Enhancing the Electrochemical Performances of Batteries: A Review. *ChemElectroChem.* **2019**, *6*, 5358−5374.
(35) Li, Y.; Zhang, J.; Chen, M. MOF-Derived Carbon and Composites as Advanced Anode Materials For Potassium Ion Batteries: A Review. *Sustainable Mater. Technol.* **2020**, *26*, No. e00217.
(36) Liang, Z.; Qu, C.; Guo, W.; Zou, R.; Xu, Q. Pristine Metal-Organic Frameworks and their Composites for Energy Storage and Conversion. *Adv. Mater.* **2018**, *30*, 1702891.
(37) Li, C.; Liu, L.; Kang, J.; Xiao, Y.; Feng, Y.; Cao, F.-F.; Zhang, H. Pristine MOF and COF Materials for Advanced Batteries. *Energy Storage Mater.* **2020**, *31*, 115−134.
(38) Hu, A.; Pang, Q.; Tang, C.; Bao, J.; Liu, H.; Ba, K.; Xie, S.; Chen, J.; Chen, J.; Yue, Y.; Tang, Y.; Li, Q.; Sun, Z. Epitaxial Growth and Integration of Insulating Metal-Organic Frameworks in Electrochemistry. *J. Am. Chem. Soc.* **2019**, *141*, 11322−11327.
(39) Sun, L.; Campbell, M. G.; Dincă, M. Electrically Conductive Porous Metal-Organic Frameworks. *Angew. Chem., Int. Ed.* **2016**, *55*, 3566−3579.
(40) Wang, Y.; Zhang, W.; Wu, X.; Luo, C.; Wang, Q.; Li, J.; Hu, L. Conducting Polymer Coated Metal-Organic Framework Nanoparticles: Facile Synthesis and Enhanced Electromagnetic Absorption Properties. *Synth. Met.* **2017**, *228*, 18−24.

https://doi.org/10.1021/acs.chemrev.2c00270
Chem. Rev. 2022, 122, 17241−17338

(41) Dhara, B.; Nagarkar, S. S.; Kumar, J.; Kumar, V.; Jha, P. K.; Ghosh, S. K.; Nair, S.; Ballav, N. Increase in Electrical Conductivity of MOF to Billion-Fold upon Filling the Nanochannels with Conducting Polymer. *J. Phys. Chem. Lett.* **2016**, *7*, 2945−2950.
(42) Wang, T.; Farajollahi, M.; Henke, S.; Zhu, T.; Bajpe, S. R.; Sun, S.; Barnard, J. S.; Lee, J. S.; Madden, J. D. W.; Cheetham, A. K.; Smoukov, S. K. Functional Conductive Nanomaterials *via* Polymerisation in Nano-Channels: PEDOT In A MOF. *Mater. Horiz.* **2017**, *4*, 64−71.
(43) Yue, T.; Xia, C.; Liu, X.; Wang, Z.; Qi, K.; Xia, B. Y. Design and Synthesis of Conductive Metal-Organic Frameworks and Their Composites for Supercapacitors. *ChemElectroChem.* **2021**, *8*, 1021−1034.
(44) Chen, Y.-C.; Chiang, W.-H.; Kurniawan, D.; Yeh, P.-C.; Otake, K.-i.; Kung, C.-W. Impregnation of Graphene Quantum Dots into a Metal-Organic Framework to Render Increased Electrical Conductivity and Activity for Electrochemical Sensing. *ACS Appl. Mater. Interfaces* **2019**, *11*, 35319−35326.
(45) Zheng, S. Q.; Lim, S. S.; Foo, C. Y.; Haw, C. Y.; Chiu, W. S.; Chia, C. H.; Khiew, P. S. Recent Progress on the Applications of Carbonaceous and Metal-Organic Framework Nanomaterials for Supercapacitors. *Front. Mater.* **2021**, *8*, 500.
(46) Liu, X.-W.; Sun, T.-J.; Hu, J.-L.; Wang, S.-D. Composites of Metal-Organic Frameworks and Carbon-Based Materials: Preparations, Functionalities and Applications. *J. Mater. Chem. A* **2016**, *4*, 3584−3616.
(47) Fleker, O.; Borenstein, A.; Lavi, R.; Benisvy, L.; Ruthstein, S.; Aurbach, D. Preparation and Properties of Metal Organic Framework/Activated Carbon Composite Materials. *Langmuir* **2016**, *32*, 4935−4944.
(48) Gogotsi, Y.; Anasori, B. The Rise of MXenes. *ACS Nano* **2019**, *13*, 8491−8494.
(49) Strachan, J.; Masters, A. F.; Maschmeyer, T. 3R-MoS2 in Review: History, Status, and Outlook. *ACS Appl. Energy Mater.* **2021**, *4*, 7405−7418.
(50) Roy, S.; Zhang, X.; Puthirath, A. B.; Meiyazhagan, A.; Bhattacharyya, S.; Rahman, M. M.; Babu, G.; Susarla, S.; Saju, S. K.; Tran, M. K.; Sassi, L. M.; Saadi, M. A. S. R.; Lai, J.; Sahin, O.; Sajadi, S. M.; Dharmarajan, B.; Salpekar, D.; Chakingal, N.; Baburaj, A.; Shuai, X.; Adumbumkulath, A.; Miller, K. A.; Gayle, J. M.; Ajnsztajn, A.; Prasankumar, T.; Harikrishnan, V. V. J.; Ojha, V.; Kannan, H.; Khater, A. Z.; Zhu, Z.; Iyengar, S. A.; Autreto, P. A. d. S.; Oliveira, E. F.; Gao, G.; Birdwell, A. G.; Neupane, M. R.; Ivanov, T. G.; Taha-Tijerina, J.; Yadav, R. M.; Arepalli, S.; Vajtai, R.; Ajayan, P. M. Structure, Properties and Applications of Two-Dimensional Hexagonal Boron Nitride. *Adv. Mater.* **2021**, *33*, 2101589.
(51) Kroto, H. W. C60: Buckminsterfullerene, The Celestial Sphere that Fell to Earth. *Angew. Chem., Int. Ed.* **1992**, *31*, 111−129.
(52) Rao, R.; Pint, C. L.; Islam, A. E.; Weatherup, R. S.; Hofmann, S.; Meshot, E. R.; Wu, F.; Zhou, C.; Dee, N.; Amama, P. B.; Carpena-Nuñez, J.; Shi, W.; Plata, D. L.; Penev, E. S.; Yakobson, B. I.; Balbuena, P. B.; Bichara, C.; Futaba, D. N.; Noda, S.; Shin, H.; Kim, K. S.; Simard, B.; Mirri, F.; Pasquali, M.; Fornasiero, F.; Kauppinen, E. I.; Arnold, M.; Cola, B. A.; Nikolaev, P.; Arepalli, S.; Cheng, H.-M.; Zakharov, D. N.; Stach, E. A.; Zhang, J.; Wei, F.; Terrones, M.; Geohegan, D. B.; Maruyama, B.; Maruyama, S.; Li, Y.; Adams, W. W.; Hart, A. J. Carbon Nanotubes and Related Nanomaterials: Critical Advances and Challenges for Synthesis toward Mainstream Commercial Applications. *ACS Nano* **2018**, *12*, 11756−11784.
(53) Novoselov, K. S.; Geim, A. K.; Morozov, S. V.; Jiang, D.; Zhang, Y.; Dubonos, S. V.; Grigorieva, I. V.; Firsov, A. A. Electric Field Effect in Atomically Thin Carbon Films. *Science* **2004**, *306*, 666−669.
(54) Allen, M. J.; Tung, V. C.; Kaner, R. B. Honeycomb Carbon: A Review of Graphene. *Chem. Rev.* **2010**, *110*, 132−145.
(55) Rahat Rahman, M.; Rashid, M. M.; Islam, M. M.; Akanda, M. M. Electrical and Chemical Properties of Graphene over Composite Materials: A Technical Review. *Mater. Sci. Res. India* **2019**, *16*, 142−163.
(56) Farjadian, F.; Abbaspour, S.; Sadatlu, M. A. A.; Mirkiani, S.; Ghasemi, A.; Hoseini-Ghahfarokhi, M.; Mozaffari, N.; Karimi, M.; Hamblin, M. R. Recent Developments in Graphene and Graphene Oxide: Properties, Synthesis, and Modifications: A Review. *ChemistrySelect* **2020**, *5*, 10200−10219.
(57) Sattar, T. Current Review on Synthesis, Composites and Multifunctional Properties of Graphene. *Top. Curr. Chem.* **2019**, *377*, 10.
(58) Geim, A. K. Graphene: Status and Prospects. *Science* **2009**, *324*, 1530−1534.
(59) Homaeigohar, S.; Elbahri, M. Graphene Membranes for Water Desalination. *NPG Asia Mater.* **2017**, *9*, e427−e427.
(60) Sun, M.; Li, J. Graphene Oxide Membranes: Functional Structures, Preparation and Environmental Applications. *Nano Today* **2018**, *20*, 121−137.
(61) Jiang, Y.; Biswas, P.; Fortner, J. D. A Review of Recent Developments in Graphene-Enabled Membranes for Water Treatment. *Environ. Sci. Water Res. Technol.* **2016**, *2*, 915−922.
(62) Hu, M.; Mi, B. Enabling Graphene Oxide Nanosheets as Water Separation Membranes. *Environ. Sci. Technol.* **2013**, *47*, 3715−3723.
(63) DeCoste, J. B.; Peterson, G. W. Metal-Organic Frameworks for Air Purification of Toxic Chemicals. *Chem. Rev.* **2014**, *114*, 5695−5757.
(64) Dhaka, S.; Kumar, R.; Deep, A.; Kurade, M. B.; Ji, S.-W.; Jeon, B.-H. Metal-Organic Frameworks (Mofs) for the Removal of Emerging Contaminants from Aquatic Environments. *Coord. Chem. Rev.* **2019**, *380*, 330−352.
(65) Russo, V.; Hmoudah, M.; Broccoli, F.; Iesce, M. R.; Jung, O.-S.; Di Serio, M. Applications of Metal Organic Frameworks in Wastewater Treatment: A Review on Adsorption and Photodegradation. *Front. Chem. Eng.* **2020**, *2*, 581487.
(66) Ahmed, I.; Mondol, M. M. H.; Lee, H. J.; Jhung, S. H. Application of Metal-Organic Frameworks in Adsorptive Removal of Organic Contaminants from Water, Fuel and Air. *Chem. Asian J.* **2021**, *16*, 185−196.
(67) Ding, M.; Cai, X.; Jiang, H.-L. Improving MOF Stability: Approaches and Applications. *Chem. Sci.* **2019**, *10*, 10209−10230.
(68) Bosch, M.; Zhang, M.; Zhou, H.-C. Increasing the Stability of Metal-Organic Frameworks. *Adv. Chem.* **2014**, *2014*, 182327.
(69) Mankins, J. C. Technology Readiness Assessments: A Retrospective. *Acta Astronaut.* **2009**, *65*, 1216−1223.
(70) Chen, Z.; Wasson, M. C.; Drout, R. J.; Robison, L.; Idrees, K. B.; Knapp, J. G.; Son, F. A.; Zhang, X.; Hierse, W.; Kühn, C.; Marx, S.; Hernandez, B.; Farha, O. K. The State of the Field: From Inception to Commercialization of Metal-Organic Frameworks. *Faraday Discuss.* **2021**, *225*, 9−69.
(71) Zhao, Y.; Seredych, M.; Jagiello, J.; Zhong, Q.; Bandosz, T. J. Insight into the Mechanism of CO2 Adsorption on Cu-BTC and its Composites with Graphite Oxide or Aminated Graphite Oxide. *Chem. Eng. J.* **2014**, *239*, 399.
(72) Policicchio, A.; Zhao, Y.; Zhong, Q.; Agostino, R. G.; Bandosz, T. J. Cu-BTC/Aminated Graphite Oxide Composites As High-Efficiency CO2 Capture Media. *ACS Appl. Mater. Interfaces* **2014**, *6*, 101−108.
(73) Lu, Y.; Zhang, Q.; Li, L.; Niu, Z.; Chen, J. Design Strategies toward Enhancing the Performance of Organic Electrode Materials in Metal-Ion Batteries. *Chem.* **2018**, *4*, 2786−2813.
(74) Miller, E. E.; Hua, Y.; Tezel, F. H. Materials for Energy Storage: Review of Electrode Materials and Methods Of Increasing Capacitance For Supercapacitors. *J. Energy Storage* **2018**, *20*, 30−40.
(75) Jayaramulu, K.; Esclance Dmello, M.; Kesavan, K.; Schneemann, A.; Otyepka, M.; Kment, S.; Narayana, C.; Kalidindi, S. B.; Varma, R. S.; Zboril, R.; Fischer, R. A. A Multifunctional Covalently Linked Graphene-MOF Hybrid as an Effective Chemiresistive Gas Sensor. *J. Mater. Chem. A* **2021**, *9*, 17434−17441.
(76) Jayaramulu, K.; Horn, M.; Schneemann, A.; Saini, H.; Bakandritsos, A.; Ranc, V.; Petr, M.; Stavila, V.; Narayana, C.; Scheibe, B.; Kment, Š; Otyepka, M.; Motta, N.; Dubal, D.; Zbořil, R.; Fischer, R. A. Covalent Graphene-MOF Hybrids for High-Performance Asymmetric Supercapacitors. *Adv. Mater.* **2021**, *33*, 2004560.

https://doi.org/10.1021/acs.chemrev.2c00270
Chem. Rev. 2022, 122, 17241−17338

(77) Jahan, M.; Bao, Q.; Yang, J.-X.; Loh, K. P. Structure-Directing Role of Graphene in the Synthesis of Metal-Organic Framework Nanowire. *J. Am. Chem. Soc.* **2010**, *132*, 14487−14495.
(78) Deping, W.; Wenming, H.; Wufeng, F.; Xiaohong, X.; Junqiang, L.; Hongbo, L. Shape-Assisted Spherical Mofs/Amine Functionalized Graphene Hybrids for High-Performance Lithium-Ion Batteries. *Microporous Mesoporous Mater.* **2021**, *323*, 111240.
(79) Vermisoglou, E. C.; Jakubec, P.; Malina, O.; Kupka, V.; Schneemann, A.; Fischer, R. A.; Zbořil, R.; Jayaramulu, K.; Otyepka, M. Hierarchical Porous Graphene-Iron Carbide Hybrid Derived From Functionalized Graphene-Based Metal-Organic Gel as Efficient Electrochemical Dopamine Sensor. *Front. Chem.* **2020**, *8*, 544.
(80) Tekalgne, M. A.; Do, H. H.; Hasani, A.; Van Le, Q.; Jang, H. W.; Ahn, S. H.; Kim, S. Y. Two-Dimensional Materials and Metal-Organic Frameworks for the CO2 Reduction Reaction. *Mater. Today Adv.* **2020**, *5*, 100038.
(81) Saini, H.; Srinivasan, N.; Šedajová, V.; Majumder, M.; Dubal, D. P.; Otyepka, M.; Zbořil, R.; Kurra, N.; Fischer, R. A.; Jayaramulu, K. Emerging MXene@Metal-Organic Framework Hybrids: Design Strategies toward Versatile Applications. *ACS Nano* **2021**, *15*, 18742−18776.
(82) Ghazi, Z. A.; Zhu, L.; Wang, H.; Naeem, A.; Khattak, A. M.; Liang, B.; Khan, N. A.; Wei, Z.; Li, L.; Tang, Z. Efficient Polysulfide Chemisorption in Covalent Organic Frameworks for High-Performance Lithium-Sulfur Batteries. *Adv. Energy Mater.* **2016**, *6*, 1601250.
(83) Xiang, W.; Zhang, Y.; Lin, H.; Liu, C.-J. Nanoparticle/Metal-Organic Framework Composites for Catalytic Applications: Current Status and Perspective. *Molecules* **2017**, *22*, 2103.
(84) Yu, J.; Mu, C.; Yan, B.; Qin, X.; Shen, C.; Xue, H.; Pang, H. Nanoparticle/MOF Composites: Preparations and Applications. *Mater. Horiz.* **2017**, *4*, 557−569.
(85) Zhao, G.; Qin, N.; Pan, A.; Wu, X.; Peng, C.; Ke, F.; Iqbal, M.; Ramachandraiah, K.; Zhu, J. Magnetic Nanoparticles@Metal-Organic Framework Composites as Sustainable Environment Adsorbents. *J. Nanomater.* **2019**, *2019*, 1454358.
(86) Wang, B.; Liu, W.; Zhang, W.; Liu, J. Nanoparticles@Nanoscale Metal-Organic Framework Composites as Highly Efficient Heterogeneous Catalysts for Size- and Shape-Selective Reactions. *Nano Res.* **2017**, *10*, 3826−3835.
(87) Wang, K.; Hui, K. N.; San Hui, K.; Peng, S.; Xu, Y. Recent Progress in Metal-Organic Framework/Graphene-Derived Materials for Energy Storage and Conversion: Design, Preparation, and Application. *Chem. Sci.* **2021**, *12*, 5737−5766.
(88) Qu, H.-j.; Huang, L.-j.; Han, Z.-y.; Wang, Y.-x.; Zhang, Z.-j.; Wang, Y.; Chang, Q.-r.; Wei, N.; Kipper, M. J.; Tang, J.-g. A Review of Graphene-Oxide/Metal-Organic Framework Composites Materials: Characteristics, Preparation and Applications. *J. Porous Mater.* **2021**, *28*, 1837−1865.
(89) Zhang, X.; Zhang, S.; Tang, Y.; Huang, X.; Pang, H. Recent Advances and Challenges of Metal-Organic Framework/Graphene-Based Composites. *Compos. B. Eng.* **2022**, *230*, 109532.
(90) Zheng, Y.; Zheng, S.; Xue, H.; Pang, H. Metal-Organic Frameworks/Graphene-Based Materials: Preparations and Applications. *Adv. Funct. Mater.* **2018**, *28*, 1804950.
(91) Wang, Z.; Huang, J.; Mao, J.; Guo, Q.; Chen, Z.; Lai, Y. Metal-Organic Frameworks and their Derivatives with Graphene Composites: Preparation and Applications in Electrocatalysis and Photocatalysis. *J. Mater. Chem. A* **2020**, *8*, 2934−2961.
(92) Novoselov, K. S.; Fal'ko, V. I.; Colombo, L.; Gellert, P. R.; Schwab, M. G.; Kim, K. A Roadmap for Graphene. *Nature* **2012**, *490*, 192−200.
(93) Shahil, K. M. F.; Balandin, A. A. Thermal Properties of Graphene and Multilayer Graphene: Applications in Thermal Interface Materials. *Solid State Commun.* **2012**, *152*, 1331−1340.
(94) Gong, X.; Liu, G.; Li, Y.; Yu, D. Y. W.; Teoh, W. Y. Functionalized-Graphene Composites: Fabrication and Applications in Sustainable Energy and Environment. *Chem. Mater.* **2016**, *28*, 8082−8118.
(95) Sharma, G.; Thakur, B.; Naushad, M.; Kumar, A.; Stadler, F. J.; Alfadul, S. M.; Mola, G. T. Applications of Nanocomposite Hydrogels for Biomedical Engineering and Environmental Protection. *Environ. Chem. Lett.* **2018**, *16*, 113−146.
(96) Petit, C.; Bandosz, T. J. MOF-Graphite Oxide Composites: Combining the Uniqueness of Graphene Layers and Metal-Organic Frameworks. *Adv. Mater.* **2009**, *21*, 4753−4757.
(97) Zhang, M.; Shan, Y.; Kong, Q.; Pang, H. Application of Metal-Organic Framework-Graphene Composite Materials in electrochemical Energy Storage. *FlatChem.* **2022**, *32*, 100332.
(98) Georgakilas, V.; Perman, J. A.; Tucek, J.; Zboril, R. Broad Family of Carbon Nanoallotropes: Classification, Chemistry, and Applications of Fullerenes, Carbon Dots, Nanotubes, Graphene, Nanodiamonds, and Combined Superstructures. *Chem. Rev.* **2015**, *115*, 4744−4822.
(99) Li, X.; Cai, W.; An, J.; Kim, S.; Nah, J.; Yang, D.; Piner, R.; Velamakanni, A.; Jung, I.; Tutuc, E.; Banerjee, S. K.; Colombo, L.; Ruoff, R. S. Large-Area Synthesis of High-Quality and Uniform Graphene Films on Copper Foils. *Science* **2009**, *324*, 1312−1314.
(100) Bae, S.; Kim, H.; Lee, Y.; Xu, X.; Park, J.-S.; Zheng, Y.; Balakrishnan, J.; Lei, T.; Ri Kim, H.; Song, Y. I.; Kim, Y.-J.; Kim, K. S.; Özyilmaz, B.; Ahn, J.-H.; Hong, B. H.; Iijima, S. Roll-To-Roll Production of 30-Inch Graphene Films for Transparent Electrodes. *Nat. Nanotechnol.* **2010**, *5*, 574−578.
(101) Hernandez, Y.; Nicolosi, V.; Lotya, M.; Blighe, F. M.; Sun, Z.; De, S.; McGovern, I. T.; Holland, B.; Byrne, M.; Gun'Ko, Y. K.; Boland, J. J.; Niraj, P.; Duesberg, G.; Krishnamurthy, S.; Goodhue, R.; Hutchison, J.; Scardaci, V.; Ferrari, A. C.; Coleman, J. N. High-Yield Production of Graphene by Liquid-Phase Exfoliation of Graphite. *Nat. Nanotechnol.* **2008**, *3*, 563−568.
(102) Dreyer, D. R.; Park, S.; Bielawski, C. W.; Ruoff, R. S. The Chemistry of Graphene Oxide. *Chem. Soc. Rev.* **2010**, *39*, 228−240.
(103) Park, S.; Ruoff, R. S. Chemical Methods for the Production of Graphenes. *Nat. Nanotechnol.* **2009**, *4*, 217−224.
(104) Nair, R. R.; Blake, P.; Grigorenko, A. N.; Novoselov, K. S.; Booth, T. J.; Stauber, T.; Peres, N. M. R.; Geim, A. K. Fine Structure Constant Defines Visual Transparency of Graphene. *Science* **2008**, *320*, 1308−1308.
(105) Castro Neto, A. H.; Guinea, F.; Peres, N. M. R.; Novoselov, K. S.; Geim, A. K. The Electronic Properties of Graphene. *Rev. Modern Phys.* **2009**, *81*, 109−162.
(106) Singh, C.; Mishra, A. K.; Paul, A. Highly Conducting Reduced Graphene Synthesis *via* Low Temperature Chemically Assisted Exfoliation and Energy Storage Application. *J. Mater. Chem. A* **2015**, *3*, 18557−18563.
(107) Balandin, A. A.; Ghosh, S.; Bao, W.; Calizo, I.; Teweldebrhan, D.; Miao, F.; Lau, C. N. Superior Thermal Conductivity of Single-Layer Graphene. *Nano Lett.* **2008**, *8*, 902−907.
(108) Schedin, F.; Geim, A. K.; Morozov, S. V.; Hill, E. W.; Blake, P.; Katsnelson, M. I.; Novoselov, K. S. Detection of Individual Gas Molecules Adsorbed on Graphene. *Nat. Mater.* **2007**, *6*, 652−655.
(109) Georgakilas, V.; Otyepka, M.; Bourlinos, A. B.; Chandra, V.; Kim, N.; Kemp, K. C.; Hobza, P.; Zboril, R.; Kim, K. S. Functionalization of Graphene: Covalent and Non-Covalent Approaches, Derivatives and Applications. *Chem. Rev.* **2012**, *112*, 6156−6214.
(110) Lazar, P.; Karlický, F.; Jurečka, P.; Kocman, M.; Otyepková, E.; Šafářová, K.; Otyepka, M. Adsorption of Small Organic Molecules on Graphene. *J. Am. Chem. Soc.* **2013**, *135*, 6372−6377.
(111) Georgakilas, V.; Tiwari, J. N.; Kemp, K. C.; Perman, J. A.; Bourlinos, A. B.; Kim, K. S.; Zboril, R. Noncovalent Functionalization of Graphene and Graphene Oxide for Energy Materials, Biosensing, Catalytic, and Biomedical Applications. *Chem. Rev.* **2016**, *116*, 5464−5519.
(112) Elias, D. C.; Nair, R. R.; Mohiuddin, T. M. G.; Morozov, S. V.; Blake, P.; Halsall, M. P.; Ferrari, A. C.; Boukhvalov, D. W.; Katsnelson, M. I.; Geim, A. K.; Novoselov, K. S. Control of Graphene's Properties by Reversible Hydrogenation: Evidence for Graphane. *Science* **2009**, *323*, 610−613.

https://doi.org/10.1021/acs.chemrev.2c00270
Chem. Rev. 2022, 122, 17241−17338

(113) Leconte, N.; Moser, J.; Ordejón, P.; Tao, H.; Lherbier, A.; Bachtold, A.; Alsina, F.; Sotomayor Torres, C. M.; Charlier, J.-C.; Roche, S. Damaging Graphene with Ozone Treatment: A Chemically Tunable Metal-Insulator Transition. *ACS Nano* **2010**, *4*, 4033−4038.
(114) Kosynkin, D. V.; Higginbotham, A. L.; Sinitskii, A.; Lomeda, J. R.; Dimiev, A.; Price, B. K.; Tour, J. M. Longitudinal Unzipping of Carbon Nanotubes to form Graphene Nanoribbons. *Nature* **2009**, *458*, 872−876.
(115) Inagaki, M.; Kang, F. Graphene Derivatives: Graphane, Fluorographene, Graphene Oxide, Graphyne and Graphdiyne. *J. Mater. Chem. A* **2014**, *2*, 13193−13206.
(116) Karlický, F.; Kumara Ramanatha Datta, K.; Otyepka, M.; Zbořil, R. Halogenated Graphenes: Rapidly Growing Family of Graphene Derivatives. *ACS Nano* **2013**, *7*, 6434−6464.
(117) Eng, A. Y. S.; Chua, C. K.; Pumera, M. Refinements to the Structure of Graphite Oxide: Absolute Quantification of Functional Groups *via* Selective Labelling. *Nanoscale* **2015**, *7*, 20256−20266.
(118) Stankovich, S.; Dikin, D. A.; Piner, R. D.; Kohlhaas, K. A.; Kleinhammes, A.; Jia, Y.; Wu, Y.; Nguyen, S. T.; Ruoff, R. S. Synthesis of Graphene-Based Nanosheets *via* Chemical Reduction of Exfoliated Graphite Oxide. *Carbon* **2007**, *45*, 1558−1565.
(119) Eda, G.; Fanchini, G.; Chhowalla, M. Large-Area Ultrathin Films of Reduced Graphene Oxide as a Transparent and Flexible Electronic Material. *Nat. Nanotechnol.* **2008**, *3*, 270−274.
(120) Nair, R. R.; Ren, W.; Jalil, R.; Riaz, I.; Kravets, V. G.; Britnell, L.; Blake, P.; Schedin, F.; Mayorov, A. S.; Yuan, S.; Katsnelson, M. I.; Cheng, H.-M.; Strupinski, W.; Bulusheva, L. G.; Okotrub, A. V.; Grigorieva, I. V.; Grigorenko, A. N.; Novoselov, K. S.; Geim, A. K. Fluorographene: A Two-Dimensional Counterpart of Teflon. *Small* **2010**, *6*, 2877−2884.
(121) Zbořil, R.; Karlický, F.; Bourlinos, A. B.; Steriotis, T. A.; Stubos, A. K.; Georgakilas, V.; Šafářová, K.; Jančík, D.; Trapalis, C.; Otyepka, M. Graphene Fluoride: A Stable Stoichiometric Graphene Derivative and its Chemical Conversion to Graphene. *Small* **2010**, *6*, 2885−2891.
(122) Chronopoulos, D. D.; Bakandritsos, A.; Pykal, M.; Zbořil, R.; Otyepka, M. Chemistry, Properties, and Applications of Fluorographene. *Appl. Mater. Today* **2017**, *9*, 60−70.
(123) Bakandritsos, A.; Pykal, M.; Błoński, P.; Jakubec, P.; Chronopoulos, D. D.; Poláková, K.; Georgakilas, V.; Čépe, K.; Tomanec, O.; Ranc, V.; Bourlinos, A. B.; Zbořil, R.; Otyepka, M. Cyanographene and Graphene Acid: Emerging Derivatives Enabling High-Yield and Selective Functionalization of Graphene. *ACS Nano* **2017**, *11*, 2982−2991.
(124) Seelajaroen, H.; Bakandritsos, A.; Otyepka, M.; Zbořil, R.; Sariciftci, N. S. Immobilized Enzymes on Graphene as Nanobiocatalyst. *ACS Appl. Mater. Interfaces* **2020**, *12*, 250−259.
(125) Blanco, M.; Mosconi, D.; Tubaro, C.; Biffis, A.; Badocco, D.; Pastore, P.; Otyepka, M.; Bakandritsos, A.; Liu, Z.; Ren, W.; Agnoli, S.; Granozzi, G. Palladium Nanoparticles Supported on Graphene Acid: A Stable and Eco-Friendly Bifunctional C-C Homo- and Cross-Coupling Catalyst. *Green Chem.* **2019**, *21*, 5238−5247.
(126) Heng Cheong, Y.; Nasir, M. Z. M.; Bakandritsos, A.; Pykal, M.; Jakubec, P.; Zbořil, R.; Otyepka, M.; Pumera, M. Cyanographene and Graphene Acid: The Functional Group of Graphene Derivative Determines the Application in Electrochemical Sensing and Capacitors. *ChemElectroChem.* **2019**, *6*, 229−234.
(127) Šedajová, V.; Jakubec, P.; Bakandritsos, A.; Ranc, V.; Otyepka, M. New Limits for Stability of Supercapacitor Electrode Material Based on Graphene Derivative. *Nanomater.* **2020**, *10*, 1731.
(128) Jayaramulu, K.; Datta, K. K. R.; Rösler, C.; Petr, M.; Otyepka, M.; Zboril, R.; Fischer, R. A. Biomimetic Superhydrophobic/Superoleophilic Highly Fluorinated Graphene Oxide and ZIF-8 Composites for Oil-Water Separation. *Angew. Chem., Int. Ed.* **2016**, *55*, 1178−1182.
(129) Wang, X.; Sun, G.; Routh, P.; Kim, D.-H.; Huang, W.; Chen, P. Heteroatom-Doped Graphene Materials: Syntheses, Properties and Applications. *Chem. Soc. Rev.* **2014**, *43*, 7067−7098.
(130) Wang, A.; Li, J.; Zhang, T. Heterogeneous Single-Atom Catalysis. *Nature Rev. Chem.* **2018**, *2*, 65−81.
(131) Zaoralová, D.; Hrubý, V.; Šedajová, V.; Mach, R.; Kupka, V.; Ugolotti, J.; Bakandritsos, A.; Medved', M.; Otyepka, M. Tunable Synthesis of Nitrogen Doped Graphene from Fluorographene under Mild Conditions. *ACS Sustain. Chem. Eng.* **2020**, *8*, 4764−4772.
(132) Zhou, H.-C.; Long, J. R.; Yaghi, O. M. Introduction to Metal−Organic Frameworks. *Chem. Rev.* **2012**, *112*, 673−674.
(133) Safaei, M.; Foroughi, M. M.; Ebrahimpoor, N.; Jahani, S.; Omidi, A.; Khatami, M. A Review on Metal-Organic Frameworks: Synthesis and Applications. *TrAC, Trends Anal. Chem.* **2019**, *118*, 401−425.
(134) Farha, O. K.; Eryazici, I.; Jeong, N. C.; Hauser, B. G.; Wilmer, C. E.; Sarjeant, A. A.; Snurr, R. Q.; Nguyen, S. T.; Yazaydın, A. Ö.; Hupp, J. T. Metal-Organic Framework Materials with Ultrahigh Surface Areas: Is the Sky the Limit? *J. Am. Chem. Soc.* **2012**, *134*, 15016−15021.
(135) Li, H.; Li, L.; Lin, R.-B.; Zhou, W.; Zhang, Z.; Xiang, S.; Chen, B. Porous Metal-Organic Frameworks for Gas Storage and Separation: Status and Challenges. *EnergyChem.* **2019**, *1*, 100006.
(136) Chen, Z.; Li, P.; Anderson, R.; Wang, X.; Zhang, X.; Robison, L.; Redfern, L. R.; Moribe, S.; Islamoglu, T.; Gomez-Gualdron, D. A.; Yildirim, T.; Stoddart, J. F.; Farha, O. K. Balancing Volumetric and Gravimetric Uptake in Highly Porous Materials for Clean Energy. *Science* **2020**, *368*, 297−303.
(137) Hönicke, I. M.; Senkovska, I.; Bon, V.; Baburin, I. A.; Bönisch, N.; Raschke, S.; Evans, J. D.; Kaskel, S. Balancing Mechanical Stability and Ultrahigh Porosity in Crystalline Framework Materials. *Angew. Chem., Int. Ed.* **2018**, *57*, 13780−13783.
(138) Chen, Z.; Kirlikovali, K. O.; Li, P.; Farha, O. K. Reticular Chemistry for Highly Porous Metal-Organic Frameworks: The Chemistry and Applications. *Acc. Chem. Res.* **2022**, *55*, 579−591.
(139) Butova, V. V.; Soldatov, M. A.; Guda, A. A.; Lomachenko, K. A.; Lamberti, C. Metal-Organic Frameworks: Structure, Properties, Methods of Synthesis and Characterization. *Russ. Chem. Rev.* **2016**, *85*, 280−307.
(140) Liu, X.; Zhang, L.; Wang, J. Design Strategies for MOF-Derived Porous Functional Materials: Preserving Surfaces and Nurturing Pores. *J. Materiomics* **2021**, *7*, 440−459.
(141) Lin, R.-B.; Xiang, S.; Zhou, W.; Chen, B. Microporous Metal-Organic Framework Materials for Gas Separation. *Chem.* **2020**, *6*, 337−363.
(142) Li, B.; Wen, H.-M.; Zhou, W.; Chen, B. Porous Metal-Organic Frameworks for Gas Storage and Separation: What, How, and Why? *J. Phys. Chem. Lett.* **2014**, *5*, 3468−3479.
(143) Chen, B.; Xiang, S.; Qian, G. Metal-Organic Frameworks with Functional Pores for Recognition of Small Molecules. *Acc. Chem. Res.* **2010**, *43*, 1115−1124.
(144) Hu, M.-L.; Razavi, S. A. A.; Piroozzadeh, M.; Morsali, A. Sensing Organic Analytes by Metal-Organic Frameworks: A New Way of Considering The Topic. *Inorg. Chem. Front.* **2020**, *7*, 1598−1632.
(145) Qiu, T.; Liang, Z.; Guo, W.; Tabassum, H.; Gao, S.; Zou, R. Metal-Organic Framework-Based Materials for Energy Conversion and Storage. *ACS Energy Lett.* **2020**, *5*, 520−532.
(146) Zhang, X.; Chen, A.; Zhong, M.; Zhang, Z.; Zhang, X.; Zhou, Z.; Bu, X.-H. Metal-Organic Frameworks (MOFs) and MOF-Derived Materials for Energy Storage and Conversion. *Electrochem. Energy Rev.* **2019**, *2*, 29−104.
(147) Bavykina, A.; Kolobov, N.; Khan, I. S.; Bau, J. A.; Ramirez, A.; Gascon, J. Metal-Organic Frameworks in Heterogeneous Catalysis: Recent Progress, New Trends, and Future Perspectives. *Chem. Rev.* **2020**, *120*, 8468−8535.
(148) Shen, Y.; Pan, T.; Wang, L.; Ren, Z.; Zhang, W.; Huo, F. Programmable Logic in Metal-Organic Frameworks for Catalysis. *Adv. Mater.* **2021**, *33*, 2007442.
(149) Lawson, H. D.; Walton, S. P.; Chan, C. Metal-Organic Frameworks for Drug Delivery: A Design Perspective. *ACS Appl. Mater. Interfaces* **2021**, *13*, 7004−7020.
(150) Sun, Y.; Zheng, L.; Yang, Y.; Qian, X.; Fu, T.; Li, X.; Yang, Z.; Yan, H.; Cui, C.; Tan, W. Metal-Organic Framework Nanocarriers for Drug Delivery in Biomedical Applications. *Nano-Micro Lett.* **2020**, *12*, 103.

https://doi.org/10.1021/acs.chemrev.2c00270
Chem. Rev. 2022, 122, 17241−17338

(151) Ettlinger, R.; Lächelt, U.; Gref, R.; Horcajada, P.; Lammers, T.; Serre, C.; Couvreur, P.; Morris, R. E.; Wuttke, S. Toxicity of Metal-Organic Framework Nanoparticles: From Essential Analyses to Potential Applications. *Chem. Soc. Rev.* **2022**, *51*, 464−484.
(152) Furukawa, H.; Cordova, K. E.; O'Keeffe, M.; Yaghi, O. M. The Chemistry and Applications of Metal-Organic Frameworks. *Science* **2013**, *341*, 1230444.
(153) Freund, R.; Canossa, S.; Cohen, S. M.; Yan, W.; Deng, H.; Guillerm, V.; Eddaoudi, M.; Madden, D. G.; Fairen-Jimenez, D.; Lyu, H.; Macreadie, L. K.; Ji, Z.; Zhang, Y.; Wang, B.; Haase, F.; Wöll, C.; Zaremba, O.; Andreo, J.; Wuttke, S.; Diercks, C. S. 25 Years of Reticular Chemistry. *Angew. Chem., Int. Ed.* **2021**, *60*, 23946−23974.
(154) Ongari, D.; Talirz, L.; Smit, B. Too Many Materials and Too Many Applications: An Experimental Problem Waiting for a Computational Solution. *ACS Cent. Sci.* **2020**, *6*, 1890−1900.
(155) Roh, D. K.; Jae, H.; Mun, H.; Jo, J. H.; Chi, W. S. Precise Tuning of Morphology and Pore Size of Amine-Functionalized MIL Metal-Organic Frameworks Using a Directing Agent. *Mater. Sci. Eng., B* **2021**, *263*, 114833.
(156) Tan, Y.-X.; He, Y.-P.; Zhang, J. Tuning MOF Stability and Porosity via Adding Rigid Pillars. *Inorg. Chem.* **2012**, *51*, 9649−9654.
(157) Howarth, A. J.; Liu, Y.; Li, P.; Li, Z.; Wang, T. C.; Hupp, J. T.; Farha, O. K. Chemical, Thermal and Mechanical Stabilities of Metal-Organic Frameworks. *Nat. Rev. Mater.* **2016**, *1*, 15018.
(158) Nguyen, J. G.; Cohen, S. M. Moisture-Resistant and Superhydrophobic Metal-Organic Frameworks Obtained via Post-synthetic Modification. *J. Am. Chem. Soc.* **2010**, *132*, 4560−4561.
(159) Sosa, J. D.; Bennett, T. F.; Nelms, K. J.; Liu, B. M.; Tovar, R. C.; Liu, Y. Metal-Organic Framework Hybrid Materials and Their Applications. *Crystals* **2018**, *8*, 325.
(160) Petit, C.; Burress, J.; Bandosz, T. J. The Synthesis and Characterization of Copper-Based Metal-Organic Framework/Graphite Oxide Composites. *Carbon* **2011**, *49*, 563−572.
(161) Petit, C.; Bandosz, T. J. Synthesis, Characterization, and Ammonia Adsorption Properties of Mesoporous Metal-Organic Framework (MIL(Fe))-Graphite Oxide Composites: Exploring the Limits of Materials Fabrication. *Adv. Funct. Mater.* **2011**, *21*, 2108−2117.
(162) Jahan, M.; Bao, Q.; Loh, K. P. Electrocatalytically Active Graphene-Porphyrin MOF Composite for Oxygen Reduction Reaction. *J. Am. Chem. Soc.* **2012**, *134*, 6707−6713.
(163) Jahan, M.; Liu, Z.; Loh, K. P. A Graphene Oxide and Copper-Centered Metal Organic Framework Composite as a Tri-Functional Catalyst for HER, OER, and ORR. *Adv. Funct. Mater.* **2013**, *23*, 5363−5372.
(164) Choi, K. M.; Jeong, H. M.; Park, J. H.; Zhang, Y.-B.; Kang, J. K.; Yaghi, O. M. Supercapacitors of Nanocrystalline Metal-Organic Frameworks. *ACS Nano* **2014**, *8*, 7451−7457.
(165) Petit, C.; Mendoza, B.; Bandosz, T. J. Reactive Adsorption of Ammonia on Cu-Based MOF/Graphene Composites. *Langmuir* **2010**, *26*, 15302−15309.
(166) Qin, X.; Dong, Y.; Wang, M.; Zhu, Z.; Li, M.; Yang, D.; Shao, Y. In Situ Growing Triethanolamine-Functionalized Metal-Organic Frameworks on Two-Dimensional Carbon Nanosheets for Electrochemiluminescent Immunoassay. *ACS Sens.* **2019**, *4*, 2351−2357.
(167) Huang, A.; Liu, Q.; Wang, N.; Zhu, Y.; Caro, J. Bicontinuous Zeolitic Imidazolate Framework ZIF-8@GO Membrane with Enhanced Hydrogen Selectivity. *J. Am. Chem. Soc.* **2014**, *136*, 14686−14689.
(168) Kong, L.; Zhang, X.; Liu, H.; Wang, T.; Qiu, J. Preparation of ZIF-8 Membranes Supported on Macroporous Carbon Tubes *via* a Dipcoating-Rubbing Method. *J. Phys. Chem. Solids* **2015**, *77*, 23−29.
(169) Karthik, P.; Vinoth, R.; Zhang, P.; Choi, W.; Balaraman, E.; Neppolian, B. π-π Interaction Between Metal-Organic Framework and Reduced Graphene Oxide for Visible-Light Photocatalytic H2 Production. *ACS Appl. Energy Mater.* **2018**, *1*, 1913−1923.
(170) Lu, M.; Li, L.; Shen, S.; Chen, D.; Han, W. Highly Efficient Removal of Pb2+ By a Sandwich Structure of Metal-Organic Framework/GO Composite with Enhanced Stability. *New J. Chem.* **2019**, *43*, 1032−1037.
(171) Su, H.; Du, Y.; Zhang, J.; Peng, P.; Li, S.; Chen, P.; Gozin, M.; Pang, S. Stabilizing Metastable Polymorphs of Metal-Organic Frameworks via Encapsulation of Graphene Oxide and Mechanistic Studies. *ACS Appl. Mater. Interfaces* **2018**, *10*, 32828−32837.
(172) Kumar, R.; Jayaramulu, K.; Maji, T. K.; Rao, C. N. R. Hybrid Nanocomposites of ZIF-8 with Graphene Oxide Exhibiting Tunable Morphology, Significant CO2 Uptake and Other Novel Properties. *Chem. Commun.* **2013**, *49*, 4947−4949.
(173) Yang, L.; Shao, Z. Tunable and Convenient Synthesis of Highly Dispersed Fe-Nx Catalysts From Graphene-Supported Zn-Fe-ZIF for Efficient Oxygen Reduction in Acidic Media. *RSC Adv.* **2019**, *9*, 42236−42244.
(174) Yang, K.; Chen, B.; Zhu, X.; Xing, B. Aggregation, Adsorption, and Morphological Transformation of Graphene Oxide in Aqueous Solutions Containing Different Metal Cations. *Environ. Sci. Technol.* **2016**, *50*, 11066−11075.
(175) Kumar, R.; Raut, D.; Ramamurty, U.; Rao, C. N. R. Remarkable Improvement in the Mechanical Properties and CO2 Uptake of MOFs Brought About by Covalent Linking to Graphene. *Angew. Chem., Int. Ed.* **2016**, *55*, 7857−7861.
(176) Han, Y.; Liu, Z.; Zheng, F.; Bai, Y.; Zhang, Z.; Li, X.; Xiong, W.; Zhang, J.; Yuan, A. Two-Dimensional Flower-Like Cobalt-Porphyrin MOF/rGO Composite Anodes for High-Performance Li-Ion Batteries. *J. Alloys. Compd.* **2021**, *881*, 160531.
(177) Nabi, S.; Sofi, F. A.; Rashid, N.; Ingole, P. P.; Bhat, M. A. Metal-Organic Framework Functionalized Sulphur Doped Graphene: A Promising Platform for Selective and Sensitive Electrochemical Sensing of Acetaminophen, Dopamine and H2O2. *New J. Chem.* **2022**, *46*, 1588−1600.
(178) Jayaramulu, K.; Geyer, F.; Petr, M.; Zboril, R.; Vollmer, D.; Fischer, R. A. Shape Controlled Hierarchical Porous Hydrophobic/Oleophilic Metal-Organic Nanofibrous Gel Composites for Oil Adsorption. *Adv. Mater.* **2017**, *29*, 1605307.
(179) Szczęśniak, B.; Choma, J.; Jaroniec, M. Ultrahigh Benzene Adsorption Capacity of Graphene-MOF Composite Fabricated *via* MOF Crystallization in 3D Mesoporous Graphene. *Microporous Mesoporous Mater.* **2019**, *279*, 387−394.
(180) Liu, S.; Sun, L.; Xu, F.; Zhang, J.; Jiao, C.; Li, F.; Li, Z.; Wang, S.; Wang, Z.; Jiang, X.; Zhou, H.; Yang, L.; Schick, C. Nanosized Cu-Mofs Induced by Graphene Oxide and Enhanced Gas Storage Capacity. *Energy Environ. Sci.* **2013**, *6*, 818−823.
(181) Wu, M.; Ai, Y.; Zeng, B.; Zhao, F. In Situ Solvothermal Growth of Metal-Organic Framework-Ionic Liquid Functionalized Graphene Nanocomposite for Highly Efficient Enrichment of Chloramphenicol and Thiamphenicol. *J. Chromatogr. A* **2016**, *1427*, 1−7.
(182) Zhuang, S.; Singh, H.; Nunna, B. B.; Mandal, D.; Boscoboinik, J. A.; Lee, E. S. Nitrogen-Doped Graphene-Based Catalyst with Metal-Reduced Organic Framework: Chemical Analysis and Structure Control. *Carbon* **2018**, *139*, 933−944.
(183) Tung, T. T.; Tran, M. T.; Feller, J.-F.; Castro, M.; Van Ngo, T.; Hassan, K.; Nine, M. J.; Losic, D. Graphene And Metal Organic Frameworks (Mofs) Hybridization for Tunable Chemoresistive Sensors for Detection of Volatile Organic Compounds (VOCs) Biomarkers. *Carbon* **2020**, *159*, 333−344.
(184) Van Ngo, T.; Moussa, M.; Tung, T. T.; Coghlan, C.; Losic, D. Hybridization of Mofs and Graphene: A New Strategy for the Synthesis of Porous 3D Carbon Composites for High Performing Supercapacitors. *Electrochim. Acta* **2020**, *329*, 135104.
(185) Kumar, R.; Jayaramulu, K.; Maji, T. K.; Rao, C. N. R. Growth of 2D Sheets of a MOF on Graphene Surfaces to Yield Composites with Novel Gas Adsorption Characteristics. *Dalton Trans.* **2014**, *43*, 7383−7386.
(186) Urbanová, V.; Jayaramulu, K.; Schneemann, A.; Kment, Š; Fischer, R. A.; Zbořil, R. Hierarchical Porous Fluorinated Graphene Oxide@Metal-Organic Gel Composite: Label-Free Electrochemical Aptasensor for Selective Detection of Thrombin. *ACS Appl. Mater. Interfaces* **2018**, *10*, 41089−41097.

https://doi.org/10.1021/acs.chemrev.2c00270
Chem. Rev. 2022, 122, 17241−17338

(187) Shen, L.; Huang, L.; Liang, S.; Liang, R.; Qin, N.; Wu, L. Electrostatically Derived Self-Assembly of NH2-Mediated Zirconium Mofs with Graphene for Photocatalytic Reduction of Cr(VI). *RSC Adv.* **2014**, *4*, 2546−2549.
(188) Andrew Lin, K.-Y.; Hsu, F.-K.; Lee, W.-D. Magnetic Cobalt-Graphene Nanocomposite Derived from Self-Assembly of Mofs with Graphene Oxide as an Activator for Peroxymonosulfate. *J. Mater. Chem. A* **2015**, *3*, 9480−9490.
(189) Yang, F.; Wu, M.; Wang, Y.; Ashtiani, S.; Jiang, H. A GO-Induced Assembly Strategy To Repair MOF Nanosheet-Based Membrane for Efficient H2/CO2 Separation. *ACS Appl. Mater. Interfaces* **2019**, *11*, 990−997.
(190) Zhang, T.; Zou, B.; Shao, M.; Chen, X.; Zhang, S.; Li, L.; Du, Q.; Li, H.; Hu, Y.; Weng, J.; Xiong, W.; Zheng, B.; Zhang, W.; Huo, F. Metal-Organic Framework Wears a Protective Cover for Improved Stability. *Chem. Eur. J.* **2017**, *23*, 7663−7666.
(191) Jayaramulu, K.; Dubal, D. P.; Schneemann, A.; Ranc, V.; Perez-Reyes, C.; Stráská, J.; Kment, Š; Otyepka, M.; Fischer, R. A.; Zbořil, R. Shape-Assisted 2D MOF/Graphene Derived Hybrids as Exceptional Lithium-Ion Battery Electrodes. *Adv. Funct. Mater.* **2019**, *29*, 1902539.
(192) Zhang, C.; Han, M.; Yu, L.; Qu, L.; Li, Z. Fabrication an Electrochemical Sensor Based on Composite of Cu-TCPP Nanosheets and PSS Functionalized Graphene for Simultaneous and Sensitive Determination of Dihydroxybenzene Isomers. *J. Electroanal. Chem.* **2021**, *890*, 115232.
(193) Mao, J.; Ge, M.; Huang, J.; Lai, Y.; Lin, C.; Zhang, K.; Meng, K.; Tang, Y. Constructing Multifunctional MOF@rGO Hydro-/Aerogels by the Self-Assembly Process for Customized Water Remediation. *J. Mater. Chem. A* **2017**, *5*, 11873−11881.
(194) Cheng, J.; Liang, J.; Dong, L.; Chai, J.; Zhao, N.; Ullah, S.; Wang, H.; Zhang, D.; Imtiaz, S.; Shan, G.; Zheng, G. Self-Assembly of 2D-Metal-Organic Framework/Graphene Oxide Membranes as Highly Efficient Adsorbents for the Removal of Cs+ from Aqueous Solutions. *RSC Adv.* **2018**, *8*, 40813−40822.
(195) Yu, D.; Ge, L.; Wei, X.; Wu, B.; Ran, J.; Wang, H.; Xu, T. A General Route to the Synthesis of Layer-By-Layer Structured Metal Organic Framework/Graphene Oxide Hybrid Films For High-Performance Supercapacitor Electrodes. *J. Mater. Chem. A* **2017**, *5*, 16865−2561.
(196) Wang, H.; Yuan, L.; Liang, G.; Gu, A. Tough and Thermally Resistant Cyanate Ester Resin with Significantly Reduced Curing Temperature and Low Dielectric Loss Based on Developing an Efficient Graphene Oxide/Mn Ion Metal-Organic Framework Hybrid. *RSC Adv.* **2016**, *6*, 3290−3300.
(197) Qiu, X.; Wang, X.; Li, Y. Controlled Growth of Dense and Ordered Metal-Organic Framework Nanoparticles on Graphene Oxide. *Chem. Commun.* **2015**, *51*, 3874−3877.
(198) Zeng, J.-Y.; Wang, X.-S.; Zhang, M.-K.; Li, Z.-H.; Gong, D.; Pan, P.; Huang, L.; Cheng, S.-X.; Cheng, H.; Zhang, X.-Z. Universal Porphyrinic Metal-Organic Framework Coating to Various Nanostructures for Functional Integration. *ACS Appl. Mater. Interfaces* **2017**, *9*, 43143−43153.
(199) Pan, Y.-T.; Wan, J.; Zhao, X.; Li, C.; Wang, D.-Y. Interfacial Growth of MOF-Derived Layered Double Hydroxide Nanosheets on Graphene Slab Towards Fabrication of Multifunctional Epoxy Nanocomposites. *Chem. Eng. J.* **2017**, *330*, 1222−1231.
(200) Tanhaei, M.; Mahjoub, A. R.; Safarifard, V. Ultrasonic-Assisted Synthesis and Characterization of Nanocomposites from Azine-Decorated Metal-Organic Framework and Graphene Oxide Layers. *Mater. Lett.* **2018**, *227*, 318−321.
(201) Yao, J.; Dong, D.; Li, D.; He, L.; Xu, G.; Wang, H. Contra-Diffusion Synthesis of ZIF-8 Films on a Polymer Substrate. *Chem. Commun.* **2011**, *47*, 2559−2561.
(202) Kim, D.; Coskun, A. Graphene Oxide-Templated Preferential Growth of Continuous MOF Thin Films. *CrystEngComm* **2016**, *18*, 4013−4017.
(203) Pendem, S.; Singuru, R.; Sarkar, C.; Joseph, B.; Lee, J.-F.; Shinde, D. B.; Lai, Z.; Mondal, J. Zeolitic Imidazolate Framework-Mediated Synthesis of Co3O4 Nanoparticles Encapsulated in N-Doped Graphitic Carbon as an Efficient Catalyst for Selective Oxidation of Hydrocarbons. *ACS Appl. Nano Mater.* **2018**, *1*, 4836−4851.
(204) Cai, S.; Wang, R.; Yourey, W. M.; Li, J.; Zhang, H.; Tang, H. An Efficient Bifunctional Electrocatalyst Derived from Layer-By-Layer Self-Assembly of a Three-Dimensional Porous Co-N-C@Graphene. *Sci. Bull.* **2019**, *64*, 968−975.
(205) Zvyagina, A. I.; Shiryaev, A. A.; Baranchikov, A. E.; Chernyshev, V. V.; Enakieva, Y. Y.; Raitman, O. A.; Ezhov, A. A.; Meshkov, I. N.; Grishanov, D. A.; Ivanova, O. S.; Gorbunova, Y. G.; Arslanov, V. V.; Kalinina, M. A. Layer-By-Layer Assembly of Porphyrin-Based Metal-Organic Frameworks on Solids Decorated with Graphene Oxide. *New J. Chem.* **2017**, *41*, 948−957.
(206) Wu, J.; Ma, G.-H. Recent Studies of Pickering Emulsions: Particles Make the Difference. *Small* **2016**, *12*, 4633−4648.
(207) Bian, Z.; Zhang, S.; Zhu, X.; Li, Y.; Liu, H.; Hu, J. In Situ Interfacial Growth of Zeolitic Imidazolate Framework (ZIF-8) Nanoparticles Induced by a Graphene Oxide Pickering Emulsion. *RSC Adv.* **2015**, *5*, 31502−31505.
(208) Bian, Z.; Xu, J.; Zhang, S.; Zhu, X.; Liu, H.; Hu, J. Interfacial Growth of Metal Organic Framework/Graphite Oxide Composites through Pickering Emulsion and Their CO2 Capture Performance in the Presence of Humidity. *Langmuir* **2015**, *31*, 7410−7417.
(209) Zhang, F.; Liu, L.; Tan, X.; Sang, X.; Zhang, J.; Liu, C.; Zhang, B.; Han, B.; Yang, G. Pickering Emulsions Stabilized by a Metal-Organic Framework (MOF) and Graphene Oxide (GO) for Producing MOF/GO Composites. *Soft Matter* **2017**, *13*, 7365−7370.
(210) Nugmanova, A. G.; Safonova, E. A.; Baranchikov, A. E.; Tameev, A. R.; Shkolin, A. V.; Mitrofanov, A. A.; Eliseev, A. A.; Meshkov, I. N.; Kalinina, M. A. Interfacial Self-Assembly of Porphyrin-Based Surmof/Graphene Oxide Hybrids with Tunable Pore Size: An Approach Toward Size-Selective Ambivalent Heterogeneous Photocatalysts. *Appl. Surf. Sci.* **2022**, *579*, 152080.
(211) He, L.; Liu, J.; Yang, L.; Song, Y.; Wang, M.; Peng, D.; Zhang, Z.; Fang, S. Copper Metal-Organic Framework-Derived CuOx-Coated Three-Dimensional Reduced Graphene Oxide and Polyaniline Composite: Excellent Candidate Free-Standing Electrodes for High-Performance Supercapacitors. *Electrochim. Acta* **2018**, *275*, 133−144.
(212) Fan, X.; Yang, F.; Huang, J.; Yang, Y.; Nie, C.; Zhao, W.; Ma, L.; Cheng, C.; Zhao, C.; Haag, R. Metal-Organic-Framework-Derived 2D Carbon Nanosheets for Localized Multiple Bacterial Eradication and Augmented Anti-infective Therapy. *Nano Lett.* **2019**, *19*, 5885−5896.
(213) Zhang, D.; Wu, Z.; Zong, X. Metal-Organic Frameworks-Derived Zinc Oxide Nanopolyhedra/S, N: Graphene Quantum Dots/Polyaniline Ternary Nanohybrid for High-Performance Acetone Sensing. *Sens. Actuators B. Chem.* **2019**, *288*, 232−242.
(214) Nan, J.; Dong, X.; Wang, W.; Jin, W.; Xu, N. Step-by-Step Seeding Procedure for Preparing HKUST-1 Membrane on Porous α-Alumina Support. *Langmuir* **2011**, *27*, 4309−4312.
(215) Yoo, Y.; Lai, Z.; Jeong, H.-K. Fabrication of MOF-5 Membranes Using Microwave-Induced Rapid Seeding and Solvothermal Secondary Growth. *Microporous Mesoporous Mater.* **2009**, *123*, 100−106.
(216) Balakrishnan, S.; Downard, A. J.; Telfer, S. G. HKUST-1 Growth on Glassy Carbon. *J. Mater. Chem.* **2011**, *21*, 19207−19209.
(217) Hu, Y.; Dong, X.; Nan, J.; Jin, W.; Ren, X.; Xu, N.; Lee, Y. M. Metal-Organic Framework Membranes Fabricated *via* Reactive Seeding. *Chem. Commun.* **2011**, *47*, 737−739.
(218) Guerrero, V. V.; Yoo, Y.; McCarthy, M. C.; Jeong, H.-K. HKUST-1 Membranes on Porous Supports Using Secondary Growth. *J. Mater. Chem.* **2010**, *20*, 3938−3943.
(219) Hu, Y.; Wei, J.; Liang, Y.; Zhang, H.; Zhang, X.; Shen, W.; Wang, H. Zeolitic Imidazolate Framework/Graphene Oxide Hybrid Nanosheets as Seeds for the Growth of Ultrathin Molecular Sieving Membranes. *Angew. Chem., Int. Ed.* **2016**, *55*, 2048−2052.
(220) Lee, C. S.; Song, E.; Park, J. T.; Kim, J. H. Ultrathin, Highly Permeable Graphene Oxide/Zeolitic Imidazole Framework Polymeric Mixed-Matrix Composite Membranes: Engineering the CO2-Philic Pathway. *ACS Sustain. Chem. Eng.* **2021**, *9*, 11903−11915.
(221) Firouzjaei, M. D.; Shamsabadi, A. A.; Aktij, S. A.; Seyedpour, S. F.; Sharifian Gh., M.; Rahimpour, A.; Esfahani, M. R.; Ulbricht, M.;

Soroush, M. Exploiting Synergetic Effects of Graphene Oxide and a Silver-Based Metal-Organic Framework To Enhance Antifouling and Anti-Biofouling Properties of Thin-Film Nanocomposite Membranes. *ACS Appl. Mater. Interfaces* **2018**, *10*, 42967−42978.
(222) Golpour, M.; Pakizeh, M. Preparation and Characterization of New PA-MOF/PPSU-GO Membrane for the Separation of KHI from Water. *Chem. Eng. J.* **2018**, *345*, 221−232.
(223) Mu, Q.; Zhu, W.; Li, X.; Zhang, C.; Su, Y.; Lian, Y.; Qi, P.; Deng, Z.; Zhang, D.; Wang, S.; Zhu, X.; Peng, Y. Electrostatic Charge Transfer for Boosting the Photocatalytic CO2 Reduction on Metal Centers of 2D MOF/rGO Heterostructure. *Appl. Catal., B* **2020**, *262*, 118144.
(224) Kaur, R.; Kim, K.-H.; Deep, A. A Convenient Electrolytic Assembly of Graphene-MOF Composite Thin Film and its Photoanodic Application. *Appl. Surf. Sci.* **2017**, *396*, 1303−1309.
(225) Kung, C.-W.; Li, Y.-S.; Lee, M.-H.; Wang, S.-Y.; Chiang, W.-H.; Ho, K.-C. In Situ Growth of Porphyrinic Metal-Organic Framework Nanocrystals on Graphene Nanoribbons for the Electrocatalytic Oxidation of Nitrite. *J. Mater. Chem. A* **2016**, *4*, 10673−10682.
(226) Wang, Y.; Cao, W.; Wang, L.; Zhuang, Q.; Ni, Y. Electrochemical Determination of 2,4,6-Trinitrophenol Using a Hybrid Film Composed of a Copper-Based Metal Organic Framework and Electroreduced Graphene Oxide. *Microchim. Acta* **2018**, *185*, 315.
(227) Rezvani Jalal, N.; Madrakian, T.; Afkhami, A.; Ghoorchian, A. In Situ Growth of Metal-Organic Framework HKUST-1 on Graphene Oxide Nanoribbons with High Electrochemical Sensing Performance in Imatinib Determination. *ACS Appl. Mater. Interfaces* **2020**, *12*, 4859−4869.
(228) Wang, B.; Kang, K.; Ji, X.; Liu, Y.; Li, X.; Wang, L.; Ren, J. Multifunctional Encapsulating Gold Nanoparticles into Cu-Hemin/Metal-Organic Frameworks for Catechol Electrochemical Detection on Graphene-Based Electrode. *Nano* **2020**, *15*, 2050155.
(229) Hatamluyi, B.; Rezayi, M.; Beheshti, H. R.; Boroushaki, M. T. Ultra-Sensitive Molecularly Imprinted Electrochemical Sensor for Patulin Detection Based on a Novel Assembling Strategy Using Au@Cu-MOF/N-Gqds. *Sens. Actuators B. Chem.* **2020**, *318*, 128219.
(230) Cao, X.; Zheng, B.; Rui, X.; Shi, W.; Yan, Q.; Zhang, H. Metal Oxide-Coated Three-Dimensional Graphene Prepared by the Use of Metal-Organic Frameworks as Precursors. *Angew. Chem., Int. Ed.* **2014**, *53*, 1404−1433.
(231) Martín-Jimeno, F. J.; Suárez-García, F.; Paredes, J. I.; Enterría, M.; Pereira, M. F. R.; Martins, J. I.; Figueiredo, J. L.; Martínez-Alonso, A.; Tascón, J. M. D. A "Nanopore Lithography" Strategy for Synthesizing Hierarchically Micro/Mesoporous Carbons from ZIF-8/Graphene Oxide Hybrids for Electrochemical Energy Storage. *ACS Appl. Mater. Interfaces* **2017**, *9*, 44740−44755.
(232) Xu, X.; Shi, W.; Li, P.; Ye, S.; Ye, C.; Ye, H.; Lu, T.; Zheng, A.; Zhu, J.; Xu, L.; Zhong, M.; Cao, X. Facile Fabrication of Three-Dimensional Graphene and Metal-Organic Framework Composites and Their Derivatives for Flexible All-Solid-State Supercapacitors. *Chem. Mater.* **2017**, *29*, 6058−6065.
(233) Shahrokhian, S.; Ezzati, M.; Hosseini, H. Fabrication of a Sensitive and Fast Response Electrochemical Glucose Sensing Platform Based on Co-Based Metal-Organic Frameworks Obtained from Rapid In Situ Conversion of Electrodeposited Cobalt Hydroxide Intermediates. *Talanta* **2020**, *210*, 120696.
(234) Barakzehi, M.; Montazer, M.; Sharif, F.; Norby, T.; Chatzitakis, A. MOF-Modified Polyester Fabric Coated with Reduced Graphene Oxide/Polypyrrole as Electrode for Flexible Supercapacitors. *Electrochim. Acta* **2020**, *336*, 135743.
(235) Lu, X. F.; Fang, Y.; Luan, D.; Lou, X. W. D. Metal-Organic Frameworks Derived Functional Materials for Electrochemical Energy Storage and Conversion: A Mini Review. *Nano Lett.* **2021**, *21*, 1555−1565.
(236) Tan, X.; Wu, Y.; Lin, X.; Zeb, A.; Xu, X.; Luo, Y.; Liu, J. Application of MOF-Derived Transition Metal Oxides and Composites as Anodes for Lithium-Ion Batteries. *Inorg. Chem. Front.* **2020**, *7*, 4939−4955.
(237) Yang, W.; Li, X.; Li, Y.; Zhu, R.; Pang, H. Applications of Metal-Organic-Framework-Derived Carbon Materials. *Adv. Mater.* **2019**, *31*, 1804740.
(238) Jayaramulu, K.; Masa, J.; Tomanec, O.; Peeters, D.; Ranc, V.; Schneemann, A.; Zboril, R.; Schuhmann, W.; Fischer, R. A. Nanoporous Nitrogen-Doped Graphene Oxide/Nickel Sulfide Composite Sheets Derived from a Metal-Organic Framework as an Efficient Electrocatalyst for Hydrogen and Oxygen Evolution. *Adv. Funct. Mater.* **2017**, *27*, 1700451.
(239) Rabiee Faradonbeh, M.; Dadkhah, A. A.; Rashidi, A.; Tasharofi, S.; Mansourkhani, F. Newly MOF-Graphene Hybrid Nanoadsorbent for Removal of Ni(II) from Aqueous Phase. *J. Inorg. Organomet. Polym. Mater.* **2018**, *28*, 829−836.
(240) Yang, K.; Yan, Y.; Wang, H.; Sun, Z.; Chen, W.; Kang, H.; Han, Y.; Zahng, W.; Sun, X.; Li, Z. Monodisperse Cu/Cu2O@C Core-Shell Nanocomposite Supported on rGO Layers as an Efficient Catalyst Derived from a Cu-Based MOF/GO Structure. *Nanoscale* **2018**, *10*, 17647−17655.
(241) Yogapriya, R.; Kasibhatta, K. R. D. Hydrophobic-Superoleophilic Fluorinated Graphene Nanosheet Composites with Metal-Organic Framework HKUST-1 for Oil-Water Separation. *ACS Appl. Nano Mater.* **2020**, *3*, 5816−5825.
(242) Matloob, A. M.; El-Hafiz, D. R. A.; Saad, L.; Mikhail, S.; Guirguis, D. Metal Organic Framework-Graphene Nano-Composites for High Adsorption Removal of DBT as Hazard Material in Liquid Fuel. *J. Hazard. Mater.* **2019**, *373*, 447−458.
(243) Khan, U. A.; Iqbal, N.; Noor, T.; Ahmad, R.; Ahmad, A.; Gao, J.; Amjad, Z.; Wahab, A. Cerium Based Metal Organic Framework Derived Composite with Reduced Graphene Oxide as Efficient Supercapacitor Electrode. *J. Energy Storage* **2021**, *41*, 102999.
(244) Beka, L. G.; Bu, X.; Li, X.; Wang, X.; Han, C.; Liu, W. A 2D Metal-Organic Framework/Reduced Graphene Oxide Heterostructure for Supercapacitor Application. *RSC Adv.* **2019**, *9*, 36123−36135.
(245) Muschi, M.; Serre, C. Progress and Challenges of Graphene Oxide/Metal-Organic Composites. *Coord. Chem. Rev.* **2019**, *387*, 262−272.
(246) Claramunt, S.; Varea, A.; López-Díaz, D.; Velázquez, M. M.; Cornet, A.; Cirera, A. The Importance of Interbands on the Interpretation of the Raman Spectrum of Graphene Oxide. *J. Phys. Chem. C* **2015**, *119*, 10123−10129.
(247) Yaghi, O. M.; O'Keeffe, M.; Ockwig, N. W.; Chae, H. K.; Eddaoudi, M.; Kim, J. Reticular Synthesis and the Design of New Materials. *Nature* **2003**, *423*, 705−714.
(248) Pepinsky, R. Crystal Engineering-New Concept in Crystallography. *Phys. Rev.* **1955**, *100*, 971.
(249) Kitagawa, S. Porous Materials and the Age of Gas. *Angew. Chem., Int. Ed.* **2015**, *54*, 10686−10687.
(250) Moghadam, P. Z.; Li, A.; Liu, X.-W.; Bueno-Perez, R.; Wang, S.-D.; Wiggin, S. B.; Wood, P. A.; Fairen-Jimenez, D. Targeted Classification of Metal-Organic Frameworks in the Cambridge Structural Database (CSD). *Chem. Sci.* **2020**, *11*, 8373−8387.
(251) Zhu, L.; Meng, L.; Shi, J.; Li, J.; Zhang, X.; Feng, M. Metal-Organic Frameworks/Carbon-Based Materials for Environmental Remediation: A State-of-the-Art Mini-Review. *J. Environ. Manage.* **2019**, *232*, 964−977.
(252) Oschatz, M.; Antonietti, M. A Search for Selectivity to Enable CO2 Capture with Porous Adsorbents. *Energy Environ. Sci.* **2018**, *11*, 57−70.
(253) Sholl, D. S.; Lively, R. P. *Nature* **2016**, *532*, 435−437.
(254) Mukherjee, S.; Desai, A. V.; Ghosh, S. K. Potential of Metal-Organic Frameworks for Adsorptive Separation of Industrially and Environmentally Relevant Liquid Mixtures. *Coord. Chem. Rev.* **2018**, *367*, 82−126.
(255) Barea, E.; Montoro, C.; Navarro, J. A. R. Toxic Gas Removal - Metal-Organic Frameworks for the Capture and Degradation of Toxic Gases and Vapours. *Chem. Soc. Rev.* **2014**, *43*, 5419−5430.
(256) Rojas, S.; Horcajada, P. Metal-Organic Frameworks for the Removal of Emerging Organic Contaminants in Water. *Chem. Rev.* **2020**, *120*, 8378−8415.

https://doi.org/10.1021/acs.chemrev.2c00270
Chem. Rev. 2022, 122, 17241−17338

(257) Mon, M.; Bruno, R.; Ferrando-Soria, J.; Armentano, D.; Pardo, E. Metal-Organic Framework Technologies for Water Remediation: Towards a Sustainable Ecosystem. *J. Mater. Chem. A* **2018**, *6*, 4912−4947.
(258) Chui, S. S.-Y.; Lo, S. M.-F.; Charmant, J. P. H.; Orpen, A. G.; Williams, I. D. A Chemically Functionalizable Nanoporous Material [Cu3(TMA)2(H2O)3]n. *Science* **1999**, *283*, 1148−1150.
(259) Dong, L.; Chen, M.; Li, J.; Shi, D.; Dong, W.; Li, X.; Bai, Y. Metal-Organic Framework-Graphene Oxide Composites: A Facile Method to Highly Improve the CO2 Separation Performance of Mixed Matrix Membranes. *J. Membr. Sci.* **2016**, *520*, 801−811.
(260) Sarfraz, M.; Ba-Shammakh, M. Synergistic Effect of Adding Graphene Oxide and ZIF-301 to Polysulfone to Develop High Performance Mixed Matrix Membranes For Selective Carbon Dioxide Separation From Post Combustion Flue Gas. *J. Membr. Sci.* **2016**, *514*, 35−43.
(261) Lee, H.; Park, S. C.; Roh, J. S.; Moon, G. H.; Shin, J. E.; Kang, Y. S.; Park, H. B. Metal-Organic Frameworks Grown on a Porous Planar Template with an Exceptionally High Surface Area: Promising Nanofiller Platforms for CO2 Separation. *J. Mater. Chem. A* **2017**, *5*, 22500−22505.
(262) Anastasiou, S.; Bhoria, N.; Pokhrel, J.; Kumar Reddy, K. S.; Srinivasakannan, C.; Wang, K.; Karanikolos, G. N. Metal-Organic Framework/Graphene Oxide Composite Fillers in Mixed-Matrix Membranes for CO2 Separation. *Mater. Chem. Phys.* **2018**, *212*, 513−522.
(263) Feijani, E. A.; Mahdavi, H.; Tavassoli, A. Synthesis and Gas Permselectivity of Cubtc-GO-PVDF Mixed Matrix Membranes. *New J. Chem.* **2018**, *42*, 12013−12023.
(264) Su, L.; Hu, J.; Wang, K.; Wang, Y.; Zhang, W.; Cao, Y.; Zhao, N. Facile Synthesis and Enhanced Adsorption Ability of Pt-GO/MOF Nanomaterials. *Mater. Manuf. Process.* **2016**, *31*, 141−145.
(265) Xiang, S.; He, Y.; Zhang, Z.; Wu, H.; Zhou, W.; Krishna, R.; Chen, B. Microporous Metal-Organic Framework with Potential for Carbon Dioxide Capture at Ambient Conditions. *Nat. Commun.* **2012**, *3*, 954.
(266) Shen, Y.; Li, Z.; Wang, L.; Ye, Y.; Liu, Q.; Ma, X.; Chen, Q.; Zhang, Z.; Xiang, S. Cobalt-Citrate Framework Armored with Graphene Oxide Exhibiting Improved Thermal Stability and Selectivity for Biogas Decarburization. *J. Mater. Chem. A* **2015**, *3*, 593−599.
(267) Rosi, N. L.; Kim, J.; Eddaoudi, M.; Chen, B.; O'Keeffe, M.; Yaghi, O. M. Rod Packings and Metal-Organic Frameworks Constructed from Rod-Shaped Secondary Building Units. *J. Am. Chem. Soc.* **2005**, *127*, 1504−1518.
(268) Asgharnejad, L.; Abbasi, A.; Shakeri, A. Ni-Based Metal-Organic Framework/GO Nanocomposites as Selective Adsorbent for CO2 Over N2. *Microporous Mesoporous Mater.* **2018**, *262*, 227−234.
(269) Zhou, X.; Huang, W.; Liu, J.; Wang, H.; Li, Z. Quenched Breathing Effect, Enhanced CO2 Uptake and Improved CO2/CH4 Selectivity of MIL-53(Cr)/Graphene Oxide Composites. *Chem. Eng. Sci.* **2017**, *167*, 98−104.
(270) Pokhrel, J.; Bhoria, N.; Anastasiou, S.; Tsoufis, T.; Gournis, D.; Romanos, G.; Karanikolos, G. N. CO2 Adsorption Behavior of Amine-Functionalized ZIF-8, Graphene Oxide, and ZIF-8/Graphene Oxide Composites Under Dry and Wet Conditions. *Microporous Mesoporous Mater.* **2018**, *267*, 53−67.
(271) Zhou, X.; Huang, W.; Miao, J.; Xia, Q.; Zhang, Z.; Wang, H.; Li, Z. Enhanced Separation Performance of a Novel Composite Material Gro@MIL-101 for CO2/CH4 Binary Mixture. *Chem. Eng. J.* **2015**, *266*, 339−344.
(272) Pourebrahimi, S.; Kazemeini, M.; Ganji Babakhani, E.; Taheri, A. Removal of the CO2 from Flue Gas Utilizing Hybrid Composite Adsorbent MIL-53(Al)/GNP Metal-Organic Framework. *Microporous Mesoporous Mater.* **2015**, *218*, 144−152.
(273) Cao, Y.; Zhang, H.; Song, F.; Huang, T.; Ji, J.; Zhong, Q.; Chu, W.; Xu, Q. UiO-66-NH2/GO Composite: Synthesis, Characterization and CO2 Adsorption Performance. *Materials* **2018**, *11*, 589.
(274) Ullah, S.; Bustam, M. A.; Al-Sehemi, A. G.; Assiri, M. A.; Abdul Kareem, F. A.; Mukhtar, A.; Ayoub, M.; Gonfa, G. Influence of Post-Synthetic Graphene Oxide (GO) Functionalization on the Selective CO2/CH4 Adsorption Behavior of MOF-200 At Different Temperatures; An Experimental and Adsorption Isotherms Study. *Microporous Mesoporous Mater.* **2020**, *296*, 110002.
(275) Chen, Y.; Lv, D.; Wu, J.; Xiao, J.; Xi, H.; Xia, Q.; Li, Z. A New MOF-505@GO Composite with High Selectivity for CO2/CH4 and CO2/N2 Separation. *Chem. Eng. J.* **2017**, *308*, 1065−1072.
(276) Li, W.; Chuah, C. Y.; Yang, Y.; Bae, T.-H. Nanocomposites Formed by In Situ Growth of NiDOBDC Nanoparticles on Graphene Oxide Sheets for Enhanced CO2 and H2 Storage. *Microporous Mesoporous Mater.* **2018**, *265*, 35−42.
(277) Cao, Y.; Zhao, Y.; Lv, Z.; Song, F.; Zhong, Q. Preparation and Enhanced CO2 Adsorption Capacity Of Uio-66/Graphene Oxide Composites. *J. Ind. Eng. Chem.* **2015**, *27*, 102−107.
(278) Szczęśniak, B.; Choma, J. Graphene-Containing Microporous Composites for Selective CO2 Adsorption. *Microporous Mesoporous Mater.* **2020**, *292*, 109761.
(279) Ning, H.; Yang, Z.; Yin, Z.; Wang, D.; Meng, Z.; Wang, C.; Zhang, Y.; Chen, Z. A Novel Strategy to Enhance the Performance of CO2 Adsorption Separation: Grafting Hyper-cross-linked Polyimide onto Composites of UiO-66-NH2 and GO. *ACS Appl. Mater. Interfaces* **2021**, *13*, 17781−17790.
(280) Kang, Z.; Xue, M.; Zhang, D.; Fan, L.; Pan, Y.; Qiu, S. Hybrid Metal-Organic Framework Nanomaterials with Enhanced Carbon Dioxide and Methane Adsorption Enthalpy by Incorporation Of Carbon Nanotubes. *Inorg. Chem. Commun.* **2015**, *58*, 79−83.
(281) Kang, Z.; Wang, S.; Wang, R.; Guo, H.; Xu, B.; Feng, S.; Fan, L.; Zhu, L.; Kang, W.; Pang, J.; Sun, H.; Du, X.; Zhang, M.; Sun, D. Sandwich Membranes Through a Two-Dimensional Confinement Strategy for Gas Separation. *Mater. Chem. Front.* **2018**, *2*, 1911−1919.
(282) Li, W.; Zhang, Y.; Su, P.; Xu, Z.; Zhang, G.; Shen, C.; Meng, Q. Metal-Organic Framework Channelled Graphene Composite Membranes for H2/CO2 Separation. *J. Mater. Chem. A* **2016**, *4*, 18747−18752.
(283) Li, W.; Shi, J.; Li, Z.; Wu, W.; Xia, Y.; Yu, Y.; Zhang, G. Hydrothermally Reduced Graphene Oxide Interfaces for Synthesizing High-Performance Metal-Organic Framework Hollow Fiber Membranes. *Adv. Mater. Interfaces* **2018**, *5*, 1800032.
(284) Taheri, A.; Babakhani, E. G.; Towfighi Darian, J. A MIL-101(Cr) and Graphene Oxide Composite for Methane-Rich Stream Treatment. *Energy Fuels* **2017**, *31*, 8792−8802.
(285) Myers, A. L.; Prausnitz, J. M. Thermodynamics of Mixed-Gas Adsorption. *AIChE J.* **1965**, *11*, 121−127.
(286) Yang, S. J.; Choi, J. Y.; Chae, H. K.; Cho, J. H.; Nahm, K. S.; Park, C. R. Preparation and Enhanced Hydrostability and Hydrogen Storage Capacity of CNT@MOF-5 Hybrid Composite. *Chem. Mater.* **2009**, *21*, 1893−1897.
(287) Lin, R.; Ge, L.; Liu, S.; Rudolph, V.; Zhu, Z. Mixed-Matrix Membranes with Metal-Organic Framework-Decorated CNT Fillers for Efficient CO2 Separation. *ACS Appl. Mater. Interfaces* **2015**, *7*, 14750−14757.
(288) Xiang, Z.; Peng, X.; Cheng, X.; Li, X.; Cao, D. CNT@Cu3(BTC)2 and Metal-Organic Frameworks for Separation of CO2/CH4Mixture. *J. Phys. Chem. C* **2011**, *115*, 19864−19871.
(289) Anbia, M.; Hoseini, V. Development of MWCNT@MIL-101 Hybrid Composite with Enhanced Adsorption Capacity for Carbon Dioxide. *Chem. Eng. J.* **2012**, *191*, 326−330.
(290) Thierfelder, C.; Witte, M.; Blankenburg, S.; Rauls, E.; Schmidt, W. G. Methane Adsorption on Graphene from First Principles Including Dispersion Interaction. *Surf. Sci.* **2011**, *605*, 746−749.
(291) Chouhan, R. K.; Ulman, K.; Narasimhan, S. Graphene Oxide as an Optimal Candidate Material for Methane Storage. *J. Chem. Phys.* **2015**, *143*, 044704.
(292) Al-Naddaf, Q.; Al-Mansour, M.; Thakkar, H.; Rezaei, F. MOF-GO Hybrid Nanocomposite Adsorbents for Methane Storage. *Ind. Eng. Chem. Res.* **2018**, *57*, 17470−17479.
(293) Peng, Y.; Krungleviciute, V.; Eryazici, I.; Hupp, J. T.; Farha, O. K.; Yildirim, T. Methane Storage in Metal-Organic Frameworks:

Current Records, Surprise Findings, and Challenges. *J. Am. Chem. Soc.* **2013**, *135*, 11887−11894.
(294) Szczęśniak, B.; Choma, J.; Jaroniec, M. Gas Adsorption Properties of Hybrid Graphene-MOF Materials. *J. Colloid Interface Sci.* **2018**, *514*, 801−813.
(295) Domán, A.; Madarász, J.; Sáfrán, G.; Wang, Y.; László, K. Copper Benzene-1,3,5-Tricarboxylate (HKUST-1) - Graphene Oxide Pellets for Methane Adsorption. *Microporous Mesoporous Mater.* **2021**, *316*, 110948.
(296) Gallagher, J. Towards Methane Targets. *Nature Energy* **2018**, *3*, 86.
(297) Petit, C.; Bandosz, T. J. Enhanced Adsorption of Ammonia on Metal-Organic Framework/Graphite Oxide Composites: Analysis of Surface Interactions. *Adv. Funct. Mater.* **2010**, *20*, 111−118.
(298) Petit, C.; Bandosz, T. J. MOF-Graphite Oxide Nanocomposites: Surface Characterization and Evaluation as Adsorbents of Ammonia. *J. Mater. Chem.* **2009**, *19*, 6521−6528.
(299) Levasseur, B.; Petit, C.; Bandosz, T. J. Reactive Adsorption of NO2 on Copper-Based Metal-Organic Framework and Graphite Oxide/Metal-Organic Framework Composites. *ACS Appl. Mater. Interfaces* **2010**, *2*, 3606−3613.
(300) Travlou, N. A.; Singh, K.; Rodríguez-Castellón, E.; Bandosz, T. J. Cu-BTC MOF-Graphene-Based Hybrid Materials as Low Concentration Ammonia Sensors. *J. Mater. Chem. A* **2015**, *3*, 11417−11429.
(301) Yin, Y.; Zhang, H.; Huang, P.; Xiang, C.; Zou, Y.; Xu, F.; Sun, L. Inducement of Nanoscale Cu-BTC on Nanocomposite of Ppy-rGO and its Performance in Ammonia Sensing. *Mater. Res. Bull.* **2018**, *99*, 152−160.
(302) Semrau, A. L.; Zhou, Z.; Mukherjee, S.; Tu, M.; Li, W.; Fischer, R. A. Surface-Mounted Metal-Organic Frameworks: Past, Present, and Future Perspectives. *Langmuir* **2021**, *37*, 6847−6863.
(303) Wang, X.; Chi, C.; Tao, J.; Peng, Y.; Ying, S.; Qian, Y.; Dong, J.; Hu, Z.; Gu, Y.; Zhao, D. Improving the Hydrogen Selectivity of Graphene Oxide Membranes by Reducing Non-Selective Pores with Intergrown ZIF-8 Crystals. *Chem. Commun.* **2016**, *52*, 8087−8090.
(304) Hu, Y.; Wu, Y.; Devendran, C.; Wei, J.; Liang, Y.; Matsukata, M.; Shen, W.; Neild, A.; Huang, H.; Wang, H. Preparation of Nanoporous Graphene Oxide by Nanocrystal-Masked Etching: Toward a Nacre-Mimetic Metal-Organic Framework Molecular Sieving Membrane. *J. Mater. Chem. A* **2017**, *5*, 16255−16262.
(305) Liu, D.; Pang, G.; Tang, Z.; Feng, S. Interfacial Engineering of Metal-Organic Frameworks/Graphene Oxide Composite Membrane by Polyethyleneimine for Efficient H2/CH4 Gas Separation. *Inorg. Chem. Front.* **2019**, *6*, 2043−2049.
(306) Li, N.; Yuan, H.; Xu, L.; Tao, J.; Ng, D. K. T.; Lee, L. Y. T.; Cheam, D. D.; Zeng, Y.; Qiang, B.; Wang, Q.; Cai, H.; Singh, N.; Zhao, D. Radiation Enhancement by Graphene Oxide on Microelectromechanical System Emitters for Highly Selective Gas Sensing. *ACS Sens.* **2019**, *4*, 2746−2753.
(307) Petit, C.; Mendoza, B.; Bandosz, T. J. Hydrogen Sulfide Adsorption on MOFs and MOF/Graphite Oxide Composites. *ChemPhysChem* **2010**, *11*, 3678−3684.
(308) Li, H.; Eddaoudi, M.; O'Keeffe, M.; Yaghi, O. M. Design and Synthesis of an Exceptionally Stable and Highly Porous Metal-Organic Framework. *Nature* **1999**, *402*, 276−279.
(309) Huang, Z.-H.; Liu, G.; Kang, F. Glucose-Promoted Zn-Based Metal-Organic Framework/Graphene Oxide Composites for Hydrogen Sulfide Removal. *ACS Appl. Mater. Interfaces* **2012**, *4*, 4942−4947.
(310) Bhoria, N.; Basina, G.; Pokhrel, J.; Kumar Reddy, K. S.; Anastasiou, S.; Balasubramanian, V. V.; AlWahedi, Y. F.; Karanikolos, G. N. Functionalization Effects on HKUST-1 and HKUST-1/Graphene Oxide Hybrid Adsorbents for Hydrogen Sulfide Removal. *J. Hazard. Mater.* **2020**, *394*, 122565.
(311) Zhang, C.; Zhang, S.; Yang, Y.; Yu, H.; Dong, X. Highly Sensitive H2S Sensors Based on Metal-Organic Framework Driven Γ-Fe2O3 on Reduced Graphene Oxide Composites at Room Temperature. *Sens. Actuators B. Chem.* **2020**, *325*, 128804.
(312) Pham, M.-H.; Vuong, G.-T.; Vu, A.-T.; Do, T.-O. Novel Route to Size-Controlled Fe-MIL-88B-NH2Metal-Organic Framework Nanocrystals. *Langmuir* **2011**, *27*, 15261−15267.
(313) McDonald, T. M.; Lee, W. R.; Mason, J. A.; Wiers, B. M.; Hong, C. S.; Long, J. R. Capture of Carbon Dioxide from Air and Flue Gas in the Alkylamine-Appended Metal-Organic Framework mmen-Mg2-(dobpdc). *J. Am. Chem. Soc.* **2012**, *134*, 7056−7065.
(314) Gu, J.; Fan, H.; Li, C.; Caro, J.; Meng, H. Robust Superhydrophobic/Superoleophilic Wrinkled Microspherical MOF@rGO Composites for Efficient Oil-Water Separation. *Angew. Chem., Int. Ed.* **2019**, *58*, 5297−5301.
(315) Eom, S.; Kang, D. W.; Kang, M.; Choe, J. H.; Kim, H.; Kim, D. W.; Hong, C. S. Fine-Tuning of Wettability In a Single Metal-Organic Framework *via* Postcoordination Modification and its Reduced Graphene Oxide Aerogel for Oil-Water Separation. *Chem. Sci.* **2019**, *10*, 2663−2669.
(316) Zhan, Y.; He, S.; Hu, J.; Zhao, S.; Zeng, G.; Zhou, M.; Zhang, G.; Sengupta, A. Robust Super-Hydrophobic/Super-Oleophilic Sandwich-Like UIO-66-F4@rGO Composites for Efficient and Multitasking Oil/Water Separation Applications. *J. Hazard. Mater.* **2020**, *388*, 121752.
(317) Ma, W.; Li, Y.; Zhang, M.; Gao, S.; Cui, J.; Huang, C.; Fu, G. Biomimetic Durable Multifunctional Self-Cleaning Nanofibrous Membrane with Outstanding Oil/Water Separation, Photodegradation of Organic Contaminants, and Antibacterial Performances. *ACS Appl. Mater. Interfaces* **2020**, *12*, 34999−35010.
(318) Li, H.; Yin, Y.; Zhu, L.; Xiong, Y.; Li, X.; Guo, T.; Xing, W.; Xue, Q. A Hierarchical Structured Steel Mesh Decorated with Metal Organic Framework/Graphene Oxide for High-Efficient Oil/Water Separation. *J. Hazard. Mater.* **2019**, *373*, 725−732.
(319) Zhu, M.; Liu, Y.; Chen, M.; Gan, D.; Wang, M.; Zeng, H.; Liao, M.; Chen, J.; Tu, W.; Niu, W. Ultrahigh Flux of Graphene Oxide Membrane Modified with Orientated Growth of MOFs for Rejection of Dyes and Oil-Water Separation. *Chin. Chem. Lett.* **2020**, *31*, 2683−2688.
(320) Zhang, R.; Cao, J.; Liu, Y.-n.; Guan, J.; He, M.; Jiang, Z. Metal-Organic Framework-Intercalated Graphene Oxide Membranes for Highly Efficient Oil/Water Separation. *Ind. Eng. Chem. Res.* **2020**, *59*, 16762−16771.
(321) Otyepková, E.; Lazar, P.; Čépe, K.; Tomanec, O.; Otyepka, M. Organic Adsorbates Have Higher Affinities to Fluorographene than to Graphene. *Appl. Mater. Today* **2016**, *5*, 142−149.
(322) Sun, L.; Tang, J. Welding Partially Reduced Graphene Oxides by MOFs into Micro-Mesoporous Hybrids for High-Performance Oil Absorption. *RSC Adv.* **2021**, *11*, 30980−30989.
(323) Hu, Z.; Peng, Y.; Kang, Z.; Qian, Y.; Zhao, D. A Modulated Hydrothermal (MHT) Approach for the Facile Synthesis of UiO-66-Type MOFs. *Inorg. Chem.* **2015**, *54*, 4862−4868.
(324) Mekonnen, M. M.; Hoekstra, A. Y. Four Billion People Facing Severe Water Scarcity. *Sci. Adv.* **2016**, *2*, No. e1500323.
(325) Rao, Z.; Feng, K.; Tang, B.; Wu, P. Surface Decoration of Amino-Functionalized Metal-Organic Framework/Graphene Oxide Composite onto Polydopamine-Coated Membrane Substrate for Highly Efficient Heavy Metal Removal. *ACS Appl. Mater. Interfaces* **2017**, *9*, 2594−26065.
(326) Yang, P.; Liu, Q.; Liu, J.; Zhang, H.; Li, Z.; Li, R.; Liu, L.; Wang, J. Interfacial Growth of a Metal-Organic Framework (UiO-66) on Functionalized Graphene Oxide (GO) as a Suitable Seawater Adsorbent for Extraction of Uranium(Vi). *J. Mater. Chem. A* **2017**, *5*, 17933−17942.
(327) Rahimi, E.; Mohaghegh, N. New Hybrid Nanocomposite of Copper Terephthalate MOF-Graphene Oxide: Synthesis, Characterization and Application as Adsorbents for Toxic Metal Ion Removal from Sungun Acid Mine Drainage. *Environ. Sci. Pollut. Res.* **2017**, *24*, 22353−22360.
(328) Samuel, M. S.; Subramaniyan, V.; Bhattacharya, J.; Parthiban, C.; Chand, S.; Singh, N. D. P. A GO-CS@MOF [Zn(BDC)(DMF)] Material for the Adsorption of Chromium(VI) Ions from Aqueous Solution. *Compos. B. Eng.* **2018**, *152*, 116−125.

https://doi.org/10.1021/acs.chemrev.2c00270
Chem. Rev. 2022, 122, 17241−17338

(329) Chowdhury, T.; Zhang, L.; Zhang, J.; Aggarwal, S. Removal of Arsenic(III) from Aqueous Solution Using Metal Organic Framework-Graphene Oxide Nanocomposite. *Nanomater.* **2018**, *8*, 1062.
(330) Samantaray, P. K.; Madras, G.; Bose, S. Water Remediation Aided by a Graphene-Oxide-Anchored Metal Organic Framework through Pore- and Charge-Based Sieving of Ions. *ACS Sustain. Chem. Eng.* **2019**, *7*, 1580−1590.
(331) Samantaray, P. K.; Baloda, S.; Madras, G.; Bose, S. Nanodelivery in Scrolls-Based Nanocarriers: Efficient Constructs for Sustainable Scavenging of Heavy Metal Ions and Inactivate Bacteria. *ACS Sustain. Chem. Eng.* **2019**, *7*, 18775−18784.
(332) Zuo, K.; Huang, X.; Liu, X.; Gil Garcia, E. M.; Kim, J.; Jain, A.; Chen, L.; Liang, P.; Zepeda, A.; Verduzco, R.; Lou, J.; Li, Q. A Hybrid Metal-Organic Framework-Reduced Graphene Oxide Nanomaterial for Selective Removal of Chromate from Water in an Electrochemical Process. *Environ. Sci. Technol.* **2020**, *54*, 13322−13332.
(333) Wei, N.; Zheng, X.; Li, Q.; Gong, C.; Ou, H.; Li, Z. Construction of Lanthanum Modified MOFs Graphene Oxide Composite Membrane for High Selective Phosphorus Recovery and Water Purification. *J. Colloid Interface Sci.* **2020**, *565*, 337−344.
(334) Wang, Z.; Zhao, D.; Wu, C.; Chen, S.; Wang, Y.; Chen, C. Magnetic Metal Organic Frameworks/Graphene Oxide Adsorbent For The Removal Of U(VI) From Aqueous Solution. *Appl. Radiat. Isot.* **2020**, *162*, 109160.
(335) Jabbari, V.; Veleta, J. M.; Zarei-Chaleshtori, M.; Gardea-Torresdey, J.; Villagrán, D. Green Synthesis of Magnetic MOF@GO and MOF@CNT Hybrid Nanocomposites with High Adsorption Capacity Towards Organic Pollutants. *Chem. Eng. J.* **2016**, *304*, 774−783.
(336) Vu, T. A.; Le, G. H.; Vu, H. T.; Nguyen, K. T.; Quan, T. T. T.; Nguyen, Q. K.; Tran, H. T. K.; Dang, P. T.; Vu, L. D.; Lee, G. D. Highly Photocatalytic Activity of Novel Fe-MIL-88B/GO Nanocomposite in the Degradation of Reactive Dye from Aqueous Solution. *Mater. Res. Express* **2017**, *4*, 035038.
(337) Wu, Z.; Yuan, X.; Zhong, H.; Wang, H.; Jiang, L.; Zeng, G.; Wang, H.; Liu, Z.; Li, Y. Highly Efficient Adsorption of Congo Red in Single and Binary Water with Cationic Dyes by Reduced Graphene Oxide Decorated NH2-MIL-68(Al). *J. Mol. Liq.* **2017**, *247*, 215−229.
(338) Ma, J.; Guo, X.; Ying, Y.; Liu, D.; Zhong, C. Composite Ultrafiltration Membrane Tailored by MOF@GO with Highly Improved Water Purification Performance. *Chem. Eng. J.* **2017**, *313*, 890−898.
(339) Abdi, J.; Vossoughi, M.; Mahmoodi, N. M.; Alemzadeh, I. Synthesis of Metal-Organic Framework Hybrid Nanocomposites Based on GO and CNT with High Adsorption Capacity for Dye Removal. *Chem. Eng. J.* **2017**, *326*, 1145−1158.
(340) Zhao, S.; Chen, D.; Wei, F.; Chen, N.; Liang, Z.; Luo, Y. Removal of Congo Red Dye from Aqueous Solution with Nickel-Based Metal-Organic Framework/Graphene Oxide Composites Prepared by Ultrasonic Wave-Assisted Ball Milling. *Ultrason. Sonochemistry* **2017**, *39*, 845−852.
(341) Tanhaei, M.; Mahjoub, A. R.; Safarifard, V. Sonochemical Synthesis of Amide-Functionalized Metal-Organic Framework/Graphene Oxide Nanocomposite for the Adsorption of Methylene Blue from Aqueous Solution. *Ultrason. Sonochemistry* **2018**, *41*, 189−195.
(342) Zhao, S.; Chen, D.; Wei, F.; Chen, N.; Liang, Z.; Luo, Y. Synthesis of Graphene Oxide/Metal-Organic Frameworks Hybrid Materials for Enhanced Removal of Methylene Blue in Acidic and Alkaline Solutions. *J. Chem. Technol. Biotechnol.* **2018**, *93*, 698−709.
(343) Li, L.; Shi, Z.; Zhu, H.; Hong, W.; Xie, F.; Sun, K. Adsorption of Azo Dyes from Aqueous Solution by the Hybrid MOFs/GO. *Water Sci. Technol.* **2016**, *73*, 1728−1737.
(344) Wan, Y.; Wang, J.; Huang, F.; Xue, Y.; Cai, N.; Liu, J.; Chen, W.; Yu, F. Synergistic Effect of Adsorption Coupled with Catalysis Based on Graphene-Supported MOF Hybrid Aerogel for Promoted Removal of Dyes. *RSC Adv.* **2018**, *8*, 34552−34559.
(345) Liu, Y.; Zhu, M.; Chen, M.; Ma, L.; Yang, B.; Li, L.; Tu, W. A Polydopamine-Modified Reduced Graphene Oxide (RGO)/MOFs Nanocomposite with Fast Rejection Capacity for Organic Dye. *Chem. Eng. J.* **2019**, *359*, 47−57.
(346) Mahmoodi, N. M.; Oveisi, M.; Asadi, E. Synthesis of NENU Metal-Organic Framework-Graphene Oxide Nanocomposites and their Pollutant Removal Ability from Water Using Ultrasound. *J. Clean. Prod.* **2019**, *211*, 198−212.
(347) Dong, R.; Chen, D.; Li, N.; Xu, Q.; Li, H.; He, J.; Lu, J. Enhancement of Organic Pollutants Bio-Decontamination from Aqueous Solution Using Newly-Designed Pseudomonas Putida-GA/MIL-100(Fe) Bio-Nanocomposites. *Environ. Res.* **2019**, *173*, 237−245.
(348) Luo, S.; Wang, J. MOF/Graphene Oxide Composite as an Efficient Adsorbent for the Removal of Organic Dyes from Aqueous Solution. *Environ. Sci. Pollut. Res.* **2018**, *25*, 5521−5528.
(349) Chang, R.; Ma, S.; Guo, X.; Xu, J.; Zhong, C.; Huang, R.; Ma, J. Hierarchically Assembled Graphene Oxide Composite Membrane with Self-Healing and High-Efficiency Water Purification Performance. *ACS Appl. Mater. Interfaces* **2019**, *11*, 46251−46260.
(350) Chen, Y.; Zhai, B.; Liang, Y. Enhanced Degradation Performance of Organic Dyes Removal by Semiconductor/MOF/Graphene Oxide Composites Under Visible Light Irradiation. *Diam. Relat. Mater.* **2019**, *98*, 107508.
(351) Azhdari, R.; Mousavi, S. M.; Hashemi, S. A.; Bahrani, S.; Ramakrishna, S. Decorated Graphene with Aluminum Fumarate Metal Organic Framework as a Superior Non-Toxic Agent for Efficient Removal of Congo Red Dye from Wastewater. *J. Environ. Chem. Eng.* **2019**, *7*, 103437.
(352) Ahsan, M. A.; Jabbari, V.; Imam, M. A.; Castro, E.; Kim, H.; Curry, M. L.; Valles-Rosales, D. J.; Noveron, J. C. Nanoscale Nickel Metal Organic Framework Decorated Over Graphene Oxide and Carbon Nanotubes for Water Remediation. *Sci. Total Environ.* **2020**, *698*, 134214.
(353) Wei, F.-h.; Ren, Q.-h.; Liang, Z.; Chen, D. Synthesis of Graphene Oxide/Metal-Organic Frameworks Composite Materials for Removal of Congo Red from Wastewater. *ChemistrySelect* **2019**, *4*, 5755−5762.
(354) Ventura, K.; Arrieta, R. A.; Marcos-Hernández, M.; Jabbari, V.; Powell, C. D.; Turley, R.; Lounsbury, A. W.; Zimmerman, J. B.; Gardea-Torresdey, J.; Wong, M. S.; Villagrán, D. Superparamagnetic MOF@GO Ni and Co Based Hybrid Nanocomposites as Efficient Water Pollutant Adsorbents. *Sci. Total Environ.* **2020**, *738*, 139213.
(355) Bai, Y.; Zhang, S.; Feng, S.; Zhu, M.; Ma, S. The First Ternary Nd-MOF/GO/Fe3O4 Nanocomposite Exhibiting an Excellent Photocatalytic Performance for Dye Degradation. *Dalton Trans.* **2020**, *49*, 10745−10754.
(356) Yang, G.; Zhang, D.; Zhu, G.; Zhou, T.; Song, M.; Qu, L.; Xiong, K.; Li, H. A Sm-MOF/GO Nanocomposite Membrane for Efficient Organic Dye Removal From Wastewater. *RSC Adv.* **2020**, *10*, 8540−8547.
(357) Eltaweil, A. S.; Abd El-Monaem, E. M.; El-Subruiti, G. M.; Abd El-Latif, M. M.; Omer, A. M. Fabrication of UiO-66/MIL-101(Fe) Binary MOF/Carboxylated-GO Composite for Adsorptive Removal of Methylene Blue Dye from Aqueous Solutions. *RSC Adv.* **2020**, *10*, 19008−19019.
(358) Sun, Y.; Chen, M.; Liu, H.; Zhu, Y.; Wang, D.; Yan, M. Adsorptive Removal of Dye and Antibiotic from Water with Functionalized Zirconium-Based Metal Organic Framework and Graphene Oxide Composite Nanomaterial UiO-66-(OH)2/GO. *Appl. Surf. Sci.* **2020**, *525*, 146614.
(359) Kumar, G.; Masram, D. T. Sustainable Synthesis of MOF-5@GO Nanocomposites for Efficient Removal of Rhodamine B from Water. *ACS Omega* **2021**, *6*, 9587−9599.
(360) Vo, T. K.; Trinh, T. P.; Nguyen, V. C.; Kim, J. Facile Synthesis of Graphite Oxide/MIL-101(Cr) Hybrid Composites for Enhanced Adsorption Performance Towards Industrial Toxic Dyes. *J. Ind. Eng. Chem.* **2021**, *95*, 224−234.
(361) Wu, Z.; Yuan, X.; Zhong, H.; Wang, H.; Zeng, G.; Chen, X.; Wang, H.; zhang, L.; Shao, J. Enhanced Adsorptive Removal of P-Nitrophenol from Water by Aluminum Metal-Organic Framework/Reduced Graphene Oxide Composite. *Sci. Rep.* **2016**, *6*, 25638.

https://doi.org/10.1021/acs.chemrev.2c00270
Chem. Rev. 2022, 122, 17241−17338

(362) Yang, Q.; Wang, J.; Zhang, W.; Liu, F.; Yue, X.; Liu, Y.; Yang, M.; Li, Z.; Wang, J. Interface Engineering of Metal Organic Framework on Graphene Oxide with Enhanced Adsorption Capacity for Organophosphorus Pesticide. *Chem. Eng. J.* **2017**, *313*, 19−26.
(363) Liu, G.; Li, L.; Xu, D.; Huang, X.; Xu, X.; Zheng, S.; Zhang, Y.; Lin, H. Metal-Organic Framework Preparation Using Magnetic Graphene Oxide-B-Cyclodextrin for Neonicotinoid Pesticide Adsorption and Removal. *Carbohydr. Polym.* **2017**, *175*, 584−591.
(364) Bayazit, Ş. S.; Yildiz, M.; Aşçi, Y. S.; Şahin, M.; Bener, M.; Eğlence, S.; Abdel Salam, M. Rapid Adsorptive Removal of Naphthalene from Water Using Graphene Nanoplatelet/MIL-101 (Cr) Nanocomposite. *J. Alloys. Compd.* **2017**, *701*, 740−749.
(365) Zheng, Y.; Chu, F.; Zhang, B.; Yan, J.; Chen, Y. Ultrahigh Adsorption Capacities of Carbon Tetrachloride on MIL-101 and MIL-101/Graphene Oxide Composites. *Microporous Mesoporous Mater.* **2018**, *263*, 71−76.
(366) Karimian, N.; Fakhri, H.; Amidi, S.; Hajian, A.; Arduini, F.; Bagheri, H. A Novel Sensing Layer Based on Metal-Organic Framework UiO-66 Modified with TiO2-Graphene Oxide: Application to Rapid, Sensitive and Simultaneous Determination of Paraoxon and Chlorpyrifos. *New J. Chem.* **2019**, *43*, 2600−2609.
(367) Abdelhameed, R. M.; el-deib, H. R.; El-Dars, F. M. S. E.; Ahmed, H. B.; Emam, H. E. Applicable Strategy for Removing Liquid Fuel Nitrogenated Contaminants Using MIL-53-NH2@Natural Fabric Composites. *Ind. Eng. Chem. Res.* **2018**, *57*, 15054−15065.
(368) Sarker, M.; Song, J. Y.; Jhung, S. H. Adsorptive Removal of Anti-Inflammatory Drugs from Water Using Graphene Oxide/Metal-Organic Framework Composites. *Chem. Eng. J.* **2018**, *335*, 74−81.
(369) Ma, X.; Zhou, X.; Yu, A.; Zhao, W.; Zhang, W.; Zhang, S.; Wei, L.; Cook, D. J.; Roy, A. Functionalized Metal-Organic Framework Nanocomposites for Dispersive Solid Phase Extraction and Enantioselective Capture of Chiral Drug Intermediates. *J. Chromatogr. A* **2018**, *1537*, 1−9.
(370) Wang, X.; Ma, X.; Huang, P.; Wang, J.; Du, T.; Du, X.; Lu, X. Magnetic Cu-MOFs Embedded Within Graphene Oxide Nanocomposites for Enhanced Preconcentration of Benzenoid-Containing Insecticides. *Talanta* **2018**, *181*, 112−117.
(371) Dai, Y.; Li, M.; Liu, F.; Xue, M.; Wang, Y.; Zhao, C. Graphene Oxide Wrapped Copper-Benzene-1,3,5-Tricarboxylate Metal Organic Framework as Efficient Absorbent for Gaseous Toluene Under Ambient Conditions. *Environ. Sci. Pollut. Res.* **2019**, *26*, 2477−2491.
(372) Jia, X.; Li, S.; Wang, Y.; Wang, T.; Hou, X. Adsorption Behavior and Mechanism of Sulfonamide Antibiotics in Aqueous Solution on a Novel MIL-101(Cr)@GO Composite. *J. Chem. Eng. Data* **2019**, *64*, 1265−1274.
(373) Şahin, S.; Abdelillah Ali Elhussein, E.; Abdel Salam, M.; Bayazit, Ş. S. Recovery of Polyphenols from Water Using Zr-Based Metal-Organic Frameworks and their Nanocomposites With Graphene Nanoplatelets. *J. Ind. Eng. Chem.* **2019**, *78*, 164−171.
(374) Ahsan, M. A.; Jabbari, V.; Islam, M. T.; Turley, R. S.; Dominguez, N.; Kim, H.; Castro, E.; Hernandez-Viezcas, J. A.; Curry, M. L.; Lopez, J.; Gardea-Torresdey, J. L.; Noveron, J. C. Sustainable Synthesis and Remarkable Adsorption Capacity of MOF/Graphene Oxide and MOF/CNT Based Hybrid Nanocomposites for the Removal of Bisphenol a from Water. *Sci. Total Environ.* **2019**, *673*, 306−317.
(375) Şahin, S.; Bayazit, Ş. S. Recovery of β-Carotene on Graphene Nanoplatelets UiO-66 Nanocomposites. *J. Chem. Eng. Data* **2020**, *65*, 821−827.
(376) Wang, K.; Wu, J.; Zhu, M.; Zheng, Y.-Z.; Tao, X. Highly Effective Ph-Universal Removal of Tetracycline Hydrochloride Antibiotics by Uio-66-(COOH)2/GO Metal-Organic Framework Composites. *J. Solid State Chem.* **2020**, *284*, 121200.
(377) Khan, N. A.; Najam, T.; Shah, S. S. A.; Hussain, E.; Ali, H.; Hussain, S.; Shaheen, A.; Ahmad, K.; Ashfaq, M. Development of Mn-PBA on GO Sheets for Adsorptive Removal of Ciprofloxacin from Water: Kinetics, Isothermal, Thermodynamic and Mechanistic Studies. *Mater. Chem. Phys.* **2020**, *245*, 122737.
(378) Jang, S.; Ka, D.; Jung, H.; Kim, M.-K.; Jung, H.; Jin, Y. Zr(OH)4/GO Nanocomposite for the Degradation of Nerve Agent Soman (GD) in High-Humidity Environments. *Materials* **2020**, *13*, 2954.
(379) Nguyen, M. B.; Hong Nhung, V. T.; Thu, V. T.; Ngoc Nga, D. T.; Pham Truong, T. N.; Giang, H. T.; Hai Yen, P. T.; Phong, P. H.; Vu, T. A.; Thu Ha, V. T. An Electrochemical Sensor Based on Copper-Based Metal-Organic Framework-Reduced Graphene Oxide Composites for Determination of 2,4-Dichlorophenol in Water. *RSC Adv.* **2020**, *10*, 42212−42220.
(380) Wang, Q.; Gu, C.; Fu, Y.; Liu, L.; Xie, Y. Ultrasensitive Electrochemical Sensor for Luteolin Based on Zirconium Metal-Organic Framework UiO-66/Reduced Graphene Oxide Composite Modified Glass Carbon Electrode. *Molecules* **2020**, *25*, 4557.
(381) Hagen, J. Economic Importance of Catalysts. *Industrial Catalysis: A Practical Approach*; Wiley-VCH Verlag GmbH & Co. KGaA, 2015; pp 459−462.
(382) Fadhel, A. Z.; Pollet, P.; Liotta, C. L.; Eckert, C. A. Combining the Benefits of Homogeneous and Heterogeneous Catalysis with Tunable Solvents and Nearcritical Water. *Molecules* **2010**, *15*, 8400−8424.
(383) Yang, X.; Wu, S.; Hu, J.; Fu, X.; Peng, L.; Kan, Q.; Huo, Q.; Guan, J. Highly Efficient N-Doped Magnetic Cobalt-Graphene Composite for Selective Oxidation of Benzyl Alcohol. *Catal. Commun.* **2016**, *87*, 90−93.
(384) Liu, X.; Zhao, X.; Zhou, M.; Cao, Y.; Wu, H.; Zhu, J. Highly Stable and Active Palladium Nanoparticles Supported on a Mesoporous UiO66@reduced Graphene Oxide Complex for Practical Catalytic Applications. *Eur. J. Inorg. Chem.* **2016**, *2016*, 3338−3343.
(385) Ibrahim, A. A.; Lin, A.; Zhang, F.; AbouZeid, K. M.; El-Shall, M. S. Palladium Nanoparticles Supported on a Metal-Organic Framework-Partially Reduced Graphene Oxide Hybrid for the Catalytic Hydrodeoxygenation of Vanillin as a Model for Biofuel Upgrade Reactions. *ChemCatChem.* **2017**, *9*, 469−480.
(386) Liu, C.; Liu, L.; Tian, X.; Wang, Y.; Li, R.; Zhang, Y.; Song, Z.; Xu, B.; Chu, W.; Qi, F.; Ikhlaq, A. Coupling Metal-Organic Frameworks and G-C3N4 to Derive Fe@N-Doped Graphene-Like Carbon for Peroxymonosulfate Activation: Upgrading Framework Stability and Performance. *Appl. Catal., B* **2019**, *255*, 117763.
(387) Ye, J.; Dai, J.; Yang, D.; Li, C.; Yan, Y.; Wang, Y. 2D/2D Confinement Graphene-Supported Bimetallic Sulfides/G-C3N4 Composites with Abundant Sulfur Vacancies as Highly Active Catalytic Self-Cleaning Membranes for Organic Contaminants Degradation. *Chem. Eng. J.* **2021**, *418*, 129383.
(388) Xu, Y.; Wang, Y.; Wan, J.; Ma, Y. Reduced Graphene Oxide-Supported Metal Organic Framework as a Synergistic Catalyst for Enhanced Performance on Persulfate Induced Degradation of Trichlorophenol. *Chemosphere* **2020**, *240*, 124849.
(389) Zhu, C.; Liu, F.; Ling, C.; Jiang, H.; Wu, H.; Li, A. Growth of Graphene-Supported Hollow Cobalt Sulfide Nanocrystals *via* MOF-Templated Ligand Exchange as Surface-Bound Radical Sinks for Highly Efficient Bisphenol A Degradation. *Appl. Catal., B* **2019**, *242*, 238−248.
(390) Tang, J.; Wang, J. Fe-Based Metal Organic Framework/Graphene Oxide Composite as an Efficient Catalyst for Fenton-Like Degradation of Methyl Orange. *RSC Adv.* **2017**, *7*, 50829−50837.
(391) Shao, W.; He, C.; Zhou, M.; Yang, C.; Gao, Y.; Li, S.; Ma, L.; Qiu, L.; Cheng, C.; Zhao, C. Core-Shell-Structured MOF-Derived 2D Hierarchical Nanocatalysts with Enhanced Fenton-Like Activities. *J. Mater. Chem. A* **2020**, *8*, 3168−3179.
(392) Bao, C.; Zhou, L.; Shao, Y.; Wu, Q.; Zhu, H.; Li, K. A Novel Au-Loaded Magnetic Metal Organic Framework/Graphene Multifunctional Composite: Green Synthesis and Catalytic Application. *J. Ind. Eng. Chem.* **2016**, *38*, 132−140.
(393) Chen, X.; Qian, P.; Zhang, T.; Xu, Z.; Fang, C.; Xu, X.; Chen, W.; Wu, P.; Shen, Y.; Li, S.; Wu, J.; Zheng, B.; Zhang, W.; Huo, F. Catalyst Surfaces with Tunable Hydrophilicity and Hydrophobicity: Metal-Organic Frameworks Toward Controllable Catalytic Selectivity. *Chem. Commun.* **2018**, *54*, 3936−3939.
(394) Song, F.-Z.; Zhu, Q.-L.; Yang, X.; Zhan, W.-W.; Pachfule, P.; Tsumori, N.; Xu, Q. Metal-Organic Framework Templated Porous Carbon-Metal Oxide/Reduced Graphene Oxide as Superior Support of

https://doi.org/10.1021/acs.chemrev.2c00270
Chem. Rev. 2022, 122, 17241−17338

Bimetallic Nanoparticles for Efficient Hydrogen Generation from Formic Acid. *Adv. Energy Mater.* **2018**, *8*, 1701416.
(395) Yan, J.-M.; Wang, Z.-L.; Gu, L.; Li, S.-J.; Wang, H.-L.; Zheng, W.-T.; Jiang, Q. AuPd-MnOx/MOF-Graphene: An Efficient Catalyst for Hydrogen Production from Formic Acid at Room Temperature. *Adv. Energy Mater.* **2015**, *5*, 1500107.
(396) Song, F.-Z.; Yang, X.; Xu, Q. Ultrafine Bimetallic Pt-Ni Nanoparticles Achieved by Metal-Organic Framework Templated Zirconia/Porous Carbon/Reduced Graphene Oxide: Remarkable Catalytic Activity in Dehydrogenation of Hydrous Hydrazine. *Small Methods* **2020**, *4*, 1900707.
(397) Liang, P.; Zhang, C.; Duan, X.; Sun, H.; Liu, S.; Tade, M. O.; Wang, S. N-Doped Graphene from Metal-Organic Frameworks for Catalytic Oxidation of p-Hydroxylbenzoic Acid: N-Functionality and Mechanism. *ACS Sustain. Chem. Eng.* **2017**, *5*, 2693−2701.
(398) Qu, J.; Chen, D.; Li, N.; Xu, Q.; Li, H.; He, J.; Lu, J. Engineering 3D Ru/Graphene Aerogel Using Metal-Organic Frameworks: Capture and Highly Efficient Catalytic CO Oxidation at Room Temperature. *Small* **2018**, *14*, 1800343.
(399) Liu, Y.; Miao, W.; Feng, Y.; Fang, X.; Li, Q.; Du, N.; Wang, D.; Mao, S. Enhanced Peroxydisulfate Oxidation *via* Cu(III) Species with a Cu-MOF-Derived Cu Nanoparticle and 3D Graphene Network. *J. Hazard. Mater.* **2021**, *403*, 123691.
(400) Tan, H.; Chen, D.; Li, N.; Xu, Q.; Li, H.; He, J.; Lu, J. Platinum-Supported Zirconia Nanotube Arrays Supported on Graphene Aerogels Modified with Metal-Organic Frameworks: Adsorption and Oxidation of Formaldehyde at Room Temperature. *Chem. Eur. J.* **2019**, *25*, 16718−16724.
(401) Huang, K.; Xu, Y. Enhancing the Catalytic Behaviour of HKUST-1 by Graphene Oxide for Phenol Oxidation. *Environ. Technol.* **2021**, *42*, 694−704.
(402) Ruan, X.; Liu, D.; Niu, X.; Wang, Y.; Simpson, C. D.; Cheng, N.; Du, D.; Lin, Y. 2D Graphene Oxide/Fe-MOF Nanozyme Nest with Superior Peroxidase-Like Activity and Its Application for Detection of Woodsmoke Exposure Biomarker. *Anal. Chem.* **2019**, *91*, 13847−13854.
(403) Insyani, R.; Verma, D.; Kim, S. M.; Kim, J. Direct One-Pot Conversion of Monosaccharides into High-Yield 2,5-Dimethylfuran Over a Multifunctional Pd/Zr-Based Metal-Organic Framework@ Sulfonated Graphene Oxide Catalyst. *Green Chem.* **2017**, *19*, 2482−2490.
(404) Sun, W.; Gao, L.; Sun, X.; Zheng, G. A Novel Route with a Cu(Ii)-MOF-Derived Structure to Synthesize Cu/Cu2O Nps@ Graphene: The Electron Transfer Leads to the Synergistic Effect of the Cu(0)-Cu(I) Phase for an Effective Catalysis of the Sonogashira Cross-Coupling Reactions. *Dalton Trans.* **2018**, *47*, 5538−5541.
(405) Wei, Y.; Hao, Z.; Zhang, F.; Li, H. A Functionalized Graphene Oxide and Nano-Zeolitic Imidazolate Framework Composite as a Highly Active and Reusable Catalyst for [3 + 3] Formal Cycloaddition Reactions. *J. Mater. Chem. A* **2015**, *3*, 14779−14785.
(406) Sun, W.; Gao, L.; Zheng, G. A Radical Capture Mechanism for Immediate Csp2-H Bond Hydroxylation *via* a Heterogeneous Cu-Graphene Catalyst. *Chem. Commun.* **2019**, *55*, 8915−8918.
(407) Zhu, Q.; Zhuang, W.; Chen, Y.; Wang, Z.; Villacorta Hernandez, B.; Wu, J.; Yang, P.; Liu, D.; Zhu, C.; Ying, H.; Zhu, Z. Nano-Biocatalysts of Cyt c@ZIF-8/GO Composites with High Recyclability via a de Novo Approach. *ACS Appl. Mater. Interfaces* **2018**, *10*, 16066−16076.
(408) Farmakes, J.; Schuster, I.; Overby, A.; Alhalhooly, L.; Lenertz, M.; Li, Q.; Ugrinov, A.; Choi, Y.; Pan, Y.; Yang, Z. Enzyme Immobilization on Graphite Oxide (GO) Surface via One-Pot Synthesis of GO/Metal-Organic Framework Composites for Large-Substrate Biocatalysis. *ACS Appl. Mater. Interfaces* **2020**, *12*, 23119−23126.
(409) Wang, S.; Ye, B.; An, C.; Wang, J.; Li, Q.; Guo, H.; Zhang, J. Exploring the Coordination Effect of GO@MOF-5 as Catalyst on Thermal Decomposition of Ammonium Perchlorate. *Nanoscale Res. Lett.* **2019**, *14*, 345.
(410) Insyani, R.; Verma, D.; Cahyadi, H. S.; Kim, S. M.; Kim, S. K.; Karanwal, N.; Kim, J. One-Pot Di- and Polysaccharides Conversion to Highly Selective 2,5-Dimethylfuran Over Cu-Pd/Amino-Functionalized Zr-Based Metal-Organic Framework (UiO-66(NH2))@SGO Tandem Catalyst. *Appl. Catal., B* **2019**, *243*, 337−354.
(411) Tang, H.; Zhou, M.-L.; Li, X.; Zhang, Y.-Y.; Han, Z.-B. A Catalyst of Pd@MIL-101@SGO Catalyzes Epoxidation and Hydroxymethoxylation Tandem Reactions of Styrene. *ChemistrySelect* **2020**, *5*, 3724−3729.
(412) Wu, Y.; Wang, H.; Guo, S.; Zeng, Y.; Ding, M. Mofs-Induced High-Amphiphilicity in Hierarchical 3D Reduced Graphene Oxide-Based Hydrogel. *Appl. Surf. Sci.* **2021**, *540*, 148303.
(413) Masa, J.; Andronescu, C.; Schuhmann, W. Electrocatalysis as the Nexus for Sustainable Renewable Energy: The Gordian Knot of Activity, Stability, and Selectivity. *Angew. Chem., Int. Ed.* **2020**, *59*, 15298−15312.
(414) Aiyappa, H. B.; Masa, J.; Andronescu, C.; Muhler, M.; Fischer, R. A.; Schuhmann, W. MOFs for Electrocatalysis: From Serendipity to Design Strategies. *Small Methods* **2019**, *3*, 1800415.
(415) Duan, J.; Chen, S.; Zhao, C. Ultrathin Metal-Organic Framework Array for Efficient Electrocatalytic Water Splitting. *Nat. Commun.* **2017**, *8*, 15341.
(416) Zhu, D.; Qiao, M.; Liu, J.; Tao, T.; Guo, C. Engineering Pristine 2D Metal-Organic Framework Nanosheets for Electrocatalysis. *J. Mater. Chem. A* **2020**, *8*, 8143−8170.
(417) Jayaramulu, K.; Masa, J.; Morales, D. M.; Tomanec, O.; Ranc, V.; Petr, M.; Wilde, P.; Chen, Y.-T.; Zboril, R.; Schuhmann, W.; Fischer, R. A. Ultrathin 2D Cobalt Zeolite-Imidazole Framework Nanosheets for Electrocatalytic Oxygen Evolution. *Adv. Sci.* **2018**, *5*, 1801029.
(418) Pang, W.; Shao, B.; Tan, X.-Q.; Tang, C.; Zhang, Z.; Huang, J. Exfoliation of Metal-Organic Frameworks into Efficient Single-Layer Metal-Organic Nanosheet Electrocatalysts by the Synergistic Action of Host-Guest Interactions and Sonication. *Nanoscale* **2020**, *12*, 3623−3629.
(419) Hod, I.; Deria, P.; Bury, W.; Mondloch, J. E.; Kung, C.-W.; So, M.; Sampson, M. D.; Peters, A. W.; Kubiak, C. P.; Farha, O. K.; Hupp, J. T. A Porous Proton-Relaying Metal-Organic Framework Material that Accelerates Electrochemical Hydrogen Evolution. *Nature Commun.* **2015**, *6*, 8304.
(420) Yang, Z.; Yao, Z.; Li, G.; Fang, G.; Nie, H.; Liu, Z.; Zhou, X.; Chen, X. a.; Huang, S. Sulfur-Doped Graphene as an Efficient Metal-free Cathode Catalyst for Oxygen Reduction. *ACS Nano* **2012**, *6*, 205−211.
(421) Li, Z.; Ge, X.; Li, C.; Dong, S.; Tang, R.; Wang, C.; Zhang, Z.; Yin, L. Rational Microstructure Design on Metal-Organic Framework Composites for Better Electrochemical Performances: Design Principle, Synthetic Strategy, and Promotion Mechanism. *Small Methods* **2020**, *4*, 1900756.
(422) Acar, C.; Dincer, I. Comparative Assessment of Hydrogen Production Methods from Renewable and Non-Renewable Sources. *Int. J. Hydrog. Energy* **2014**, *39*, 1−12.
(423) Mazloomi, K.; Gomes, C. Hydrogen as an Energy Carrier: Prospects and Challenges. *Renew. Sustain. Energy Rev.* **2012**, *16*, 3024−3033.
(424) Bičáková, O.; Straka, P. Production of Hydrogen from Renewable Resources and its Effectiveness. *Int. J. Hydrog. Energy* **2012**, *37*, 11563−11578.
(425) Fan, L.; Liu, P. F.; Yan, X.; Gu, L.; Yang, Z. Z.; Yang, H. G.; Qiu, S.; Yao, X. Atomically Isolated Nickel Species Anchored on Graphitized Carbon for Efficient Hydrogen Evolution Electrocatalysis. *Nat. Commun.* **2016**, *7*, 10667.
(426) Zeradjanin, A. R.; Grote, J.-P.; Polymeros, G.; Mayrhofer, K. J. J. A Critical Review on Hydrogen Evolution Electrocatalysis: Re-Exploring the Volcano-Relationship. *Electroanalysis* **2016**, *28*, 2256−2269.
(427) Liu, J.; Hou, S.; Li, W.; Bandarenka, A. S.; Fischer, R. A. Recent Approaches to Design Electrocatalysts Based on Metal-Organic

Frameworks and Their Derivatives. *Chem. Asian J.* **2019**, *14*, 3474−3501.
(428) Makhafola, M. D.; Hato, M. J.; Ramohlola, K. E.; Ramaripa, P. S.; Maponya, T. C.; Monama, G. R.; Molapo, K. M.; Iwuoha, E. I.; Katata-Seru, L. M.; Makgopa, K. *Carbon Related Materials*; Springer, 2021; pp 23−54.
(429) Rui, K.; Zhao, G.; Lao, M.; Cui, P.; Zheng, X.; Zheng, X.; Zhu, J.; Huang, W.; Dou, S. X.; Sun, W. Direct Hybridization of Noble Metal Nanostructures on 2D Metal-Organic Framework Nanosheets To Catalyze Hydrogen Evolution. *Nano Lett.* **2019**, *19*, 8447−8453.
(430) Xu, S.; Yang, F.; Han, S.; Zhang, S.; Wang, Q.; Jiang, C. MOF-Derived Pdnico Alloys Encapsulated in Nitrogen-Doped Graphene for Robust Hydrogen Evolution Reactions. *CrystEngComm* **2020**, *22*, 6063−6070.
(431) Monama, G. R.; Mdluli, S. B.; Mashao, G.; Makhafola, M. D.; Ramohlola, K. E.; Molapo, K. M.; Hato, M. J.; Makgopa, K.; Iwuoha, E. I.; Modibane, K. D. Palladium Deposition on Copper(II) Phthalocyanine/Metal Organic Framework Composite and Electrocatalytic Activity of the Modified Electrode Towards the Hydrogen Evolution Reaction. *Renew. Energy* **2018**, *119*, 62−72.
(432) Xu, S.; Li, Z.; Chu, K.; Yao, G.; Xu, Y.; Niu, P.; Zheng, F. Niru Nanoparticles Encapsulated in a Nitrogen-Doped Carbon Matrix as a Highly Efficient Electrocatalyst for the Hydrogen Evolution Reaction. *Dalton Trans.* **2020**, *49*, 13647−13654.
(433) Makhafola, M. D.; Ramohlola, K. E.; Maponya, T. C.; Somo, T. R.; Iwuoha, E. I.; Makgopa, K.; Hato, M. J.; Molapo, K. M.; Modibane, K. D. Electrocatalytic Activity of Graphene Oxide/Metal Organic Framework Hybrid Composite on Hydrogen Evolution Reaction Properties. *Int. J. Electrochem. Sci.* **2020**, *15*, 4884−4899.
(434) Xu, X.; Liu, X.; Zhong, W.; Zhang, L.; Liu, G.; Du, Y. Nanostructured Nico2s4@NiCo2O4-Reduced Graphene Oxide as an Efficient Hydrogen Evolution Electrocatalyst in Alkaline Electrolyte. *J. Colloid Interface Sci.* **2021**, *601*, 570−580.
(435) Schlichte, K.; Kratzke, T.; Kaskel, S. Improved Synthesis, Thermal Stability and Catalytic Properties of the Metal-Organic Framework Compound Cu3(BTC)2. *Microporous Mesoporous Mater.* **2004**, *73*, 81−88.
(436) Zhu, C.; Wang, K.; Lei, T.; Xiao, T.; Liu, L. Facile Synthesis of MoS2/rGO-MOF Hybrid Material as Highly Efficient Catalyst for Hydrogen Evolution. *Mater. Lett.* **2018**, *216*, 243−247.
(437) Li, J.-S.; Li, J.-Y.; Wang, X.-R.; Zhang, S.; Sha, J.-Q.; Liu, G.-D. Reduced Graphene Oxide-Supported MoP@P-Doped Porous Carbon Nano-Octahedrons as High-Performance Electrocatalysts for Hydrogen Evolution. *ACS Sustain. Chem. Eng.* **2018**, *6*, 10252−10259.
(438) Hughes, J. P.; Clipsham, J.; Chavushoglu, H.; Rowley-Neale, S. J.; Banks, C. E. Polymer Electrolyte Electrolysis: A Review of the Activity and Stability of Non-Precious Metal Hydrogen Evolution Reaction and Oxygen Evolution Reaction Catalysts. *Renew. Sustain. Energy Rev.* **2021**, *139*, 110709.
(439) Song, X. Z.; Zhang, N.; Wang, X. F.; Tan, Z. Recent Advances of Metal-Organic Frameworks and their Composites Toward Oxygen Evolution Electrocatalysis. *Mater. Today Energy* **2021**, *19*, 100597.
(440) Xie, A.; Du, J.; Tao, F.; Tao, Y.; Xiong, Z.; Luo, S.; Li, X.; Yao, C. Three-Dimensional Graphene Surface-Mounted Nickel-Based Metal Organic Framework for Oxygen Evolution Reaction. *Electrochim. Acta* **2019**, *305*, 338−348.
(441) Yaqoob, L.; Noor, T.; Iqbal, N.; Nasir, H.; Sohail, M.; Zaman, N.; Usman, M. Nanocomposites of Cobalt Benzene Tricarboxylic Acid MOF With rGO: An Efficient and Robust Electrocatalyst for Oxygen Evolution Reaction (OER). *Renew. Energy* **2020**, *156*, 1040−1054.
(442) Huang, M.; Liu, W.; Wang, L.; Liu, J.; Chen, G.; You, W.; Zhang, J.; Yuan, L.; Zhang, X.; Che, R. Self-Transforming Ultrathin A-Co(OH)2 Nanosheet Arrays from Metal-Organic Framework Modified Graphene Oxide with Sandwichlike Structure for Efficient Electrocatalytic Oxygen Evolution. *Nano Res.* **2020**, *13*, 810−817.
(443) Fang, X.; Jiao, L.; Zhang, R.; Jiang, H.-L. Porphyrinic Metal-Organic Framework-Templated Fe-Ni-P/Reduced Graphene Oxide for Efficient Electrocatalytic Oxygen Evolution. *ACS Appl. Mater. Interfaces* **2017**, *9*, 23852−23858.
(444) Zhao, J.; Zhang, J.-J.; Li, Z.-Y.; Bu, X.-H. Recent Progress on NiFe-Based Electrocatalysts for the Oxygen Evolution Reaction. *Small* **2020**, *16*, 2003916.
(445) Mohammed-Ibrahim, J. A Review on Nife-Based Electrocatalysts for Efficient Alkaline Oxygen Evolution Reaction. *J. Power Sources* **2020**, *448*, 227375.
(446) Bu, F.; Chen, W.; Gu, J.; Agboola, P. O.; Al-Khalli, N. F.; Shakir, I.; Xu, Y. Microwave-Assisted CVD-Like Synthesis of Dispersed Monolayer/Few-Layer N-Doped Graphene Encapsulated Metal Nanocrystals for Efficient Electrocatalytic Oxygen Evolution. *Chem. Sci.* **2018**, *9*, 7009−7016.
(447) Chen, C.; Wang, J.; Li, P.; Tian, Q.; Xiao, Z.; Li, S.; Cai, N.; Xue, Y.; Chen, W.; Yu, F. Bimetal-organic Framework Encapsulated in Graphene Aerogel-grafted Ni Foam: An Efficient Electrocatalyst for the Oxygen Evolution Reaction. *ChemCatChem.* **2021**, *13*, 346−352.
(448) Khiarak, B. N.; Hasanzadeh, M.; Mojaddami, M.; Shahriyar Far, H.; Simchi, A. In Situ Synthesis of Quasi-Needle-Like Bimetallic Organic Frameworks on Highly Porous Graphene Scaffolds for Efficient Electrocatalytic Water Oxidation. *Chem. Commun.* **2020**, *56*, 3135−3138.
(449) Liu, Y.; Wang, C.; Ju, S.; Li, M.; Yuan, A.; Zhu, G. Feco-Based Hybrid MOF Derived Active Species for Effective Oxygen Evolution. *Prog. Nat. Sci.* **2020**, *30*, 185−191.
(450) Meng, J.; Zhou, Y.; Chi, H.; Li, K.; Wan, J.; Hu, Z. Bimetallic Porphyrin MOF Anchored onto rGO Nanosheets as a Highly Efficient 2D Electrocatalyst for Oxygen Evolution Reaction in Alkaline Conditions. *ChemistrySelect* **2019**, *4*, 8661−8670.
(451) Chen, Y.; Huang, N.; Liang, Y. Preparation of CeO2/Cu-MOF/GO Composite for Efficient Electrocatalytic Oxygen Evolution Reaction. *Ionics* **2021**, *27*, 4347−4360.
(452) Wang, C.-P.; Feng, Y.; Sun, H.; Wang, Y.; Yin, J.; Yao, Z.; Bu, X.-H.; Zhu, J. Self-Optimized Metal-Organic Framework Electrocatalysts with Structural Stability and High Current Tolerance for Water Oxidation. *ACS Catal.* **2021**, *11*, 7132−7143.
(453) Cheng, F.; Chen, J. Metal-Air Batteries: From Oxygen Reduction Electrochemistry to Cathode Catalysts. *Chem. Soc. Rev.* **2012**, *41*, 2172−2192.
(454) Hu, C.; Liu, D.; Xiao, Y.; Dai, L. Functionalization of Graphene Materials by Heteroatom-Doping for Energy Conversion and Storage. *Prog. Nat. Sci.* **2018**, *28*, 121−132.
(455) Lu, X. F.; Xia, B. Y.; Zang, S.-Q.; Lou, X. W. Metal-Organic Frameworks Based Electrocatalysts for the Oxygen Reduction Reaction. *Angew. Chem., Int. Ed.* **2020**, *59*, 4634−4650.
(456) Kazakova, M. A.; Koul, A.; Golubtsov, G. V.; Selyutin, A. G.; Ishchenko, A. V.; Kvon, R. I.; Kolesov, B. A.; Schuhmann, W.; Morales, D. M. Nitrogen and Oxygen Functionalization of Multi-Walled Carbon Nanotubes for Tuning the Bifunctional Oxygen Reduction/Oxygen Evolution Performance of Supported FeCo Oxide Nanoparticles. *ChemElectroChem.* **2021**, *8*, 2803−2816.
(457) Bezerra, C. W. B.; Zhang, L.; Lee, K.; Liu, H.; Marques, A. L. B.; Marques, E. P.; Wang, H.; Zhang, J. A Review of Fe-N/C and Co-N/C Catalysts for the Oxygen Reduction Reaction. *Electrochim. Acta* **2008**, *53*, 4937−4951.
(458) Zhou, R.; Jaroniec, M.; Qiao, S.-Z. Nitrogen-Doped Carbon Electrocatalysts Decorated with Transition Metals for the Oxygen Reduction Reaction. *ChemCatChem.* **2015**, *7*, 3808−3817.
(459) Lv, X.; Xue, X.; Gan, X.; Lv, C.; Sun, X.; Wang, Y.; Li, L.; Wang, H. Bottom-Up Fabrication of a Sandwich-Like Carbon/Graphene Heterostructure with Built-In FeNC Dopants as Non-Noble Electrocatalyst for Oxygen Reduction Reaction. *Chem. Asian J.* **2020**, *15*, 432−439.
(460) Sohrabi, S.; Dehghanpour, S.; Ghalkhani, M. Three-Dimensional Metal-Organic Framework Graphene Nanocomposite as a Highly Efficient and Stable Electrocatalyst for the Oxygen Reduction Reaction in Acidic Media. *ChemCatChem.* **2016**, *8*, 2356−2366.
(461) Zhang, Y.; Wang, P.; Yang, J.; Li, K.; Long, X.; Li, M.; Zhang, K.; Qiu, J. Fabrication of Core-Shell Nanohybrid Derived from Iron-Based Metal-Organic Framework Grappled on Nitrogen-Doped Graphene for Oxygen Reduction Reaction. *Chem. Eng. J.* **2020**, *401*, 126001.

https://doi.org/10.1021/acs.chemrev.2c00270
Chem. Rev. 2022, 122, 17241−17338

(462) Wei, J.; Hu, Y.; Liang, Y.; Kong, B.; Zheng, Z.; Zhang, J.; Jiang, S. P.; Zhao, Y.; Wang, H. Graphene Oxide/Core-Shell Structured Metal-Organic Framework Nano-Sandwiches and their Derived Cobalt/N-Doped Carbon Nanosheets for Oxygen Reduction Reactions. *J. Mater. Chem. A* **2017**, *5*, 10182−10189.
(463) Wu, G.; Nie, Y.; Zhang, D.; Zhang, C.; Guo, J.; Zhang, D.; Qi, G.; Jiao, W.; Yuan, Z. The MOF/GO-Based Derivatives with Co@Coo Core-Shell Structure Supported on the N-Doped Graphene as Electrocatalyst for Oxygen Reduction Reaction. *J. Chin. Chem. Soc.* **2020**, *67*, 1189−1194.
(464) Zhao, K.; Liu, S.; Ye, G.; Wei, X.; Su, Y.; Zhu, W.; Zhou, Z.; He, Z. Ultrasmall 2 D CoxZn2-x(Benzimidazole)4 Metal-Organic Framework Nanosheets and their Derived Co Nanodots@Co,N-Codoped Graphene for Efficient Oxygen Reduction Reaction. *ChemSusChem* **2020**, *13*, 1556−1567.
(465) Tang, B.; Wang, S.; Li, R.; Gou, X.; Long, J. Urea Treated Metal Organic Frameworks-Graphene Oxide Composites Derived N-Doped Co-Based Materials as Efficient Catalyst for Enhanced Oxygen Reduction. *J. Power Sources* **2019**, *425*, 76−86.
(466) An, L.; Jiang, N.; Li, B.; Hua, S.; Fu, Y.; Liu, J.; Hao, W.; Xia, D.; Sun, Z. A Highly Active and Durable Iron/Cobalt Alloy Catalyst Encapsulated in N-Doped Graphitic Carbon Nanotubes for Oxygen Reduction Reaction by a Nanofibrous Dicyandiamide Template. *J. Mater. Chem. A* **2018**, *6*, 5962−5970.
(467) Guo, D.; Han, S.; Ma, R.; Zhou, Y.; Liu, Q.; Wang, J.; Zhu, Y. In Situ Formation of Iron-Cobalt Sulfides Embedded in N,S-Doped Mesoporous Carbon as Efficient Electrocatalysts for Oxygen Reduction Reaction. *Microporous Mesoporous Mater.* **2018**, *270*, 1−9.
(468) Elumeeva, K.; Kazakova, M. A.; Morales, D. M.; Medina, D.; Selyutin, A.; Golubtsov, G.; Ivanov, Y.; Kuznetzov, V.; Chuvilin, A.; Antoni, H.; Muhler, M.; Schuhmann, W.; Masa, J. Bifunctional Oxygen Reduction/Oxygen Evolution Activity of Mixed Fe/Co Oxide Nanoparticles with Variable Fe/Co Ratios Supported on Multiwalled Carbon Nanotubes. *ChemSusChem* **2018**, *11*, 1204−1214.
(469) Li, Q.; Xu, P.; Gao, W.; Ma, S.; Zhang, G.; Cao, R.; Cho, J.; Wang, H.-L.; Wu, G. Graphene/Graphene-Tube Nanocomposites Templated from Cage-Containing Metal-Organic Frameworks for Oxygen Reduction in Li-O2 Batteries. *Adv. Mater.* **2014**, *26*, 1378−1386.
(470) Mousavi, S. A.; Mehrpooya, M. Fabrication of Copper Centered Metal Organic Framework and Nitrogen, Sulfur Dual Doped Graphene Oxide Composite as a Novel Electrocatalyst for Oxygen Reduction Reaction. *Energy* **2021**, *214*, 119053.
(471) Zhuang, S.; Nunna, B. B.; Lee, E. S. Metal Organic Framework-Modified Nitrogen-Doped Graphene Oxygen Reduction Reaction Catalyst Synthesized by Nanoscale High-Energy Wet Ball-Milling Structural and Electrochemical Characterization. *MRS Commun.* **2018**, *8*, 40−48.
(472) Singh, H.; Zhuang, S.; Nunna, B. B.; Lee, E. S. Thermal Stability and Potential Cycling Durability of Nitrogen-Doped Graphene Modified by Metal-Organic Framework for Oxygen Reduction Reactions. *Catalysts* **2018**, *8*, 607.
(473) Xia, W.; Tang, J.; Li, J.; Zhang, S.; Wu, K. C. W.; He, J.; Yamauchi, Y. Defect-Rich Graphene Nanomesh Produced by Thermal Exfoliation of Metal-Organic Frameworks for the Oxygen Reduction Reaction. *Angew. Chem., Int. Ed.* **2019**, *58*, 13354−13359.
(474) Ania, C. O.; Seredych, M.; Rodriguez-Castellon, E.; Bandosz, T. J. New Copper/GO Based Material as an Efficient Oxygen Reduction Catalyst in an Alkaline Medium: The Role of Unique Cu/rGO Architecture. *Appl. Catal., B* **2015**, *163*, 424−435.
(475) Masa, J.; Xia, W.; Muhler, M.; Schuhmann, W. On the Role of Metals in Nitrogen-Doped Carbon Electrocatalysts for Oxygen Reduction. *Angew. Chem., Int. Ed.* **2015**, *54*, 10102−10120.
(476) Yan, Y.; Xia, B. Y.; Zhao, B.; Wang, X. A Review on Noble-Metal-Free Bifunctional Heterogeneous Catalysts for Overall Electrochemical Water Splitting. *J. Mater. Chem. A* **2016**, *4*, 17587−17603.
(477) Kim, J.; Park, J.; Lee, J.; Lim, W.-G.; Jo, C.; Lee, J. Biomass-Derived P, N Self-Doped Hard Carbon as Bifunctional Oxygen Electrocatalyst and Anode Material for Seawater Batteries. *Adv. Funct. Mater.* **2021**, *31*, 2010882.
(478) Wang, H.-F.; Xu, Q. Materials Design for Rechargeable Metal-Air Batteries. *Matter* **2019**, *1*, 565−595.
(479) Morales, D. M.; Kazakova, M. A.; Purcel, M.; Masa, J.; Schuhmann, W. The Sum is More than its Parts: Stability of MnFe Oxide Nanoparticles Supported on Oxygen-Functionalized Multi-Walled Carbon Nanotubes at Alternating Oxygen Reduction Reaction and Oxygen Evolution Reaction Conditions. *J. Solid State Electrochem.* **2020**, *24*, 2901−2906.
(480) Qiao, H.; Yang, Y.; Dai, X.; Zhao, H.; Yong, J.; Yu, L.; Luan, X.; Cui, M.; Zhang, X.; Huang, X. Amorphous (Fe)Ni-MOF-Derived Hollow (Bi)Metal/Oxide@N-Graphene Polyhedron as Effectively Bifunctional Catalysts in Overall Alkaline Water Splitting. *Electrochim. Acta* **2019**, *318*, 430−439.
(481) Bu, F.; Chen, W.; Aly Aboud, M. F.; Shakir, I.; Gu, J.; Xu, Y. Microwave-Assisted Ultrafast Synthesis of Adjustable Bimetal Phosphide/Graphene Heterostructures from Mofs for Efficient Electrochemical Water Splitting. *J. Mater. Chem. A* **2019**, *7*, 14526−14535.
(482) Pumera, M.; Iwai, H. Metallic Impurities within Residual Catalyst Metallic Nanoparticles Are in Some Cases Responsible for "Electrocatalytic" Effect of Carbon Nanotubes. *Chem. Asian J.* **2009**, *4*, 554−560.
(483) Morales, D. M.; Masa, J.; Andronescu, C.; Schuhmann, W. Promotional Effect of Fe Impurities in Graphene Precursors on the Activity of MnOX/Graphene Electrocatalysts for the Oxygen Evolution and Oxygen Reduction Reactions. *ChemElectroChem.* **2017**, *4*, 2835−2841.
(484) Parkash, A. Metal-Organic Framework Derived Ultralow-Loading Platinum-Copper Catalyst: A Highly Active and Durable Bifunctional Electrocatalyst for Oxygen-Reduction and Evolution Reactions. *Nanotechnology* **2021**, *32*, 325703.
(485) Ma, L.; Chen, S.; Pei, Z.; Huang, Y.; Liang, G.; Mo, F.; Yang, Q.; Su, J.; Gao, Y.; Zapien, J. A.; Zhi, C. Single-Site Active Iron-Based Bifunctional Oxygen Catalyst for a Compressible and Rechargeable Zinc-Air Battery. *ACS Nano* **2018**, *12*, 1949−1958.
(486) Xu, Y.; Deng, P.; Chen, G.; Chen, J.; Yan, Y.; Qi, K.; Liu, H.; Xia, B. Y. 2D Nitrogen-Doped Carbon Nanotubes/Graphene Hybrid as Bifunctional Oxygen Electrocatalyst for Long-Life Rechargeable Zn-Air Batteries. *Adv. Funct. Mater.* **2020**, *30*, 1906081.
(487) Huang, X.; Wang, J.; Bao, H.; Zhang, X.; Huang, Y. 3D Nitrogen, Sulfur-Codoped Carbon Nanomaterial-Supported Cobalt Oxides with Polyhedron-Like Particles Grafted onto Graphene Layers as Highly Active Bicatalysts for Oxygen-Evolving Reactions. *ACS Appl. Mater. Interfaces* **2018**, *10*, 7180−7190.
(488) Zhang, H.; Wang, X.; Yang, Z.; Yan, S.; Zhang, C.; Liu, S. Space-Confined Synthesis of Lasagna-like N-Doped Graphene-Wrapped Copper-Cobalt Sulfides as Efficient and Durable Electrocatalysts for Oxygen Reduction and Oxygen Evolution Reactions. *ACS Sustain. Chem. Eng.* **2020**, *8*, 1004−1014.
(489) Liu, T.; Yang, F.; Cheng, G.; Luo, W. Reduced Graphene Oxide-Wrapped Co9-xFexS8/Co,Fe-N-C Composite as Bifunctional Electrocatalyst for Oxygen Reduction and Evolution. *Small* **2018**, *14*, 1703748.
(490) Fang, H.; Huang, T.; Sun, Y.; Kang, B.; Liang, D.; Yao, S.; Yu, J.; Dinesh, M. M.; Wu, S.; Lee, J. Y.; Mao, S. Metal-Organic Framework-Derived Core-Shell-Structured Nitrogen-Doped Cocx/FeCo@C Hybrid Supported by Reduced Graphene Oxide Sheets as High Performance Bifunctional Electrocatalysts for ORR and OER. *J. Catal.* **2019**, *371*, 185−195.
(491) Li, M.; Bao, C.; Liu, Y.; Meng, J.; Liu, X.; Cai, Y.; Wuu, D.; Zong, Y.; Loh, T.-P.; Wang, Z. Reduced Graphene Oxide-Supported Cobalt Oxide Decorated N-Doped Graphitic Carbon for Efficient Bifunctional Oxygen Electrocatalysis. *RSC Adv.* **2019**, *9*, 16534−16540.
(492) Yang, W.; Zhang, Y.; Liu, X.; Chen, L.; Jia, J. In Situ Formed Fe-N Doped Metal Organic Framework@Carbon Nanotubes/Graphene Hybrids for a Rechargeable Zn-Air Battery. *Chem. Commun.* **2017**, *53*, 12934−12937.

https://doi.org/10.1021/acs.chemrev.2c00270
Chem. Rev. 2022, 122, 17241−17338

(493) Liu, S.; Wang, M.; Sun, X.; Xu, N.; Liu, J.; Wang, Y.; Qian, T.; Yan, C. Facilitated Oxygen Chemisorption in Heteroatom-Doped Carbon for Improved Oxygen Reaction Activity in All-Solid-State Zinc-Air Batteries. *Adv. Mater.* **2018**, *30*, 1704898.
(494) Zheng, X.; Cao, Y.; Liu, D.; Cai, M.; Ding, J.; Liu, X.; Wang, J.; Hu, W.; Zhong, C. Bimetallic Metal-Organic-Framework/Reduced Graphene Oxide Composites as Bifunctional Electrocatalysts for Rechargeable Zn-Air Batteries. *ACS Appl. Mater. Interfaces* **2019**, *11*, 15662−15669.
(495) Hao, Y.; Xu, Y.; Liu, J.; Sun, X. Nickel-Cobalt Oxides Supported on Co/N Decorated Graphene as an Excellent Bifunctional Oxygen Catalyst. *J. Mater. Chem. A* **2017**, *5*, 5594−5600.
(496) Wahab, A.; Iqbal, N.; Noor, T.; Ashraf, S.; Raza, M. A.; Ahmad, A.; Khan, U. A. Thermally Reduced Mesoporous Manganese MOF@ Reduced Graphene Oxide Nanocomposite as Bifunctional Electrocatalyst for Oxygen Reduction and Evolution. *RSC Adv.* **2020**, *10*, 27728−27742.
(497) Peng, X.; Wei, L.; Liu, Y.; Cen, T.; Ye, Z.; Zhu, Z.; Ni, Z.; Yuan, D. Cobalt Nanoparticles Embedded in N-Doped Carbon Nanotubes on Reduced Graphene Oxide as Efficient Oxygen Catalysts for Zn-Air Batteries. *Energy Fuels* **2020**, *34*, 8931−8938.
(498) Xiao, Y.; Guo, B.; Zhang, J.; Hu, C.; Ma, R.; Wang, D.; Wang, J. A Bimetallic MOF@Graphene Oxide Composite as an Efficient Bifunctional Oxygen Electrocatalyst for Rechargeable Zn-Air Batteries. *Dalton Trans.* **2020**, *49*, 5730−5735.
(499) Zou, H.; Li, G.; Duan, L.; Kou, Z.; Wang, J. In Situ Coupled Amorphous Cobalt Nitride with Nitrogen-Doped Graphene Aerogel as a Trifunctional Electrocatalyst Towards Zn-Air Battery Deriven Full Water Splitting. *Appl. Catal., B* **2019**, *259*, 118100.
(500) Wang, H.; Liu, G.; Chen, C.; Tu, W.; Lu, Y.; Wu, S.; O'Hare, D.; Xu, R. Single-Ni Sites Embedded in Multilayer Nitrogen-Doped Graphene Derived from Amino-Functionalized MOF for Highly Selective CO2 Electroreduction. *ACS Sustain. Chem. Eng.* **2021**, *9*, 3792−3801.
(501) Liu, A.; Gao, M.; Ren, X.; Meng, F.; Yang, Y.; Gao, L.; Yang, Q.; Ma, T. Current Progress in Electrocatalytic Carbon Dioxide Reduction to Fuels on Heterogeneous Catalysts. *J. Mater. Chem. A* **2020**, *8*, 3541−3562.
(502) Abdelkader-Fernández, V. K.; Fernandes, D. M.; Freire, C. Carbon-Based Electrocatalysts for CO2 Electroreduction Produced *via* MOF, Biomass, and Other Precursors Carbonization: A Review. *J. CO2 Util.* **2020**, *42*, 101350.
(503) Pan, F.; Zhang, H.; Liu, Z.; Cullen, D.; Liu, K.; More, K.; Wu, G.; Wang, G.; Li, Y. Atomic-Level Active Sites of Efficient Imidazolate Framework-Derived Nickel Catalysts for CO2 Reduction. *J. Mater. Chem. A* **2019**, *7*, 26231−26237.
(504) Zhang, Y.; Li, K.; Chen, M.; Wang, J.; Liu, J.; Zhang, Y. Cu/Cu2O Nanoparticles Supported on Vertically ZIF-L-Coated Nitrogen-Doped Graphene Nanosheets for Electroreduction of CO2 to Ethanol. *ACS Appl. Nano Mater.* **2020**, *3*, 257−263.
(505) Hwang, S.-M.; Choi, S. Y.; Youn, M. H.; Lee, W.; Park, K. T.; Gothandapani, K.; Grace, A. N.; Jeong, S. K. Investigation on Electroreduction of CO2 to Formic Acid Using Cu3(BTC)2 Metal-Organic Framework (Cu-MOF) and Graphene Oxide. *ACS Omega* **2020**, *5*, 23919−23930.
(506) Ghavam, S.; Vahdati, M.; Wilson, I. A. G.; Styring, P. Sustainable Ammonia Production Processes. *Front. Energy Res.* **2021**, *9*, 34.
(507) Shen, H.; Choi, C.; Masa, J.; Li, X.; Qiu, J.; Jung, Y.; Sun, Z. Electrochemical Ammonia Synthesis: Mechanistic Understanding and Catalyst Design. *Chem.* **2021**, *7*, 1708−1754.
(508) Cui, Q.; Qin, G.; Wang, W.; K. R., G.; Du, A.; Sun, Q. Mo-Based 2D MOF as a Highly Efficient Electrocatalyst for Reduction of N2 to NH3: A Density Functional Theory Study. *J. Mater. Chem. A* **2019**, *7*, 14510−14518.
(509) Wang, C.; Zhao, Y.-N.; Zhu, C.-Y.; Zhang, M.; Geng, Y.; Li, Y.-G.; Su, Z.-M. A Two-Dimensional Conductive Mo-Based Covalent Organic Framework as an Efficient Electrocatalyst for Nitrogen Fixation. *J. Mater. Chem. A* **2020**, *8*, 23599−23606.
(510) Chen, S.; Jang, H.; Wang, J.; Qin, Q.; Liu, X.; Cho, J. Bimetallic Metal-Organic Framework-Derived MoFe-PC Microspheres for Electrocatalytic Ammonia Synthesis Under Ambient Conditions. *J. Mater. Chem. A* **2020**, *8*, 2099−2104.
(511) Zhao, L.; Kuang, X.; Chen, C.; Sun, X.; Wang, Z.; Wei, Q. Boosting Electrocatalytic Nitrogen Fixation *via* Energy-Efficient Anodic Oxidation of Sodium Gluconate. *Chem. Commun.* **2019**, *55*, 10170−10173.
(512) Liu, Y.; Li, C.; Guan, L.; Li, K.; Lin, Y. Oxygen Vacancy Regulation Strategy Promotes Electrocatalytic Nitrogen Fixation by Doping Bi into Ce-MOF-Derived CeO2 Nanorods. *J. Phys. Chem. C* **2020**, *124*, 18003−18009.
(513) Zhang, R.; Jiao, L.; Yang, W.; Wan, G.; Jiang, H.-L. Single-Atom Catalysts Templated by Metal-Organic Frameworks for Electrochemical Nitrogen Reduction. *J. Mater. Chem. A* **2019**, *7*, 26371−26377.
(514) Mukherjee, S.; Yang, X.; Shan, W.; Samarakoon, W.; Karakalos, S.; Cullen, D. A.; More, K.; Wang, M.; Feng, Z.; Wang, G.; Wu, G. Atomically Dispersed Single Ni Site Catalysts for Nitrogen Reduction toward Electrochemical Ammonia Synthesis Using N2 and H2O. *Small Methods* **2020**, *4*, 1900821.
(515) Lawrence, R. M.; Unni, S. M. Defect Induced Nitrogen Reduction Reaction of Carbon Nanomaterials. *Sust. Energy Fuels* **2021**, *5*, 3765−3790.
(516) Gao, Y.; Han, Z.; Hong, S.; Wu, T.; Li, X.; Qiu, J.; Sun, Z. ZIF-67-Derived Cobalt/Nitrogen-Doped Carbon Composites for Efficient Electrocatalytic N2 Reduction. *ACS Appl. Energy Mater.* **2019**, *2*, 6071−6077.
(517) Luo, S.; Li, X.; Zhang, B.; Luo, Z.; Luo, M. MOF-Derived Co3O4@NC with Core-Shell Structures for N2 Electrochemical Reduction under Ambient Conditions. *ACS Appl. Mater. Interfaces* **2019**, *11*, 26891−26897.
(518) Yang, B.; Ding, W.; Zhang, H.; Zhang, S. Recent Progress in Electrochemical Synthesis of Ammonia from Nitrogen: Strategies to Improve the Catalytic Activity and Selectivity. *Energy Environ. Sci.* **2021**, *14*, 672−687.
(519) Wang, J.; Liu, Y.-p.; Zhang, H.; Huang, D.-j.; Chu, K. Ambient Electrocatalytic Nitrogen Reduction on a MoO2/Graphene Hybrid: Experimental and DFT Studies. *Catal. Sci. Technol.* **2019**, *9*, 4248−4254.
(520) Zhang, F.; Wang, X.; Liu, H.; Liu, C.; Wan, Y.; Long, Y.; Cai, Z. Recent Advances and Applications of Semiconductor Photocatalytic Technology. *Appl. Sci.* **2019**, *9*, 2489.
(521) Huang, L.; Liu, B. Synthesis of a Novel and Stable Reduced Graphene Oxide/MOF Hybrid Nanocomposite and Photocatalytic Performance for the Degradation of Dyes. *RSC Adv.* **2016**, *6*, 17873−17879.
(522) Reynal, A.; Lakadamyali, F.; Gross, M. A.; Reisner, E.; Durrant, J. R. Parameters Affecting Electron Transfer Dynamics from Semiconductors to Molecular Catalysts for the Photochemical Reduction of Protons. *Energy Environ. Sci.* **2013**, *6*, 3291−3300.
(523) Kang, X.; Liu, S.; Dai, Z.; He, Y.; Song, X.; Tan, Z. Titanium Dioxide: From Engineering to Applications. *Catalysts* **2019**, *9*, 191.
(524) Li, Y.; Xu, H.; Ouyang, S.; Ye, J. Metal-rganic Frameworks for Photocatalysis. *Phys. Chem. Chem. Phys.* **2016**, *18*, 7563−7572.
(525) Li, Z.; Zhou, H.-Y.; Zhao, F.-L.; Wang, T.-X.; Ding, X.; Han, B.-H.; Feng, W. Three-dimensional Covalent Organic Frameworks as Host Materials for Lithium-Sulfur Batteries. *Chin. J. Polym. Sci.* **2020**, *38*, 550−557.
(526) Guo, M.; Zhang, M.; Liu, R.; Zhang, X.; Li, G. State-of-the-Art Advancements in Photocatalytic Hydrogenation: Reaction Mechanism and Recent Progress in Metal-Organic Framework (MOF)-Based Catalysts. *Adv. Sci.* **2022**, *9*, 2103361.
(527) Zhang, C.; Ai, L.; Jiang, J. Graphene Hybridized Photoactive Iron Terephthalate with Enhanced Photocatalytic Activity for the Degradation of Rhodamine B under Visible Light. *Ind. Eng. Chem. Res.* **2015**, *54*, 153−163.

https://doi.org/10.1021/acs.chemrev.2c00270
Chem. Rev. 2022, 122, 17241−17338

(528) Liu, D.; Jin, Z.; Bi, Y. Charge Transmission Channel Construction Between a MOF and rGO by Means of Co-Mo-S Modification. *Catal. Sci. Technol.* **2017**, *7*, 4478−4488.
(529) Wang, Y.; Ling, L.; Zhang, W.; Ding, K.; Yu, Y.; Duan, W.; Liu, B. A Strategy to Boost H2 Generation Ability of Metal-Organic Frameworks: Inside-Outside Decoration for the Separation of Electrons and Holes. *ChemSusChem* **2018**, *11*, 666−671.
(530) Lin, R.; Shen, L.; Ren, Z.; Wu, W.; Tan, Y.; Fu, H.; Zhang, J.; Wu, L. Enhanced Photocatalytic Hydrogen Production Activity *via* Dual Modification of MOF and Reduced Graphene Oxide on CdS. *Chem. Commun.* **2014**, *50*, 8533−8535.
(531) Wu, Y.; Luo, H.; Zhang, L. Pd Nanoparticles Supported on MIL-101/Reduced Graphene Oxide Photocatalyst: An Efficient and Recyclable Photocatalyst for Triphenylmethane Dye Degradation. *Environ. Sci. Pollut. Res.* **2015**, *22*, 17238−17243.
(532) Vu, H. T.; Nguyen, M. B.; Vu, T. M.; Le, G. H.; Pham, T. T. T.; Nguyen, T. D.; Vu, T. A. Synthesis and Application of Novel Nano Fe-BTC/GO Composites as Highly Efficient Photocatalysts in the Dye Degradation. *Top. Catal.* **2020**, *63*, 1046−1055.
(533) Thi, Q. V.; Tamboli, M. S.; Thanh Hoai Ta, Q.; Kolekar, G. B.; Sohn, D. A Nanostructured MOF/Reduced Graphene Oxide Hybrid for Enhanced Photocatalytic Efficiency Under Solar Light. *Mater. Sci. Eng., B* **2020**, *261*, 114678.
(534) Fakhri, H.; Bagheri, H. Highly Efficient Zr-MOF@WO3/Graphene Oxide Photocatalyst: Synthesis, Characterization and Photodegradation of Tetracycline and Malathion. *Mater. Sci. Semicond. Process.* **2020**, *107*, 104815.
(535) Tang, B.; Dai, Y.; Sun, Y.; Chen, H.; Wang, Z. Graphene and MOFs Co-Modified Composites for High Adsorption Capacity and Photocatalytic Performance to Remove Pollutant Under Both UV- and Visible-Light Irradiation. *J. Solid State Chem.* **2020**, *284*, 121215.
(536) Xiao, S.; Pan, D.; Liang, R.; Dai, W.; Zhang, Q.; Zhang, G.; Su, C.; Li, H.; Chen, W. Bimetal MOF Derived Mesocrystal ZnCo2O4 On rGO with High Performance in Visible-Light Photocatalytic NO Oxidization. *Appl. Catal., B* **2018**, *236*, 304−313.
(537) Li, T.; Tian, T.; Chen, F.; Liu, X.; Zhao, X. Pd Nanoparticles Incorporated Within a Zr-Based Metal-Organic Framework/Reduced Graphene Oxide Multifunctional Composite for Efficient Visible-Light-Promoted Benzyl Alcohol Oxidation. *Aust. J. Chem.* **2019**, *72*, 334−340.
(538) Zhang, S.; Lu, Y.; Wan, X.; Duan, Y.; Gao, J.; Ge, Z.; Wei, L.; Chen, Y.; Ma, Y.; Chen, Y. Hot Electron Prompted Highly Efficient Photocatalysis Based on 3D Graphene/Non-Precious Metal Nanoparticles. *RSC Adv.* **2020**, *10*, 42054−42061.
(539) Olowoyo, J. O.; Saini, U.; Kumar, M.; Valdés, H.; Singh, H.; Omorogie, M. O.; Babalola, J. O.; Vorontsov, A. V.; Kumar, U.; Smirniotis, P. G. Reduced Graphene Oxide/NH2-MIL-125(Ti) Composite: Selective CO2 Photoreduction to Methanol Under Visible Light and Computational Insights into Charge Separation. *J. CO2 Util.* **2020**, *42*, 101300.
(540) Liu, D.; Jin, Z.; Zhang, Y.; Wang, G.; Ma, B. Light Harvesting and Charge Management by Ni4S3Modified Metal-Organic Frameworks and rGO in the Process of Photocatalysis. *J. Colloid Interface Sci.* **2018**, *529*, 44−52.
(541) Bag, P. P.; Wang, X.-S.; Sahoo, P.; Xiong, J.; Cao, R. Efficient Photocatalytic Hydrogen Evolution under Visible Light by Ternary Composite CdS@NU-1000/RGO. *Catal. Sci. Technol.* **2017**, *7*, 5113−5119.
(542) Bu, Y.; Li, F.; Zhang, Y.; Liu, R.; Luo, X.; Xu, L. Immobilizing CdS Nanoparticles And MoS2/RGO On Zr-Based Metal-Organic Framework 12-Tungstosilicate@UiO-67 Toward Enhanced Photocatalytic H2 Evolution. *RSC Adv.* **2016**, *6*, 40560−40566.
(543) Wu, Y.; Luo, H.; Wang, H. Synthesis of Iron(Iii)-Based Metal-Organic Framework/Graphene Oxide Composites with Increased Photocatalytic Performance for Dye Degradation. *RSC Adv.* **2014**, *4*, 40435−40438.
(544) Yuan, X.; Wang, H.; Wu, Y.; Zeng, G.; Chen, X.; Leng, L.; Wu, Z.; Li, H. One-Pot Self-Assembly and Photoreduction Synthesis of Silver Nanoparticle-Decorated Reduced Graphene Oxide/MIL-125(Ti) Photocatalyst with Improved Visible Light Photocatalytic Activity. *Appl. Organomet. Chem.* **2016**, *30*, 289−296.
(545) Liu, N.; Huang, W.; Zhang, X.; Tang, L.; Wang, L.; Wang, Y.; Wu, M. Ultrathin Graphene Oxide Encapsulated in Uniform MIL-88A(Fe) for Enhanced Visible Light-Driven Photodegradation of RhB. *Appl. Catal., B* **2018**, *221*, 119−128.
(546) Samuel, M. S.; Suman, S.; Venkateshkannan; Selvarajan, E.; Mathimani, T.; Pugazhendhi, A. Immobilization of Cu3(Btc)2 on Graphene Oxide-Chitosan Hybrid Composite for the Adsorption and Photocatalytic Degradation of Methylene Blue. *J. Photochem. Photobiol., B* **2020**, *204*, 111809.
(547) Hou, X.; Hu, K.; Zhang, H.; Tao, Z.; Yang, M.; Wang, G. Construction of 2D MOFs@reduced Graphene Oxide Nanocomposites with Enhanced Visible Light-induced Fenton-like Catalytic Performance by Seeded Growth Strategy. *ChemCatChem.* **2019**, *11*, 4411−4419.
(548) Mohaghegh, N.; Tasviri, M.; Rahimi, E.; Gholami, M. R. Comparative Studies on Ag3PO4/BiPO4-Metal-Organic Framework-Graphene-Based Nanocomposites for Photocatalysis Application. *Appl. Surf. Sci.* **2015**, *351*, 216−224.
(549) Yang, C.; You, X.; Cheng, J.; Zheng, H.; Chen, Y. A Novel Visible-Light-Driven In-Based MOF/Graphene Oxide Composite Photocatalyst with Enhanced Photocatalytic Activity Toward the Degradation of Amoxicillin. *Appl. Catal., B* **2017**, *200*, 673−680.
(550) Wu, Q.; Liu, Y.; Jing, H.; Yu, H.; Lu, Y.; Huo, M.; Huo, H. Peculiar Synergetic Effect of Γ-Fe2O3 Nanoparticles and Graphene Oxide on MIL-53 (Fe) for Boosting Photocatalysis. *Chem. Eng. J.* **2020**, *390*, 124615.
(551) El-Fawal, E. M.; Younis, S. A.; Zaki, T. Designing AgFeO2-Graphene/Cu2(BTC)3 MOF Heterojunction Photocatalysts for Enhanced Treatment of Pharmaceutical Wastewater Under Sunlight. *J. Photochem. Photobiol., A* **2020**, *401*, 112746.
(552) Hao, X.; Jin, Z.; Yang, H.; Lu, G.; Bi, Y. Peculiar Synergetic Effect of MoS2 Quantum Dots and Graphene on Metal-Organic Frameworks for Photocatalytic Hydrogen Evolution. *Appl. Catal., B* **2017**, *210*, 45−56.
(553) Ling, L.; Wang, Y.; Zhang, W.; Ge, Z.; Duan, W.; Liu, B. Preparation of a Novel Ternary Composite of TiO2/UiO-66-NH2/Graphene Oxide with Enhanced Photocatalytic Activities. *Catal. Lett.* **2018**, *148*, 1978−1984.
(554) Wang, Y.; Yu, Y.; Li, R.; Liu, H.; Zhang, W.; Ling, L.; Duan, W.; Liu, B. Hydrogen Production with Ultrahigh Efficiency under Visible Light by Graphene Well-Wrapped Uio-66-NH2 Octahedrons. *J. Mater. Chem. A* **2017**, *5*, 20136−20140.
(555) Yao, J.; Chen, J.; Shen, K.; Li, Y. Phase-Controllable Synthesis of MOF-Templated Maghemite-Carbonaceous Composites for Efficient Photocatalytic Hydrogen Production. *J. Mater. Chem. A* **2018**, *6*, 3571−3582.
(556) Jing, D.; Guo, L. A Novel Method for the Preparation of a Highly Stable and Active CdS Photocatalyst with a Special Surface Nanostructure. *J. Phys. Chem. B* **2006**, *110*, 11139−11145.
(557) Li, A.; Liu, Y.; Xu, X.; Zhang, Y.; Si, Z.; Wu, X.; Ran, R.; Weng, D. MOF-Derived (MoS2, Γ-Fe2O3)/Graphene Z-Scheme Photocatalysts with Excellent Activity for Oxygen Evolution Under Visible Light Irradiation. *RSC Adv.* **2020**, *10*, 17154−17162.
(558) Sadeghi, N.; Sharifnia, S.; Do, T.-O. Enhanced CO2 Photoreduction by a Graphene-Porphyrin Metal-Organic Framework under Visible Light Irradiation. *J. Mater. Chem. A* **2018**, *6*, 18031−18035.
(559) Liu, N.; Tang, M.; Wu, J.; Tang, L.; Huang, W.; Li, Q.; Lei, J.; Zhang, X.; Wang, L. Boosting Visible-Light Photocatalytic Performance for CO2 Reduction via Hydroxylated Graphene Quantum Dots Sensitized MIL-101(Fe). *Adv. Mater. Interfaces* **2020**, *7*, 2000468.
(560) Inoue, T.; Fujishima, A.; Konishi, S.; Honda, K. Photoelectrocatalytic Reduction of Carbon Dioxide in Aqueous Suspensions of Semiconductor Powders. *Nature* **1979**, *277*, 637−638.
(561) Meng, J.; Chen, Q.; Lu, J.; Liu, H. Z-Scheme Photocatalytic CO2 Reduction on a Heterostructure of Oxygen-Defective ZnO/

Reduced Graphene Oxide/UiO-66-NH2 under Visible Light. *ACS Appl. Mater. Interfaces* **2019**, *11*, 550−562.
(562) Yang, Z.; Xu, X.; Liang, X.; Lei, C.; Gao, L.; Hao, R.; Lu, D.; Lei, Z. Fabrication of Ce Doped UiO-66/Graphene Nanocomposites with Enhanced Visible Light Driven Photoactivity for Reduction of Nitroaromatic Compounds. *Appl. Surf. Sci.* **2017**, *420*, 276−285.
(563) Cai, J.; Lu, J.-Y.; Chen, Q.-Y.; Qu, L.-L.; Lu, Y.-Q.; Gao, G.-F. Eu-Based MOF/Graphene Oxide Composite: A Novel Photocatalyst for the Oxidation of Benzyl Alcohol Using Water as Oxygen Source. *New J. Chem.* **2017**, *41*, 3882−3886.
(564) Li, X.; Le, Z.; Chen, X.; Li, Z.; Wang, W.; Liu, X.; Wu, A.; Xu, P.; Zhang, D. Graphene Oxide Enhanced Amine-Functionalized Titanium Metal Organic Framework for Visible-Light-Driven Photocatalytic Oxidation of Gaseous Pollutants. *Appl. Catal., B* **2018**, *236*, 501−508.
(565) Zhao, Y.; Cai, W.; Chen, J.; Miao, Y.; Bu, Y. A Highly Efficient Composite Catalyst Constructed From NH2-MIL-125(Ti) and Reduced Graphene Oxide for CO2 Photoreduction. *Front. Chem.* **2019**, *7*, 789.
(566) Xu, J.; He, S.; Zhang, H.; Huang, J.; Lin, H.; Wang, X.; Long, J. Layered Metal-Organic Framework/Graphene Nanoarchitectures for Organic Photosynthesis under Visible Light. *J. Mater. Chem. A* **2015**, *3*, 24261−24271.
(567) Wang, H.; Zhu, Q.-L.; Zou, R.; Xu, Q. Metal-Organic Frameworks for Energy Applications. *Chem.* **2017**, *2*, 52−80.
(568) Lei, Z.; Zhang, J.; Zhang, L. L.; Kumar, N. A.; Zhao, X. S. Functionalization of Chemically Derived Graphene for Improving its Electrocapacitive Energy Storage Properties. *Energy Environ. Sci.* **2016**, *9*, 1891−1930.
(569) Xia, W.; Mahmood, A.; Zou, R.; Xu, Q. Metal-Organic Frameworks and their Derived Nanostructures for Electrochemical Energy Storage and Conversion. *Energy Environ. Sci.* **2015**, *8*, 1837−1866.
(570) Zhu, Q.-L.; Xu, Q. Metal-Organic Framework Composites. *Chem. Soc. Rev.* **2014**, *43*, 5468−5512.
(571) Li, Z.; Ge, X.; Li, C.; Dong, S.; Tang, R.; Wang, C.; Zhang, Z.; Yin, L. Rational Microstructure Design on Metal-Organic Framework Composites for Better Electrochemical Performances: Design Principle, Synthetic Strategy, and Promotion Mechanism. *Small Methods* **2020**, *4*, 1900756.
(572) Zheng, Y.; Zheng, S.; Xue, H.; Pang, H. Metal-Organic Frameworks/Graphene-Based Materials: Preparations and Applications. *Adv. Funct. Mater.* **2018**, *28*, 1804950.
(573) Dubal, D. P.; Chodankar, N. R.; Kim, D. H.; Gomez-Romero, P. Towards Flexible Solid-State Supercapacitors for Smart and Wearable Electronics. *Chem. Soc. Rev.* **2018**, *47*, 2065−2129.
(574) Jayaramulu, K.; Dubal, D. P.; Nagar, B.; Ranc, V.; Tomanec, O.; Petr, M.; Datta, K. K. R.; Zboril, R.; Gomez-Romero, P.; Fischer, R. A. Ultrathin Hierarchical Porous Carbon Nanosheets for High-Performance Supercapacitors and Redox Electrolyte Energy Storage. *Adv. Mater.* **2018**, *30*, No. 1705789.
(575) Kumar, N. A.; Baek, J.-B. Doped Graphene Supercapacitors. *Nanotechnology* **2015**, *26*, 492001.
(576) Zheng, S.; Li, X.; Yan, B.; Hu, Q.; Xu, Y.; Xiao, X.; Xue, H.; Pang, H. Transition-Metal (Fe, Co, Ni) Based Metal-Organic Frameworks for Electrochemical Energy Storage. *Adv. Energy Mater.* **2017**, *7*, 1602733.
(577) Zhou, Y.; Mao, Z.; Wang, W.; Yang, Z.; Liu, X. In-Situ Fabrication of Graphene Oxide Hybrid Ni-Based Metal-Organic Framework (Ni-MOFs@GO) with Ultrahigh Capacitance as Electrochemical Pseudocapacitor Materials. *ACS Appl. Mater. Interfaces* **2016**, *8*, 28904−28916.
(578) Banerjee, P. C.; Lobo, D. E.; Middag, R.; Ng, W. K.; Shaibani, M. E.; Majumder, M. Electrochemical Capacitance of Ni-Doped Metal Organic Framework and Reduced Graphene Oxide Composites: More than the Sum of Its Parts. *ACS Appl. Mater. Interfaces* **2015**, *7*, 3655−3664.
(579) Li, W.; Xu, A.; Zhang, Y.; Yu, Y.; Liu, Z.; Qin, Y. Metal-Organic Framework-Derived Mn3O4 Nanostructure on Reduced Graphene Oxide as High-Performance Supercapacitor Electrodes. *J. Alloys. Compd.* **2022**, *897*, 162640.
(580) Liu, L.; Yan, Y.; Cai, Z.; Lin, S.; Hu, X. Growth-Oriented Fe-Based MOFs Synergized with Graphene Aerogels for High-Performance Supercapacitors. *Adv. Mater. Interfaces* **2018**, *5*, 1701548.
(581) Xiao, P.; Bu, F.; Zhao, R.; Aly Aboud, M. F.; Shakir, I.; Xu, Y. Sub-5 nm Ultrasmall Metal-Organic Framework Nanocrystals for Highly Efficient Electrochemical Energy Storage. *ACS Nano* **2018**, *12*, 3947−3953.
(582) Du, Y.; Li, G.; Ye, L.; Che, C.; Yang, X.; Zhao, L. Sandwich-Like Ni-Zn Hydroxide Nanosheets Vertically Aligned on Reduced Graphene Oxide *via* MOF Templates Towards Boosting Supercapacitive Performance. *Chem. Eng. J.* **2021**, *417*, 129189.
(583) Ashourdan, M.; Semnani, A.; Hasanpour, F.; Moosavifard, S. E. Synthesis of Nickel Cobalt Manganese Metal Organic Framework@ High Quality Graphene Composites as Novel Electrode Materials for High Performance Supercapacitors. *J. Electroanal. Chem.* **2021**, *895*, 115452.
(584) Zhang, W.; Wang, Y.; Guo, X.; Liu, Y.; Zheng, Y.; Zhang, M.; Li, R.; Peng, Z.; Xie, H.; Zhao, Y. Graphene-Carbon Nanotube @ Cobalt Derivatives from ZIF-67 for All-Solid-State Asymmetric Supercapacitor. *Appl. Surf. Sci.* **2021**, *568*, 150929.
(585) Cao, X.; Zheng, B.; Shi, W.; Yang, J.; Fan, Z.; Luo, Z.; Rui, X.; Chen, B.; Yan, Q.; Zhang, H. Reduced Graphene Oxide-Wrapped MoO3 Composites Prepared by Using Metal-Organic Frameworks as Precursor for All-Solid-State Flexible Supercapacitors. *Adv. Mater.* **2015**, *27*, 4695−4701.
(586) Dubal, D. P.; Ayyad, O.; Ruiz, V.; Gomez-Romero, P. Hybrid Energy Storage: The Merging of Battery and Supercapacitor Chemistries. *Chem. Soc. Rev.* **2015**, *44*, 1777−1790.
(587) Han, Y.; Liu, Z.; Zheng, F.; Bai, Y.; Zhang, Z.; Li, X.; Xiong, W.; Zhang, J.; Yuan, A. Two-Dimensional Flower-Like Cobalt-Porphyrin MOF/rGO Composite Anodes for High-Performance Li-Ion Batteries. *J. Alloys Compd.* **2021**, *881*, 160531.
(588) Gao, C.; Wang, P.; Wang, Z.; Kær, S. K.; Zhang, Y.; Yue, Y. The Disordering-Enhanced Performances of the Al-MOF/Graphene Composite Anodes for Lithium Ion Batteries. *Nano Energy* **2019**, *65*, 104032.
(589) Liu, C.; Tian, R.; Sun, D.; Liu, H.; Duan, H. MOF-Derived 3D Hollow Porous Carbon/Graphene Composites for Advanced Lithium-Ion Battery Anodes. *J. Solid State Chem.* **2020**, *290*, 121568.
(590) Liu, X.; Zhang, S.; Xing, Y.; Wang, S.; Yang, P.; Li, H. MOF-Derived, N-Doped Porous Carbon Coated Graphene Sheets as High-Performance Anodes for Lithium-Ion Batteries. *New J. Chem.* **2016**, *40*, 9679−9683.
(591) Wang, C.; Mutahir, S.; Wang, L.; Lei, W.; Xia, X.; Jiao, X.; Hao, Q. Hierarchical MOF-Derived Layered Fe3O4 QDs@C Imbedded on Graphene Sheets as a High-Performance Anode for Lithium-Ion Storage. *Appl. Surf. Sci.* **2020**, *509*, 144882.
(592) Li, S.; Liu, Y.; Zhou, J.; Hong, S.; Dong, Y.; Wang, J.; Gao, X.; Qi, P.; Han, Y.; Wang, B. Monodispersed MnO Nanoparticles in Graphene-an interconnected N-Doped 3D Carbon Framework as a Highly Efficient Gas Cathode in Li-CO2 Batteries. *Energy Environ. Sci.* **2019**, *12*, 1046−1054.
(593) Jayaramulu, K.; Dubal, D. P.; Schneemann, A.; Ranc, V.; Perez-Reyes, C.; Stráská, J.; Kment, Š; Otyepka, M.; Fischer, R. A.; Zboril, R. Shape-Assisted 2D MOF/Graphene Derived Hybrids as Exceptional Lithium-Ion Battery Electrodes. *Adv. Funct. Mater.* **2019**, *29*, 1902539.
(594) Gao, M.; Liu, X.; Yang, H.; Yu, Y. FeP Nanoparticles Derived fom Metal-Organic Frameworks/GO as High-Performance Anode Material for Lithium Ion Batteries. *Sci. China Chem.* **2018**, *61*, 1151−1158.
(595) Horn, M. R.; Singh, A.; Alomari, S.; Goberna-Ferrón, S.; Benages-Vilau, R.; Chodankar, N.; Motta, N.; Ostrikov, K.; MacLeod, J.; Sonar, P.; Gomez-Romero, P.; Dubal, D. Polyoxometalates (Poms): From Electroactive Clusters to Energy Materials. *Energy Environ. Sci.* **2021**, *14*, 1652−1700.
(596) Dubal, D. P.; Suarez-Guevara, J.; Tonti, D.; Enciso, E.; Gomez-Romero, P. A High Voltage Solid State Symmetric Supercapacitor Based on Graphene-Polyoxometalate Hybrid Electrodes with a

Hydroquinone Doped Hybrid Gel-Electrolyte. *J. Mater. Chem. A* **2015**, *3*, 23483−23492.
(597) Wei, T.; Zhang, M.; Wu, P.; Tang, Y.-J.; Li, S.-L.; Shen, F.-C.; Wang, X.-L.; Zhou, X.-P.; Lan, Y.-Q. POM-Based Metal-Organic Framework/Reduced Graphene Oxide Nanocomposites with Hybrid Behavior of Battery-Supercapacitor for Superior Lithium Storage. *Nano Energy* **2017**, *34*, 205−214.
(598) Yao, J.; Zhang, M.; Han, G.; Wang, X.; Wang, Z.; Wang, J. Reduced Graphene Oxide Coated Fe-Soc as a Cathode Material for High-Performance Lithium-Sulfur Batteries. *Ceram. Int.* **2020**, *46*, 24155−24161.
(599) Jin, J.; Cai, W.; Cai, J.; Shao, Y.; Song, Y.; Xia, Z.; Zhang, Q.; Sun, J. MOF-Derived Hierarchical Cop Nanoflakes Anchored on Vertically Erected Graphene Scaffolds as Self-Supported and Flexible Hosts for Lithium-Sulfur Batteries. *J. Mater. Chem. A* **2020**, *8*, 3027−3034.
(600) Song, C.-L.; Li, Z.-H.; Li, M.-Z.; Huang, S.; Hong, X.-J.; Si, L.-P.; Zhang, M.; Cai, Y.-P. Iron Carbide Dispersed on Nitrogen-Doped Graphene-like Carbon Nanosheets for Fast Conversion of Polysulfides in Li-S Batteries. *ACS Appl. Nano Mater.* **2020**, *3*, 9686−9693.
(601) Xu, F.; Dong, C.; Jin, B.; Li, H.; Wen, Z.; Jiang, Q. MOF-Derived LDH Wrapped with rGO as an Efficient Sulfur Host for Lithium-Sulfur Batteries. *J. Electroanal. Chem.* **2020**, *876*, 114545.
(602) Wei, R.; Dong, Y.; Zhang, Y.; Zhang, R.; Al-Tahan, M. A.; Zhang, J. In-Situ Self-Assembled Hollow Urchins F-Co-MOF on rGO as Advanced Anodes for Lithium-Ion and Sodium-Ion Batteries. *J. Colloid Interface Sci.* **2021**, *582*, 236−245.
(603) Zhang, Y.; Wu, Y.; Zhong, W.; Xiao, F.; Kashif Aslam, M.; Zhang, X.; Xu, M. Highly Efficient Sodium-Ion Storage Enabled by an rGO-Wrapped FeSe2 Composite. *ChemSusChem* **2021**, *14*, 1336−1343.
(604) Lu, C.; Li, Z.; Xia, Z.; Ci, H.; Cai, J.; Song, Y.; Yu, L.; Yin, W.; Dou, S.; Sun, J.; Liu, Z. Confining MOF-Derived Snse Nanoplatelets in Nitrogen-Doped Graphene Cages *via* Direct CVD for Durable Sodium Ion Storage. *Nano Res.* **2019**, *12*, 3051−3058.
(605) Zhang, Z.; Wu, C.; Chen, Z.; Li, H.; Cao, H.; Luo, X.; Fang, Z.; Zhu, Y. Spatially Confined Synthesis of a Flexible and Hierarchically Porous Three-Dimensional Graphene/Fep Hollow Nanosphere Composite Anode for Highly Efficient and Ultrastable Potassium Ion Storage. *J. Mater. Chem. A* **2020**, *8*, 3369−3378.
(606) Xiao, P.; Li, S.; Yu, C.; Wang, Y.; Xu, Y. Interface Engineering between the Metal-Organic Framework Nanocrystal and Graphene toward Ultrahigh Potassium-Ion Storage Performance. *ACS Nano* **2020**, *14*, 10210−10218.
(607) Deng, Q.; Luo, Z.; Liu, H.; Zhou, Y.; Zhou, C.; Yang, R.; Wang, L.; Yan, Y.; Xu, Y. Facile Synthesis of Fe-Based Metal-Organic Framework and Graphene Composite as an Anode Material for K-Ion Batteries. *Ionics* **2020**, *26*, 5565−5573.
(608) Xie, J.; Zhu, Y.; Zhuang, N.; Lei, H.; Zhu, W.; Fu, Y.; Javed, M. S.; Li, J.; Mai, W. Rational Design of Metal Organic Framework-Derived FeS2 Hollow Nanocages@Reduced Graphene Oxide for K-Ion Storage. *Nanoscale* **2018**, *10*, 17092−17098.
(609) Li, C.; Hu, C.; Zhao, Y.; Song, L.; Zhang, J.; Huang, R.; Qu, L. Decoration of Graphene Network with Metal-Organic Frameworks for Enhanced Electrochemical Capacitive Behavior. *Carbon* **2014**, *78*, 231−242.
(610) Hao, G.-P.; Zhang, Q.; Sin, M.; Hippauf, F.; Borchardt, L.; Brunner, E.; Kaskel, S. Design of Hierarchically Porous Carbons with Interlinked Hydrophilic and Hydrophobic Surface and Their Capacitive Behavior. *Chem. Mater.* **2016**, *28*, 8715−8725.
(611) Fu, D.; Zhou, H.; Zhang, X.-M.; Han, G.; Chang, Y.; Li, H. Flexible Solid-State Supercapacitor of Metal-Organic Framework Coated on Carbon Nanotube Film Interconnected by Electrochemically-Codeposited PEDOT-GO. *ChemistrySelect* **2016**, *1*, 285−289.
(612) Zhao, K.; Lyu, K.; Liu, S.; Gan, Q.; He, Z.; Zhou, Z. Ordered Porous Mn3O4@N-Doped Carbon/Graphene Hybrids Derived from Metal-Organic Frameworks for Supercapacitor Electrodes. *J. Mater. Sci.* **2017**, *52*, 446−457.
(613) Kumar, S.; Sekar, S.; Kaliamurthy, A. K.; Lee, S. Bifunctional rGO-NiCo2S4MOF Hybrid with High Electrochemical and Catalytic Activity for Supercapacitor and Nitroarene Reduction. *J. Mater. Res. Technol.* **2021**, *12*, 2489−2501.
(614) Yang, Y.; Zhong, Z.; Li, J.; Du, H.; Wang, W.; Huang, J. Fast and Low-Consumption Granular NiCo-LDH/Graphene Nanosheet Composites for High-Performance Supercapacitor Electrodes. *J. Mater. Sci. Mater. Electron.* **2021**, *32*, 23750−23761.
(615) Wu, C.-L.; Chen, D.-H. Fabrication of rGO/CoSx-rGO/rGO Hybrid Film *via* Coassembly and Sulfidation of 2D Metal Organic Framework Nanoflakes and Graphene Oxide as Free-Standing Supercapacitor Electrode. *J. Alloys. Compd.* **2021**, *872*, 159702.
(616) Li, S.; Shi, C.; Pan, Y.; Wang, Y. 2D/2D NiCo-MOFs/GO Hybrid Nanosheets for High-Performance Asymmetrical Supercapacitor. *Diam. Relat. Mater.* **2021**, *115*, 108358.
(617) Li, X.; Li, J.; Zhang, Y.; Zhao, P. Synthesis of Ni-MOF Derived NiO/rGO Composites as Novel Electrode Materials for High Performance Supercapacitors. *Colloids Surf., A* **2021**, *622*, 126653.
(618) Hira, S. A.; Park, K. H. Nitrogen-Doped Zeolitic Imidazolate Framework and Particle-Reduced Graphene Oxide Composites as Electrochemical Sensors and Battery-Type Supercapacitors. *ACS Appl. Nano Mater.* **2021**, *4*, 7870−7878.
(619) Zhu, L.; Hao, C.; Wang, X.; Guo, Y. Fluffy Cotton-Like GO/Zn-Co-Ni Layered Double Hydroxides Form from a Sacrificed Template GO/ZIF-8 for High Performance Asymmetric Supercapacitors. *ACS Sustain. Chem. Eng.* **2020**, *8*, 11618−11629.
(620) Wang, B. R.; Hu, Y.; Pan, Z.; Wang, J. MOF-Derived Manganese Oxide/Carbon Nanocomposites with Raised Capacitance for Stable Asymmetric Supercapacitor. *RSC Adv.* **2020**, *10*, 34403−34412.
(621) Eswaramoorthi, T.; Ganesan, S.; Marimuthu, M.; Santhosh, K. Thin Niobium and Iron-Graphene Oxide Composite Metal-Organic Framework Electrodes for High Performance Supercapacitors. *New J. Chem.* **2020**, *44*, 12664−12673.
(622) Tan, Q.; Chen, X.; Wan, H.; Zhang, B.; Liu, X.; Li, L.; Wang, C.; Gan, Y.; Liang, P.; Wang, Y.; Zhang, J.; Wang, H.; Miao, L.; Jiang, J.; van Aken, P. A.; Wang, H. Metal-Organic Framework-Derived High Conductivity Fe3C with Porous Carbon on Graphene as Advanced Anode Materials for Aqueous Battery-Supercapacitor Hybrid Devices. *J. Power Sources* **2020**, *448*, 227403.
(623) Wang, Y.-F.; Yang, S.-Y.; Yue, Y.; Bian, S.-W. Conductive Copper-Based Metal-Organic Framework Nanowire Arrays Grown on Graphene Fibers for Flexible All-Solid-State Supercapacitors. *J. Alloys. Compd.* **2020**, *835*, 155238.
(624) Hu, X.; Li, J.; Wu, Q.; Chen, R. MOF-Derived CoS2 Porous Nanocubes Assembled on Graphene Oxide Nanosheets as Electrode for Supercapacitor Applications. *Ionics* **2020**, *26*, 1045−1050.
(625) Sundriyal, S.; Shrivastav, V.; Mishra, S.; Deep, A. Enhanced Electrochemical Performance of Nickel Intercalated ZIF-67/rGO Composite Electrode for Solid-State Supercapacitors. *Int. J. Hydrog. Energy* **2020**, *45*, 30859−30869.
(626) Huang, N.; Lee, K. H.; Yue, Y.; Xu, X.; Irle, S.; Jiang, Q.; Jiang, D. A Stable and Conductive Metallophthalocyanine Framework for Electrocatalytic Carbon Dioxide Reduction in Water. *Angew. Chem., Int. Ed.* **2020**, *59*, 16587−16593.
(627) Ren, C.; Jia, X.; Zhang, W.; Hou, D.; Xia, Z.; Huang, D.; Hu, J.; Chen, S.; Gao, S. Hierarchical Porous Integrated Co1- xS/CoFe2O4@rGO Nanoflowers Fabricated via Temperature-Controlled In Situ Calcining Sulfurization of Multivariate CoFe-MOF-74@rGO for High-Performance Supercapacitor. *Adv. Funct. Mater.* **2020**, *30*, 2004519.
(628) Liu, X.; Ding, S.; Ye, L.; Du, Y.; Zhao, L.; Zhu, Y. Optimizing the Supercapacitive Performance *via* Encasing MOF-Derived Hollow (Ni,Co)Se2 Nanocubes into Reduced Graphene Oxide. *Chem. Eng. J.* **2020**, *399*, 125789.
(629) Wang, P.; Zhou, H.; Meng, C.; Wang, Z.; Akhtar, K.; Yuan, A. Cyanometallic Framework-Derived Hierarchical Co3O4-NiO/Graphene Foam as High-Performance Binder-Free Electrodes for Supercapacitors. *Chem. Eng. J.* **2019**, *369*, 57−63.

https://doi.org/10.1021/acs.chemrev.2c00270
Chem. Rev. 2022, 122, 17241−17338

(630) Guo, D.; Song, X.; Tan, L.; Ma, H.; Sun, W.; Pang, H.; Zhang, L.; Wang, X. A Facile Dissolved and Reassembled Strategy Towards Sandwich-Like rGO@NiCoAl-LDHs with Excellent Supercapacitor Performance. *Chem. Eng. J.* **2019**, *356*, 955−963.
(631) Rajak, R.; Saraf, M.; Mobin, S. M. Robust Heterostructures of a Bimetallic Sodium-Zinc Metal-Organic Framework and Reduced Graphene Oxide for High-Performance Supercapacitors. *J. Mater. Chem. A* **2019**, *7*, 1725−1736.
(632) Li, Z.; Liu, X.; Wang, L.; Bu, F.; Wei, J.; Pan, D.; Wu, M. Hierarchical 3D All-Carbon Composite Structure Modified with N-Doped Graphene Quantum Dots for High-Performance Flexible Supercapacitors. *Small* **2018**, *14*, No. 1801498.
(633) Qu, C.; Zhang, L.; Meng, W.; Liang, Z.; Zhu, B.; Dang, D.; Dai, S.; Zhao, B.; Tabassum, H.; Gao, S.; Zhang, H.; Guo, W.; Zhao, R.; Huang, X.; Liu, M.; Zou, R. MOF-Derived α-NiS Nanorods on Graphene as an Electrode for High-Energy-Density Supercapacitors. *J. Mater. Chem. A* **2018**, *6*, 4003−4012.
(634) Vilian, A. T. E.; Dinesh, B.; Rethinasabapathy, M.; Hwang, S.-K.; Jin, C.-S.; Huh, Y. S.; Han, Y.-K. Hexagonal Co3O4 Anchored Reduced Graphene Oxide Sheets for High-Performance Supercapacitors and Non-Enzymatic Glucose Sensing. *J. Mater. Chem. A* **2018**, *6*, 14367−14379.
(635) Wang, P.; Li, C.; Wang, W.; Wang, J.; Zhu, Y.; Wu, Y. Hollow Co9S8fFrom Metal Organic Framework Supported on rGO as Electrode Material for Highly Stable Supercapacitors. *Chin. Chem. Lett.* **2018**, *29*, 612−615.
(636) Bai, X.; Liu, Q.; Lu, Z.; Liu, J.; Chen, R.; Li, R.; Song, D.; Jing, X.; Liu, P.; Wang, J. Rational Design of Sandwiched Ni-Co Layered Double Hydroxides Hollow Nanocages/Graphene Derived from Metal-Organic Framework for Sustainable Energy Storage. *ACS Sustain. Chem. Eng.* **2017**, *5*, 9923−9934.
(637) Jayakumar, A.; Antony, R. P.; Wang, R.; Lee, J. M. MOF-Derived Hollow Cage Nix Co3-x O4 and Their Synergy with Graphene for Outstanding Supercapacitors. *Small* **2017**, *13*, 1603102.
(638) Punde, N. S.; Rawool, C. R.; Rajpurohit, A. S.; Karna, S. P.; Srivastava, A. K. Hybrid Composite Based on Porous Cobalt-Benzenetricarboxylic Acid Metal Organic Framework and Graphene Nanosheets as High Performance Supercapacitor Electrode. *ChemistrySelect* **2018**, *3*, 11368−11380.
(639) Lv, Z.; Zhong, Q.; Bu, Y. In-Situ Conversion of rGO/Ni2P Composite from GO/Ni-MOF Precursor with Enhanced Electrochemical Property. *Appl. Surf. Sci.* **2018**, *439*, 413−419.
(640) Samuel, E.; Joshi, B.; Park, C.; Aldalbahi, A.; Rahaman, M.; Yoon, S. S. Supersonically Sprayed rGO/ZIF-8 on Nickel Nanocone Substrate for Highly Stable Supercapacitor Electrodes. *Electrochim. Acta* **2020**, *362*, 137154.
(641) Bao, W. Z.; Zhang, Z. A.; Qu, Y. H.; Zhou, C. K.; Wang, X. W.; Li, J. Confine Sulfur in Mesoporous Metal-Organic Framework@ Reduced Graphene Oxide for Lithium Sulfur Battery. *J. Alloys. Compd.* **2014**, *582*, 334−340.
(642) Chen, R.; Zhao, T.; Tian, T.; Cao, S.; Coxon, P. R.; Xi, K.; Fairen-Jimenez, D.; Vasant Kumar, R.; Cheetham, A. K. Graphene-Wrapped Sulfur/Metal Organic Framework-Derived Microporous Carbon Composite for Lithium Sulfur Batteries. *APL Mater.* **2014**, *2*, 124109.
(643) Zhao, Z. X.; Wang, S.; Liang, R.; Li, Z.; Shi, Z. C.; Chen, G. H. Graphene-Wrapped Chromium-MOF(MIL-101)/Sulfur Composite for Performance Improvement of High-Rate Rechargeable Li-S Batteries. *J. Mater. Chem. A* **2014**, *2*, 13509−13512.
(644) He, J.; Chen, Y.; Manthiram, A. MOF-derived Cobalt Sulfide Grown on 3D Graphene Foam as an Efficient Sulfur Host for Long-Life Lithium-Sulfur Batteries. *iScience* **2018**, *4*, 36−43.
(645) Xu, J.; Zhang, W. X.; Chen, Y.; Fan, H. B.; Su, D. W.; Wang, G. X. MOF-Derived Porous N-Co3O4@N-C Nanododecahedra Wrapped with Reduced Graphene Oxide as a High Capacity Cathode for Lithium-Sulfur Batteries. *J. Mater. Chem. A* **2018**, *6*, 2797−2807.
(646) Cai, D.; Lu, M.; Li, L.; Cao, J.; Chen, D.; Tu, H.; Li, J.; Han, W. A Highly Conductive MOF of Graphene Analogue Ni3(HITP)2 as a Sulfur Host for High-Performance Lithium-Sulfur Batteries. *Small* **2019**, *15*, No. 1902605.
(647) Wu, Y.; Jiang, H.; Ke, F. S.; Deng, H. Three-Dimensional Hierarchical Constructs of MOF-on-Reduced Graphene Oxide for Lithium-Sulfur Batteries. *Chem. Asian J.* **2019**, *14*, 3577−3582.
(648) Baumann, A. E.; Downing, J. R.; Burns, D. A.; Hersam, M. C.; Thoi, V. S. Graphene-Metal-Organic Framework Composite Sulfur Electrodes for Li-S Batteries with High Volumetric Capacity. *ACS Appl. Mater. Interfaces* **2020**, *12*, 37173−37181.
(649) Xu, F. C.; Dong, C. W.; Jin, B.; Li, H.; Wen, Z.; Jiang, Q. MOF-Derived LDH Wrapped with rGO as an Efficient Sulfur Host for Lithium-Sulfur Batteries. *J. Electroanal. Chem.* **2020**, *876*, 114545.
(650) Li, Z. Q.; Yin, L. W. Sandwich-Like Reduced Graphene Oxide Wrapped MOF-Derived ZnCo2O4-ZnO-C On Nickel Foam as Anodes for High Performance Lithium Ion Batteries. *J. Mater. Chem. A* **2015**, *3*, 21569−21577.
(651) Jin, Y.; Zhao, C. C.; Sun, Z. X.; Lin, Y. C.; Chen, L.; Wang, D. Y.; Shen, C. Facile Synthesis of Fe-MOF/RGO and its Application as a High Performance Anode in Lithium-Ion Batteries. *RSC Adv.* **2016**, *6*, 30763−30768.
(652) Liu, X.; Zhang, S. C.; Xing, Y. L.; Wang, S. B.; Yang, P. H.; Li, H. L. MOF-Derived, N-Doped Porous Carbon Coated Graphene Sheets as High-Performance Anodes for Lithium-Ion Batteries. *New J. Chem.* **2016**, *40*, 9679−9683.
(653) Ji, D.; Zhou, H.; Tong, Y.; Wang, J.; Zhu, M.; Chen, T.; Yuan, A. Facile Fabrication of MOF-Derived Octahedral CuO Wrapped 3D Graphene Network as Binder-Free Anode for High Performance Lithium-Ion Batteries. *Chem. Eng. J.* **2017**, *313*, 1623−1632.
(654) Li, C.; Lou, X.; Yang, Q.; Zou, Y.; Hu, B. Remarkable Improvement in the Lithium Storage Property of Co2(OH)2BDC MOF by Covalent Stitching to Graphene and the Redox Chemistry Boosted by Delocalized Electron Spins. *Chem. Eng. J.* **2017**, *326*, 1000−1008.
(655) Zhou, X.; Chen, S.; Yang, J.; Bai, T.; Ren, Y.; Tian, H. Metal-Organic Frameworks Derived Okra-like SnO2 Encapsulated in Nitrogen-Doped Graphene for Lithium Ion Battery. *ACS Appl. Mater. Interfaces* **2017**, *9*, 14309−14318.
(656) Gan, Q.; Liu, B.; Zhao, K.; He, Z.; Liu, S. Flower-Like NiCo2O4 from Ni-Co 1,3,5-Benzenetricarboxylate Metal Organic Framework Tuned by Graphene Oxide for High-Performance Lithium Storage. *Electrochim. Acta* **2018**, *279*, 152−160.
(657) Gao, M.; Liu, X. W.; Yang, H.; Yu, Y. Fep Nanoparticles Derived from Metal-Organic Frameworks/GO as High-Performance Anode Material for Lithium Ion Batteries. *Sci. China Chem.* **2018**, *61*, 1151−1158.
(658) Zhang, L.; Liu, W.; Shi, W.; Xu, X.; Mao, J.; Li, P.; Ye, C.; Yin, R.; Ye, S.; Liu, X.; Cao, X.; Gao, C. Boosting Lithium Storage Properties of MOF Derivatives through a Wet-Spinning Assembled Fiber Strategy. *Chem. Eur. J.* **2018**, *24*, 13792−13799.
(659) Cao, Y.; Lu, Y.; Ang, E. H.; Geng, H.; Cao, X.; Zheng, J.; Gu, H. MOF-Derived Uniform Ni Nanoparticles Encapsulated in Carbon Nanotubes Grafted on rGO Nanosheets as Bifunctional Materials for Lithium-Ion Batteries and Hydrogen Evolution Reaction. *Nanoscale* **2019**, *11*, 15112−15119.
(660) Gao, C. W.; Wang, P. X.; Wang, Z. Y.; Kaer, S. K.; Zhang, Y. F.; Yue, Y. Z. The Disordering-Enhanced Performances of the Al-MOF/Graphene Composite Anodes for Lithium Ion Batteries. *Nano Energy* **2019**, *65*, 104032.
(661) Yu, H.; Zhu, W. J.; Zhou, H.; Liu, J. F.; Yang, Z.; Hu, X. C.; Yuan, A. H. Porous Carbon Derived from Metal-Organic Framework@ Graphene Quantum Dots as Electrode Materials for Supercapacitors and Lithium-Ion Batteries. *RSC Adv.* **2019**, *9*, 9577−9583.
(662) Gao, C. W.; Jiang, Z. J.; Wang, P. X.; Jensen, L. R.; Zhang, Y. F.; Yue, Y. Z. Optimized Assembling of MOF/SnO2/Graphene Leads to Superior Anode for Lithium Ion Batteries. *Nano Energy* **2020**, *74*, 104868.
(663) Guo, C.; Xie, Y.; Pan, K.; Li, L. MOF-Derived Hollow SiOx Nanoparticles Wrapped in 3D Porous Nitrogen-Doped Graphene

https://doi.org/10.1021/acs.chemrev.2c00270
Chem. Rev. 2022, 122, 17241−17338

Aerogel and their Superior Performance as the Anode for Lithium-Ion Batteries. *Nanoscale* **2020**, *12*, 13017−13027.
(664) Liu, C. H.; Tian, R.; Sun, D.; Liu, H. Z.; Duan, H. N. MOF-Derived 3D Hollow Porous Carbon/Graphene Composites for Advanced Lithium-Ion Battery Anodes. *J. Solid State Chem.* **2020**, *290*, 121568.
(665) Wang, C. X.; Mutahir, S.; Wang, L.; Lei, W.; Xia, X. F.; Jiao, X. Y.; Hao, Q. L. Hierarchical MOF-Derived Layered Fe3O4 QDs@C Imbedded on Graphene Sheets as a High-Performance Anode for Lithium-Ion Storage. *Appl. Surf. Sci.* **2020**, *509*, 144882.
(666) Bu, F.; Xiao, P.; Chen, J.; Aly Aboud, M. F.; Shakir, I.; Xu, Y. Rational Design of Three-Dimensional Graphene Encapsulated Core-Shell Fes@Carbon Nanocomposite as a Flexible High-Performance Anode for Sodium-Ion Batteries. *J. Mater. Chem. A* **2018**, *6*, 6414−6421.
(667) Yang, M.-Q.; Xu, Y.-J. Basic Principles for Observing the Photosensitizer Role of Graphene in the Graphene-Semiconductor Composite Photocatalyst from a Case Study on Graphene-ZnO. *J. Phys. Chem. C* **2013**, *117*, 21724−21734.
(668) Tang, Y.; Wu, H.; Cao, W.; Cui, Y.; Qian, G. Luminescent Metal-Organic Frameworks for White LEDs. *Adv. Opt. Mater.* **2021**, *9*, 2001817.
(669) Gu, Y.; Qiu, Z.; Müllen, K. Nanographenes and Graphene Nanoribbons as Multitalents of Present and Future Materials Science. *J. Am. Chem. Soc.* **2022**, *144*, 11499−11524.
(670) Liu, K.; Li, J.; Qi, H.; Hambsch, M.; Rawle, J.; Vázquez, A. R.; Nia, A. S.; Pashkin, A.; Schneider, H.; Polozij, M.; Heine, T.; Helm, M.; Mannsfeld, S. C. B.; Kaiser, U.; Dong, R.; Feng, X. A Two-Dimensional Polyimide-Graphene Heterostructure with Ultra-fast Interlayer Charge Transfer. *Angew. Chem., Int. Ed.* **2021**, *60*, 13859−13864.
(671) Liu, Y.; Weiss, N. O.; Duan, X.; Cheng, H.-C.; Huang, Y.; Duan, X. Van der Waals Heterostructures and Devices. *Nat. Rev. Mater.* **2016**, *1*, 16042.
(672) Rizzo, D. J.; Veber, G.; Cao, T.; Bronner, C.; Chen, T.; Zhao, F.; Rodriguez, H.; Louie, S. G.; Crommie, M. F.; Fischer, F. R. Topological Band Engineering of Graphene Nanoribbons. *Nature* **2018**, *560*, 204−208.
(673) Wang, X.; Ma, J.; Zheng, W.; Osella, S.; Arisnabarreta, N.; Droste, J.; Serra, G.; Ivasenko, O.; Lucotti, A.; Beljonne, D.; Bonn, M.; Liu, X.; Hansen, M. R.; Tommasini, M.; De Feyter, S.; Liu, J.; Wang, H. I.; Feng, X. Cove-Edged Graphene Nanoribbons with Incorporation of Periodic Zigzag-Edge Segments. *J. Am. Chem. Soc.* **2022**, *144*, 228−235.
(674) Xu, K.; Urgel, J. I.; Eimre, K.; Di Giovannantonio, M.; Keerthi, A.; Komber, H.; Wang, S.; Narita, A.; Berger, R.; Ruffieux, P.; Pignedoli, C. A.; Liu, J.; Müllen, K.; Fasel, R.; Feng, X. On-Surface Synthesis of a Nonplanar Porous Nanographene. *J. Am. Chem. Soc.* **2019**, *141*, 7726−7730.
(675) Yankowitz, M.; Ma, Q.; Jarillo-Herrero, P.; LeRoy, B. J. Van der Waals Heterostructures Combining Graphene and Hexagonal Boron Nitride. *Nature Rev. Phys.* **2019**, *1*, 112−125.
(676) Waterman, K. C. *Handbook of Stability Testing in Pharmaceutical Development: Regulations, Methodologies, and Best Practices*; Huynh-Ba, K., Ed.; Springer New York, New York, 2009; pp 21−41.

https://doi.org/10.1021/acs.chemrev.2c00270
Chem. Rev. 2022, 122, 17241−17338